Cobalt core-shell nanoparticles as precursors for cobalt-based Fischer-Tropsch synthesis catalysts

Alisa Govender

MSc. (Chemistry), University of Kwa-Zulu Natal

Thesis submitted to the University of Cape Town in fulfilment of
the requirements for the degree of
Doctor of Philosophy

Catalysis Research Unit
Department of Chemical Engineering
Rondebosch
December 2018

Declaration

I, Alisa Govender, certify that this submission is my own, unaided work, except for the information obtained from literature sources, my prescribed supervisors and my collaborators for external analyses. All sources of information have been adequately acknowledged and referenced. I have not received assistance from any other source in completing this submission.

Signature: Signed by candidate Date: 04 December 2018

A. Govender

Declaration: Inclusion of publications in thesis

I, Alisa Govender, hereby confirm that I have been granted permission by the University of Cape Town's Doctoral Degrees Board to include the following publication(s) in my PhD thesis, and where co-authorships are involved, my co-authors have agreed that I may include the publications(s):

1. Alisa Govender, Werner Barnard, Ezra J. Olivier, Roy P. Forbes, Eric van Steen and Johannes H. Neethling, Synthesis and characterization of $NiFe_2O_4@Co_3O_4$ core-shell nanoparticles, *Mater. Charac.*, 121 (2016) 93 – 102, DOI: 10.1016/j.matchar.2016.09.036.

2. Alisa Govender, Ezra J. Olivier, Emanuela Carleschi, Eric Prestat, Sarah J. Haigh, Hendrik van Rensburg, Bryan P. Doyle, Werner Barnard, Roy P. Forbes, Eric van Steen and Johannes H. Neethling, Exploring $MFe_2O_4@Co_3O_4$ (M = Ni, Zn) core-shell nanoparticles as precursors for Fischer-Tropsch catalysts, *Submitted*.

3. A. Govender, E. J. Olivier, S. J. Haigh, D. Kelly, M. Smith, H. van Rensburg, R. P. Forbes, E. van Steen and J. H. Neethling, The influence of mild reduction conditions on the Fischer-Tropsch synthesis performance of $NiFe_2O_4@Co_3O_4$ core-shell nanoparticles, *To be submitted*.

4. A. Govender, E. J. Olivier, E. Carleschi, H. van Rensburg, B. P. Doyle, J. van de Loosdrecht, R. P. Forbes, E. van Steen and J. H. Neethling, Silica supported $NiFe_2O_4@Co_3O_4$ core-shell nanoparticles for Fischer-Tropsch synthesis, *To be submitted*.

Signature: Signed by candidate Student number: GVNALI002 Date: 04 December 2018

A. Govender

Acknowledgements

First and foremost, I would like to thank God for helping me through this PhD journey and guiding me toward achieving this long-time goal. Then, I would like to say thank you to my son Cadence Zachariah for bearing with me through the years of studying. You were a toddler when I started and may my journey teach you to never give up, to keep on trying and to believe in yourself. I am thankful to my parents, especially my mom, Ronica Govender, who always motivated me. I also thank my husband, Calvin Naidoo for his support. I would also like to thank my supervisors, Professor Eric van Steen, Dr Jaco Olivier, Dr Roy Forbes and Professor Jan Neethling for their support, teachings and guidance.

I am extremely grateful to Sasol Group Technology for funding my research, allowing me time to work on my PhD and giving me access to their research facilities. More so, I would like to thank Dr Petrie Steynberg for ensuring that I got the opportunity to study whilst working. Dr Pheladi Mohlala is thanked for motivating me to pursue the opportunity of studying through Sasol. I would also like to thank Dr Tracy Bromfield, Willem Erasmus, Khedaren Govender, Dr Glenda Webber and Dr Cathy Dwyer for ensuring that my studies were funded and that I had the necessary support.

Through this PhD, I have seen the goodness of people and how helpful my colleagues are at R & T. Many people have guided me, listened to my challenges and provided avenues to look at that I did not think of. They also trained me on equipment and data analysis and were available to assist at any time. These people are: Dr Jana Potgieter, Melene Hauman, Jolandie Davel, Dr Zandile Chonco, Dr Denzil Moodley, Dr Jan van de Loosdrecht, Dr Pheladi Mohlala, Dr Pieter Barnard, Dr Thabiso Phadi, Khosi Mthembu, Gerda de Jager, Letisha Naicker, Dr Stanley Manzini, Bongani Xaba, Dr Werner Barnard, Dr Leigh-Anne de Jongh-Daly, Dr Esna du Plessis Dr Matthew Coombes and Marietjie du Toit-Meyer. My friends and colleagues, Harry Moloto, Moses Leakwe, Dr Leigh-Anne de Jongh-Daly, Dr Mzamo Shozi, Letisha Naicker, Dr Tanya Hughes and Dr Veronica Patterson, are thanked for their support and encouragement. I would like to mention Dr Daleen van Dyk who, during the times of difficulty with writing up, gave me advice and constantly asked how it was going, and that propelled me to keep going.

Lastly, Bongani Xaba and Dr Werner Barnard were the biggest support during my research. They have seen the blood, sweat and tears that led to the culmination of this goal. Thank you to you both.

Presentations and publications

Poster presentation

1. Syngas convention 2018, Cape Town, South Africa
   $NiFe_2O_4@Co_3O_4$ core-shell nanoparticles for the Fischer-Tropsch synthesis

Oral presentations

1. Microscopy Society of Southern Africa 2016, Port Elizabeth, South Africa
   A direct route to the synthesis of $NiFe_2O_4@Co_3O_4$ core-shell nanoparticles

2. Sasol University Collaboration Seminar 2017, Johannesburg, South Africa
   $NiFe_2O_4@Co_3O_4$ core-shell nanoparticles for the Fischer-Tropsch synthesis

Publications resulting from this work

1. A. Govender, W. Barnard, E. J. Olivier, R. P. Forbes, E. van Steen and J. H. Neethling, Synthesis and characterization of $NiFe_2O_4@Co_3O_4$ core-shell nanoparticles, *Materials Characterization*, 2016, doi.org/10.1016/j.matchar.2016.09.036.
2. A. Govender E. J. Olivier, E. Carleschi, E. Prestat, S. J. Haigh, H. van Rensburg, B. P. Doyle, W. Barnard, R. P. Forbes, E. van Steen and J. H. Neethling, $MFe_2O_4@Co_3O_4$ (M = Ni, Zn) core-shell nanoparticles for Fischer-Tropsch synthesis, In preparation.
3. A. Govender, E. J. Olivier, S. J. Haigh, D. Kelly, M. Smith, H. van Rensburg, P. van Helden, T. T. Phadi, R. P. Forbes, E. van Steen and J. H. Neethling, The influence of mild reduction conditions on the Fischer-Tropsch synthesis performance of $NiFe_2O_4@Co_3O_4$ core-shell nanoparticles, In preparation.
4. A. Govender, E. J. Olivier, E. Carleschi, H. van Rensburg, B. P. Doyle, Jan van de Loosdrecht, R. P. Forbes, E. van Steen and J. H. Neethling, Silica supported $NiFe_2O_4@Co_3O_4$ core-shell nanoparticles for Fischer-Tropsch synthesis, In preparation.

Abstract

Core-shell nanoparticles may have an economic advantage over traditional nanoparticles as a catalyst, since the expensive, catalytically active material, which is subsurface, may be replaced with a cheaper counterpart. Furthermore, core-shell nanoparticles may be tailored to have a specific structure and composition at the nanoscale, due to a mixing of electronic properties of each phase and/or geometric effects. In this study, nickel ferrite ($NiFe_2O_4$) and zinc ferrite ($ZnFe_2O_4$) were chosen as core materials around which a cobalt (II, III) oxide (Co_3O_4) shell was grown. These ferrites were chosen due to their structural similarity to Co_3O_4 as this was expected to allow an epitaxial growth of the Co_3O_4 shell onto the ferrite core. Additionally, the difference in the lattice parameter between each ferrite core and the Co_3O_4 shell was postulated to introduce a varying degree of strain onto the shell, particularly after reduction when metallic cobalt should be present.

Core-shell nanoparticles with either a nickel ferrite ($NiFe_2O_4$) core or a zinc ferrite ($ZnFe_2O_4$) core and a cobalt (II, III) oxide (Co_3O_4) shell ($NiFe_2O_4$@Co_3O_4 and $ZnFe_2O_4$@Co_3O_4 respectively) were synthesized, characterized and tested for their performance in the Fischer-Tropsch synthesis. These core-shell systems were compared to each other to evaluate the influence of the core and the applicability of $NiFe_2O_4$ or $ZnFe_2O_4$ as core nanoparticles in a cobalt-based Fischer-Tropsch catalyst. $NiFe_2O_4$@Co_3O_4 core-shell nanoparticles were also supported on Stöber silica spheres to determine the effect of the support on its properties and performance. The influence of two different reduction conditions, *viz*. 180°C (1 hour) or 230°C (2 hours), on the structure and Fischer-Tropsch synthesis performance of unsupported and Stöber silica spheres supported $NiFe_2O_4$@Co_3O_4 core-shell nanoparticles was also studied.

Prior to the preparation of the core-shell nanoparticles, each ferrite core was prepared using the citrate precursor method. A Fe/M mole % ratio (where M is Ni or Zn) of 2.3 and calcination temperature of 450°C yielded phase pure $NiFe_2O_4$ or $ZnFe_2O_4$ nanoparticles with an average size of 14 nm. Using nickel ferrite ($NiFe_2O_4$) nanoparticles as a core, the growth of cobalt (II, III) oxide (Co_3O_4) around the core was studied by following a homogeneous precipitation synthesis. It was established that a two-step synthesis route was needed to synthesize the core-shell material with a fairly uniform Co_3O_4 shell. It was found that for both $NiFe_2O_4$@Co_3O_4 and $ZnFe_2O_4$@Co_3O_4 core-shell nanoparticles, the as-synthesized materials had a Co_3O_4 shell around the ferrite core with an average thickness of 2 nm.

$NiFe_2O_4$@Co_3O_4 and $ZnFe_2O_4$@Co_3O_4 core-shell nanoparticles were compared to each other as precursors for Fischer-Tropsch synthesis catalysts. Here, the first report on the nanoscale restructuring during reduction of these core-shell nanoparticles in pure hydrogen at 230°C and 250°C, respectively, was observed. This resulted in the formation of small cobalt islands on the ferrite surface. Catalytic testing of the core-shell materials, $NiFe_2O_4$@Co_3O_4 and $ZnFe_2O_4$@Co_3O_4, after reduction showed a

cobalt-time yield of 13.64 $\mu mol_{CO} \cdot g_{Co}^{-1} \cdot s^{-1}$ and 4.27 $\mu mol_{CO} \cdot g_{Co}^{-1} \cdot s^{-1}$ and a C_{5+} selectivity of 47 C-% and 68 C-%, respectively. The observed difference in cobalt-time yield and selectivity between $NiFe_2O_4@Co_3O_4$ and $ZnFe_2O_4@Co_3O_4$ core-shell nanoparticles was due to a combination of effects that included the presence of cobalt islands over the surface of the core and the difference in extent of reduction of each core under Fischer-Tropsch synthesis conditions.

The core-shell structure in $NiFe_2O_4@Co_3O_4$ core-shell nanoparticles was found to be retained with the use of mild reduction conditions of 180°C (1 hour). Thus, the performance in the Fischer-Tropsch synthesis of a system with a true core-shell structure with a cobalt shell was established. The former has not been reported to date. Owing to the former, strain effects may have contributed to $NiFe_2O_4@Co_3O_4$ core-shell (reduced at 180°C, 1 hour) having a low cobalt-time yield of 8.40 $\mu mol_{CO} \cdot g_{Co}^{-1} \cdot s^{-1}$ and a C_{5+} selectivity of 38 C-% during the Fischer-Tropsch synthesis. It was also shown that $NiFe_2O_4@Co_3O_4$ core-shell nanoparticles reduced at 180 °C (1 hour) had a similar activity to unsupported Co_3O_4, however, the former had a higher C_{5+} selectivity. The differences in the performance between $NiFe_2O_4@Co_3O_4$ core-shell (reduced at 180°C, 1 hour) and unsupported Co_3O_4 may have been due to strain effects. The nanoscale structural and compositional differences induced by each reduction condition applied may have been the cause for the inferior Fischer-Tropsch synthesis performance of these core-shell nanoparticles after reduction at 180°C for 1 hour than 230°C for 2 hours.

The effect of a Stöber silica spheres support on the characteristics and Fischer-Tropsch synthesis behavior of $NiFe_2O_4@Co_3O_4$ core-shell nanoparticles was also investigated. Prior to characterization and the Fischer-Tropsch synthesis, $NiFe_2O_4@Co_3O_4/SiO_2$ was reduced at either 180°C for 1 hour or 230°C for 2 hours. A higher cobalt-time yield (23.80 $\mu mol_{CO} \cdot g_{Co}^{-1} \cdot s^{-1}$) with a lower C_{5+} selectivity (44 C-%) was obtained with reduction at 230°C (2 hours) than 180°C (1 hour). After reduction at 230°C (2 hours), the influence of the support was clearly seen due to the higher activity obtained with $NiFe_2O_4@Co_3O_4/SiO_2$. However, the unsupported and supported $NiFe_2O_4@Co_3O_4$ nanoparticles had similar product selectivities. After reduction at 230°C for 2 hours and exposure to Fischer-Tropsch synthesis conditions, the core-shell structure was retained in $NiFe_2O_4@Co_3O_4/SiO_2$ possibly due to reducing the contact between the individual core-shell nanoparticles due to the presence of the support. This would be enhanced by anchoring the core-shell nanoparticles onto the Stöber silica spheres support.

Table of contents

List of figures

List of tables

Nomenclature

Abbreviation	**Description**
ASF	Anderson-Schulz-Flory
BET	Brunauer-Emmett-Teller
BF-TEM	Bright Field-TEM
CHRTEM	Centre for High Resolution Electron Microscopy
CNF	Carbon NanoFibers
Cs	Spherical aberration
CSD	Crystallite Size Distribution
EDS	Energy Dispersive X-ray Spectroscopy
EELS	Electron Energy Loss Spectroscopy
FFT	Fast Fourier Transform
FID	Flame Ionization Detector
FT	Fischer-Tropsch
FTS	Fischer-Tropsch synthesis
HAADF	High Angle Annular Dark Field
HR-STEM	High resolution-Scanning Transmission Electron Microscopy
HTFT	High-Temperature Fischer Tropsch synthesis
LTFT	Low-Temperature Fischer Tropsch synthesis
L_{vol}-IB	Volume weighted average crystallite size determined from the Integral Breadth
MEMS	Micro-ElectroMechanical Systems
MWCNTs	Multi-Walled Carbon Nanotubes
PZC	Point of Zero Charge
S	Selectivity
SI	Spectrum Imaging
STEM	Scanning Transmission Electron Microscopy
SUK	Sasol United Kingdom
SV	Space Velocity
TCD	Thermal Conductivity Detector
TEM	Transmission Electron Microscopy
TEOS	Tetraethyoxysilane
TPD	Temperature Programmed Desorption
TPR	Temperature Programmed Reduction
XPS	X-ray Photoelectron Spectroscopy
XRD	X-ray powder Diffraction
ZLP	Zero Loss Peak

1 Introduction and literature review

Nearly a century ago, Franz Fischer and Hans Tropsch used the findings of Mittasch and Schneider to develop the technology nowadays known as the Fischer–Tropsch Synthesis (FTS) [1, 2]. In this reaction, synthesis gas derived from a suitable carbon source (coal, natural gas, biomass, or even municipal waste) is converted into long chain organic product compounds *via* a surface polymerization over a catalyst [3-6]. Both saturated and unsaturated hydrocarbons (linear and branched paraffin's and olefins) and oxygenates (alcohols, aldehydes, ketones, etc.) are produced in the reaction [3, 4]. Many researchers have focused on developing catalysts with high activity and selectivity to liquid products (often denoted as C_{5+}) since the Fischer-Tropsch synthesis is attractive for converting solid or gaseous feedstock into liquid fuels (e.g. diesel) [7, 8].

The production of valuable products from the Fischer-Tropsch synthesis has resulted in continued interest in the process. As a result, a number of commercial plants have been built and are in operation worldwide. Franz Fischer and Hans Tropsch researched the FTS for approximately 20 years before it was commercialized in the 1940s in Germany with plants operating at a capacity of over 600 metric tons per year [1]. Subsequently, a plant was built in Texas, which operated for six years (1951 – 1957) and one plant in Sasolburg, South Africa (Sasol, 1955). [1] Post the 1950s, various companies such as Shell, Sasol, PetroSA and Chevron, either as single or joint ventures, have built plants in different regions around the world (China, Malaysia, Qatar, Nigeria and South Africa). Locations such as China, Uzbekistan, USA and Qatar are possibilities for future developments. [1, 9-11]

1.1 The Fischer-Tropsch synthesis reactions

In the Fischer-Tropsch synthesis (Equation 1.1), the reactants hydrogen (H_2) and carbon monoxide (CO) are converted on the surface of a catalyst, into water and hydrocarbons of various chain lengths. The reaction is exothermic and involves a series of steps that can be grouped into chain initiation, propagation or termination reactions. Water is the main product by weight and by the number of moles formed, but of interest are the linear paraffins, olefins, oxygenates (alcohols, aldehydes, ketones, etc.) and branched paraffins which are also formed. [1, 12, 13] Iron-based catalysts are active for an additional reaction which is the water-gas-shift reaction (Equation 1.2). This property of these catalysts makes them desirable for the conversion of CO deficient gas feedstock such as those derived from coal. [1, 6, 13, 14]

$$\mathbf{CO + 2H_2 \rightarrow (\text{-}CH_2\text{-}) + H_2O \qquad \Delta H_{R,\ 513K} = -153.7\ kJ/mol \qquad Equation\ 1.1}$$

$$\mathbf{CO + H_2O \rightarrow CO_2 + H_2 \qquad \Delta H_{R,\ 513K} = -41.1\ kJ/mol \qquad Equation\ 1.2}$$

Equation 1.1 is a general description of the Fischer-Tropsch synthesis reaction. In reality, the Fischer-Tropsch synthesis is a complex set of surface polymerization reactions that occur when carbon monoxide that is adsorbed on the surface is hydrogenated into a C_1-species which acts as a monomer in this polymerization. The following reaction steps occur during the Fischer-Tropsch synthesis:

- Associative adsorption of CO
- Cleavage of the carbon-oxygen bond
- Dissociative adsorption of H_2
- Reaction of hydrogen with oxygen to yield water
- Desorption of water
- Hydrogenation of surface carbon and CH_x and
- Carbon-carbon coupling. [1, 12, 13]

The above reactions, although occurring on the catalyst's surface, may take place at various sites of the catalyst [13, 15-20]. Various mechanisms have been reported to describe the path that the set of FT reactions follow [1, 4, 21-28]. Four commonly accepted mechanisms are the 'alkyl'; 'alkenyl'; 'enol' and 'CO-insertion' mechanism. A detailed description of each is given by Claeys *et al.*[24]. Irrespective of the mechanism, the FTS leads to the production of various products with a particular distribution. The product distribution obtained during the Fischer-Tropsch synthesis can vary depending on the catalyst and operating conditions used. Two Fischer-Tropsch synthesis operating modes or conditions have traditionally been recognized. The first is the high-temperature Fischer-Tropsch synthesis (HTFT) which operates between 300 and 350°C over an iron catalyst and the second process which typically operates between 200 and 275°C is the low-temperature Fischer-Tropsch synthesis (LTFT) with either iron or cobalt as a catalyst. [1, 6, 13]

1.2 The Fischer-Tropsch product distribution

Due to the nature of the Fischer-Tropsch synthesis reaction [3-5], a variety of product compounds with various chain lengths are formed. Chain termination may lead to a variety of different products. [6] The main products of the reaction are α-olefins and n-paraffins with different oxygenates (alcohols, aldehydes, etc.) and branched compounds being formed as secondary products [3, 6, 24]. The type of products formed is not influenced by the operating conditions of the FTS however the distribution of these products can be influenced by temperature, feed gas composition, pressure, catalyst type and promoters [6].

Although the product distribution is influenced by various process parameters, the individual products tend to be connected in a manner that is independent of the process variables that were changed. This is since there is a step-wise growth process that occurs on the catalyst's surface (Figure 1.1) where CO molecules are the precursors to the C_1 monomer units. The hydrogenation of CO leads to the formation of CH, CH_2 and CH_3 species, which undergoes a stepwise oligomerization. During the growth process, the adsorbed hydrocarbon specie can either desorb, be hydrogenated or continue the oligomerization reaction.

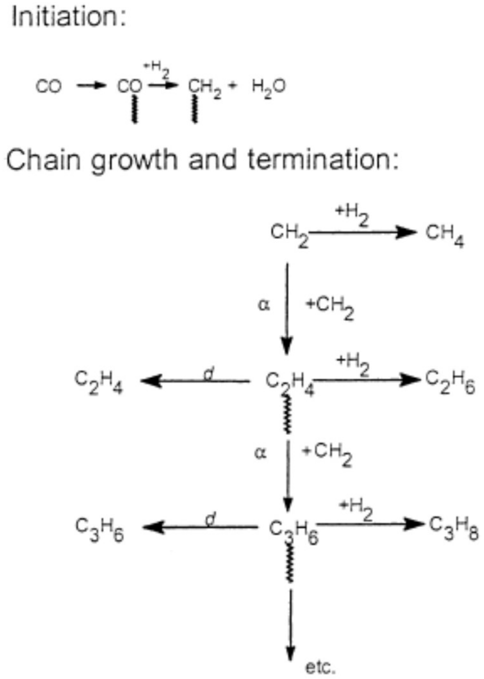

Figure 1.1. The proposed stepwise growth process using CH_2 species for the Fischer-Tropsch synthesis (adapted from [6]).

The stepwise growth which governs the polymerization reaction occurring during the FTS results in a high degree of order with the products following a statistical hydrocarbon distribution known as the Anderson-Schulz-Flory (ASF) distribution [6, 13, 24]. The ASF distribution can describe the product distribution and makes the Fischer-Tropsch non-selective for a desired range of hydrocarbons. This distribution is a function of the chain growth probability ($\alpha = \frac{R_p}{(R_p+R_t)}$) which is determined by the rates of chain growth (R_p) and chain termination (R_t). In the ideal case, the chain growth probability is independent of the carbon chain length [13]. Assuming an ideal chain growth, the molar fraction of a hydrocarbon with a chain length or carbon number of *n* in the total organic product spectrum can be expressed as [13]:

$$\mathbf{Mn = (1-\alpha)\alpha^{n-1}} \qquad \textbf{Equation 1.3}$$

The ideal polymerization reaction assumes the growth of only one type of product. In the ideal chain growth mechanism (Figure 1.2), CO and H_2 are adsorbed on the catalysts surface and form monomers and chain starters (C_1 surface species, Sp_1) after dissociation. These surface species can either desorb to form a C_1 product molecule (Pr_1) or continue to grow *via* the insertion of a C_1 monomer.[24]

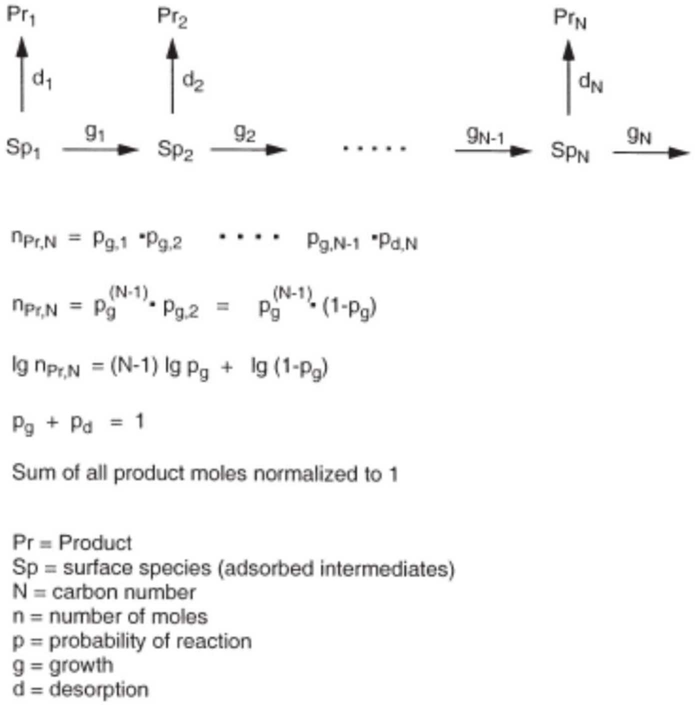

Figure 1.2. Ideal chain growth mechanism of the ideal Fischer-Tropsch polymerization model which assumes the formation of one class of product (adapted from [12]).

The intricacy of the surface polymerization reactions occurring during the FTS, often causes the ASF distribution obtained from real Fischer-Tropsch synthesis to deviate from ideality. This is mainly due to more than one product type being formed and the reversibility of the chain termination step [12, 24, 29]. Since the equation that describes the ASF distribution (Equation 1.3) is a function of the chain growth probability, changes to this value as a function of chain length [30] can result in deviations from ideality. Typical deviations from the ideal ASF distribution include a higher C_1 quantity, lower C_2 content and the curvature of the ASF distribution [24, 29, 31]. The deviation of the product distribution from the ideal one may be because of the presence of differently structured sites, promoter sites and 'frustrated' reactions [12, 32]. One example that is used to explain the deviation is the reversible nature of olefin desorption which results in secondary reactions. These reactions include hydrogenation, double bond isomerization, the incorporation into growing chains and to a lesser extent, hydroformylation and hydrogenolysis [24].

1.3 Fischer-Tropsch catalysts

Catalysts based on metals such as iron (Fe), cobalt (Co), nickel (Ni), ruthenium (Ru) and rhodium (Rh) have been found to be active for the Fischer-Tropsch synthesis [1, 3, 13, 14, 33]. Of these metals, higher activity with operating at a lower temperature (~150°C) can be obtained with Ru-based catalysts, thus producing high molecular weight products. However, due to its high cost and limited availability, Ru catalysts are not used industrially. [1, 13, 14] Like Ru, Ni-based catalyst are capable of producing high molecular weight products, however, with increasing temperature, the selectivity shifts mainly toward methane [1]. Industrially, both Co- and Fe-based catalysts are used. Cobalt-based catalysts also favor the formation of methane with increasing temperature, although to a lesser extent than Ni-based catalysts.

Iron-based catalysts are used for the low temperature Fischer-Tropsch reaction as well as the high temperature Fischer Tropsch reaction (Section 1.1). Iron is cheaper than cobalt and can be operated under a variety of temperatures and H_2/CO ratios with minimal impact on the methane selectivity. These catalysts, though, are prone to carbon dioxide formation and undergo rapid deactivation. Challenges still exist to overcome the former. A wide range of products (dependent on reaction conditions) is formed with these catalysts which include linear alkane fuels, alkenes and/or oxygenates. Promoters, such as K and Cu, are added to the catalyst to improve its performance [9, 13, 19, 34-36]. Iron-based catalysts are complex materials due to the combination of multiple elements and different metal oxide phases. It is generally accepted that under reaction conditions the catalyst is comprised of carbidic iron and iron oxides with each having a particular role during the Fischer-Tropsch synthesis [35, 37, 38]. Metallic iron and surface carbidic iron are speculated to each contribute to the overall activity of the iron based catalyst [35]. Various iron carbide phases exist in the iron FT catalyst and are made *in-situ* during activation (if carbon monoxide or syngas is used) or under FT reaction conditions. These carbides are Hägg carbide (χ-Fe_5C_2; forms above 250°C from Fe_2C); hexagonal carbide (ε-Fe_2C and ε'-$Fe_{2.2}C$; may form at low temperatures) and cementite (θ-Fe_3C; forms when χ-Fe_5C_2 decomposes above 450°C) [35, 39].

Despite its high cost, cobalt-based catalysts are used for the low temperature Fischer-Tropsch reaction to produce middle distillates and long-chain linear hydrocarbons [6, 9]. In comparison to iron-based catalysts, cobalt-based catalysts have a high activity at high level of CO conversion, high selectivity to linear paraffins, low water-gas shift activity and stability to deactivation by water. These catalysts are ideal for operating under a high H_2/CO ratio generated from natural gas due to their low propensity for the formation of CO_2 [5, 6, 9, 13, 33, 40]. In order to justify the higher costs associated with cobalt catalysts, it is necessary that they operate for a longer period of time and have a better overall productivity than iron catalysts. For this reason, cobalt is typically supported on an inorganic support such as silica, titania or alumina to increase the cobalt's surface area, stabilize the metallic cobalt against sintering during the

Fischer-Tropsch synthesis and maintain the mechanical integrity of the catalyst whilst allowing mass or heat transfer in a diffusion limited or exothermic reaction. The size of the cobalt crystallites is also optimized to enhance the cobalt's dispersion over the support. [6, 9, 13, 14, 33, 41, 42]

The optimization of the cobalt crystallite size is on the basis that the rate of the Fischer-Tropsch synthesis is proportional to the active metal surface area for dispersions less than 10%. Although early work by Borg *et al*.[43] found that there was no correlation between the cobalt crystallite size and the cobalt site-time yield it was later established by Bezemer *et al*.[7] that the intrinsic activity (activity per unit surface area) varied with crystallite size with a maximum in the mass specific activity as a function of crystallite size being in the range of 6 – 8 nm. For optimum FT activity, certain sites on the cobalt metal surface should be exposed. As a result, Bezemer *et al*.[7] proposed that such sites may be unstable or present in inadequate ratios when crystallites become too small. Den Breejen *et al*.[44] found that low-coordinated surface sites was present for crystallites smaller than 6 nm and sites that contribute to the FT activity were blocked whilst small terrace sites that result in a low intrinsic activity, were present. It should also be noted that low (<50%) C_{5+} selectivity can be evidenced when the cobalt crystallite size is smaller than 6 nm. Fischer *et al*.[45] also showed the dependency of the intrinsic activity on the cobalt crystallite size. However, they found a maximum intrinsic activity with cobalt crystallites with a size of 4.7 and 6.3 nm. Their work also looked at the impact of the crystallite size on the selectivity to the various FT products and showed that the C_{5+} selectivity decreased with decreasing crystallite size. Prieto *et al*.[46] supported the notion that the intrinsic activity increases with an increase in cobalt crystallite size.

Apart from the optimization of the cobalt crystallite size as a means to improve the performance of the catalyst, the addition of promoters such as platinum or ruthenium can also be done. These metals are used to modify the chemical properties of the catalyst, usually by increasing the degree of reduction. Furthermore, the dispersion of the cobalt metal can be improved with the use of an appropriate metal promoter. This allows for the activity of the catalyst to be tuned as a means to justify its cost. [7, 13, 47-50] The development of regenerative procedures of deactivated cobalt catalysts is another measure taken to improve the overall economics of the cobalt-based Fischer-Tropsch process [51].

Another method to lower the cost of the cobalt-based catalyst is to replace sub-surface cobalt in the catalyst, which is not directly involved in the reaction, with a cheaper alternative. In an industrial catalyst, only *ca*. 12% of cobalt should be on the surface [7, 43, 44, 46, 52]. Cobalt, which is not on the surface is not directly involved in the reaction, and may thus be replaced by a less expensive material. This would result in the formation of a core-shell catalyst, in which the shell of cobalt is combined with a core of a less expensive material.

1.4 Core-shell nanoparticles

Core-shell materials can be described as nanoparticles that comprise of a core (inner shell material) and a shell (outer layer material) (Figure 1.3). Core-shell nanoparticles are characterized by their modified properties, which differ from their individual or alloyed counter-parts, and is created by employing two different materials. The active-phase topology is tailored to have a specific structure and composition at the nanoscale but in a manner that allows for scale up [53-55]. The core can vary in size and shape and the shell can have different thicknesses and surface morphology [54-62]. The constituting material may also be changed to alter the core-shell nanoparticle's properties [55]. The general understanding is that these materials have new electronic, geometric and catalytic properties and can be stable during the reaction [54, 63-65]. However, a proper understanding of its characteristics that justifies this behavior is lacking. The core and shell may each be comprised of a different material yielding classifications which are (a) inorganic/inorganic; (b) inorganic/organic; (c) organic/inorganic and (d) organic/organic.[55] The varying classification of such nanoparticles allows for them to be used in various fields such as medical biotechnology and catalysis [54-62].

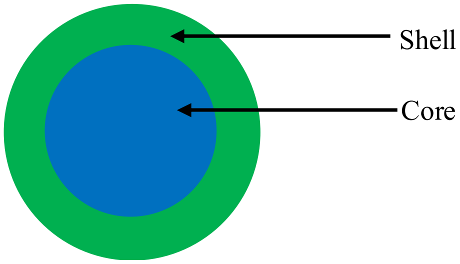

Figure 1.3. Schematic of a spherical core-shell nanoparticle (adapted from [56]).

The uniqueness of the properties of the core-shell nanoparticles has made it an area of growing interest in recent years. Furthermore, such materials are important from an economic point of view as expensive or rare materials can be coated over inexpensive materials to reduce the overall cost and consumption of the expensive material [55, 61]. As an example, a core comprised of a nickel-iron oxide ($NiFe_2O_4$) of approximately 14 nm in size with a 3 nm cobalt oxide shell (core/particle radius of 0.8) could yield a cost saving of 75% on the raw material cost in comparison to cobalt oxide (see Figure 1.4). It is also worth noting that cost savings can still be achieved upon increasing the cobalt oxide shell thickness (keeping the core radius constant).

Different types of core-shell structures exist (see Figure 1.5) with the most common type being the spherical core-shell nanoparticle. Shaped nanoparticles are also of interest and require that the core material be first synthesized with the shape required for the core-shell material (rod-shaped, hexagonal, etc.) [57-

60, 62]. Other types of core-shell structures such as multi-layered or hollow structures (Figure 1.5 (d) and (e)) require the use of spacers or materials that can be removed after the desired structure is obtained.[55]

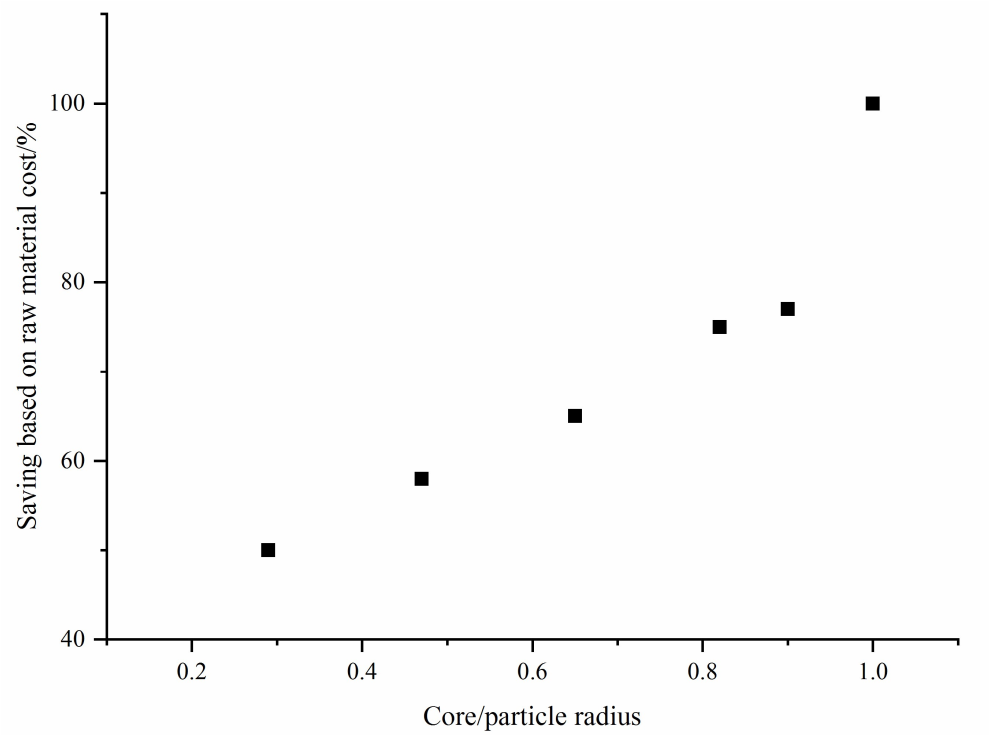

Figure 1.4. Comparing raw material cost saving for the production of spherical core-shell nanoparticles with a $NiFe_2O_4$ core of a constant size of 14 nm and a cobalt oxide shell.

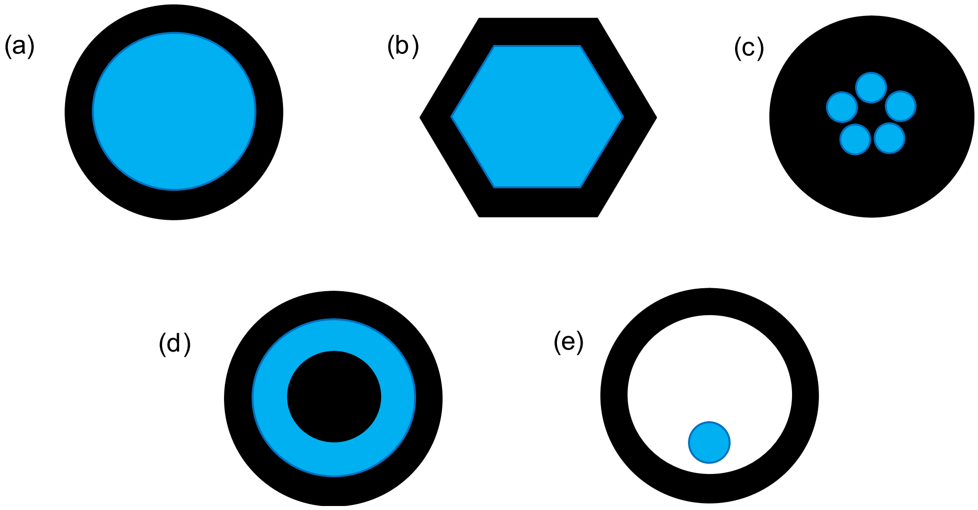

Figure 1.5. Different core-shell structures: (a) spherical, (b) hexagonal; (c) Single shell coating multiple core materials; (d) multi-layered and (e) hollow shell material with a movable core (adapted from [55]).

1.4.1 Synthesis of core-shell nanoparticles

Chaudhuri and Paria [55], Kumar *et al*. [61] and Gawande *et* al.[66] reviewed the various synthesis methods that have been used to prepare different core-shell nanoparticles. This work focused on the preparation of core-shell nanoparticles that had an inorganic core and shell and routes to form such nanoparticles are summarized in Figure 1.6. Such nanoparticles may either have a silica-based or metal-based shell [55, 66] and therefore a number of synthesis routes can be used to prepare these nanoparticles (see Figure 1.6).

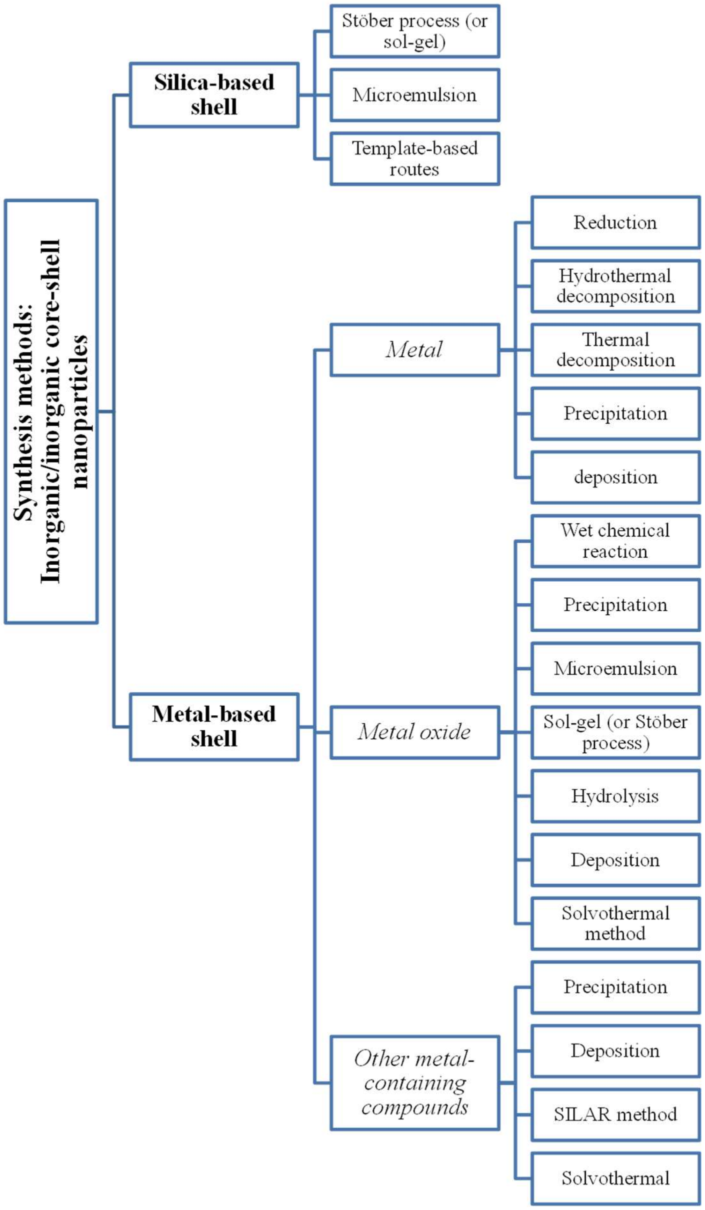

Figure 1.6. A list showing the various synthesis routes applied for the formation of inorganic/inorganic core-shell nanoparticles (adapted from Gawande *et al*.[66]).

Of particular focus in this work is the formation of a metal oxide shell as well as a metal oxide core. Such materials can be prepared using sol-gel, precipitation, deposition, hydrolysis or solvothermal routes. This does require that the core material is synthesized first and the shell material is then grown on its surface. In this regard, it was of interest in this work, to form core-shell nanoparticles with a cobalt oxide (Co_3O_4) shell. Calderone *et al*. [54] documented the synthesis of Fe_3O_4@Co_3O_4 core-shell nanoparticles where a precipitation reaction using sodium hydroxide and cobalt nitrate solutions as reactants was used to form cobalt oxide on pre-made magnetite crystallites. The authors state that a cobalt oxide shell was present around the magnetite core as determined using EDX line scans. In a separate work, these authors described a homogeneous deposition-precipitation reaction for preparing core-shell nanoparticles with a cobalt shell [67]. In this synthesis route, cobalt carbonate, ammonium carbonate and ammonia solution were used as reactants which form ammine or ammine carbonate complexes. No clear indication of the properties of the core-shell nanoparticle was provided however the cobalt oxide can be easily obtained.

The homogeneous deposition-precipitation reaction used by Calderone *et al*.[67] allows for the concentration of the metal precursor in solution to gradually increase during the evaporation process. As a result, the initial pH of the reaction mixture is high. Upon heating at temperatures above 70°C, ammonia evaporates which results in a drop in the pH and induces the precipitation of hydroxyl carbonate species onto the support. The precipitate can be aged for a period of time in solution. Due to the high pH, the surface charge of the support is negative and allows for an interaction between the metal cations and the charged support surface. These adsorbed cations may become nucleation sites for the deposition of the hydroxyl carbonate compounds formed during the evaporation of ammonia.[68]

The advantage of homogenous deposition precipitation over the traditional precipitation reaction is that it involves the slow and homogeneous addition/generation of the precipitating agent to/in the reaction mixture. By doing so, the active phase is deposited onto the surface of the support [69]. A vital condition to the success of the synthesis is that bulk precipitation in solution should be avoided [70]. The presence of the support in solution does aid in shifting the precipitation toward surface precipitation by reducing the surface free energy of small nuclei or by stabilizing the precipitate [70]. Another parameter that should be considered to minimize or prevent bulk precipitation is the concentration of the metal solution which should be below super saturation [70]. Since surface precipitation may be achieved with deposition-precipitation by ammonia evaporation, this synthesis route was a promising option to investigate in this study for the formation of core-shell nanoparticles.

1.5 Core-shell nanoparticles as catalysts

Traditional supported catalysts have been used for various reactions and its structural properties may be optimized to obtain a desirable activity, selectivity and stability to ensure an economically viable overall process [71]. The productivity of supported catalysts has been altered by changing the dispersion of the active metal over the support surface, promotion with a noble metal and the use of bimetallic catalysts [6, 14, 41, 42, 72]. However, current interest has been in the use of core-shell nanoparticles as an alternative for an efficient catalyst [71]. Core-shell nanoparticles have amongst others been used to catalyze reactions such as hydrolytic dehydrogenation of ammonia borane [56, 73-77], photocatalysis [78-80], oxygen reduction reaction [81-86] and preferential CO oxidation [87, 88]. Both the activity and selectivity obtained with core-shell catalysts may differ from the one obtained with pure metal catalysts. This is mainly due to the effect of the core material on the active metal shell in a manner that induces structural change (geometric effects, e.g. due to lattice strain) and/or electronic change [54, 63-65, 89-93]. The core material and the thickness of the active metal shell could impact whether none, one or both of these effects play a role.

More specifically, in the Fischer-Tropsch synthesis over cobalt-based catalysts, core-shell nanoparticles have been studied as catalyst precursors for the reaction [54, 67, 94-99]. In particular, systems with cobalt in the core and ruthenium or a metal oxide as a shell, seems to result in an increased activity. Haghtalab and Mosayebi [100] prepared core-shell nanoparticles containing a CoO core and a RuO_2 shell (Co@Ru) on the surface of γ-Al_2O_3. The variation in the Co/Ru weight ratios resulted in the formation of core-shell nanoparticles with RuO_2 shell thicknesses in the range of 4 nm – 7 nm and a CoO core diameter between 13 nm and 15 nm. It was seen that the CO conversion and selectivity to heavier hydrocarbons was improved upon increasing the Ru shell thickness. The methane selectivity was minimized and reached a plateau when the Co/Ru weight ratio was 2.5. In comparison to Co/γ-Al_2O_3, favorable changes to the catalyst performance was seen and was attributed to a close interaction between Co and Ru that caused a strong electronic interaction to the shell surface atoms [100].

Xie *et al.*[98] reported on the use of core-shell nanoparticles with a Co_3O_4 core and an inactive mesoporous silica shell (Co_3O_4@*m*-SiO_2). This type of core-shell nanoparticles present an advantage in the protection and modification of the active metal core as well as in the change in catalytic performance due to the space-confined structure imposed by the mesoporous shell. These core-shell nanoparticles showed a CO conversion of 61% which was 15% higher than the traditional supported catalyst system and the methane selectivity was also low (14%). In other work, Xie *et al.* [99] incorporating an additional shell layer comprising of carbon resulting in a higher CO conversion (65%), superior stability and higher selectivity toward the C_5 – C_{18} fraction (70%). Kruse *et al.*[97] prepared core-shell nanoparticles with a zeolite shell, however a marginal increase in the methane selectivity during the Fischer-Tropsch synthesis was observed. Qin *et al.*[96] found that the use of a carbon-based shell around the cobalt core yielded a favorable change to the catalytic behavior due to a reduced hydrogen dissociative adsorption energy and the presence of graphitic carbon which may enhance electronic conductivity between the Co metal and CO molecules thereby altering the activity and selectivity seen during the FTS.

Wang *et al.*[95] took a different approach in the design of their catalysts for the Fischer-Tropsch synthesis. In their work, a core-shell support, Al_2O_3@Al composite was used for preparing Co/Al_2O_3@Al. The performance of this material was compared to the traditional alumina support cobalt catalyst, Co/Al_2O_3. It was found that core-shell structured catalyst had a higher CO conversion and C_{5+} selectivity whilst the CH_4 and CO_2 selectivity was low. The lower CH_4 and CO_2 selectivity was attributed to the macro-mesoporous structure of the support.

Systems with a cobalt oxide shell around a metal oxide has also shown promise as an efficient catalyst for the Fischer-Tropsch synthesis [54, 101]. Calderone *et al.*[54, 67] reported on the coating of a Fe_3O_4 core with a cobalt-rich shell which was confirmed using High Resolution-Transmission Electron Microscopy (HR-TEM) together with the energy dispersive X-ray spectroscopy (EDX). However, it should be noted that both Fe_3O_4 and Co_3O_4 have a similar average atomic number and density and thus phase identification based on contrast difference only is difficult. Furthermore, the EDX line scan showed the presence of Co and Fe throughout the whole particle, with an implied Co/Fe ratio in the shell of *ca.* 1 and in the core of *ca.* 0.7. The resulting catalyst, obtained after supporting the core-shell nanoparticles on alumina, was tested for the Fischer-Tropsch synthesis at 240°C and 20 bar pressure and a selectivity of 40% to $C_5 – C_{27}$ was obtained at 20% CO conversion. This catalytic performance though was obtained after reduction of the nanoparticles in hydrogen at 435°C for 10 hours although the temperature programed reduction showed that at this temperature, both the Fe_3O_4 and Co_3O_4 would be reduced possibly destroying the core-shell structure during activation. Hence, the observed performance may have been due to the intrinsic activity of both cobalt and iron. More recent work by Calderone and co-workers [101] reported similar results on the synthesis and characterization of such core-shell nanoparticles. The core, however, was either magnetite or hematite and a mesoporous silica was used as the support. In this work, they claimed, based on the TPR profiles, that the presence of the support may have been beneficial for retaining the core-shell structure under reducing conditions.

Anchoring of core-shell nanoparticles on supports such as carbon and alumina might be beneficial [54, 94, 95, 99, 100, 102-108]. Similar to traditional catalysts, the advantage of utilizing a support lies in the stabilization of the active metal crystallite and in improving its dispersion and metallic surface area. [9] Owing to the former, it was shown by Beltram *et al.*[103] and Yang *et al.*[109] that an improved catalytic performance could be obtained by supporting Pd@CeO_2 and Ni_{1-x}@Pt_x core-shell nanoparticles, respectively, onto a carbon-based support. The support may also induce structural and electronic changes to the active metal, improve the mechanical integrity of the catalyst and influence the diffusion of reactants and products.[9] The presence of a support was also shown to limit the migration and aggregation of the elements in the core-shell nanoparticles [89]. Other possibilities that have been demonstrated is that the use of a support for core-shell nanoparticles may allow mass diffusion/transportation and maintain stability and recyclability by minimizing hotspot formation [110]

1.5.1 The effect of lattice strain on the catalytic behavior of core-shell catalysts

With core-shell catalysts being comprised of two different materials, a difference in the lattice constants of these materials may exist. This will result in strain in the contact region. The type of strain (compressive *versus* tensile) might alter the adsorption properties on the surface of the shell [13, 53, 111-114] as shown for the oxygen reduction and methanol oxidation [13, 53, 90, 102, 111-118].

Lattice strain may affect the catalytic behavior of metals by altering the adsorption energy and subsequent dissociation of molecules as predicted using density functional theory [111, 114, 115, 119]. Bhattarai *et al.*[120] and Zhang *et al.*[118, 120] showed that changes to the thickness of the shell material may also influence the properties of the shell material by altering the compressive strain. Lattice strain may also alter the electronic structure of the metal by causing a shift in the center of the metal *d* band, which plays an important role in the interaction between the surface and the adsorbate. Zhang *et al.*[53] deduced that compressive strain would result in a downshift of the center of the *d*-band (ε_d) whilst the opposite is the case for tensile strain (narrowing brings the *d* band closer to the Fermi level) [53, 91]. Furthermore, compressive strain leads to a greater overlap between electrons and a widening of the *d* band whilst an expansion reduces the *d*-orbital and the *d* band narrows [91]. The *d*-band structure of a metal, specifically, the center of the *d*-band (ε_d), is an important parameter characterizing the surface reactivity since the surface *d*-electrons participate in bonding to the adsorbate. This parameter together with other surface properties (degree of filling of the bands (f_d) and coupling matrix element between the adsorbate states and the metal d-states (V_{ad})) governs the ability of the surface to form and break adsorbate bonds. Thus, the surface reactivity of the active metal is affected thereby influencing the catalytic performance.[121]

Characterization techniques such as HR-TEM and X-ray diffraction (XRD) have also been used to study the presence of lattice strain. Chen *et al.*[117] showed the presence of lattice compression in the Pt lattice for Ru-Pt and lattice expansion in the Pt shell for the Co-Pt core-shell catalysts using X-ray diffraction (XRD) and HR-TEM. Aberration-corrected high-resolution transmission electron microscopy (Cs-HRTEM) was used by Gan *et al.*[113] which showed the lattice strain distributions in individual dealloyed Pt-Fe catalyst nanoparticles. This was done by representing the lattice contraction in the nanoparticles as a two-dimensional map of the lattice strain relative to bulk Pt on the Ångstrom scale (Figure 1.7). The lattice strain map, shown in Figure 1.7 revealed a percolated lattice-contracted Pt-Fe core and a Pt shell in the core-shell catalysts relative to the bulk Pt nanoparticle. The lattice contraction in the core caused a gradient compressive strain in the Pt shell indicating a possible strain effect that may account for the enhanced oxygen reduction reaction activity [113, 120].

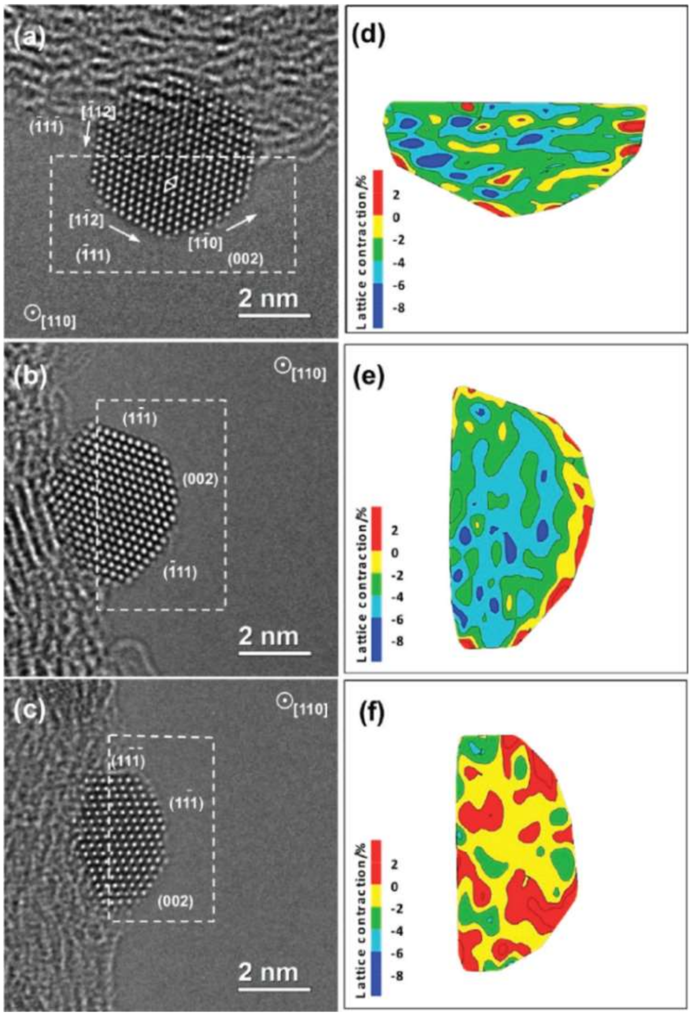

Figure 1.7. Cs-HRTEM images of: (a) and (b) dealloyed Pt-Fe nanoparticles and (c) pure Pt nanoparticle with (d) – (f) showing the maps of the lattice contraction relative to the bulk Pt lattice in the dashed rectangle of (a) – (c). Re-used with permission from [113]. Copyright (2012) American Chemical Society.

1.5.2 The effect of electronic structure changes on the catalytic behavior of core-shell catalysts

Another fundamental effect that can arise in a core-shell catalyst is the ligand effect. This effect is caused when two dissimilar surface metal atoms are close to each other inducing electronic charge transfer between atoms thereby affecting their electronic band structures [119]. Such changes to the electronic structure of the shell's material in core-shell catalysts for various reactions have been linked to increases in the core-shell catalyst's activity [87, 89, 91-93, 115, 117, 122-126].

Heemeier and co-workers [127] demonstrated that electronic aspects affect the strength of CO-adsorption by observing a lowering of the desorption temperature, compared to the parent counterpart, in the CO-TPD for Co-Pd/Al_2O_3 where Co covers the Pd core. Structural effects may also have resulted in a change in the desorption temperature [127]. Charge transfer between core and shell elements have been confirmed using X-ray absorption near edge spectroscopy (XANES) for PtNiN [115] and Ru-Pt and Co-Pt [117] core-shell materials. This effect can also be studied experimentally using X-ray photoelectron spectroscopy (XPS) [125, 128].

Changes to the dissociative adsorption and binding energy of reactant molecules due to electronic effects can be studied using DFT. This was used by Tang *et al.*[91] to study core-shell nanoparticles, with a Pd shell and either a noble metal, Co or Mo core, for the oxygen reduction reaction. They calculated the energetics of the dissociative oxygen adsorption on core-shell nanoparticles with a 1 nm Pd shell and determined the correlation between the binding energy of oxygen with the center of the *d* band. Tang *et al.*[91] further studied the observed enhanced reactivity of the Pd@Co and Pd@Mo core-shell nanoparticles by examining strain and ligand effects. Strain was measured as the average bond length between Pd surface atoms and plotted as a function of the *d* band center (Figure 1.8 (a)). It was also shown that there was a relationship between the *d*-band width and the *d*-band center (Figure 1.8 (b)) where a lowering of the *d*-band center occurred due to band broadening and band filling from charge redistribution. They stated that as two metals are placed in close contact with each other, charge would flow from the metal with the higher Fermi level to the lower [91]. Both geometric and ligand effects were responsible for the improved catalytic behavior of the Pd shell. Additionally, the *d* band center, *d* band width, charge redistribution and the presence of strain are inter-related and should be considered when the catalytic behavior of a core-shell catalyst needs to be understood [91].

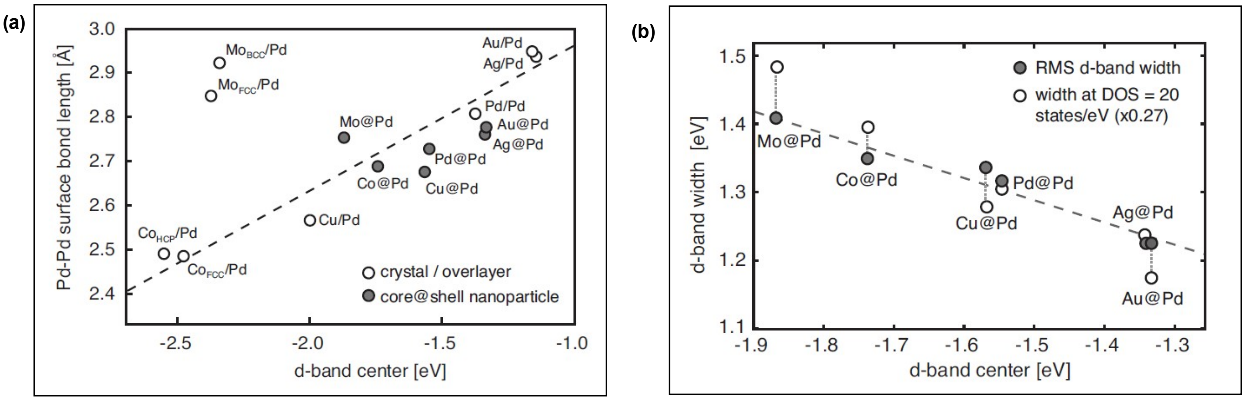

Figure 1.8. **A**verage surface bond length between Pd atoms and (a) the center of the *d* band and the *d*-band center and width (b) as a function of the *d*-band center. Re-used with permission from [91]. Copyright (2009) AIP Publishing LLC.

1.5.3 Core-shell catalysts resistance to deactivation

The initial catalytic activity of a material may be surprisingly high, but of great importance is always whether the activity and/or selectivity remain over a long period of time. In the case of core-shell catalysts, Calderone *et al.*[54] observed a more stable CO conversion in the Fischer-Tropsch synthesis with Fe_3O_4@Co_3O_4 core-shell catalysts compared to Fe_3O_4 nanoparticles; however no reasoning for the observation catalytic stability was provided (Figure 1.9). Xie *et al*.[99] also showed that the CO conversion remained fairly constant for the duration of the Fischer-Tropsch synthesis with Co_3O_4@C-*m*-SiO_2 core-shell nanoparticles (Figure 1.10). The lack of catalyst deactivation seen was linked to presence of two shell layers that resulted in a confined structure. Similar results were seen by Qin *et al*.[96] where a slow drop in CO conversion during the Fischer-Tropsch synthesis was seen with Co@C core-shell nanoparticles in comparison to Co supported on activated carbon. The improved stability obtained was attributed to the graphite framework of the carbon shell which may have restricted the aggregation of the cobalt nanoparticles in the core during activation and reaction processes. Similar discussions were presented by Li *et al.*[129] in their review of the resistance to deactivation of various core-shell nanoparticles. The reactions covered in this review were syngas production, CO oxidation and high temperature fuel cells. It was also demonstrated by Lucchini *et al*.[130] where nickel nanoparticles were coated with a porous silica shell that no sintering nor coke formation was evidenced during CO methanation. A similar observation was made by Wei *et al*.[131] for Au@Pt core-shell nanoparticles used in the oxidation of soot and by An *et al*.[132] for SiO_2@Pt@SiO_2 core-shell nanoparticles used in the catalytic reforming of *n*-hexane (see Figure 1.11). It was also noted by An *et al.*[132] that an incomplete shell, as was the case for the SiO_2@Pt@TiO_2 core-shell system, resulted in the sintering of the Pt nanoparticles (Figure 1.11). Other researchers have also reported that the activity obtained with core-shell nanoparticles remains stable during the reaction under investigation and/or after multiple recycles [115, 129-138].

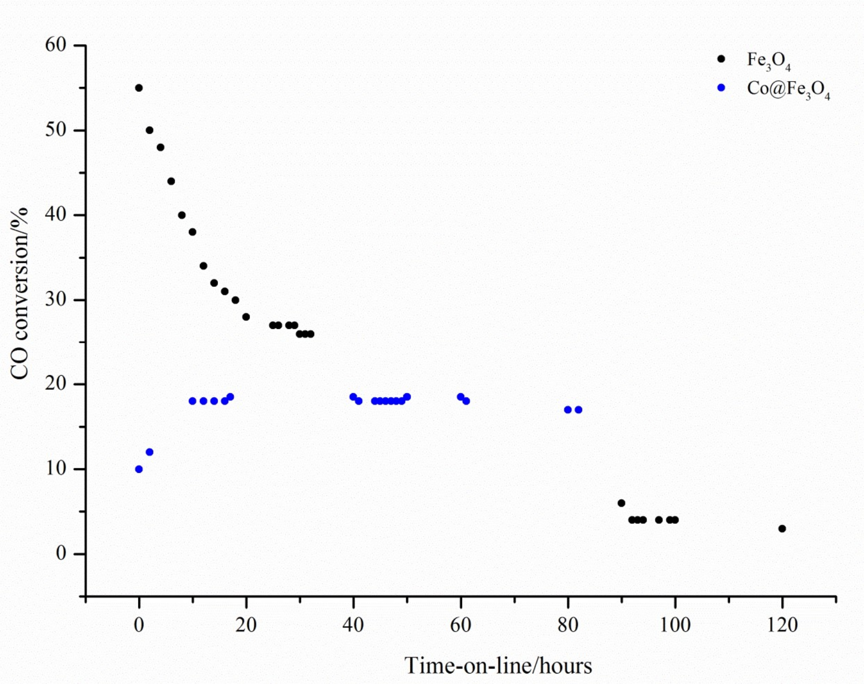

Figure 1.9. Performance of $Co@Fe_3O_4$ in the Fischer-Tropsch synthesis at 240°C and 20 bar [54]. Re-drawn from the data reported by Calderone *et al.*[54].

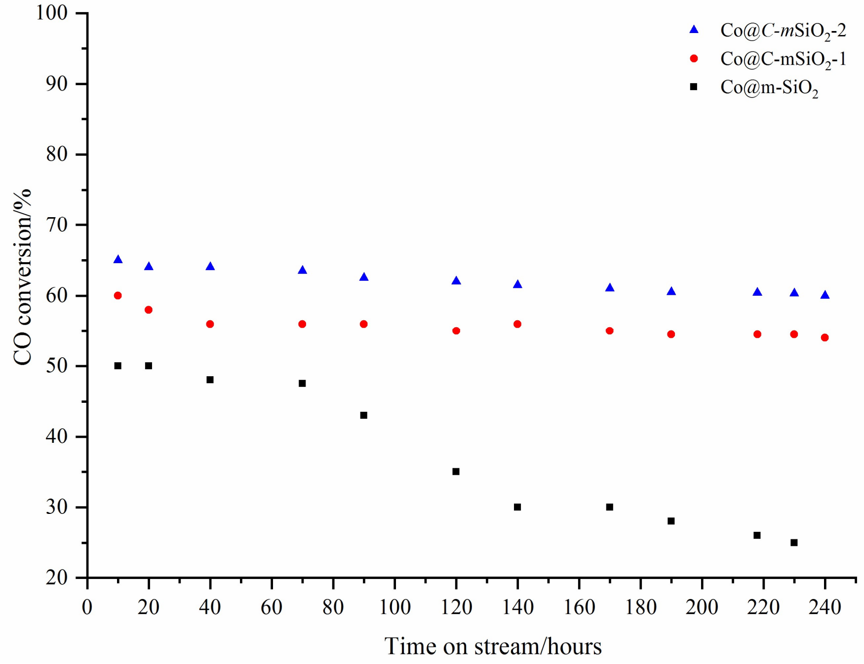

Figure 1.10. CO conversion of cobalt core-shell catalysts in the Fischer-Tropsch synthesis. Re-drawn from the data reported by Xie *et al.*[99].

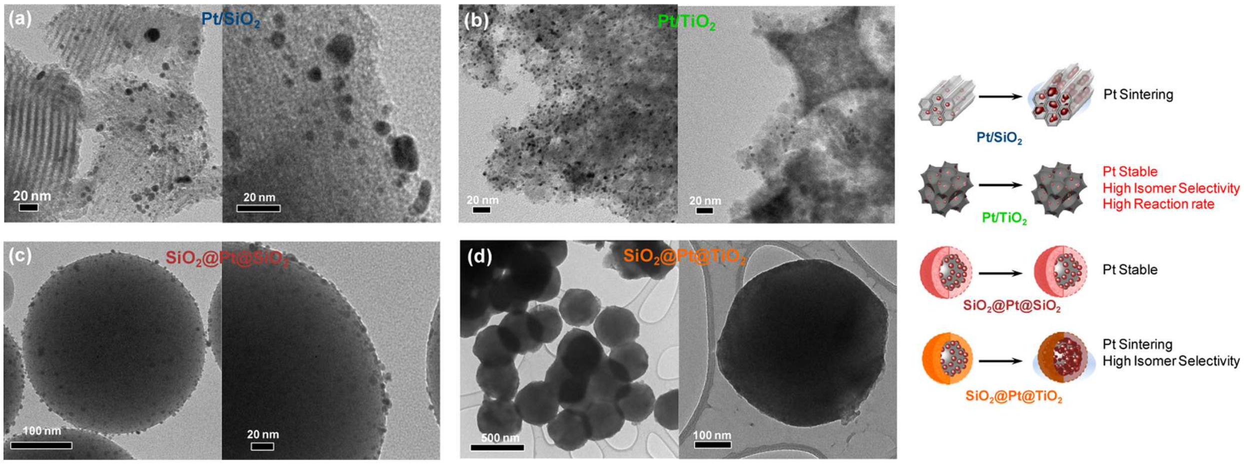

Figure 1.11. TEM images and corresponding schemes of (a) Pt/SiO_2, (b) Pt/TiO_2, (c) $SiO_2@Pt@SiO_2$, and (d) $SiO_2@Pt@TiO_2$ showing the changes in the Pt crystallite size after reforming reaction at 500°C. Re-used from An *et al.*[132]. Copyright (2014) American Chemical Society.

The reason for the stability of core-shell nanoparticles against deactivation may be dependent on the reaction being investigated and the deactivation mechanism that posed a performance decline risk. Resistance to sintering [65, 139-142], coking [72] or oxidation [143, 144] are possibilities for the nanoparticle's stability. Importantly, the structure of the nanoparticles plays a vital role in the catalytic performance and therefore the influence of activation and/or reaction conditions on the structure of the core-shell nanoparticles is pivotal to gaining insight on the observed catalytic behavior.

1.6 Influence of reactive conditions on the structure of core-shell nanoparticles

It is known that nanoparticles may undergo a restructuring when exposed to activation and/or reaction conditions thereby altering the initial structure of the nanoparticle as well as its composition [145-150]. Reaction-driven restructuring can also occur where the core-shell structure is maintained but the surface composition is altered. This can occur when the metal atoms in the shell migrate into the core while the metal atoms in the core segregate to the surface due to exposure to various reactant gases [148]. Strain can also induce changes to the core-shell nanoparticle by causing the reconstruction of the surface [151].

Typically, changes in to the core-shell nanoparticle occur to adapt the geometric and electronic structure to the environment to which the nanoparticle is exposed to [146]. Whilst little is understood at the molecular level regarding the *in-situ* dynamic changes often encountered by the nanoparticle, it is known that atomistic restructuring may occur for thermodynamic reasons where the nanoparticle may evolve into different structures that have a lower free energy [145, 146, 152]. Zhang *et al.*[148] explained that the evolution of the surface composition of core-shell nanoparticles after exposure to various gases is either due to the surface energy of the constituent metals or the formation energies of surface compounds. The importance in studying whether or not changes occur to the core-shell nanoparticle after exposure to reactive conditions is because any changes to the core-shell nanoparticle could alter its physical and chemical properties and thus the active sites. [145, 153, 154]

The morphology, structure and/or chemical composition of core-shell nanoparticles could be altered by thermal treatment. *In-situ* XPS and TEM was used by Bonifacio and co-workers [155] to demonstrate the changes that Ni-Co core-shell nanoparticles undergo during thermal treatment. The structure and composition of the Ni-Co core-shell nanoparticles was altered during annealing (Figure 1.12) and metal segregation and migration to the surface of the nanoparticle were noted. The former changes occurred to lower the surface free energy of the nanoparticle. The formation of a homogeneous Ni-Co mixed alloy at temperatures above 500°C was due to the solid solubility of both elements. The influence of annealing on the structural transformation of Co-Pt and Co-Au core-shell nanoparticles was studied by Wen *et al.*[153] using molecular dynamics. They showed that with increasing temperature, the Co-Pt core-shell nanoparticles first undergo a phase change (hcp Co to fcc Co in the core) and with progressive increases in temperature, a mixed metal alloy is formed (Figure 1.13). No phase change was seen for the Co core in the Co-Au core-shell nanoparticles but with increasing temperature, liquid Au was formed around the hcp-Co core due to its lower melting temperature. Further increases in temperature also resulted in the formation of a mixed metal alloy (Figure 1.13). Huang *et al.* [156] did a similar study on Pd@Pt and Pt@Pd core-shell nanoparticles where it was shown that Pd atoms preferentially segregated to the shell layer.

Carenco *et al.*[157] showed that the structure and composition of CuCo core-shell nanoparticles were altered after exposure to pre-treatment conditions and syngas (Figure 1.14). After oxidation in pure oxygen and reduction in pure hydrogen, the core-shell structure was transformed into a hollow structure with a Co-rich shell. These nanoparticles were exposed to syngas which resulted in a surface composition change in some of the nanoparticles due to the segregation of Co. On the other hand, after exposure to carbon monoxide, there was no compositional change seen. Structural and compositional changes after exposure to pre-treatment and reaction conditions were also observed by Liu *et al.*[142]. Au@CuO nanoparticles transformed after reduction in pure H_2 at 500°C to a Au_3Cu_1 intermetallic phase nanoparticle that was anchored to the support by a Cu_2O interfacial layer. Upon exposure to reaction conditions (CO and O_2), the metallic Cu species was oxidized and segregated to the surface of the nanoparticle forming CuO_x patches.

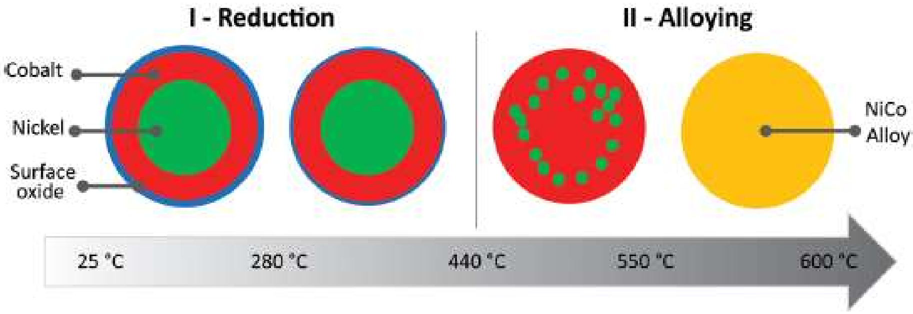

Figure 1.12. Reconfiguration of the Ni-Co core-shell nanoparticle upon annealing. Re-used with permission from Bonifacio *et al.*[155]. Copyright (2015) American Chemical Society.

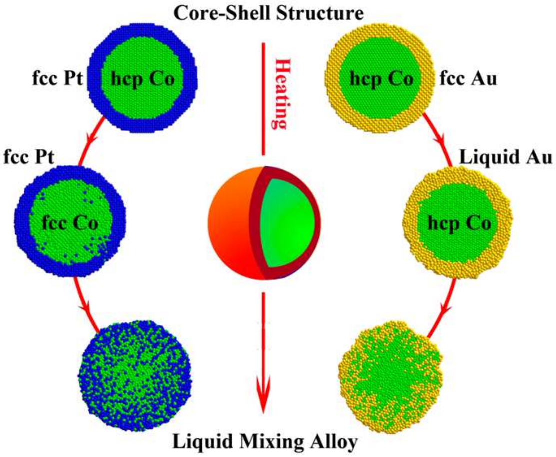

Figure 1.13. Illustration of the structural changes that occur, determined using molecular dynamics, in Co-Pt and Co-Au core-shell nanoparticles during annealing as. Re-used with permission from Wen *et al.*[153]. Copyright (2017) American Chemical Society.

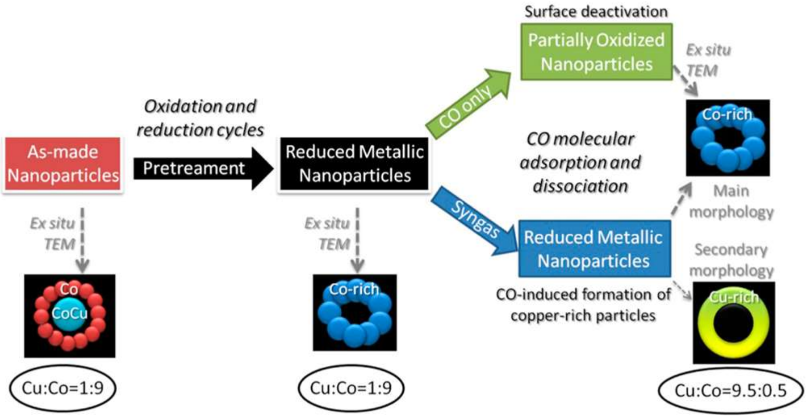

Figure 1.14. Step-by-step observations from *in-situ* and *ex-situ* techniques of the structural and compositional changes for CuCo core-shell nanoparticles with exposure to different gaseous environments [157]. Re-used with permission from Carenco *et al.*[157]. Copyright (2013) American Chemical Society.

Depending on the material used for the core and shell, variations in the stability of the core-shell structure against changes upon exposure to activation and/or reaction conditions may be seen [153]. Pd@CeO_2 core-shell catalysts were grafted onto planar yttria-stabilized zirconia and the core-shell structure remained intact upon calcination in air at temperatures up to 900°C due to the strong interaction between the ceria shell and the support [134]. Zhang *et al.*[135] showed that the Pd@Pt core-shell nanoparticles maintained their initial structure even after reduction and use in the hydrogenation of *p*-chloronitrobenzene. This was ascribed to strong binding between the Pt surfaces and the reactants/products in the reaction thus stabilizing the Pt surfaces by strong coordination.

1.7 Scope of the thesis

In this present work, cobalt-based core-shell nanoparticles were synthesized, characterized and tested for their performance in the Fischer-Tropsch synthesis. Two core-shell systems were investigated, namely, a nickel ferrite core with a cobalt (II, III) oxide shell ($NiFe_2O_4$@Co_3O_4) nanoparticles and a zinc ferrite core with a cobalt (II, III) oxide shell ($ZnFe_2O_4$@Co_3O_4) nanoparticles. The core-shell systems were compared to each other. The effect of two different reduction (activation) conditions on the structure and Fischer-Tropsch synthesis performance of $NiFe_2O_4$@Co_3O_4 core-shell nanoparticles was also studied. These nanoparticles were supported on silica and further examined to determine the effect of a support.

Nickel ferrite ($NiFe_2O_4$) and zinc ferrite ($ZnFe_2O_4$) were chosen as core materials due to their structural similarity to Co_3O_4 allowing for epitaxial growth of the Co_3O_4 shell onto the ferrite core. Additionally, the difference in the lattice parameter between each ferrite and Co_3O_4 may introduce a varying degree of strain onto the shell particularly after reduction when metallic cobalt should be present. The use of different core materials may result in a varying Fischer-Tropsch synthesis performance, structural stability and phase composition of the core-shell nanoparticles under reaction conditions due to the difference in reducibility of each ferrite and the strength of interaction between the shell and the core. Thus, it was expected that a different Fischer-Tropsch synthesis activity and/or selectivity may be obtained with the core-shell nanoparticles in comparison to a cobalt-based catalyst and between each core-shell system studied.

1.8 References

[1] H. Schulz, Short history and present trends of Fischer–Tropsch synthesis, Appl. Catal. A: Gen., 186 (1999) 3-12.

[2] J. L. Casci, C. M. Lok, M. D. Shannon, Fischer-Tropsch catalysis: the basis for an emerging industry with origins in the early 20th century, Catal. Today, 145 (2009) 38-44.

[3] A. K. Dalai, B. H. Davis, A review of water effects on the performances of unsupported and supported Co catalysts, Appl. Catal. A: Gen., 348 (2008) 1-15.

[4] B. H. Davis, Fischer–Tropsch synthesis: current mechanism and futuristic needs, Fuels Processing Technol., 71 (2001) 157-166.

[5] E. van Steen, H. Schulz, Polymerisation kinetics of the Fischer-Tropsch CO hydrogenation using iron and cobalt based catalysts, Appl. Catal. A: Gen., 186 (1999) 309-320.

[6] M. E. Dry, The Fischer-Tropsch process: 1950-2000, Catal. Today, 71 (2002) 227-241.

[7] G. L. Bezemer, J. H. Bitter, H. P. C. E. Kuipers, H. Oosterbeek, J. E. Holewijn, X. Xu, F. Kapteijn, A. J. van Dillen, K. P. de Jong, Cobalt particle size effects in the Fischer-Tropsch reaction studied with carbon nanofiber supported catalysts, J. Am. Chem. Soc., 128 (2006) 3956-3964.

[8] W.-P. Ma, Y.-J. Ding, L.-W. Lin, Fischer-Tropsch synthesis over activated-carbon-supported cobalt catalysts: effect of Co loading and promoters on catalyst performance, Ind. Eng. Chem. Res., 43 (2004) 2391-2398.

[9] A. Y. Khodakov, W. Chu, P. Fongarland, Advances in the development of novel cobalt Fischer-Tropsch catalysts for the synthesis of long-chain hydrocarbons and clean fuels, Chem. Rev., 107 (2007) 1692-1744.

[10] J. van de Loosdrecht, F. G. Botes, I. M. Ciobica, A. Ferreira, P. Gibson, D. J. Moodley, A. M. Saib, J. L. Visagie, C. J. Weststrate, J. W. Niemantsverdiet, Fischer-Tropsch synthesis: Catalysts and chemistry. In comprehensive inorganic chemistry, Elsevier, Oxford, 2013.

[11] J. van de Loosdrecht, I. M. Ciobica, P. Gibson, N. S. Govender, D. J. Moodley, A. M. Saib, C. J. Westsrate, J. W. Niemantsverdiet, Providing fundamental and applied insights into Fischer-Tropsch catalysis: Sasol-Eindhoven University of Technology collaboration, ACS Catal., 6 (2016) 3840-3855.

[12] H. Schulz, Major and minor reactions in Fischer-Tropsch synthesis on cobalt catalysts, Topics in Catal., 26 (2003) 73-85.

[13] Q. Zhang, J. Kang, Y. Wang, Development of novel catalysts for the Fischer-Tropsch synthesis: Tuning the product selectivity, Chem. Cat. Chem., 2 (2010) 1030-1058.

[14] E. Iglesia, Fischer-Tropsch synthesis on cobalt catalysts: Structural requirements and reaction pathyways, Studies in Surf. Sci. Catal., 107 (1997) 153-162.

[15] H. Schulz, Z. Nie, F. Ousmanov, Construction of the Fischer-Tropsch regime with cobalt catalysts, Catal. Today, 71 (2002) 351-360.

[16] H. Schulz, Spatial constraints and frustrated reactions in Fischer-Tropsch synthesis, Catal. Today, 84 (2003) 67-70.

[17] H. Schulz, Comparing Fischer-Tropsch synthesis on iron- and cobalt catalysts The dynamics of structure and function, in: B.H.Davis, M.L.Occelli (Eds.) Fischer-Tropsch Synthesis, Catalysts and Catalysis, Elsevier, 2007, pp. 177-199.

[18] J. J. C. Geerlings, J. H. Wilson, G. J. Kramer, H. P. C. E. Kuipers, A. Hoek, H. M. Huisman, Fischer-Tropsch technology: from active sites to commercial process, Appl. Catal. A: Gen., 186 (1999) 27-40.

[19] S. Li, W. Ding, G. D. Meitzner, E. Iglesia, Spectroscopic and transient kinetic studies of site requirements in iron-catalyzed Fischer-Tropsch synthesis, J. Phys. Chem. B, 106 (2002) 85-91.

[20] Z.-P. Liu, P. Hu, A new insight into Fischer-Tropsch synthesis, J. Am. Chem. Soc., 124 (2002) 11568-11569.

[21] C. K. R. DePoorter, A comprehensive mechanism for the Fischer-Tropsch synthesis, Chem. Rev., 81 (1981) 447-474.

[22] H. Schulz, K. Beck, E. Erich, Mechanism of the Fischer Tropsch process, Studies in Surf. Sci. and Catal., 36 (1988) 457-471.

[23] J. Gaube, H.-F. Klein, Studies on the reaction mechanism of the Fischer-Tropsch synthesis on iron and cobalt, J. Molec. Catal. A: Chem., 283 (2008) 60-68.

[24] M. Claeys, E. van Steen, Basic studies, Studies in Surf. Sci. and Catal., 152 (2004) 601-680.

[25] M. Kollár, A. de Stefanis, H. E. Solt, M. R. Mihályi, J. Valyon, A. A. G. Tomlinson, The mechanism of the Fischer-Tropsch reaction over supported cobalt catalysts, J. Molec. Catal. A: Chem., 333 (2010) 37-45.

[26] P. M. Maitlis, R. Quyoum, H. C. Long, M. L. Turner, Towards a chemical understanding of the Fischer-Tropsch reaction: alkene formation, Appl. Catal. A: Gen., 186 (1999) 363-374.

[27] R. A. van Santen, I. M. Ciobîcâ, E. van Steen, M. M. Ghouri, Mechanistic issues in the Fischer-Tropsch catalysis, Adv. in Catal., 54 (2011) 127.

[28] R. C. Brady III, R. Pettit, On the mechanism of the Fischer-Tropsch reaction. The chain propagation step, J. Am. Chem. Soc., 103 (1981) 1287-1289.

[29] N. Fischer, Preparation of nano and Ångstrøm sized cobalt ensembles and their performance in the Fischer-Tropsch Synthesis, PhD, 2011.

[30] R. Snel, Deviations of Fischer-Tropsch products from an Anderson-Schulz-Flory distribution, Catal. Lett., 1 (1988) 327-330.

[31] K. D. Kruit, D. Vervloet, F. Kapteijn, J. R. van Ommen, Selectivity of the Fischer-Tropsch process: Deviations from single alpha product distribution explained by gradients in process conditions, Catal. Sci. Technol., 3 (2013) 2210-2213.

[32] J. Patzlaff, Y. Liu, C. Graffmann, J. Gaube, Studies on product distributions of iron and cobalt catalyzed Fischer-Tropsch synthesis, Appl. Catal. A: Gen., 186 (1999) 109-119.

[33] A. Y. Khodakov, Fischer-Tropsch Synthesis: relations between structure of cobalt catalysts and their catalytic performance, Catal. Today, 144 (2009) 251-257.

[34] A. P. Steynberg, R. L. Espinoza, B. Jager, A. C. Vosloo, High temperature Fischer-Tropsch synthesis in commercial practice, Appl. Catal. A: Gen., 186 (1999) 41-54.

[35] E. de Smit, B. M. Weckhuysen, The renaissance of iron-based Fischer-Tropsch synthesis: on the multifaceted catalyst deactivation behaviour, Chem. Soc. Rev., 57 (2007) 2758-2781.

[36] S. Li, S. Krishnamoorthy, A. Li, G. D. Meitzner, E. Iglesia, Promoted iron-based catalysts for the Fischer-Tropsch Synthesis: Design, synthesis, site densities and catalytic properties, J. Catal., 206 (2002) 202-217.

[37] Z. H. Chonco, L. Lodya, M. Claeys, E. van Steen, Copper ferrites: A model for investigating the role of copper in the dynamic iron-based Fischer-Tropsch catalyst, J. Catal., 308 (2013) 363-373.

[38] Z. H. Chonco, A. Ferreira, L. Lodya, M. Claeys, E. van Steen, Comparing silver and copper as promoters in Fe-based Fischer-Tropsch catalysts using delafossite as a model compound, J. Catal., 307 (2013) 283-294.

[39] M. K. Gnanamani, H. H. Hamdeh, G. Jacobs, D. Qian, F. Liu, S. D. Hopps, G. A. Thomas, W. D. Shafer, Q. Xiao, Y. Hu, B. H. Davis, Fischer-Tropsch synthesis: effect of Cu, Mn and Zn addition on the activity and product selectivity of cobalt ferrite, RSC Adv., 6 (2016) 62356-62367.

[40] E. van Steen, M. Claeys, K. P. Möller, D. Nabaho, Comparing a cobalt-based catalyst with iron-based catalysts for the Fischer-Tropsch XTL-process operating at high conversion, Appl. Catal. A: Gen., 549 (2018) 51-59.

[41] A. Y. Khodakov, R. Bechara, A. Griboval-Constant, Fischer-Tropsch synthesis over silica supported cobalt catalysts: mesoporous structure versus cobalt surface density, Appl. Catal. A: Gen., 254 (2003) 273-288.

[42] E. Iglesia, S. L. Soled, R. A. Fiato, Fischer-Tropsch synthesis on cobalt and ruthenium. Metal dispersion and support effects on reaction rates and selectivity, J. Catal., 137 (1992) 212-224.

[43] Ø. Borg, P. D. C. Dietzel, A. I. Spjelkavik, E. Z. Tvetenc, J. C. Walmsley, S. Diplas, S. Eri, A. Holmen, E. Rytter, Fischer-Tropsch synthesis: cobalt particle size and support effects on intrinsic activity and product distribution, J. Catal., 259 (2008) 161-164.

[44] J. P. den Breejen, P. B. Radstake, G. L. Bezemer, J. H. Bitter, V. Frøseth, A. Holmen, K. P. de Jong, On the origin of the cobalt particle size effects in Fischer-Tropsch catalysis, J. Am. Chem. Soc., 131 (2009) 7197-7203.

[45] N. Fischer, E. van Steen, M. Claeys, Structure sensitivity of the Fischer-Tropsch activity and selectivity on alumina supported cobalt catalysts, J. Catal., 299 (2013) 67-80.

[46] G. Prieto, A. Martínez, P. Concepción, R. Moreno-Tost, Cobalt particle size effects in Fischer-Tropsch synthesis: structural and in-situ spectroscopic characterisation on reverse micelle-synthesised Co/ITQ-2 model catalysts, J. Catal., 266 (2009) 129-144.

[47] A. Bao, K. Liew, J. Li, Fischer-Tropsch synthesis on CaO-promoted Co/Al_2O_3 catalysts, J. Molec. Catal. A: Chem., 304 (2009) 47-51.

[48] B. C. Dunn, D. J. Covington, P. Cole, R. J. Pugmire, H. L. C. Meuzelaar, R. D. Ernst, E. C. Heider, E. M. Eyring, Silica xerogel supported cobalt metal Fischer-Tropsch catalysts for syngas to diesel range fuel conversion, Energy & Fuels, 18 (2004) 1519-1521.

[49] F. Diehl, A. Y. Khodakov, Promotion of cobalt Fischer-Tropsch catalysts with noble metals: a review, Oil & Gas Sci. Technol., 64 (2009) 11-24.

[50] W. Chu, P. A. Chernavskii, L. Gengembre, G. A. Pankina, P. Fongarland, A. Y. Khodakov, Cobalt species in promoted cobalt alumina-supported Fischer-Tropsch catalysts, J. Catal., 252 (2007) 215-230.

[51] A. M. Saib, D. J. Moodley, I. M. Ciobica, M. M. Hauman, B. H. Sigwebela, C. J. Westrate, J. W. Niemantsverdiet, J. van de Loosdrecht, Fundamental understanding of deactivation and regeneration of cobalt Fischer-Tropsch synthesis catalysts, Catal. Today, 154 (2010) 271-282.

[52] Z.-J. Wang, S. Skiles, F. Yang, Z. Yan, D. W. Goodman, Particle size effects in Fischer-Tropsch synthesis by cobalt, Catal. Today, 181 (2012) 75-81.

[53] J. Zhang, F. H. B. Lima, M. H. Shao, K. Sasaki, J. X. Wang, J. Hanson, R. R. Adzic, Platinum monolayer on nonnoble metal - noble metal core-shell nanoparticle electrocatalysts for O_2 reduction, J. Phys. Chem. B, 109 (2005) 22701-22704.

[54] V. R. Calderone, N. R. Shiju, D. Curulla-Ferre, S. Chambrey, A. Y. Khodakov, A. Rose, J. Thiessen, A. Jess, G. Rothenberg, De novo design of nanostructured iron-cobalt Fischer-Tropsch catalysts, Angew. Chem. Int. Ed., 52 (2013) 4397-4401.

[55] R. G. Chaudhuri, S. Paria, Core/Shell nanoparticles: classes, properties, synthesis mechanisms, characterization and applications, Chem. Rev., 112 (2012) 2373-2433.

[56] J.-M. Yan, X.-B. Zhang, T. Akita, M. Haruta, Q. Xu, One-step seeding growth of magnetically recyclable Au@Co core-shell nanoparticles: highly efficient catalyst for hydrolytic dehydrogenation of ammonia borane, J. Am. Chem. Soc., 132 (2010) 5326-5327.

[57] M. Jin, H. Zhang, J. Wang, X. Zhong, N. Lu, Z. Li, Z. Xie, M. J. Kim, Y. Xia, Copper can still be epitaxially deposited on palladium nanocrystals to generate core shell nanocubes despite their large lattice mismatch, ACS Nano, 6 (2012) 2566-2573.

[58] M. Tsuji, D. Yamaguchi, M. Matsunaga, M. J. Alam, Epitaxial growth of Au@Cu core-shell nanocrystals prepared using the PVP-assisted polyol reduction method, Crystal Growth & Design, 10 (2010) 5129-5135.

[59] S. E. Habas, H. Lee, V. Radmilovic, G. A. Somorjai, P. Yang, Shaping binary metal nanocrystals through epitaxial seeded growth, Nat. Mater., 6 (2007) 692-697.

[60] S. H. Joo, J. Y. Park, C.-K. Tsung, Y. Yamada, P. Yang, G. A. Somorjai, Thermally stable Pt/mesoporous silica core-shell nanocatalysts for high-temperature reactions, Nat. Mater., 8 (2009) 126-131.

[61] K. S. Kumar, V. B. Kumar, P. Paik, Recent advancement in functional core-shell nanoparticles of polymers: Synthesis, physical properties and applications in medical biotechnology, J. Nanoparticles, 2013 (2013) 1-24.

[62] W. Annan, P. Qing, L. Yadong, Rod-shaped Au-Pd core-shell nanostructures, Chem. Mater., 23 (2011) 3217-3222.

[63] C.-J. Zhong, M. M. Maye, Core-Shell nanoparticles as catalysts, Adv. Mater., 13 (2001) 1507-1511.

[64] O. S. Alexeev, B. C. Gates, Supported bimetallic cluster catalysts, Ind. Eng. Chem. Res., 42 (2003) 1571-1587.

[65] X. Duan, G. Qian, X. Zhou, D. Chen, W. Yuan, MCM-41 supported Co-Mo bimetallic catalysts for enhanced hydrogen production by ammonia decomposition, Chem. Eng. J., 207-208 (2012) 103-108.

[66] M. B. Gawande, A. Goswami, T. Asefa, H. Guo, A. V. Biradar, D.-L. Peng, R. Zboril, R. S. Varma, Core-shell nanoparticles: Synthesis and applications in catalysis and electrocatalysis, Chem. Soc. Rev., 44 (2015) 7540-7590.

[67] V. R. Calderone, N. R. Shiju, G. Rothenberg, D. Curulla-Ferre, Core-shell particles with catalytic activity and the process of their preparation. Method of preparation of Fischer-Tropsch catalyst comprising said particles, European Patent Office, Europe, EP2740534A1, 2014.

[68] C. Louis, Deposition-precipitation synthesis of supported metal catalysts, in: J.Regalbuto (Ed.) Catalysis preparation science and engineering, CRC Press, Taylor & Francis, Broken Sound Parkway NW, 2007, pp. 319-338.

[69] K. P. de Jong, Synthesis of supported catalysts, Curr. Opin. Solid State Mater. Sci., 4 (1999) 55-62.

[70] P. Munnik, P. E. de Jongh, K. P. de Jong, Recent developments in the synthesis of supported catalysts, Chem. Rev., 115 (2015) 6687-6718.

[71] S. Garcia, R. M. Anderson, H. Celio, N. Dahal, A. Dolocan, J. Zhou, S. M. Humphrey, Microwave synthesis of Au-Rh core-shell nanoparticles and implications of the shell thickness in hydrogenation catalysis, Chem. Commun., 49 (2013) 4241-4243.

[72] E. Iglesia, S. L. Soled, R. A. Fiato, G. H. Via, Bimetallic synergy in cobalt ruthenium Fischer-Tropsch synthesis catalysts, J. Catal., 143 (1993) 345-368.

[73] K. Aranishi, H.-L. Jiang, T. Akita, M. Haruta, Q. Xu, One-step synthesis of magnetically recyclable Au/Co/Fe triple-layered core-shell nanoparticles for the hydrolytic dehydrogenation of ammonia borane, Nano Research, 4 (2011) 1233-1241.

[74] S. B. Kalindindi, U. Sanyal, B. R. Jagirdar, Nanostructured Cu and Cu@Cu_2O core-shell catalysts for hydrogen generation from ammonia borane, Phys. Chem. Chem. Phys., 10 (2008) 5870-5874.

[75] Z.-H. Lu, H.-L. Jiang, M. Yadav, K. Aranishi, Q. Xu, Synergistic catalysis of Au-Co@SiO_2 nanospheres in hydrolytic dehydrogenation of ammonia borane, in: J. Mater. Chem., 2012, pp. 5065.

[76] Q. Yao, Z.-H. Lu, Y. Wang, X. Chen, G. Feng, Synergistic catalysis of non-noble bimetallic Cu-Co nanoparticles embedded in SiO_2 nanospheres in hydrolytic dehydrogenation of ammonia borane, J. Phys. Chem. C, 119 (2015) 14167-14174.

[77] Y. Hu, Y. Wang, Z.-H. Lu, X. Chen, L. Xiong, Core-shell nanospheres Pt@SiO_2 for catalytic hydrogen production, Appl. Surf. Sci., 341 (2015) 185-189.

[78] T. Hirakawa, P. V. Kamat, Charge separation and catalytic activity of Ag@TiO_2 core-shell composite clusters under UV-irradiation, J. Am. Chem. Soc., 127 (2005) 3928-3924.

[79] N. Zhang, S. Liu, Y.-J. Xu, Recent progress on metal core@semiconductor shell nanocomposites as a promising type of photocatalyst, Nanoscale, 4 (2012) 2227-2238.

[80] M. Wang, X. Pang, D. Zheng, Y. He, L. Sun, C. Lin, Z. Lin, Nonepitaxial growth of uniform and precisely size-tunable core/shell nanoparticles and their enhanced plasmon-driven photocatalysis, J. Mater. Chem. A, 4 (2016) 7190-7199.

[81] L. Bu, N. Zhang, S. Guo, X. Zhang, J. Li, J. Yao, T. Wu, G. Lu, J.-Y. Ma, D. Su, X. Huang, Biaxially strained PtPd/Pt core/shell nanoplate boosts oxygen reduction catalysis, Science, 354 (2016) 1410-1414.

[82] J. Shin, J.-H. Choi, P.-R. Cha, S. K. Kim, I. Kim, S.-C. Lee, D. S. Jeong, Catalytic activity for oxygen reduction reaction on platinum-based core-shell nanoparticles: All-electron density functional theory, Nanoscale, 7 (2016) 15830-15839.

[83] L. Luo, L. Zhang, G. Henkelman, R. M. Crooks, Unusual activity trend for CO oxidation on Pd_xAu_{140-x}@Pt core@shell nanoparticle electrocatalysts, J. Phys. Chem. Lett., 6 (2015) 2562-2568.

[84] S. Guo, X. Zhang, W. Zhu, K. He, D. Su, A. Mendoza-Garcia, S. F. Ho, G. Lu, S. Sun, Nanocatalyst superior to Pt for oxygen reduction reactions: The case of core/shell Ag(Au)/CuPd nanoparticles, J. Am. Chem. Soc., 136 (2014) 15026-15033.

[85] M. Ren, Y. Zhou, F. Tao, Z. Zou, D. L. Akins, H. Yang, Controllable modification of the electronic structure of carbon-supported core-shell Cu@Pd catalysts for formic acid oxidation, J. Phys. Chem. C, 118 (2014) 12669-12675.

[86] Z. Zhuang, W. Sheng, Y. Yan, Synthesis of monodispere Au@Co_3O_4 core-shell nanocrystals and their enhanced catalytic activity for oxygen evolution reaction, Adv. Mater., 26 (2014) 3950-3955.

[87] A. U. Nilekar, S. Alayoglu, B. Eichhorn, M. Mavrikakis, Preferential CO oxidation in hydrogen: Reactivity of core-shell nanoparticle, J. Am. Chem. Soc., 132 (2010) 7418-7428.

[88] S. F. Chen, J. P. Li, W. P. Xu, Y. Lu, W. X. Huang, S. H. Yu, Large scale photochemical synthesis of M@TiO_2 nanocomposites (M = Ag, Pd, Au, Pt) and their optical properties, CO oxidation performance and antibacterial effect, Nano Res., 3 (2010) 244-255.

[89] H.-L. Jiang, T. Akita, T. Ishida, M. Haruta, Q. Xu, Synergistic catalysis of Au@Ag core-shell nanoparticles stabilized on metal-organic framework, J. Am. Chem. Soc., 133 (2011) 1304-1306.

[90] S. Alayoglu, P. Zavalij, B. Eichhorn, Q. Wang, A. I. Frenkel, P. Chupas, Structural and architectural evaluation of bimetallic nanoparticles: A case study of Pt-Ru core-shell and alloy nanoparticles, ACS Nano, 3 (2009) 3127-3137.

[91] W. Tang, G. Henkelman, Charge redistribution in core-shell nanoparticles to promote oxygen reduction, J. Chem. Physics, 130 (2009) 194504.

[92] H. M. Song, D. H. Anjum, R. Sougrat, M. N. Hedhili, N. M. Khashab, Hollow Au@Pd and Au@Pt core-shell nanoparticles as electrocatalysts for ethanol oxidation reactions, J. Mater. Chem. A, 22 (2012) 25003-25010.

[93] S. S. Kim, C. Kim, H. Lee, Shape- and composition-controlled Pt-Fe-Co nanoparticles for electrocatalytic methanol oxidation, Topics in Catal., 53 (2010) 686-693.

[94] A. Mosayebi, A. Haghtalab, The comprehensive kinetic modelling of the Fischer-Tropsch synthesis over Co@Ru/Al_2O_3 core-shell structure catalyst, Chem. Eng. J., 259 (2015) 191-204.

[95] D. Wang, C. Chen, J. Wang, L. Jia, B. Hou, D. Li, High thermal conductive core-shell structured Al_2O_3@Al composite supported cobalt catalyst for Fischer-Tropsch synthesis, Appl. Catal. A: Gen., 527 (2016) 60-71.

[96] H. Qin, S. King, Y. Wang, H. Li, Z. Ni, Y. Huang, Y. Li, X. Li, Lignin-based fabrication of Co@C core-shell nanoparticles as efficient catalyst for selective Fischer-Tropsch synthesis of C_{5+} compounds, ACS Sustainable Chem. Eng., 4 (2016) 1240-1247.

[97] N. Kruse, A. G. Machoke, W. Schwieger, R. Güttel, Nanostructured encapsulated catalysts for combination of Fischer-Tropsch synthesis and hydroprocessing, Chem. Cat. Chem., 7 (2015) 1018-1022.

[98] R. Xie, D. Li, B. Hou, J. Wang, L. Jia, Y. Sun, Solvothermally derived Co_3O_4@*m*-SiO_2 nanocomposite for Fischer-Tropsch synthesis, Catal. Comm., 12 (2011) 380-383.

[99] R. Xie, H. Wang, P. Gao, L. Xia, Z. Zhang, T. Zhao, Y. Sun, Core@shell Co_3O_4@C-*m*-SiO_2 catalysts with inert C modified mesoporous channel for desired middle distillate, Appl. Catal. A: Gen., 492 (2015) 93-99.

[100] A. Haghtalab, A. Mosayebi, Co@Ru nanoparticle with core-shell structure supported over γ-Al_2O_3 for Fischer-Tropsch synthesis, Int. J. Hydrogen Energy, 39 (2014) 18882-18893.

[101] V. R. Calderone, N. R. Shiju, G. Rothenberg, D. Curulla-Ferre, Core-shell particles with catalytic activity, United States Patent, United States, US 9,539,563 B2, 2018.

[102] K. Sasaki, K. A. Kuttiyiel, L. Barrio, D. Su, A. I. Frenkel, N. Marinkovic, D. Mahajan, R. R. Adzic, Carbon-supported IrNi core-shell nanoparticles: Synthesis, characterization and catalytic activity, J. Phys. Chem. C, 115 (2011) 9894-9902.

[103] A. Beltram, M. Melchionna, T. Montini, L. Nasi, R. J. Gorte, M. Prato, P. Fornasiero, Improved activity and stability of Pd@CeO_2 core-shell catalysts hybridized with multi-walled carbon nanotubes in the water gas shift reaction, Catal. Today, 253 (2015) 142-148.

[104] R. Wang, H. Li, H. Feng, H. Wang, Z. Lei, Preparation of carbon-supported core@shell PdCu@PtRu nanoparticles for methanol oxidation, J. Powers Sources, 195 (2010) 1099-1102.

[105] A. Mosayebi, R. Abedini, H. Bakhshi, Ni@Pd nanoparticle with core-shell structure supported over γ-Al_2O_3 for partial oxidation process of butane to syngas, Int. J. Hydrogen Energy, 42 (2017) 94118-18950.

[106] Y. Zhao, X. Yang, J. Tian, F. Wang, L. Zhan, Methanol electro-oxidation on Ni@Pd core-shell nanoparticles supported on multi-walled carbon nanotubes in alkaline media, Int. J. Hydrogen Energy, 35 (2010) 3249-3257.

[107] J. Zeng, J. Yang, J. Y. Lee, W. Zhou, Preparation of carbon-supported core-shell Au-Pt nanoparticle for methanol oxidation reaction: The promotional effect of the Au core, J. Phys. Chem. B, 110 (2006) 24606-24611.

[108] S. Gaur, S. Johansson, F. Mohammad, C. S. S. R. Kumar, J. J. Spivey, Catalytic activity of titania-supported core-shell Fe_3O_4@Au nanocatalysts for CO oxidation, J. Phys. Chem. C, 116 (2012) 22319-22326.

[109] X. Yang, F. Cheng, J. Liang, Z. Tao, J. Chen, Carbon-supported Ni_{1-x}@Pt_x ($x = 0.32, 0.43, 0.60, 0.67$ and 0.80) core-shell nanoparticles as catalysts for hydrogen generation from hydrolysis of ammonia borane, Int. J. Hydrogen Energy, 36 (2011) 1984-1990.

[110] W. Gao, Y. Zhao, H. Chen, H. Chen, Y. Li, S. He, Y. Zhang, M. Wei, D. G. Evans, X. Duan, Core-shell Cu@(CuCo-alloy)/Al_2O_3 catalysts for the synthesis of higher alcohols from synthesis gas, Green Chem., 17 (2015) 1525-1534.

[111] J. X. Wang, H. Inada, L. Wu, Y. Zhu, Y. Choi, P. Liu, W.-P. Zhou, R. R. Adzic, Oxygen reduction on well-defined core-shell nanocatalysts: particle size, facet and Pt shell thickness effects, J. Am. Chem. Soc., 131 (2009) 17298-17302.

[112] J. X. Wang, C. Ma, Y. Choi, D. Su, Y. Zhu, P. Liu, R. Si, M. B. Vukmirovic, Y. Zhang, R. R. Adzic, Kirkendall effect and lattice contraction in nanocatalysts: a new strategy to enhance sustainable activity, J. Am. Chem. Soc., 133 (2011) 13551-13557.

[113] L. Gan, R. Yu, J. Luo, Z. Cheng, J. Zhu, Lattice strain distributions in individual dealloyed Pt-Fe catalyst nanoparticles, J. Phys. Chem. Lett., 3 (2012) 934-938.

[114] M. Mavrikakis, B. Hammer, J. K. Nørskov, Effect of strain on the reactivity of metal surfaces, Phys. Rev. Lett., 81 (1998) 2819.

[115] K. A. Kuttiyiel, K. Sasaki, Y. Choi, D. Su, P. Liu, R. R. Adzic, Nitride stabilized PtNi core-shell nanocatalyst for high oxygen reduction activity, Nano Lett., 12 (2012) 6266-6271.

[116] L. Gan, M. Heggen, S. Rudi, P. Strasser, Core-shell compositional fine structures of dealloyed Pt_xNi_{1-x} nanoparticles and their impact on oxygen reduction catalysis, Nano Lett., 12 (2012) 5423-5430.

[117] T.-Y. Chen, T.-J. M. Luo, Y.-W. Yang, Y.-C. Wei, K.-W. Wang, T.-L. Lin, T.-C. Wen, C. H. Lee, Core dominated surface activity of core-shell nanocatalysts on methanol electrooxidation, J. Phys. Chem. C, 116 (2012) 16969-16978.

[118] X. Zhang, H. Wang, J. Key, V. Linkov, S. Ji, X. Wang, Z. Lei, R. Wang, Strain effect of core-shell Co@Pt/C nanoparticle catalysts with enhanced electrocatalytic activity for methanol oxidation, J. Electrochem. Soc., 159 (2012) B270-B276.

[119] P. Strasser, S. Koh, T. Anniyev, J. Greeley, K. More, C. Yu, Z. Liu, S. Kaya, D. Nordlund, H. Ogasawara, M. F. Toney, A. Nilsson, Lattice-strain control of the activity in dealloyed core-shell fuel cell catalysts, Nat. Chem., 2 (2010) 454-460.

[120] N. Bhattarai, G. Casillas, A. Ponce, M. Jose-Yacaman, Strain-release mechanisms in bimetallic core-shell nanoparticles as revealed by Cs-corrected STEM, Surf. Sci., 609 (2013) 161-166.

[121] A. Ruban, B. Hammer, P. Stoltze, H. L. Skriver, J. K. Norskov, Surface electronic structure and reactivity of transition and noble metals, J. Molec. Catal. A: Chem., 115 (1997) 421-429.

[122] S. Alayoglu, B. Eichhorn, Rh-Pt bimetallic catalysts: Synthesis, characterization and catalysis of core-shell, alloy and monometallic nanoparticles, J. Am. Chem. Soc., 130 (2008) 17479-17486.

[123] G. Chen, S. Desinan, R. Nechache, R. Rosei, F. Rosei, D. Ma, Bifunctional catalytic/magnetic Ni@Ru core-shell nanoparticles, Chem. Commun., 47 (2011) 6308-6310.

[124] Z. Ai, L. Zhang, S. Lee, W. Ho, Interfacial hydrothermal synthesis of $Cu@Cu_2O$ core-shell microspheres with enhanced visible-light-driven photocatalytic activity, J. Phys. Chem. C, 113 (2009) 20896-20902.

[125] J. Kang, R. Wang, H. Wang, S. Liao, J. Key, V. Linkov, S. Ji, Effect of Ni core structure on the electrocatalytic activity of Pt-Ni/C in methanol oxidation, Materials, 6 (2013) 2689-2700.

[126] H.-L. Jiang, T. Akita, Q. Xu, A one-pot protocol for synthesis of non-noble metal-based core-shell nanoparticles under ambient conditions: towards highly active cost-effective catalysts for hydrolytic dehydrogenation of NH_3BH_3, Chem. Commun., 47 (2011) 10999-11001.

[127] M. Heemeier, A. F. Carlsson, M. Naschitzki, M. Schmal, M. Baumer, H.-J. Freund, Preparation and characterization of a model bimetallic catalyst: Co-Pd nanoparticles supported on Al_2O_3, Angew. Chem. Int. Ed., 41 (2002) 4073-4076.

[128] S. Hu, L. Scudiero, S. Ha, Effect of Au and Ru in Au@Pd and Ru@Pd core-shell nanoparticles for direct formic acid fuel cells, ECS Trans., 64 (2014) 1121-1127.

[129] Z. Li, M. Li, Z. Bian, Y. Kathiraser, S. Kawi, Design of highly stable and selective core/yolk-shell nanocatalysts: A review, Appl. Catal. B: Environ., 188 (2016) 324-341.

[130] M. A. Lucchini, A. Testino, A. Kambolis, C. Proff, C. Ludwig, Sintering and coking resistant core-shell microporous silica-nickel nanoparticles for CO methanation: Towards advanced catalysts production, Appl. Catal. B: Environ., 182 (2016) 94-101.

[131] Y. Wei, Z. Zhao, J. Liu, S. Liu, C. Xu, A. Duan, G. Jiang, Multifunctional catalysts of three-dimensionally ordered macroporous oxide-supported Au@Pt core–shell nanoparticles with high catalytic activity and stability for soot oxidation, J. Catal., 317 (2014) 62-74.

[132] K. An, Q. Zhang, S. Alayoglu, N. Musselwhite, J.-Y. Shin, G. A. Somorjai, High-Temperature catalytic reforming of n-Hexane over supported and core-shell Pt nanoparticle catalysts: Role of oxide-metal interface and thermal stability, Nano Lett., 14 (2014) 4907-4912.

[133] K. A. Kuttiyiel, Y. Choi, S.-M. Hwang, G.-G. Park, T.-H. Yang, D. Su, K. Sasaki, P. Liu, R. R. Adzic, Enhancement of the oxygen reduction on nitride stabilized pt-M (M=Fe,Co,and Ni) core-shell nanoparticle electrocatalysts, Nano Energy, 13 (2015) 442-449.

[134] L. Adijanto, D. A. Bennett, C. Chen, A. S. Yu, M. Cargnello, P. Fornasiero, R. J. Gorte, J. M. Vohs, Exceptional thermal stability of Pd@CeO2 core-shell catalyst nanostructures grafted onto an oxide surface, Nano Lett., 13 (2013) 2252-2257.

[135] P. Zhang, Y. Hu, B. Li, Q. Zhang, C. Zhou, H. Yu, X. Zhang, L. Chen, B. Eichhorn, S. Zhou, Kinetically stabilized Pd@Pt core-shell octahedral nanoparticles with thin Pt layers for enhanced catalytic hydrogenation performance, ACS Catal., 5 (2015) 1335-1343.

[136] Q. Wang, X. Wang, J. Liu, Y. Yang, Cu-Ni core-shell nanoparticles: Structure, stability, electronic and magnetic properties: A spin-polarized density functional theory study, J. Nanopart. Res., 19 (2017) 1-12.

[137] V. K. Gupta, N. Atar, M. L. Yola, Z. Üstündag, L. Uzun, A novel magnetic Fe@Au core-shell nanoparticles anchored graphene oxide recyclable nanocatalyst for the reduction of nitrophenol compounds, Water Res., 48 (2014) 210-217.

[138] Z. Dong, X. Le, C. Dong, W. Zhang, X. Li, J. Ma, Ni@Pd core-shell nanoparticles modified fibrous silica nanospheres as highly efficient and recoverable catalyst for the reduction of 4-nitrophenol and hydrodechlorination of 4-chlorophenol, Appl. Catal. B: Environ., 162 (2015) 372-380.

[139] A. Cao, R. Lu, G. Veser, Stabilizing metal nanoparticles for heterogeneous catalysis, Phys. Chem. Chem. Phys., 12 (2010) 13499-13510.

[140] H. Wang, W. Zhou, J.-X. Liu, R. Si, G. Sun, M.-Q. Zhong, H.-Y. Su, H.-B. Zhao, J. A. Rodriguez, S. J. Pennycook, J.-C. Idrobo, W.-X. Li, Y. Kou, D. Ma, Platinum-modulated cobalt nanocatalysts for low-temperature aqueous-phase Fischer Tropsch synthesis, J. Am. Chem. Soc., 135 (2013) 4149-4158.

[141] J. Zhang, J.-O. Muller, W. Zheng, D. Wang, D. Su, R. Schlogl, Individual Fe-Co alloy nanoparticles and carbon nanotubes: structural and catalytic properties, Nano Lett., 8 (2008) 2738-2743.

[142] X. Liu, A. Wang, L. Li, T. Zhang, C.-Y. Mou, J.-F. Lee, Structural changes of Au–Cu bimetallic catalysts in CO oxidation: In situ XRD, EPR, XANES, and FT-IR characterizations, J. Catal., 278 (2011) 288-296.

[143] K. Takanabe, K. Nagaoka, K. Nariai, K.-I. Aika, Titania-supported cobalt and nickel bimetallic catalysts for carbon dioxide reforming of methane, J. Catal., 232 (2005) 268-275.

[144] T. Nowitzki, A. F. Carlsson, O. Martyanov, M. Naschitzki, V. Zielasek, T. Risse, M. Schmal, H.-J. Freund, M. Bäumer, Oxidation of alumina-supported Co and Co-Pd model catalysts for the Fischer-Tropsch reaction, J. Phys. Chem. C, 111 (2007) 8566-8572.

[145] G.-F. Wei, Z.-P. Liu, Restructuring and hydrogen evolution on Pt nanoparticle, Chem. Sci., 6 (2015) 1485-1490.

[146] F. F. Tao, M. Salmeron, In situ studies of chemistry and structure of material in reactive environments, Science, 331 (2011) 171-174.

[147] E. Prestat, M. A. Kulzick, P. J. Dietrich, M. Smith, E.-P. Tien, M. G. Burke, S. J. Haigh, N. J. Zaluzec, In Situ industrial bimetallic catalyst characterization using scanning transmission electron microscopy and X-ray absorption spectroscopy at one atmosphere and elevated temperature, Chem. Phys. Chem., 18 (2017) 2151-2156.

[148] S. Zhang, L. Nguyen, Y. Zhu, S. Zhan, C.-K. Tsung, F. F. Tao, In-situ studies of nanocatalysis, Accounts of chemical research, 46 (2013) 1731-1739.

[149] F. Tao, M. E. Grass, Y. Zhang, D. R. Butcher, F. Aksoy, S. Aloni, V. Altoe, S. Alayoglu, J. R. Renzas, C.-K. Tsung, Z. Zhu, Z. Liu, M. Salmeron, G. A. Somorjai, Evolution of structure and chemistry of bimetallic nanoparticle catalysts under reaction conditions, J. Am. Chem. Soc., 132 (2010) 8697-8703.

[150] P. L. Hansen, J. B. Wagner, S. Helveg, J. R. Rostrup-Nielsen, B. S. Clausen, H. Topsoe, Atom-resolved imaging of dynamic shape changes in supported copper nanocrystals, Science, 295 (2002) 2053-2055.

[151] E. Panizon, R. Ferrando, Strain-induced restructuring of the surface in core@shell nanoalloys, Nanoscale, 8 (2016) 15911-15919.

[152] F. Calvo, Thermodynamics of nanoalloys, Phys. Chem. Chem. Phys., 17 (2015) 27922-27939.

[153] Y.-H. Wen, R. Huang, G.-F. Shao, S.-G. Sun, Thermal stability of Co-Pt and Co-Au core-shell structured nanoparticles: Insights from molecular dynamics simulations, J. Phys. Chem. Lett., 8 (2017) 4273-4278.

[154] Y.-F. Zhu, N. Zhao, B. Jin, M. Zhao, Q. Jiang, High thermal stability of core-shell structures dominated by negative interface energy, Phys. Chem. Chem. Phys., 19 (2017) 9253-9260.

[155] C. S. Bonifacio, S. Carenco, C. H. Wu, S. D. House, H. Bluhm, J. C. Yang, Thermal stability of core-shell nanoparticles: A combined in situ study by XPS and TEM, Chem. Mater., 27 (2015) 6960-6968.

[156] R. Huang, Y.-H. Wen, Z.-Z. Zho, S.-G. Sun, Pt-Pd bimetallic catalysts: Structural and thermal stabilities of core-shell and alloyed nanoparticles, J. Phys. Chem. C, 116 (2012) 8664-8671.

[157] S. Carenco, A. Tuxen, M. Chintapalli, E. Pach, C. Escudero, T. D. Ewers, P. Jiang, F. Borondics, G. Thornton, A. P. Alivisatos, H. Bluhm, J. Guo, M. Salmeron, Dealloying of cobalt from CuCo nanoparticles under syngas exposure, J. Phys. Chem. C, 117 (2013) 6259-6266.

2 Synthesis and characterization of MFe_2O_4 (M = Ni or Zn) nanoparticles

$NiFe_2O_4$ and $ZnFe_2O_4$ nanoparticles were synthesized using the citrate precursor method. The synthesis method was optimized using $NiFe_2O_4$ as the model substrate by varying the Fe/Ni mole % ratio (2.0 to 2.4) and calcination temperature (350°C to 800°C). The optimization experiments showed that ratios of 2.2 and higher (calcination at 550°C) prevented the formation of NiO although hematite was formed as a minor phase. There was no clear correlation between the mole % ratio, $NiFe_2O_4$ crystallite size and the relative phase abundance of the different phases. However, the lowest abundance of hematite was formed at a mole % ratio of 2.3 which was used to study the effect of calcination temperature. The crystallite size of $NiFe_2O_4$ increased with increasing calcination temperature. Phase pure $NiFe_2O_4$ nanoparticles were obtained using a mole % ratio of 2.3 and a calcination temperature of 450°C. These conditions were also used to synthesize phase pure $ZnFe_2O_4$.

2.1. Introduction

Nickel ferrite ($NiFe_2O_4$) and zinc ferrite ($ZnFe_2O_4$) were used as core materials around which a cobalt (II, III) oxide (Co_3O_4) shell would be grown. These ferrite nanoparticles were chosen as core materials because of its similarity in crystal structure to Co_3O_4 [1]. Typically, a lattice mismatch of lower than 5% is required for epitaxial growth to occur [2]. Co_3O_4 has a spinel structure ($M^{2+}M^{3+}{}_2O_4$) and a unit cell length of 8.084 Å. This means that, in addition to a spinel structure, the core material should have a unit cell length between 8.084 Å and 8.448 Å to maintain a lattice mismatch below 5%. This is an additional reason for using nickel ferrite ($NiFe_2O_4$, 8.325 Å) and zinc ferrite ($ZnFe_2O_4$, 8.447 Å) as core materials. The varying unit cell length between $NiFe_2O_4$ and $ZnFe_2O_4$ may result in different strain being introduced in the MFe_2O_4@Co_3O_4 core-shell nanoparticle.

Nickel ferrite, $NiFe_2O_4$, is a spinel type compound that has an inverted structure and belongs to the space group $Fd\bar{3}m$. In the $NiFe_2O_4$ structure (Figure 2.1), the Ni^{2+} cations occupy the octahedral (B) site whilst the Fe^{3+} cations are distributed between the tetrahedral (A) and octahedral sites. The structure is completed by a cubic close-packed array of oxygen atoms [3-6]. As nanoparticles, $NiFe_2O_4$ has unique magnetic and catalytic properties and is used for various applications such as magnetic storage devices and site-specific drug delivery [3-6].

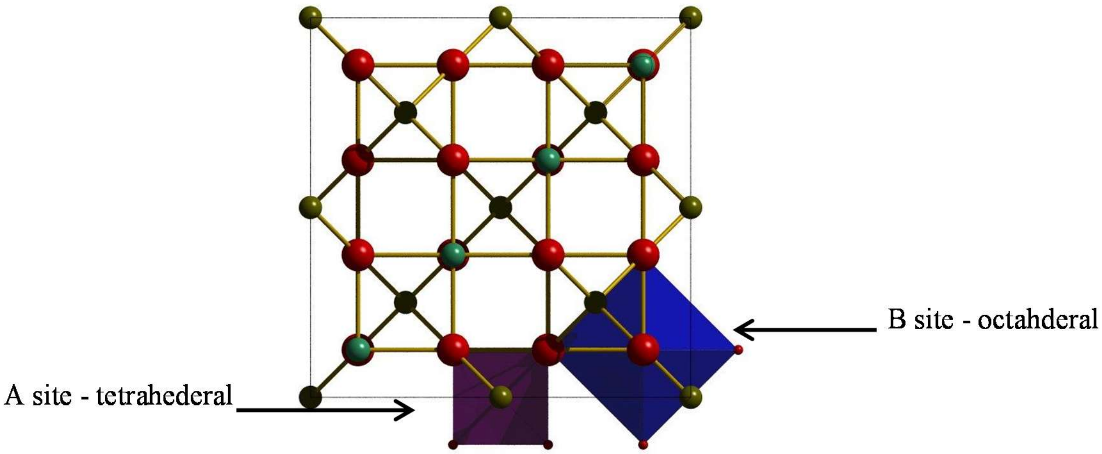

Figure 2.1. Unit cell representation of $NiFe_2O_4$ ($Fd\bar{3}m$) (viewed along the unique crystallographic b axis) with the tetrahedral and octahedral geometry shown at specific lattice sites. Note: the oxygen atom is shown in red; the nickel atom is shown in green and the iron atom is shown in black.

Like $NiFe_2O_4$, $ZnFe_2O_4$ is a spinel compound belonging to the $Fd\bar{3}m$ space group. However, $ZnFe_2O_4$ has a normal spinel structure in which the tetrahedral sites (A) are occupied by Zn^{2+}, the octahedral sites (B) are filled with Fe^{3+} and O^{2-} ions are arranged in a cubic close packing where $^1/_8$ of A and $^1/_2$ of B interstitial sites are occupied (see Figure 2.2) [7, 8]. In contrast to $NiFe_2O_4$ and other spinel ferrites, $ZnFe_2O_4$ has unique magnetic properties such as a low ordering temperature (10 ± 1 K) and is antiferromagnetic [7, 9] which may be due to the super-exchange interactions taking place at a 90° angle of the Fe-O-Fe pathway. Nano-sized $ZnFe_2O_4$, on the other hand, is likely to demonstrate a different magnetic behavior to bulk $ZnFe_2O_4$ since it is often in a mixed spinel state ($(Zn_{1-x}Fe_x)_{Td}[Fe_{2-x}Zn_x]_{Oh}$ with x being the inversion parameter) where Zn^{2+} and Fe^{3+} are distributed along the A and B sites [7].

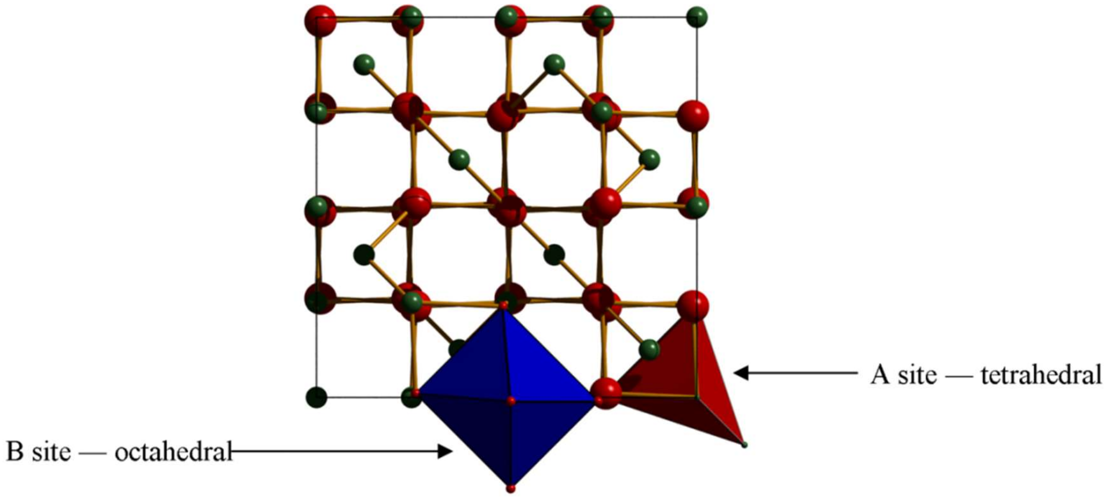

Figure 2.2. Unit cell representation of $ZnFe_2O_4$ ($Fd\bar{3}m$) (viewed along the unique crystallographic b axis) with the tetrahedral and octahedral geometry shown at specific lattice sites. Note: the oxygen atom is shown in red; the zinc atom is shown in green and the iron atom is shown in black.

Various simple synthetic routes have been used to prepare mixed metal oxide compounds using relatively inexpensive materials [10-16]. It has been shown that ultrafine particles can be obtained using the citrate precursor method [17-21]. Therefore, this synthesis route was used to prepare MFe_2O_4 (M = Ni or Zn) nanoparticles. X-ray powder diffraction (XRD) was used to characterize the various nanoparticles prepared during the optimization study. $NiFe_2O_4$ and $ZnFe_2O_4$ nanoparticles prepared using the optimized M/Fe mole % ratio and calcination temperature were further characterized using Mössbauer Spectroscopy and transmission electron microscopy (TEM).

2.2. Experimental

2.2.1. Preparation of $NiFe_2O_4$ nanoparticles for the optimization study

The citrate precursor method was used for the synthesis of $NiFe_2O_4$ nanoparticles. The masses used for each synthesis was dependent on the Fe/Ni molar ratio which ranged between 2 – 2.4 (Table 2.1). In all syntheses, the number of moles of citric acid was equal to the total number of moles of metal ions used.

In a typical synthesis (Fe/Ni = 2), $Fe(NO_3)_3.9H_2O$ (Sigma-Aldrich) was dissolved in ethanol (Sigma Aldrich) (2.7*M*). Similarly, $Ni(NO_3)_2.6H_2O$ (Sigma-Aldrich) was dissolved in ethanol (1.4*M*). Then, ethanol was placed in a water bath at 30°C and citric acid (Sigma-Aldrich) was added to form a 4.0*M* solution which was stirred until it dissolved. Thereafter, the $Fe(NO_3)_3.9H_2O$ solution was added to the citric acid solution followed by the addition of the $Ni(NO_3)_2.6H_2O$ solution. The metal nitrate-citric acid solution was allowed to stir for 95 minutes before the temperature of the water bath was increased to 60°C. The metal nitrate-citric acid solution was kept at this temperature for two hours whilst stirring. After this time, a brown gel formed which was oven-dried at 110°C for 24 hours. The as-formed resin was then calcined in a muffle furnace at 550°C for five hours. To investigate the influence of calcination temperature, the as-formed resin with a Fe/Ni mole ratio of 2.3 was calcined in a muffle furnace at different temperatures (Table 2.2) for five hours.

Table 2.1. Summary of reagent masses used to prepare $NiFe_2O_4$ with varying Fe/Ni mole ratios.

Sample	Fe/Ni mole ratio	Moles iron nitrate/mol	Moles nickel nitrate/mol	Moles citric acid/mol
NF1	2.0	0.08077	0.04040	0.1212
NF2	2.2	0.08081	0.03674	0.1176
NF3	2.3	0.08080	0.03514	0.1160
NF4	2.4	0.08079	0.03366	0.1145

Table 2.2. Summary of calcination temperatures used to prepare $NiFe_2O_4$ with a Fe/Ni mole ratio of 2.3.

Sample name	Calcination temperature/°C
NF5	350
NF6	400
NF7	450
NF8	550
NF9	600
NF10	800

2.2.2. Synthesis of $ZnFe_2O_4$ nanoparticles

The procedure similar to that described in Section 2.2.1 was followed for the preparation of $ZnFe_2O_4$ nanoparticles. Briefly, the iron nitrate solution (2.69*M*) was added to a stirred citric acid solution (3.87*M*) followed by the addition of the zinc nitrate solution (1.17*M*) using an Fe/Zn mole % ratio of 2.3 to avoid the formation of side products. The resulting metal nitrate-citric acid solution was stirred for 95 minutes before increasing the temperature to 60°C, at which temperature it was kept for two hours under stirring. A brown gel was formed which was subsequently oven-dried at 110°C for 24 hours. The as-formed resin was then calcined in a muffle furnace at 450°C for five hours.

2.2.3. Characterization methods

X-ray powder diffraction (XRD) patterns were collected on a Bruker D8 Advance X-ray diffractometer equipped with a Co-Kα X-ray source ($\lambda = 1.78897$ Å). Phase identification of the diffraction data was done using Bruker DIFFRAC.EVA Version 2 software while average crystallite sizes and relative phase abundances were obtained from Rietveld refinements using Bruker AXS Topas Version 4.1.

Mössbauer spectroscopy (MS) experiments were performed at room temperature (RT) using a conventional constant acceleration spectrometer operating in absorption mode and equipped with a ^{57}Co/Rh source. Low temperature experiments were performed at 4.2 K in zero applied field (LT) and in a 10 T applied magnetic field (AF) using an Oxford Instruments Spectromag SM4000-10 cryomagnet. The Mössbauer spectra were analyzed by means of a least squares program, Normos, that models them using sextet subspectra based on a Lorentzian line-shape profile. Identification of the spectral components was based on the comparison of their isomeric shift (δ), quadruple splitting (ΔE_Q) and hyperfine magnetic field (B_{hf}) values with those reported in the literature. All isomer shift and magnetic hyperfine field values are reported relative to metallic iron (α-Fe).

Prior to the TEM analysis, the sample was prepared by crushing and mixing with ethanol to form a suspension. The suspension was placed in an ultrasonic bath to disperse the particles into fine particulates. After ultrasonication, a small amount of sample was transferred into a copper TEM grid (SPI Supplies, 300 mesh) using a pipette. The copper grid was placed in a single-tilt TEM specimen holder and transferred into the TEM for analysis. An FEI Technai Osiris Electron Microscope was used for low magnification TEM analysis. The instrument has a field emission gun as an electron source. Bright field (BF) images were acquired on a Gatan CCD camera that was controlled by Gatan Digital Micrograph software.

2.3. Results and discussion

2.3.1. Optimization study

2.3.1.1. Effect of Fe/Ni molar ratio

Stoichiometrically, a molar ratio of $M^{3+}/M^{2+} = 2$ (stoichiometric amount), whether the sol-gel or citrate precursor method is employed, should be used to prepare spinel-type compounds [10, 12, 13, 15, 19, 22-

27]. Sample NF1 was prepared using this ratio, however, the X-ray powder diffraction pattern of this sample (Figure 2.3 (a)) showed that peaks characteristic of $NiFe_2O_4$, nickel oxide (NiO) and hematite (Fe_2O_3) were also present. Upon increasing the Fe/Ni mole ratio to 2.2 (sample NF2), only Fe_2O_3 was identified as an additional phase to the $NiFe_2O_4$ (Figure 2.3 (b)). Further increases in the Fe/Ni mole ratio (to a maximum of 2.4, samples NF3 and NF4) yielded similar crystalline phases as sample NF2.

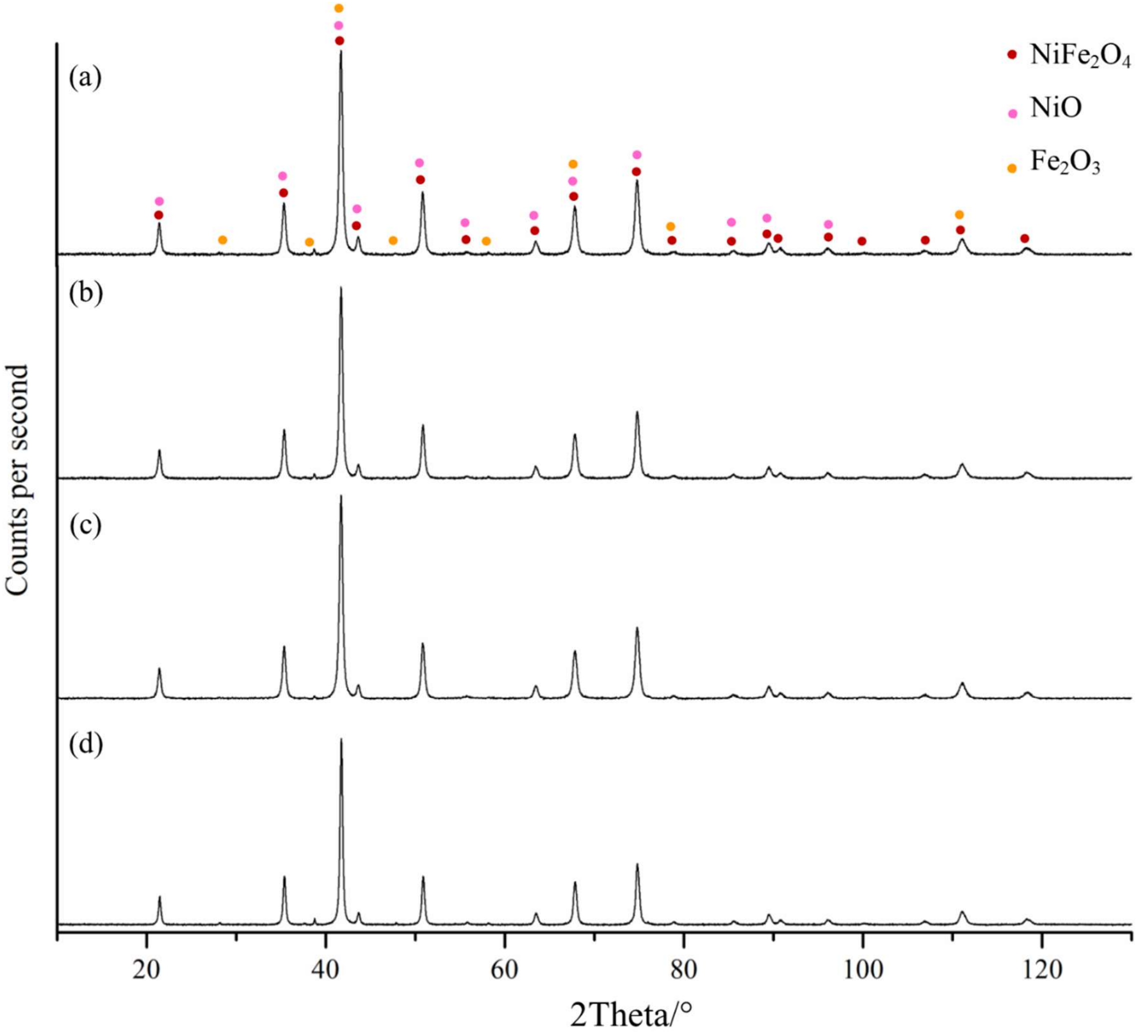

Figure 2.3. X-ray powder diffraction patterns of sample (a) NF1; (b) NF2; (c) NF3 and (d) NF4. Peaks corresponding to the different phases in the sample are marked in (a).

The calculated parameters obtained from the Rietveld refinement of the experimental powder diffraction data, given in Table 2.3, produced a good fit as was evident from the goodness-of-fit (χ^2) and the residual weighted R-factor (R_{wp}) of 1.2% and 2.3% respectively. Only a small amount of hematite was present in all samples. The absence of NiO at Fe/Ni ratios of 2.2 – 2.4 indicate that whilst the formation of $NiFe_2O_4$

should be stoichiometric ($Fe^{3+}/Ni^{2+} = 2$) [4, 6, 12, 15, 25, 26], there might be a difference between the actual and theoretical molar mass of each nitrate, affecting the number of moles actually present. Due to the hygroscopic nature of the metal nitrate salt [23, 28], the composition of each compound may not be exact therefore causing some stoichiometric uncertainty in the synthesis of the ferrite. An additional factor to consider was reported by Gadalla and Yu [29] who showed that the actual waters of hydration in both nitrate compounds was lower than what was expected from the structural formula consequently influencing the amount of metal present.

The volume weighted average crystallite size (L_{Vol}-IB determined from the integral breadth) calculated using Rietveld refinement of the experimental X-ray powder diffraction patterns varied amongst the samples (Table 2.3) and no observable trend between the mole % ratio and the crystallite size was present. However, the variations in the crystallite size amongst the different samples may indicate that there were inconsistencies in the heating conditions during calcination.

Table 2.3. Calculated parameters obtained from the Rietveld refinement of the experimental X-ray powder diffraction patterns shown in Figure 2.3.

Sample	**L_{Vol}-IB/nm$^{\#}$**	**Relative phase abundance/mass %$^{\#}$**		
		NiO	Fe_2O_3	$NiFe_2O_4$
NF1	22.6 (0.4)	2 (0.08)	0.2 (0.02)	97.8 (0.02)
NF2	24.8 (0.4)	-	0.2 (0.02)	99.8 (0.02)
NF3	23.4 (0.4)	-	0.1 (0.02)	99.9 (0.02)
NF4	21.3 (0.2)	-	0.2 (0.02)	99.8 (0.02)

$^{\#}$ Error is shown in parenthesis.

A clear observation with the variation in mole % ratio is that ratios in the range of 2.2 – 2.4 can be used to obtain $NiFe_2O_4$ with only a small amount of hematite present as a secondary phase. However, the lack of clarity on whether changes in the mole % ratio affects the crystallite size makes it difficult to choose the optimum Fe/Ni mole % ratio. The lower percentage of hematite (0.1 ± 0.02 %) obtained at a ratio of 2.3 was therefore the basis on which this ratio was selected for further work.

2.3.1.2. Effect of calcination temperature

The calcination temperature was investigated since it is known that it can affect the size of crystallites where increases thereof lead to the sintering of crystallites [30-33]. The relative phase abundance of NiO, Fe_2O_3 and $NiFe_2O_4$ obtained from the Rietveld refinement of the experimental X-ray powder diffraction patterns of the samples calcined between 350 – 800 °C (samples NF5 – NF10) is given in Table 2.4. The M^{2+} oxide and hematite are intermediate, secondary crystalline phases often formed together with the ferrite [3, 24, 25, 31-35]. At 350°C (NF5); the predominant phase is $NiFe_2O_4$ whilst 9.4% NiO is also present. Increasing the calcination temperature to 400°C resulted in a decrease in the relative phase abundance of NiO (1.7%) consequently yielding 98.3% $NiFe_2O_4$. At 450°C, the phase pure spinel structure of $NiFe_2O_4$ was formed. Thereafter, increases in the calcination temperature resulted in a progressive increase in the relative phase abundance of hematite.

Table 2.4. Relative phase abundance obtained from Rietveld refinement of the X-ray powder diffraction patterns of samples calcined at various temperatures.

Sample	**Calcination temperature/°C**	**Relative phase abundance/mass %#**		
		NiO	Fe_2O_3	$NiFe_2O_4$
NF5	350	9.4 (0.2)	-	90.6 (0.2)
NF6	400	1.7 (0.2)	-	98.3 (0.2)
NF7	450	-	-	100
NF8	550	-	0.1 (0.02)	99.9 (0.02)
NF9	600	-	0.2 (0.02)	99.8 (0.02)
NF10	800	-	0.8 (0.02)	99.2 (0.02)

Error is shown in parenthesis.

A multi-step process is responsible for the formation of the ferrite [31], where the initial step which occurs between 270 and 300°C is the formation of an amorphous material from the precursor. Both Yang and Yen [31] and Zubets [34] emphasize the need to have maghemite (γ-Fe_2O_3) present, irrespective of how it is formed, during the intermediate stages of ferrite formation (300°C – 400°C). A reaction between the M^{2+} oxide and γ-Fe_2O_3 occurs between 325°C and 450°C where the ferrite is formed. The ferrite that forms is dependent on the cation distribution which is a function of the extent of reaction. Two types of the ferrite can form as is shown in Equations 2.1 and 2.2. According to Yang *et al.*[31] the ferrite shown in Equation 2.1 is non-stoichiometric and heating of this compound at temperatures greater than 500°C yields the thermodynamically stable phases, α-Fe_2O_3 and $NiFe_2O_4$. Thus, the presence of hematite at calcination temperatures of 550°C and higher is likely due to the formation of the non-stoichiometric form of the ferrite, a likely consequence of an excess quantity of iron used during synthesis (Fe/Ni mole % ratio = 2.3).

$$\gamma\text{-}Fe_2O_{3(s)} + xM^{2+} \rightarrow M^{2+}{}_{x}Fe_{(8-2x)/3}\,\blacksquare_{(1-x)/3}\,O_{4(s)} \qquad \textbf{Equation 2.1}$$

$$M^{2+}{}_{x}Fe_{(8-2x)/3}\,\blacksquare_{(1-x)/3}\,O_{4(s)} \rightarrow M^{2+}{}_{x+y}Fe_{(8-2(x+y))/3}\,\blacksquare_{(1-(x+y))/3}\,O_{4(s)} \qquad \textbf{Equation 2.2}$$

The volume-weighted average crystallite size (L_{Vol}-IB) as a function of calcination temperature (Figure 2.4) shows an exponential growth of the crystallite with increasing calcination temperature. The crystallite size increases from 9 nm at 350°C to 130 nm at 800°C. Philip *et al.*[32] attributed the growth of $ZnFe_2O_4$ crystallites to the coalescence of particles by solid state diffusion whilst Yang *et al.*[36] hypothesized that an interfacial reaction was responsible for the growth of $NiFe_2O_4$ nanoparticles. Essentially, with the increase in calcination temperature, the crystallites sinter as a means to reduce its free energy by reducing the surface area of the nanoparticles.

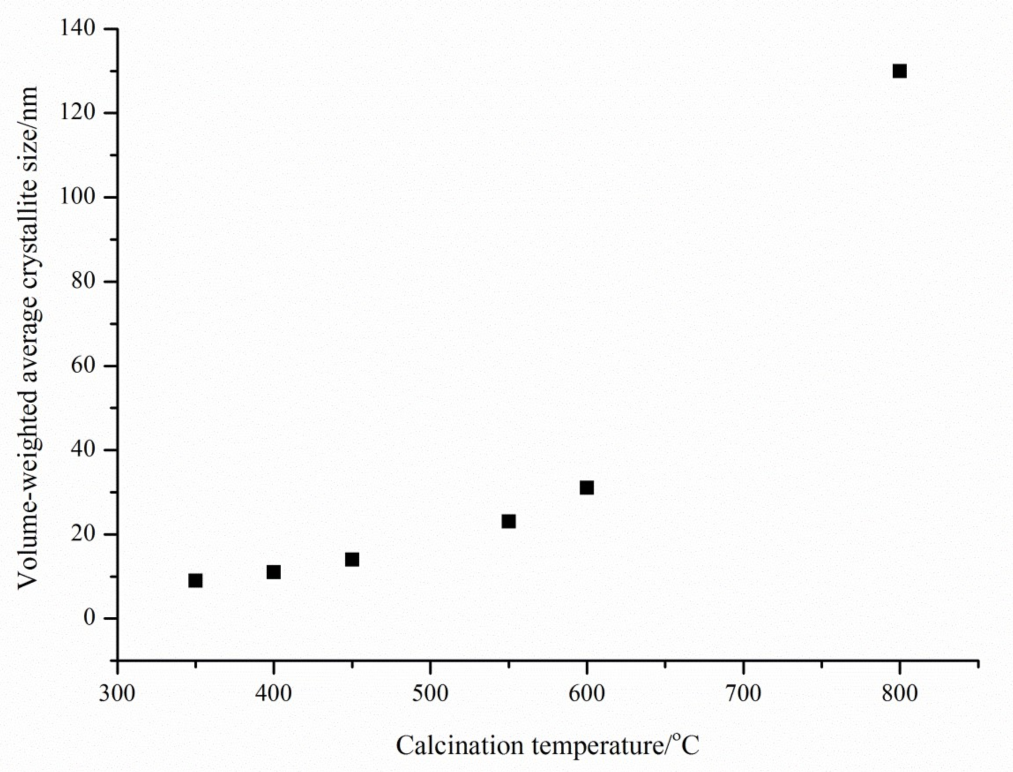

Figure 2.4. The change in the volume-weighted average crystallite size with increasing calcination temperature.

The Schott equation (Equation 2.3) can be used to further describe the changes in crystallite size due to calcination temperature by approximately indicating the growth rate of nanoparticles [32, 36].

$$\mathbf{D = C\, e^{(-E/RT)}} \qquad \textbf{Equation 2.3}$$

In this equation, D represents the crystallite size, E is the activation energy for crystal growth, C is a constant, R is the ideal gas constant and T is the absolute temperature [32, 36]. Applying the Schott equation to the data represented in Figure 2.4 yields the best fit (Figure 2.5) with an activation energy, E, of 32.2

kJ/mol. Yang *et al.*[36] found an activation energy of 16.6 kJ/mol for the growth of their $NiFe_2O_4$ nanoparticles in a calcination temperature range of 600 – 800°C. The slightly higher activation energy obtained in this present study may be due a difference in the calcination conditions (static air used here *versus* flowing air used by Yang *et al.*[36]) or the wider calcination temperature range used (350 – 800°C *versus* 600 – 800°C). A variation in the initial size of the crystallite prior to calcination may also influence the activation energy [37].

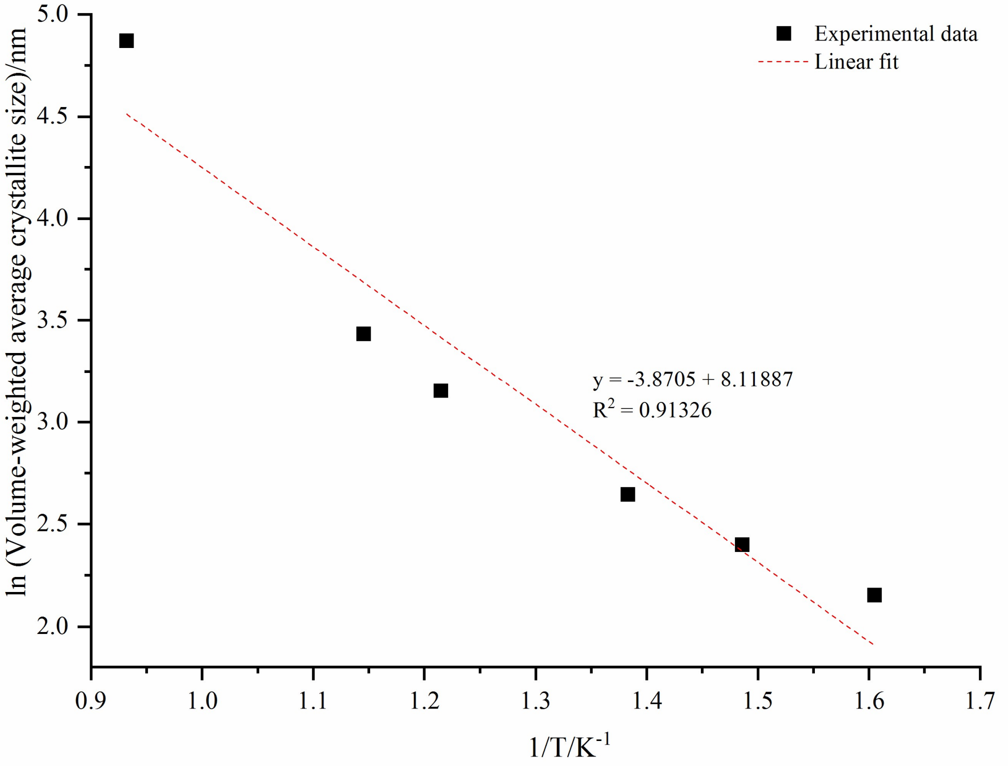

Figure 2.5. A plot showing ln (volume averaged crystallite size (L Vol-IB)) as a function of 1/T.

Since the desired properties for the $NiFe_2O_4$ nanoparticles (phase pure, crystallite size 14 ± 3 nm) was obtained at a calcination temperature of 450°C, it was chosen as the optimum temperature with the Fe/Ni mole % ratio of 2.3.

2.3.2. Characterization of $NiFe_2O_4$ nanoparticles synthesized using optimized conditions

Further characterization of NF7 was done using Mössbauer spectroscopy and transmission electron microscopy. The room temperature Mössbauer spectrum of $NiFe_2O_4$ (Figure 2.6 (a)) shows the presence of two sextets [38]. The isomer shifts (δ), relative to metallic iron, were found to be 0.15 and 0.24 mm/s (Table 2.5) for iron present in the tetrahedral and in the octahedral sites respectively. This is consistent with high spin Fe^{3+} for both sites [39]. Furthermore, the low quadrupole splitting values ($\Delta E_{Q,\ tet}$ = -0.02 mm/s and $\Delta E_{Q,\ oct}$ = -0.04 mm/s) are consistent with an overall cubic symmetry around Fe^{3+} at both sites [8, 38, 39]. The hyperfine magnetic splitting (B_{hf}) values were 48.3 and 52.1T for the tetrahedral and octahedral sites respectively, which are similar to what is expected for ferrimagnetic $NiFe_2O_4$ [40, 41].

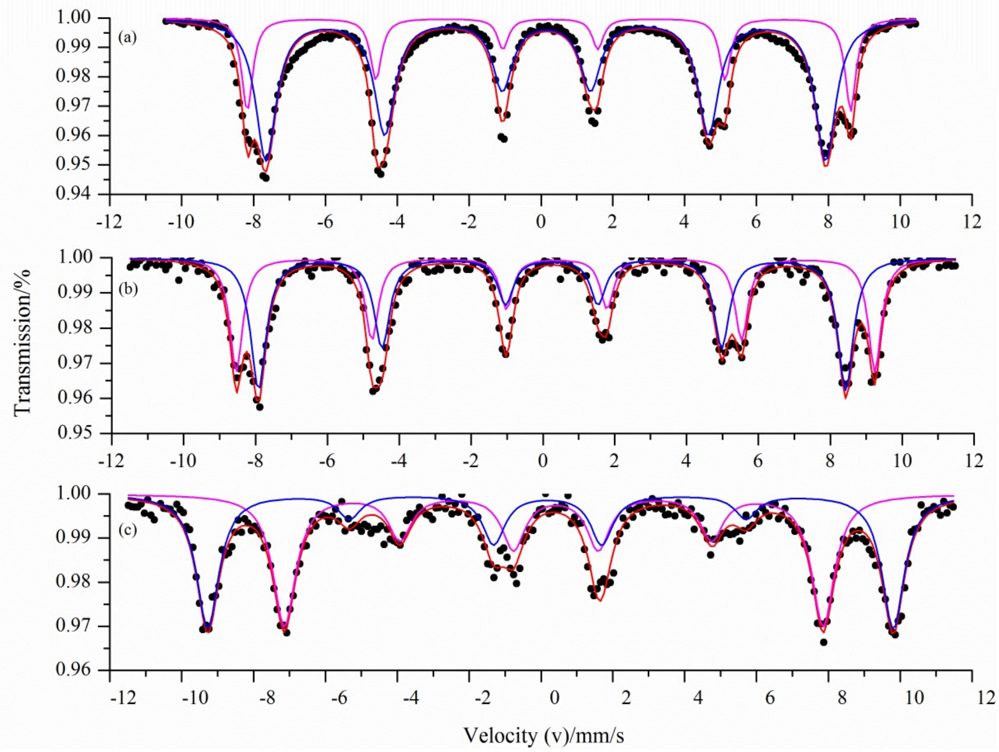

Figure 2.6. Mössbauer spectrum of $NiFe_2O_4$ obtained at (a) room temperature, (b) 4.2K and (c) 4.2K with an applied external magnetic field of 10T.

The low temperature Mössbauer spectrum (4.2K) is shown in Figure 2.6 (b) and it displayed only two sextets that correspond to Fe^{3+} in the tetrahedral and octahedral sites. The absence of additional sextets indicated that other iron oxide phases were not present in measurable quantities and confirmed that the material comprised only of $NiFe_2O_4$. The $Fe^{3+}_{tet}/Fe^{3+}_{oct}$ was determined to be 0.8 (Table 2.5), below the value expected for an exact inverse spinel. This may be due to the presence of defects in the crystal structure of $NiFe_2O_4$ [40, 41].

Figure 2.6 (c) shows the Mössbauer spectrum obtained at 4.2K and 10T where the $Fe^{3+}_{tet}/Fe^{3+}_{oct}$ was found to be 0.9 in this case (Table 2.5). The deviation of this ratio from 1.0 may be due to an increased amount of Fe^{3+} in the octahedral site, a possible consequence of the excess iron used to synthesize the $NiFe_2O_4$. The high-field Mössbauer spectrum also showed the presence of line 2 and 5 in the sextets. For a ferrimagnetic spinel with collinear opposed moments in the two sublattices in an external magnetic field parallel to the photon beam, it is expected for these lines to be absent [42].

The ratio of line 2 to 3 for the tetrahedral ($A_{23,\text{ tet}}$) and octahedral sites ($A_{23,\text{ oct}}$) was found to be 0.5 and 0.8 respectively. For a stoichiometric (Fe/Ni = 2) fully inverted spinel without defects, a ratio of zero is expected. Thus, the $NiFe_2O_4$ prepared in this work (NF7) showed the presence of spin canting which appeared predominantly at the octahedral site. The former indicates that the spins are not completely aligned along the external magnetic field and that the $NiFe_2O_4$ synthesized deviates from a collinear Néel-type spin arrangement $(Fe\uparrow)[Ni\downarrow Fe\downarrow]O_4)$ [41]. Such occurrences may be due to a reduced number of magnetic ions around the surface atoms, cation vacancies or that the nanoparticle has a different magnetic spin structure to the bulk material.[43, 44]

Table 2.5. Mössbauer parameters for $NiFe_2O_4$ from least-squares fitting of the spectrum obtained at various conditions.

Analysis	Iron site	δ/mm/s	ΔE_Q/mm/s	B/T*	A_{23}	Area/%
RT	tetrahedral	0.15	-0.02	48.3	--	23
	octahedral	0.24	-0.04	52.1	--	77
4.2 K, 0 T	tetrahedral	0.25	0.01	50.7	1.9	44
	octahedral	0.37	-0.03	55.1	1.6	56
4.2 K, 10 T	tetrahedral	0.23	0.08	59.2	0.5	47
	octahedral	0.39	-0.06	46.5	0.8	53

* In the absence of a magnetic field (0 T), B represents the hyperfine magnetic splitting whilst in the presence of a magnetic field (10 T), B represents the measured value that includes the effect of the applied field.

The BF-TEM image of $NiFe_2O_4$ (Figure 2.7 (a)) showed that the particles have various shapes which include round and oval. A wide crystallite size distribution (CSD) was obtained (Figure 2.7 (b)) with crystallite sizes ranging from 6 – 40 nm and a mean crystallite size of 17 nm. Further examination of the crystallites using HR-STEM revealed the presence of a well-defined crystalline structure free from lattice defects as seen from the lattice fringes present (Figure 2.8). The diffractograms obtained from the FFT analysis (inset in Figure 2.8 (a)) showed spots associated with the spinel ferrite phase. Specifically, the [3 1 0] image shows the perpendicular fringes projected from the (1 3 1) and (0 0 4) planes of $NiFe_2O_4$ with a lattice spacing of d_{hkl} = 0.26 nm and d_{hkl} = 0.21 nm respectively.

An additional observation from the images was that the surface of the crystallites appeared defected. There was also evidence in some images of numerous boundaries (as indicated by the rectangle in Figure 2.8 (b)) suggesting that crystallites merged, a possible outcome of the calcination step during synthesis that could account for the larger sizes evidenced in the CSD. The FFT analysis of the lattice image (Figure 2.8 (b)), viewed along the [3 1 4] zone axis, showed the lattice spacing of d_{hkl} = 0.48 nm; 0.24 nm; 0.16 nm and 0.12 nm which correspond to the (1 1 1), (2 2 2), (3 3 3) and (4 4 4) planes in $NiFe_2O_4$ respectively.

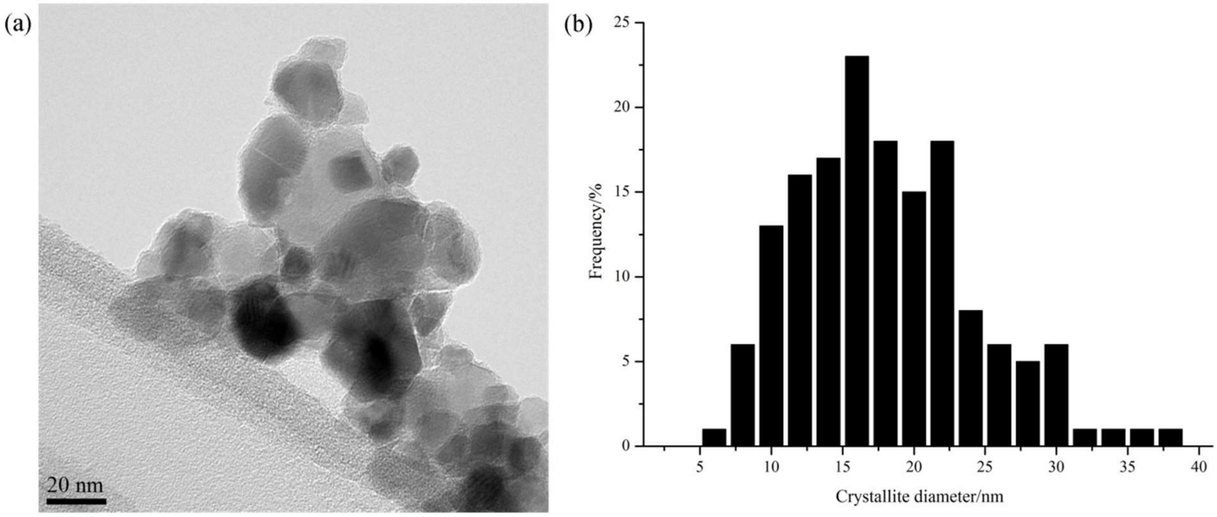

Figure 2.7. (a) BF-TEM image of $NiFe_2O_4$ and (b) Number frequency histogram showing the crystallite size distribution of $NiFe_2O_4$.

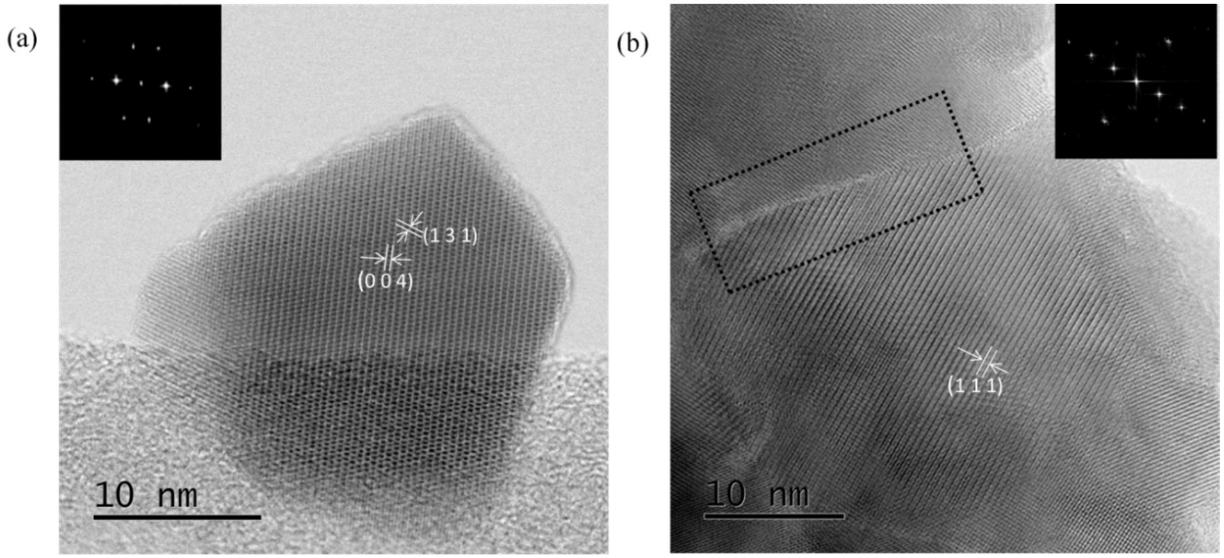

Figure 2.8. HR-STEM image of a $NiFe_2O_4$ nanoparticle showing (a) lattice fringes with the insert showing the FFT pattern constructed from the lattice image viewed along the [3 1 0] zone axis and (b) showing the presence of a boundary (indicated by rectangle) with the insert showing the FFT pattern constructed from the lattice image viewed along the [3 1 4] zone axis.

2.3.3. Characterization of $ZnFe_2O_4$ nanoparticles

The XRD pattern of $ZnFe_2O_4$ (Figure 2.9) showed all major peaks belonging to the desired oxide. The Rietveld refinement procedure of the experimental powder diffraction data yielded a good fit (the goodness-of-fit (χ^2) and the residual weighted R-factor (R_{wp})) and confirmed that a phase pure material with volume-weighted averaged crystallite size (L_{vol}-IB) of 14 nm was produced (Table 2.6).

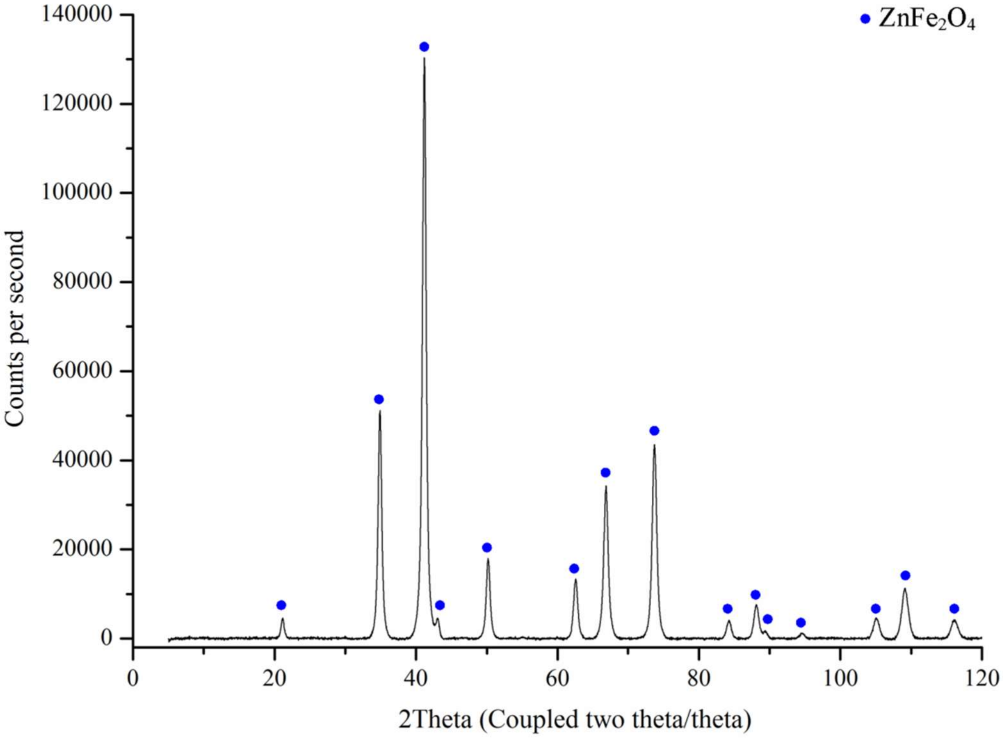

Figure 2.9. X-ray powder diffraction pattern of $ZnFe_2O_4$.

Table 2.6. Phases present in $ZnFe_2O_4$ and their average crystallite size as determined using Rietveld refinement of the XRD data.

Sample	**χ^2/%**	**R_{wp}/%**	**Phases**	**Relative abundance/mass %**	**L_{vol}-IB/nm**
$ZnFe_2O_4$	2.6	1.7	$ZnFe_2O_4$	100	14

The zero field Mössbauer spectrum obtained at room temperature (Figure 2.10 (a)) shows the presence of two doublets whose hyperfine parameters (Table 2.7) are typical of Fe^{3+} in $ZnFe_2O_4$ [9, 45, 46]. At low temperature (4.2K), the Mössbauer spectrum displays three sextets (Figure 2.10 (b)). The isomer shifts (δ), relative to metallic iron, were consistent with Fe^{3+} whist the magnetic hyperfine splitting values were indicative of Fe^{3+} in both the tetrahedral and octahedral sites (Table 2.7). This was consistent with the observed shape of the Mössbauer spectrum which suggested that Fe^{3+} was present in different atomic environments [45]. The transition from a six line hyperfine pattern at low temperature to a two line quadropolar hyperfine pattern at room temperature suggests a superparamagnetic state of the $ZnFe_2O_4$ nanoparticles [7, 45, 47, 48]. The high-field Mössbauer spectrum (4.2K, 10T) is given in Figure 2.10 (c) which also shows the presence of three sextets. The hyperfine parameters (Table 2.7) corresponded to Fe^{3+} in the octahedral site whilst two sextets were due to these ions being present in the tetrahedral site with differing atomic environments. This was also observed with the low temperature zero field spectrum.

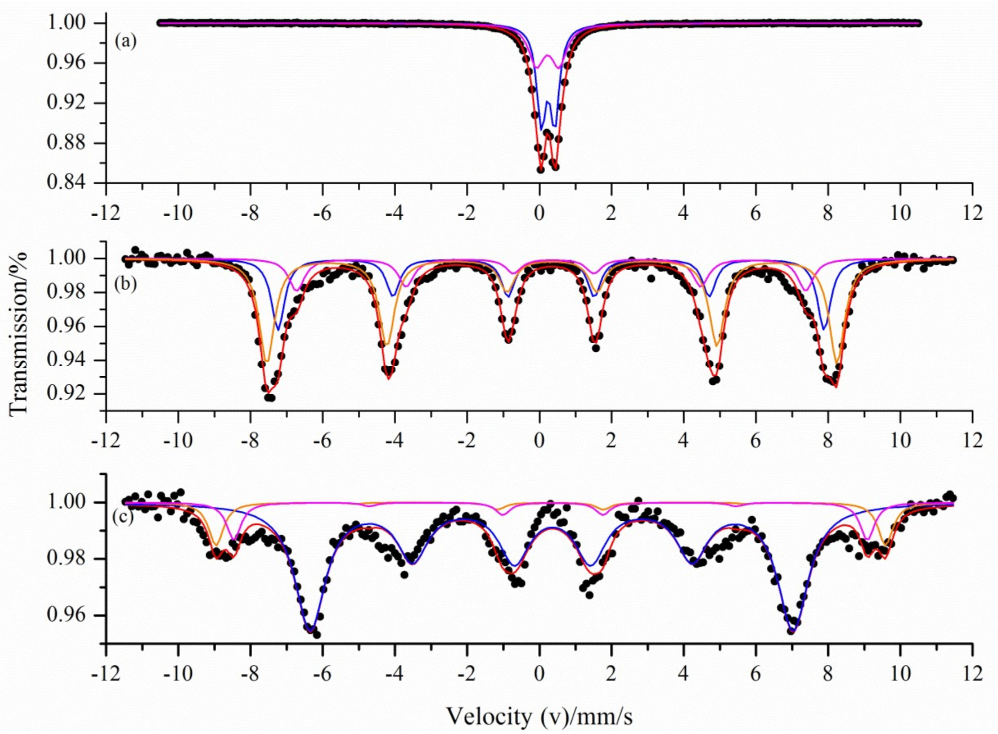

Figure 2.10. Mössbauer spectrum of $ZnFe_2O_4$ obtained at (a) room temperature, (b) 4.2K and (c) 4.2K with an applied external magnetic field of 10T.

The BF-TEM image of $ZnFe_2O_4$ nanoparticles (Figure 2.11 (a)) shows the presence of variously shaped and sized nanoparticles. There was a wide crystallite size distribution (Figure 2.11 (b)) with sizes ranging from 9 – 45 nm. The mean crystallite size of the $ZnFe_2O_4$ nanoparticles was 26 nm.

Table 2.7. Mössbauer parameters for $ZnFe_2O_4$ from least-squares fitting of the spectrum obtained at various conditions.

Analysis	Iron site	δ/mm/s	ΔE_Q/mm/s	B/T*	A_{23}	Area/%
RT	octahedral	0.35	0.37	-	-	50.8
	octahedral	0.34	0.59	-	-	49.2
4.2 K, 0 T	Octahedral-type	0.47	0.00	43.7	1.9	17.7
	Tetrahedral-type	0.43	0.00	46.9	1.0	29.4
	Tetrahedral-type	0.45	0.00	49.0	2.7	52.9
4.2 K, 10 T	Octahedral-type	0.46	-0.03	41.5	1.0	82.5
	Tetrahedral-type	0.42	-0.02	57.5	-	8.5
	Tetrahedral-type	0.42	-0.09	54.4	0.5	9.0

* In the absence of a magnetic field (0 T), B represents the hyperfine magnetic splitting whilst in the presence of a magnetic field (10 T), B represents the measured value that includes the effect of the applied field.

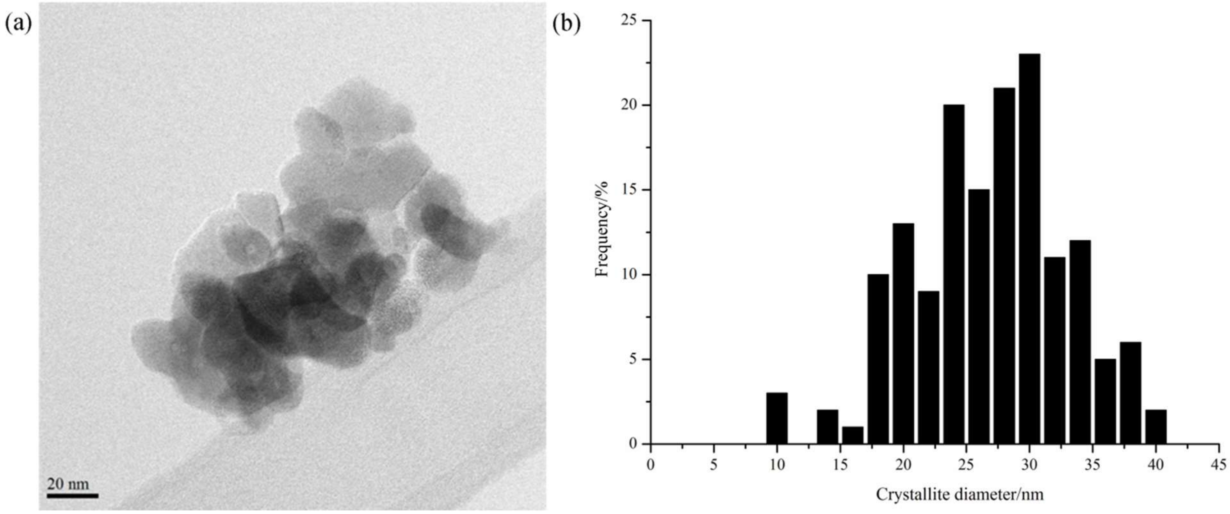

Figure 2.11. (a) BF-TEM image of $ZnFe_2O_4$ (b) Number frequency histogram showing the crystallite size distribution of $ZnFe_2O_4$.

2.4. Chapter summary

The citrate precursor method was used to synthesize $NiFe_2O_4$ and $ZnFe_2O_4$ nanoparticles. The synthesis method was optimized, using $NiFe_2O_4$ as the basis of comparison, and different Fe/Ni mole % ratios and calcination temperature were investigated. It was found that the calculated mole % ratio required to produce $NiFe_2O_4$ nanoparticles with only hematite as an impurity, was non-stoichiometric when the calcination temperature was 550°C. The lowest relative phase abundance of hematite was obtained with a ratio of 2.3. Using this ratio, the calcination temperature was varied between 350 and 800°C, where it was found that phase pure $NiFe_2O_4$ nanoparticles with a volume-weighted average crystallite size of 14 nm was obtained at 450°C. These conditions also resulted in the formation of phase pure $ZnFe_2O_4$ with a larger crystallite size. For both ferrites, Mössbauer spectroscopy confirmed the purity of the materials.

2.5. References

[1] G. Russo, P. Smereka, Computation of strained epitaxial growth in three dimensions by kinetic Monte Carlo, J. Comput. Phys., 214 (2006) 809-828.

[2] M. Jin, H. Zhang, J. Wang, X. Zhong, N. Lu, Z. Li, Z. Xie, M. J. Kim, Y. Xia, Copper can still be epitaxially deposited on palladium nanocrystals to generate core shell nanocubes despite their large lattice mismatch, ACS Nano, 6 (2012) 2566-2573.

[3] A. Sutka, G. Mezinskis, Sol-gel auto-combustion synthesis of spinel-type ferrite nanomaterials, Front. Mater. Sci., 6 (2012) 128.

[4] D. Carta, M. F. Casula, A. Falqui, D. Loche, G. Mountjoy, C. Sangregorio, A. Corrias, A structural and magnetic investigation of the inversion degree in ferrite noncrystalline MFe_2O_4 (M = Mn, Co, Ni), J. Phys. Chem. C, 113 (2009) 8606.

[5] K. I. Lilova, K. Shih, C.-W. Pao, J.-F. Lee, A. Navrotsky, Thermodynamics of $NiAl_2O_4$-$NiFe_2O_4$ spinel solid solutions, J. Am. Chem. Soc., 95 (2012) 423.

[6] R. Mukherjee, T. Sahu, S. Sen, P. Sahu, Structural and microsctructural evolution due to increasing Co substitution in $Ni_{1-x}Co_xFe_2O_4$: An X-ray diffraction study using the Rietveld method, Materials Chem. Phys., 128 (2011) 365.

[7] V. B. Gutiérrez, F. Jiménez-Villacorta, P. Bonville, M. J. Torralvo-Fernández, R. Sáez-Puche, X-ray absorption spectroscopy and Mossbauer spectroscopy studies of superparamagnetic $ZnFe_2O_4$ nanoparticles, J. Phys. Chem. C, 115 (2011) 1627-1634.

[8] Z. Z. Lazarevîc, C. Jovalekic, A. Milutinovic, M. J. Romcevic, N. Z. Romcevic, Preparation and characterization of nano ferrites, Acta. Phys. Pol. A, 121 (2012) 682.

[9] G. F. Goya, E. R. Leite, Ferrimagnetism and spin canting of $Zn^{57}Fe_2O_4$ nanoparticles embedded in ZnO matrix, J. Phys. : Condens. Matter, 15 (2003) 641-669.

[10] D.-H. Chen, X.-R. He, Synthesis of nickel ferrite nanoparticles by sol-gel method, Materials Research Bulletin, 36 (2001) 1369-1377.

[11] J. Park, J. Joo, S. G. Kwon, Y. Jang, T. Hyeon, Synthesis of monodisperse spherical nanocrystals, Angew. Chem. Int. Ed., 46 (2007) 4630-4660.

[12] M. A. Ahmed, N. Okasha, S. I. El-Dek, Preparation and characterization of nanometric Mn ferrite via different methods, Nanotechnol., 19 (2008) 1-6.

[13] M. Srivastava, S. Chaubey, A. K. Ojha, Investigation on size dependent structural and magnetic behavior of nickel ferrite prepared by sol-gel and hydrothermal methods, Materials Chem. Phys., 118 (2009) 174-180.

[14] M. Zayat, D. Levy, Blue $CoAl_2O_4$ particles prepared by the sol-gel and citrate-gel methods, Chem. Mater., 12 (2000) 2763-2769.

[15] A. Verma, T. C. Goel, R. C. Mendiratta, R. G. Gupta, High-resistivity nickel zinc ferrites by the citrate precursor method, J. Magn. Magn. Mater., 192 (1999) 271-276.

[16] P. A. Jadhav, R. S. Devan, Y. D. Kolekar, B. A. Chougule, Structural, electrical and magnetic characterizations of Ni.Cu.Zn ferrite synthesized by citrate precursor method, J. Phys. Chem. Solids, 70 (2009) 396-400.

[17] A. Douy, M. Odier, The polyacrylamide gel: A novel route to ceramic and glassy oxide powders, Mater. Res. Bull., 24 (1989) 1119.

[18] J.-H. Choi, Y.-S. Han, J.-T. Kim, Y.-H. Kim, Citrate route to ultra-fine barium polytitanates with microwave dielectric properties, J. Mater. Chem., 5 (1995) 57.

[19] S. Prasad, N. S. Gajbhiye, Magnetic studies of nanosized nickel ferrite particles synthesized by the citrate precursor technique, J. Alloys and Comp., 265 (1998) 87.

[20] V. K. Sankaranarayanan, Q. A. Pankhurst, D. P. E. Dickson, C. E. Johnson, Ultrafine particles of barium ferrite from a citrate precursor, J. Magn. Magn. Mater., 120 (1993) 73.

[21] V. K. Sankaranarayanan, Q. A. Pankhurst, D. P. E. Dickson, C. E. Johnson, Synthesis and characterization of ultrafine lithium ferrite from a citrate precursor, J. Magn. Magn. Mater., 130 (1994) 288.

[22] A. Verma, T. C. Goel, R. G. Mendiratta, Low temperature processing of NiZn ferrite by citrate precursor method and study or properties, Mater. Sci. and Technol., 16 (2000) 712.

[23] C.-C. Hwang, J.-S. Tsai, T.-H. Huang, C.-H. Peng, S.-Y. Chen, Combustion synthesis of Ni-Zn ferrite powder - influence of oxygen balance value, J. Solid State Chem., 178 (2005) 382-389.

[24] H.-C. Lu, J.-E. Chang, W.-W. Vong, H.-T. Chen, Y.-L. Chen, Porous ferrite synthesis and catalytic effect on benzene degradation, Int. J. Phys. Sci., 6 (2011) 855.

[25] J. Azadmanjiri, S. A. S. Ebrahimi, Influence of stoichiometry and calcination condition on the microstructure and phase constitution of $NiFe_2O_4$ powders prepared by sol-gel autocombustion method, Phys. Stat. Sol., 12 (2004) 3414.

[26] W.-O. Choi, J.-G. Lee, B.-S. Kang, K. P. Chae, Crystallographic and magnetic properties of anno-sized nickel substituted cobalt ferrites synthesized by the sol-gel method, J. Magn. Mag. Mater, 19 (2014) 59.

[27] Z. H. Zhou, J. M. Xue, J. Wang, H. S. O. Chan, T. Yu, Z. X. Shen, $NiFe_2O_4$ nanoparticles formed *in situ* in silica matrix by mechanical activation, J. Appl. Physics, 91 (2002) 6015.

[28] Z. K. Karakas, R. Boncukcouglu, I. H. Karakas, M. Ertugrul, The effects of fuel type in synthesis of $NiFe_2O_4$ nanoparticles by microwave assisted combustion method, J. Magn. Magn. Mater., 374 (2015) 298-306.

[29] A. M. Gadalla, H.-F. Yu, Thermal behaviour of some Ni^{II} and Fe^{III} salts, Thermochimica Acta, 164 (1990) 21.

[30] B. J. Hwang, R. Santhanam, D. G. Liu, Effect of various synthetic parameters on purity of $LiMn_2O_4$ spinel synthesized by a sol-gel method at low temperature, J. Powers Sources, 101 (2001) 86.

[31] J. M. Yang, F. S. Yen, Evolution of intermediate phases in the synthesis of zinc ferrite nanopowders prepared by the tartrate precursor method, J. Alloys and Comp., 450 (2008) 387.

[32] J. Philip, G. Gnanaprakash, G. Panneerselvam, M. P. Antony, T. Jayakumar, B. Raj, Effect of thermal annealing under vacuum on the crystal structure, size and magnetic properties of $ZnFe_2O_4$ nanoparticles, J. Appl. Physics, 102 (2007) 054305.

[33] R. Köferstein, T. Walther, D. Hesse, S. G. Ebbinghaus, Crystallite-growth, phase transitions, magnetic properties and sintering behaviour of nano-$CuFe_2O_4$ powders prepared by a combustion-like process, J. Solid State Chem., 213 (2014) 57.

[34] A. V. Zubets, Mechanism of ferrite spinel formation revisited, Inorg. Mater., 38 (2002) 718.

[35] K. Nadeem, T. Traussnig, I. Letofsky-Papst, H. Krenn, U. Bossmann, R. Würschum, Sol-gel synthesis and characterization of single-phase Ni ferrite nanoparticles dispersed in SiO_2 matrix, J. Alloys and Comp., 493 (2010) 385.

[36] H. Yang, X. Zhang, W. Ao, G. Qiu, Formation of $NiFe_2O_4$ nanoparticles by mechanochemical reaction, Mater. Res. Bull., 39 (2004) 833.

[37] G. Gnanaprakash, J. Philip, T. Jayakumar, B. Raj, Effect of digestion time and alkali addition rate on physical properties of magnetite nanoparticles, J. Phys. Chem. B, 111 (2007) 7978.

[38] S. S. Umare, R. S. Ningthoujam, S. J. Sharma, S. Shrivastava, S. Kurian, N. S. Gajbhiye, Mössbauer and magnetic studies on nanocrystalline $NiFe_2O_4$ particles prepared by ethylene glycol route, Hyperfine Interact., 184 (2008) 235-243.

[39] S. J. Kim, W. C. Kim, C. S. Kim, S. W. Lee, Mössbauer studies of superexchange interactions in $NiFe_2O_4$, J. Korean Phys. Soc., 36 (2000) 430-434.

[40] A. Cosovic, V .Cosovic, T. Zak, B. David, N. Talijan, Structure and properties of nanosize $NiFe_2O_4$ prepared by the template and precipitation methods, J. Min. Metall. Sect. B-Metall., 49 (2013) 271.

[41] V. Sepelák, D. Baabe, D. Mienert, D. Schultze, F. Krumeich, F. J. Litterst, K. D. Becker, Evolution of structure and magnetic properties with annealing temperature in nanoscale high-energy-milled nickel ferrite, J. Magn. Magn. Mater., 257 (2003) 377-386.

[42] A. G. Maddick, Mössbauer spectroscopy principles and applications of the technique, in, Horwood publishing, England, 1997.

[43] S. Guillemet-Fritsch, C. Tenailleau, H. Bordeneuve, A. Rousset, Magnetic properties of cobalt and mangenese oxide spinels ceramics, Adv. Sci. Technol., 67 (2010) 143-148.

[44] S. Morup, E. Brok, C. Frandsen, Spin Structures in Magnetic Nanoparticles, J. Nanomater., 2013 (2013) 1-8.

[45] C. N. Chinnasamy, A. Narayanasamy, N. Ponpandian, K. Chattopadhyay, H. Guérault, J.-M. Greneche, Magnetic properties of nanostructured ferrimagnetic zinc ferrite, J. Phys.: Condens. Matter, 12 (2000) 7795-7805.

[46] J. Battle, T. Clark, B. Evans, ^{57}Fe Mössbauer spectroscopy of zinc ferrite prepared by a variety of synthetic methods, J. de Physique IV Colloque, 07 (C1) (1997) C1-257-C251-258.

[47] J. F. Hochepied, P. Bonville, M. P. Pileni, Nonstoichiometric zinc ferrite nanocrystals: Syntheses and unusual magnetic properties, J. Phys. Chem. B, 104 (2000) 9095-9912.

[48] V. B. Gutiérrez, M. J. Torralvo, R. S. Puche, P. Bonville, Magnetic properties of solvothermally synthesized $ZnFe_2O_4$ nanoparticles, J. Phys.: Conf. Ser., 200 (2010) 072013-072017.

3 Synthesis and characterization of $NiFe_2O_4$@Co_3O_4 core-shell nanoparticles

Nickel ferrite ($NiFe_2O_4$) nanoparticles were used as a core around which cobalt (II, III) oxide (Co_3O_4) was grown. In an attempt to vary the shell thickness, the concentration of cobalt used was varied following a one-step homogeneous deposition-precipitation synthesis. It was found that the concentration of cobalt in solution dictated whether Co_3O_4 formed on the surface but not its thickness. Concentrations of 6.3 wt.% cobalt in solution and 7.6 wt.% cobalt in solution yielded a partial shell around some $NiFe_2O_4$ nanoparticles. A concentration of 11.0 wt.% cobalt in solution resulted in the formation of Co_3O_4 nanoparticles on the ferrite surface whilst a concentration of 19.1 wt.% cobalt in solution yielded Co_3O_4 nanoparticles amongst the $NiFe_2O_4$ nanoparticles. Using a final concentration of 7.6 wt.% cobalt in solution, but applying the synthesis procedure twice, yielded the core-shell structure with most nickel ferrite nanoparticles having a Co_3O_4 shell.

3.1 Introduction

Cobalt catalysts based on Co_3O_4 have intriguing properties and thus find application in a variety of catalytic reactions, such as oxidation reactions in environmental applications [1-5], NO decomposition [6], electro-catalytic applications [7, 8], and after reduction in hydrogenation reactions [9-11], such as the Fischer-Tropsch synthesis [9, 10]. Despite the high activity typically gained with these catalysts, the cost of cobalt can significantly increase the cost associated with the catalytic process. This would mean that routes to lower the cost of cobalt-based catalysts are constantly being sought. One such way would be to replace the catalytically inaccessible cobalt oxide in the catalyst with a cheaper alternative.

In an industrial catalyst, only a small percentage of cobalt oxide is on the surface. Subsurface cobalt oxide is not directly involved in the reaction, and can thus be replaced by a less expensive material. This would result in the formation of a core-shell catalyst, in which the shell of cobalt oxide is combined with a core of a less expensive material. Core-shell materials can be described as nanoparticles that are comprised of a core and a shell (outer layer material) with the active-phase topology tailored to have a specific structure and composition at the nanoscale but in a manner that allows for scale up [12, 13]. The core can vary in size and shape and the shell can have different thicknesses and surface morphologies [13-20]. These materials may have different electronic and geometric properties around the catalytically active center resulting in novel catalytic properties. [10, 13, 21-23]

The main attraction of core-shell catalysts is the reduction in costs that can be obtained. For instance, replacing cobalt oxide with another metal oxide core-shell catalyst may result in a catalyst cost saving of up to 50% if the core is composed of oxides of Fe, Zn, Ti or Si [10]. Calderone *et al.*[10] stated that achieving a particular cobalt shell thickness for a certain crystallite size whilst maintaining an overall cost saving and producing a high performance material does require a cheap, simple and scalable method. This means that the shell should be epitaxially grown onto the core material [24] thus requiring minimal lattice mismatch between the core and the shell.

$NiFe_2O_4$ is a suitable candidate that fits this criterion due to the similarity of its crystal structure with that of Co_3O_4. Using $NiFe_2O_4$ as a core would allow for the preparation of a cheaper nanoparticle than one containing only cobalt oxide as the cost of nickel and iron is low by comparison. Here we present, a simple precipitation route [13] using cobalt carbonate ($CoCO_3$), ammonium carbonate ($(NH_4)_2CO_3$) and ammonia solution (NH_3/NH_4OH) as reactants to produce a Co_3O_4 shell around a $NiFe_2O_4$ core.

3.2 Experimental

3.2.1. Preparation of $NiFe_2O_4@Co_3O_4$

The synthesis procedure was based on the work done by Calderone *et al.*[13] although a higher synthesis temperature was used to force the formation of Co_3O_4 within a 24 hour period. In a typical synthesis, $(NH_4)_2CO_3$ (Sigma Aldrich) (5.1 mmol) was dissolved in deionized water and 25 wt.% ammonia aqueous solution (Sigma Aldrich) was added. $CoCO_3$ (Sigma Aldrich) (5.8 mmol) was then added (pH = 11.5). This suspension was then stirred at 45°C for two hours, during which the cobalt carbonate formed the cobalt hexamine precursor. This was evidenced when the pink suspension turned a clear violet color. The solution was then filtered. This filtrate (pH = 10.8) was added to a round bottom flask containing $NiFe_2O_4$ and was stirred at 85°C for six hours. The temperature was then increased to 95°C and the mixture was allowed to stir for 24 hours. The solvent was removed under vacuum and the dried solid was rinsed with water and dried under vacuum. The solid obtained was oven-dried at 110°C, overnight. The synthesis procedure should result in the formation of Co_3O_4, since the cobalt hexamine precursor decomposes below 100°C to yield $Co(OH)_2$ [25] which by further heating in air is transformed into Co_3O_4 [26].

A multi-step synthesis procedure was used to minimize self-nucleation and in an attempt to improve the coverage of the core nanoparticle by the shell. For the two-step synthesis, the above procedure was followed for step 1 using the reactant quantities indicated in Table 3.1. In step 2, the cobalt precursor solution was made as per step 1; however, a suspension made from the dried solid from step 1. The synthesis then followed the process outlined above.

In order to investigate whether the Co_3O_4 shell thickness can be varied, the concentration of Co in the synthesis solution was varied (Table 3.1). This was achieved by increasing the mass of the $CoCO_3$ whilst keeping the mass of $NiFe_2O_4$ the same. The quantities of $(NH_4)_2CO_3$ and aqueous NH_3 solution were adjusted stoichiometrically.

Table 3.1. Summary of masses used for the synthesis of the various $NiFe_2O_4$@ Co_3O_4 nanoparticles.

Sample	Mass $CoCO_3$/g	Mass $(NH_4)_2CO_3$/g	Volume NH_3(aq)/mL	Concentration/wt.% Co
1	0.0693	0.4866	3.0	6.3
2	0.0847	0.5872	3.6	7.6
3	0.1263	0.9663	6.0	11.0
4	0.2429	1.9384	10.4	19.1
5 Step 1	0.0408	0.3239	1.8	3.8
5 Step 2	0.0408	0.3239	1.8	3.8

3.2.2. Characterization methods

For the TEM analysis, the sample was prepared by crushing and mixing with ethanol to form a suspension. The suspension was placed in an ultrasonic bath to disperse the particles into fine particulates. After ultrasonication, a small amount of sample was transferred onto a copper TEM grid (SPI Supplies, 300 mesh) using a pipette. The copper grid was placed in a single-tilt TEM specimen holder and transferred into the TEM for analysis. An FEI Technai Osiris Electron Microscope was used for low magnification TEM analysis. The instrument has a field emission gun as an electron source. Bright field (BF) images were acquired on a Gatan CCD camera that was controlled by Gatan Digital Micrograph software. Scanning Transmission Electron Microscopy (STEM) images were captured by a High Angle Annular Dark Field (HAADF) detector that was controlled by FEI TIA software. Energy Dispersive X-ray Spectroscopy (EDS) elemental mapping was performed using ChemiSTEM EDX detector system controlled by Bruker Espirit software. A double spherical aberration (Cs) corrected JEOL ARM 200F transmission electron microscope operated at 200 kV was also used in the present study which is situated at the Centre for High Resolution Transmission Electron Microscopy (CHRTEM) at Nelson Mandela University. STEM- HAADF as well as bright field (BF) STEM imaging at atomic resolution was used. Electron energy loss spectroscopy (EELS) Spectrum Imaging (SI) was performed using the DualEELS^{TM} mode on the Gatan GIF Quantum ERS^{TM} spectrometer. This allows for acquisition of the intense zero loss peak (ZLP) and the elemental edges at virtually the same time. The convergence semi-angle of 21.4 mrad was used for the STEM probe and the collection semi-angle of the spectrometer was 54.3 mrad at a camera length of 1 cm.

For Raman spectroscopy, the powders were placed on a microscope slide and measured using an inVia Raman system utilizing the 785 nm line of a solid-state diode laser. The beam was focused with a Leica microscope using a x20 objective. Data were collected for the region 50 – 2000 cm^{-1} for 10 seconds, scanned 20 times using a laser power of 0.1%. Wire Version 4.1 software was used for data capturing and instrument control. The Raman band of pure Si was measured before data accumulation commenced for calibration purposes.

X-ray photoelectron Spectroscopy (XPS) spectra were recorded on a KRATOS Axis Ultra DLD at Sasol United Kingdom (SUK) Ltd. with the analyzer operating at the fixed pass energy of 160 eV for the survey spectrum and 40 eV for the individual regions. The measurements were carried out using an Al K_α monochromated source. Due to the nature of the materials, neutralization was necessary during the acquisition. All the spectra presented in this report have been corrected in energy using the C 1s at 284.6 eV and checked versus the position of other peaks, especially Al 2p expected at ~74.2 eV. All the samples, detailed in Table 3.1, were mounted as loose powders in a molybdenum sample holder. On average 10 mg of material was used for each measurement.

3.3. Results and discussion

The characterization of $NiFe_2O_4$ nanoparticles (NF7) used as the core to synthesize the various $NiFe_2O_4$@Co_3O_4 core-shell nanoparticles was discussed in Chapter 2. The HR-STEM images of samples 1 – 5 (Figure 3.1) showed similar particle morphology to that of $NiFe_2O_4$ nanoparticles. However, at a low magnification, small nanoparticles were present on the surface of and between the $NiFe_2O_4$ nanoparticles in samples 3 and 4 (Figure 3.2 (a) and (c) respectively). The EDS maps of these samples (Figure 3.2 (b) and (d)) showed that in regions with such particles, Co was present, indicating that the Co phase formed as individual nanoparticles in Samples 3 and 4. These nanoparticles had an average size of 3.2 nm. A possibility that may explain the formation of these nanoparticles is related to self-nucleation where the growth of nuclei into crystals is governed by self-nucleation beyond a certain concentration. In fact, the concentration of Co was changed during synthesis (6.3 – 19.1 wt.% Co) and could have reached a critical point for samples 3 and 4, thus enabling the nucleation resulting into formation of cobalt-containing nanoparticles.[27-29]

STEM-EDS mapping was also used to determine the elemental distribution present in samples 1, 2 and 5 (Figure 3.3). All EDS maps show a homogeneous distribution of Ni and Fe in the $NiFe_2O_4$ nanoparticle with Co present on its surface. The maps also show that the Co layer around the $NiFe_2O_4$ nanoparticle appears to have formed, although only partially and non-uniformly, in samples 1 and 2. On the other hand, the two-step synthesis (sample 5) seems to have allowed for the formation of a more complete Co shell around the $NiFe_2O_4$.

Further analysis of samples 2 and 5 was done using EELS to determine the thickness of the cobalt shell. These samples were chosen since the STEM-EDS maps showed an indication of the presence of a surface Co layer. Although sample 1 showed some evidence of a layer, the occurrence of it was sparse and therefore there was no further analysis. The Co surface layer, where present, in sample 2 had a thickness in the range of 1 – 5 nm while sample 5 showed a shell thickness of 1 – 3 nm (Figure 3.4). However after examining a few particles, as was observed with the STEM-EDS maps, the coating was partially around the nanoparticle in sample 2 and some particles did not have a cobalt shell. Sample 5, on the other hand, showed a more complete coating. This revealed that to form the core-shell material, a two-step synthesis is ideal since the concentration of Co in the synthesis solution is kept low thus minimizing self-nucleation. Additionally, allowing the growth of the Co shell in multiple steps allows for better coverage/growth around the core nanoparticles. It also increases the probability of nanoparticles forming the core-shell structure.

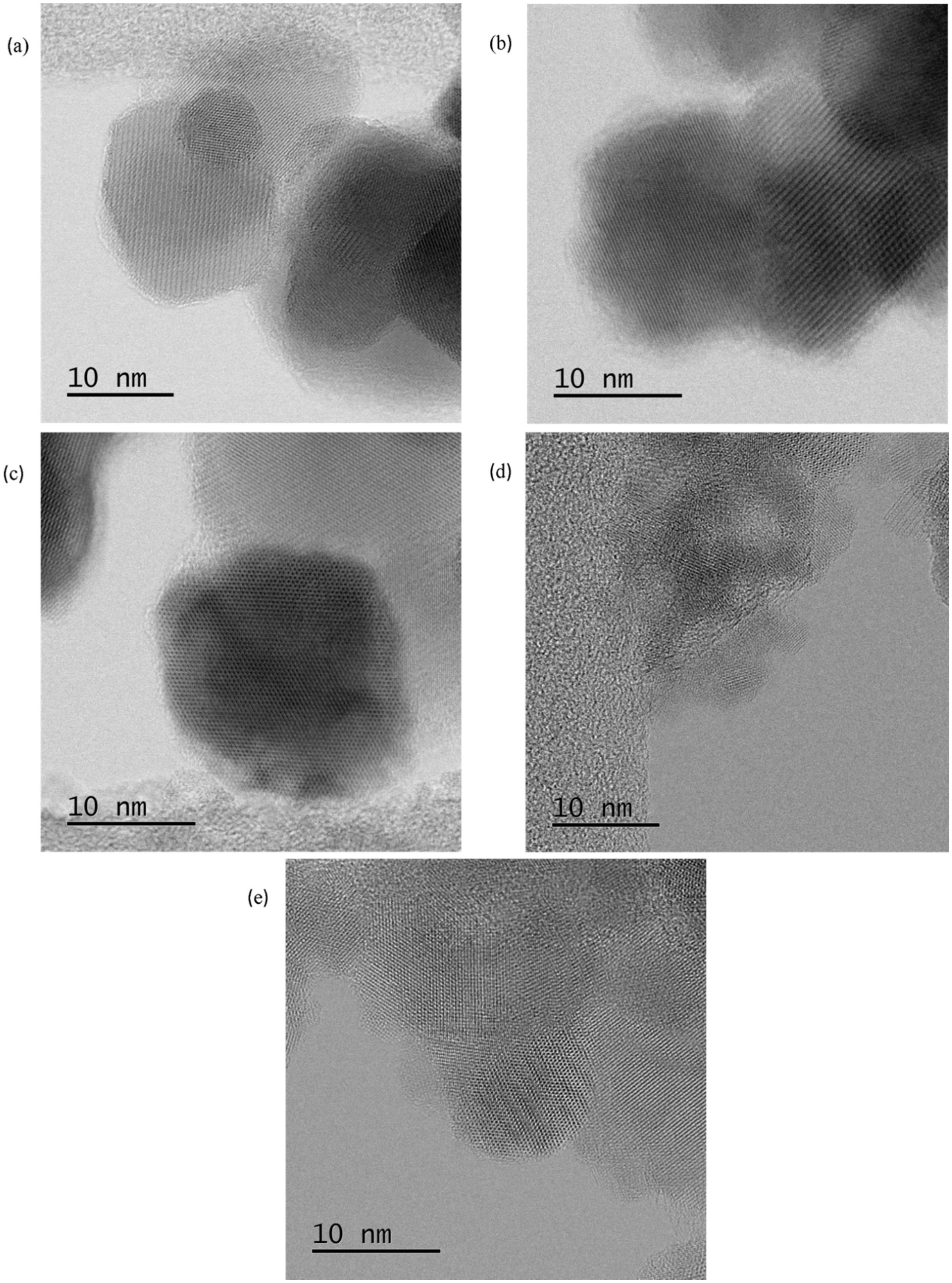

Figure 3.1. HR-STEM image of (a) sample 1; (b) sample 2; (c) sample 3; (d) sample 4 and (e) sample 5

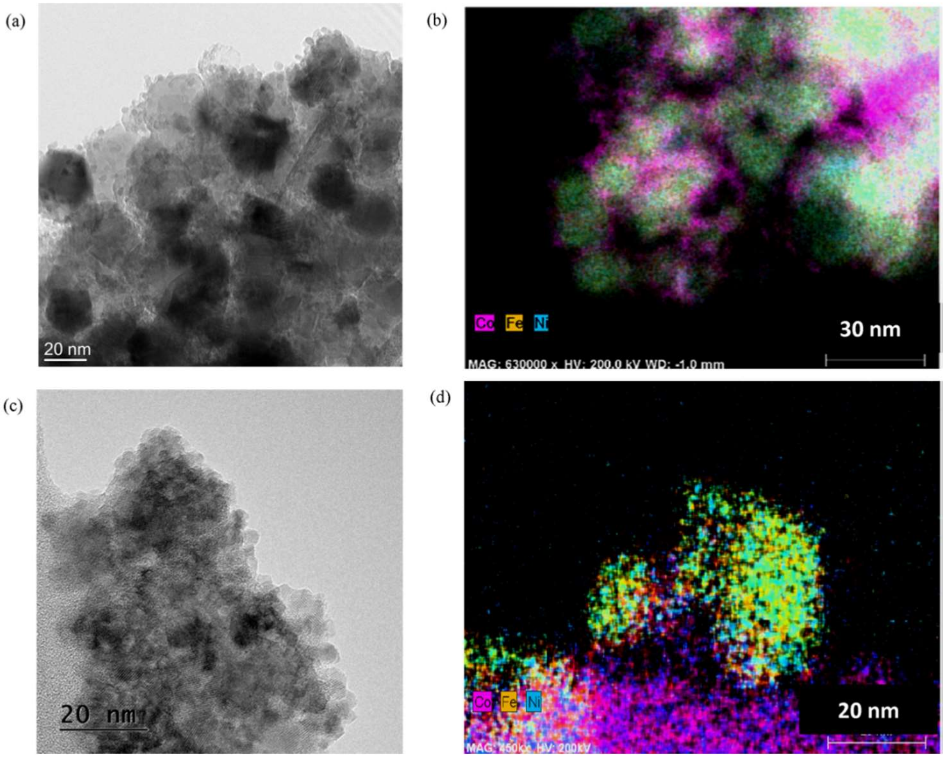

Figure 3.2. TEM image of (a) sample 3 and (c) sample 4 and STEM-EDS maps of (b) sample 3 and (d) sample 4.

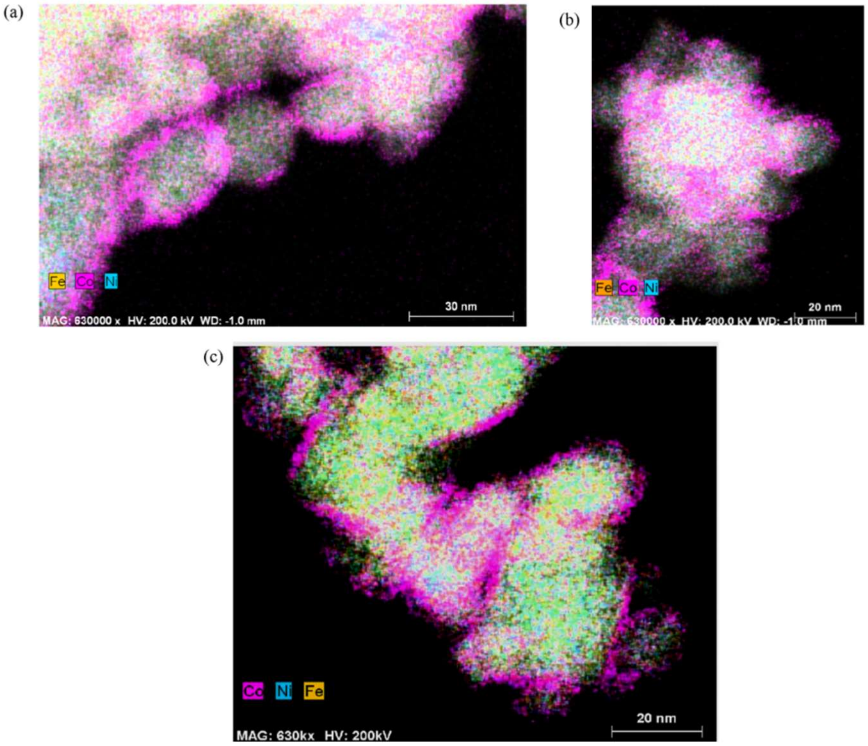

Figure 3.3. EDS maps of (a) sample 1, (b) sample 2 and (c) sample 5.

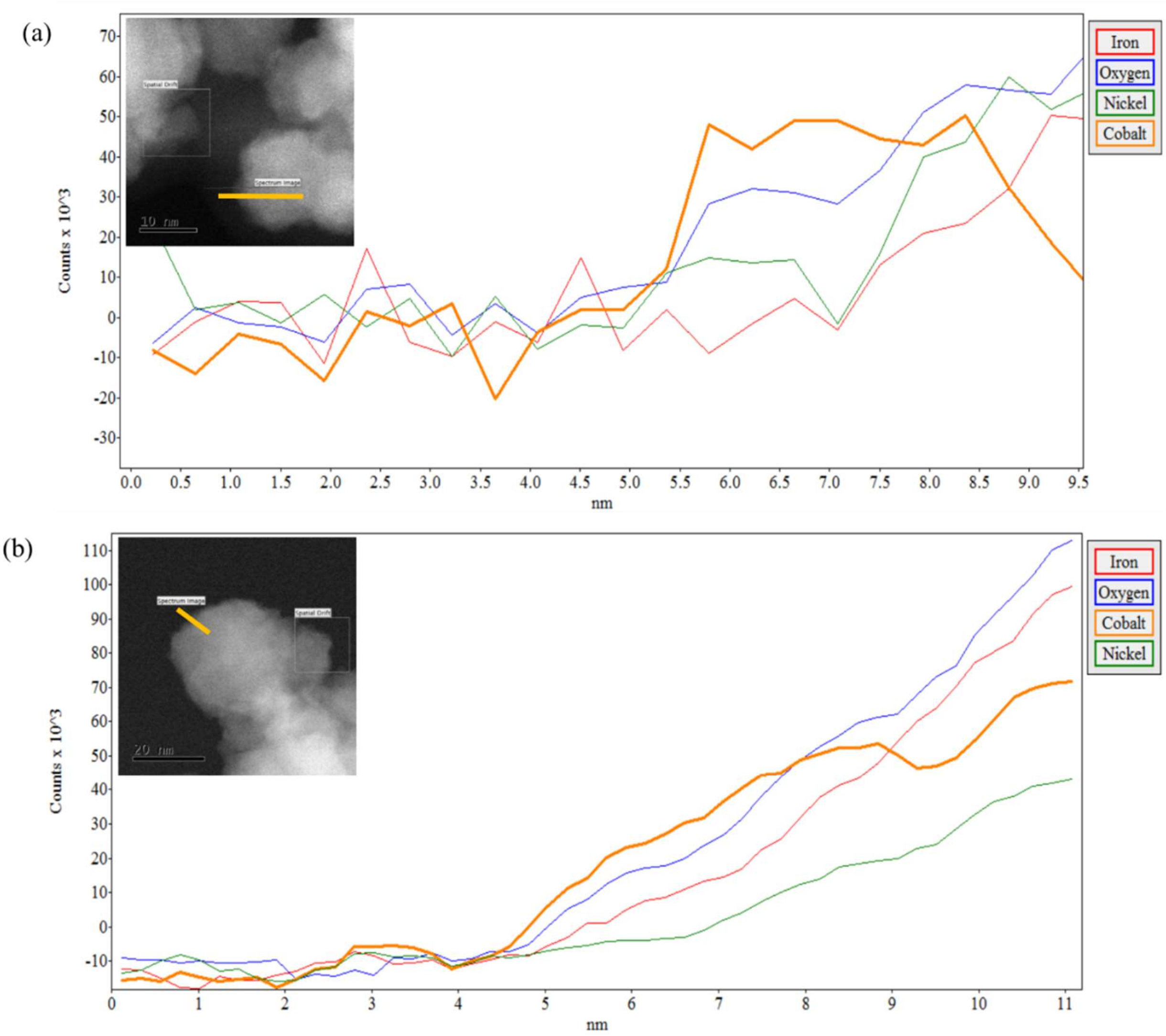

Figure 3.4. EELS line profiles for (a) sample 2 and (b) sample 5 with the STEM-HAADF image shown as an insert.

The STEM-EDS and EELS analysis showed that samples 1 – 5 contained cobalt. In order to determine the phases present, Raman Spectroscopy was used (see Figure 3.5). The data was obtained using the 785 nm laser line, where resonance of Co_3O_4 is typically evident. In all spectra, the five Raman active modes of $NiFe_2O_4$ were present at 213 cm^{-1} (F^1_{2g}), 333 cm^{-1} (E_g), 484 cm^{-1} (F^2_{2g}), 571 cm^{-1} (A_{1g}) with shoulder bands at 587 cm^{-1}, 702 cm^{-1} and 680 cm^{-1} [30]. The Raman active modes of Co_3O_4 are found at 193 cm^{-1} (F^1_{2g}), 483 cm^{-1} (E_g), 520 cm^{-1} (F^2_{2g}), 671 cm^{-1} (F^3_{2g}) and 688 cm^{-1} (A_{1g}) [31] thus indicating that Co_3O_4 is present in all samples.

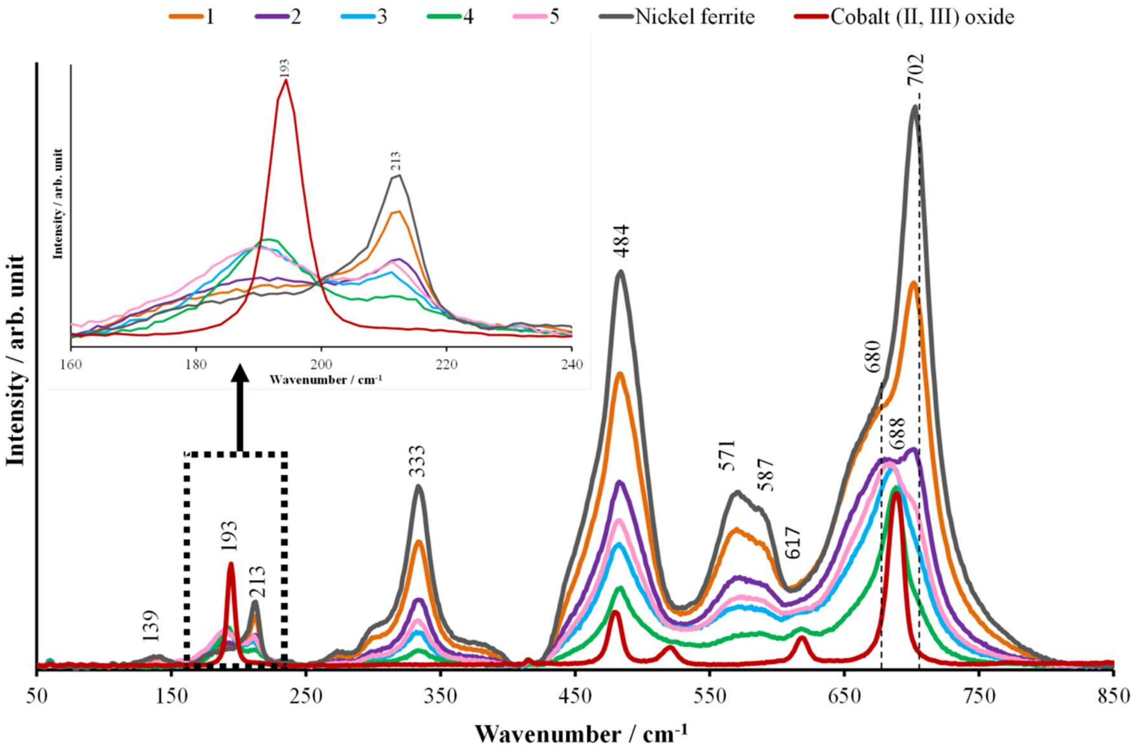

Figure 3.5. Raman spectra of the various nanoparticles prepared.

Owing to the similarity in the structure of $NiFe_2O_4$ and Co_3O_4, bands of Co_3O_4 at 193 cm^{-1} and 484 cm^{-1} overlap with bands of $NiFe_2O_4$. The position of the A_{1g} of Co_3O_4 (688 cm^{-1}) overlaps with the shoulder of the A_{1g} band of $NiFe_2O_4$. However, the A_{1g} band of Co_3O_4 increases in intensity in sample 3, 4 and 5 may be due to the formation of Co_3O_4 nanoparticles (samples 3 and 4) and the more uniform shell layer (sample 5) as evidenced with TEM. The former is also clearly evidenced at 193 cm^{-1} (see insert in Figure 3.5) where this band increases in intensity in samples 3, 4 and 5. Although the concentration of Co used to prepare sample 5 was similar to that for sample 2, its Raman spectrum is similar to that for sample 3, likely due to the better uniformity of the shell around the $NiFe_2O_4$ nanoparticle due to the two-step preparation. The intensity of the bands assigned to $NiFe_2O_4$ decrease in all samples containing cobalt (demonstrated with band 213 cm^{-1} in insert of Figure 3.5). This reveals that in all Co-containing samples, Co_3O_4 may be present in proportional amounts. Furthermore, the intensity decrease correlates with the increase in the Co concentration used for synthesis (samples 1 – 4).

The XP Co 2p, Fe 2p, Ni 2p and O 1s spectra (see Figure 3.6 – Figure 3.9) were fitted using multiple components following a method similar to the one proposed by Biesinger *et al.*[32]. The resulting fit was used to confirm the main species that were assumed based on the shape of the profiles alone as well as to give an indication of any minor species that were present and to what extent. The spectral fitting for the various species also allowed for comparison amongst the samples.

The Co 2p spectra of sample 1, 2 and 4 (Figure 3.6) showed a main peak centered at 779.8eV, 779.7eV and 779.6eV, respectively. Sample 3 and 5, on the other hand, showed a main peak centered at 780.0eV and 780.1eV respectively (Table 3.2). These binding energies do correspond to Co $2p_{3/2}$ and correlated well with that reported in literature for Co_3O_4 [32-34] supporting the Raman Spectroscopy findings. The slightly higher binding energy for samples 3 and 5 is indicative of a chemical shift that arises from different electronic environments of the ejected photoelectron [35]. The former occurs when there is a change in the core energy level of an element due to a change in the chemical bonding and can occur when there is a withdrawal of electronic charge amongst other reasons [35]. The chemical shift seen for the Co 2p main peak of sample 3 and 5 could possibly be related to the presence of Co_3O_4 crystallites in sample 3 and the uniform shell layer present in sample 5 as is evidenced from the TEM analyses.

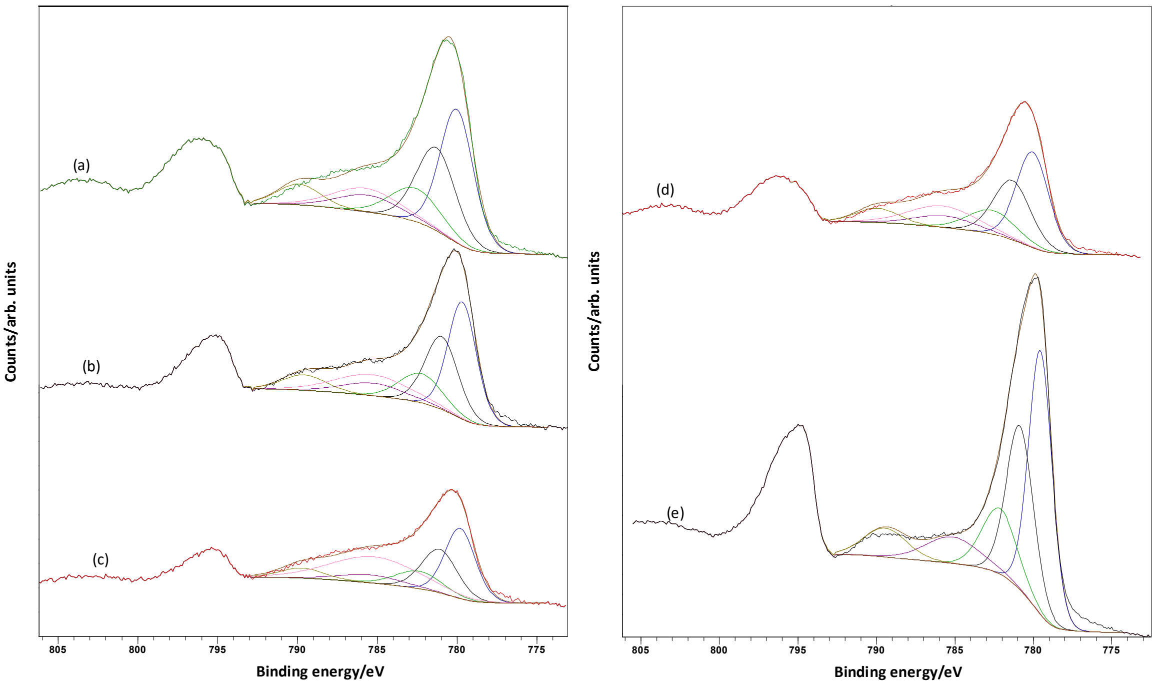

Figure 3.6. Co 2p spectra for (a) sample 1; (b) sample 2; (c) sample 3; (d) sample 5 and (e) sample 4.

The main Fe $2p_{3/2}$ peak is centered at 709.6eV and 709.7eV for samples 1 and 2 and 3 and 5 respectively (see Figure 3.7, Table 3.2). This is expected for Fe^{3+} in the $NiFe_2O_4$ structure [32]. However, sample 4, showed a slightly higher binding energy (710.6eV) for the main Fe 2p peak due to the significant contribution of the Co Auger peak to the Fe 2p spectra. The increase in the contribution of the Co Auger peak to the Fe 2p spectrum causes some difficulty during the fitting of the Fe 2p peak thus shifting its binding energy to higher values. The binding energy of the main Ni 2p peak centered at ~ 854eV in all samples (Figure 3.8, Table 3.2). This is typical of Ni $2p_{3/2}$ (Ni^{2+}) in the $NiFe_2O_4$ structure [32].

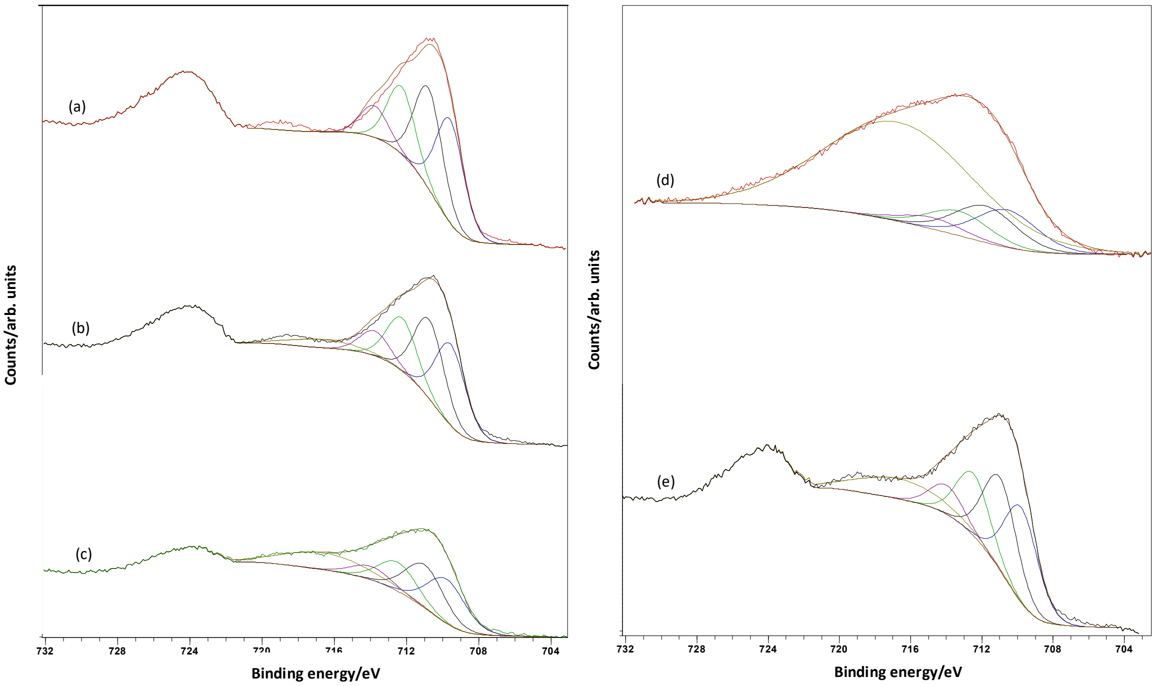

Figure 3.7. Fe 2p spectra for (a) Sample 1; (b) Sample 2; (c) Sample 3; (d) Sample 4 and (e) Sample 5.

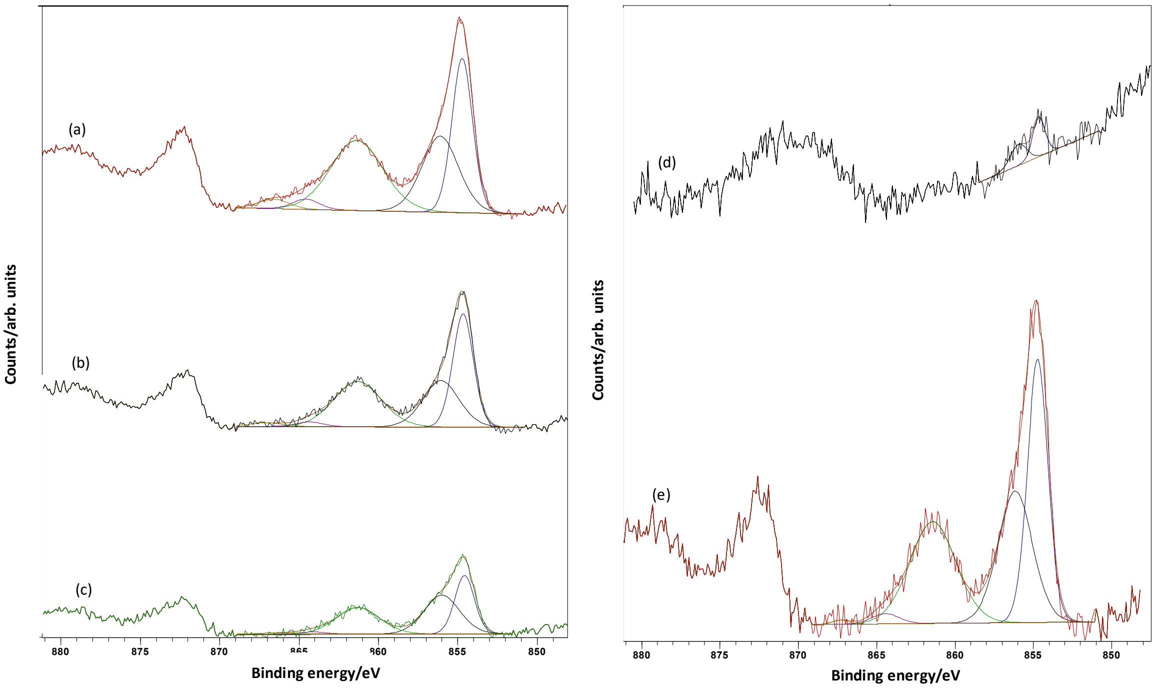

Figure 3.8. Ni 2p spectra for (a) sample 1; (b) sample 2; (c) sample 3; (d) sample 4 and (e) sample 5.

The O 1s spectra showed the presence of two peaks in all samples (Figure 3.9). The peak at ~ 529eV is typical of the O 1s lattice oxide whilst that observed at ~ 531eV is often ascribed to a defective oxide component inherent to the oxides present in these samples (Table 3.2) [32, 34] An interesting finding of the spectral fitting was that the ratio of % total area for defective oxide to lattice oxide (% total area defective oxide/% total area lattice oxide) varied from samples 1 – 5 (see Table 3.3). The variation was such that this ratio increased in the order: sample 1 ~ sample 2 < sample 5 < sample 3 ~ sample 4. The Raman spectroscopy work showed that bands associated with Co_3O_4 was clearly visible for samples 3, 4 and 5 and thus the increase in the % defective oxide seen with XPS may be attributed to this phase.

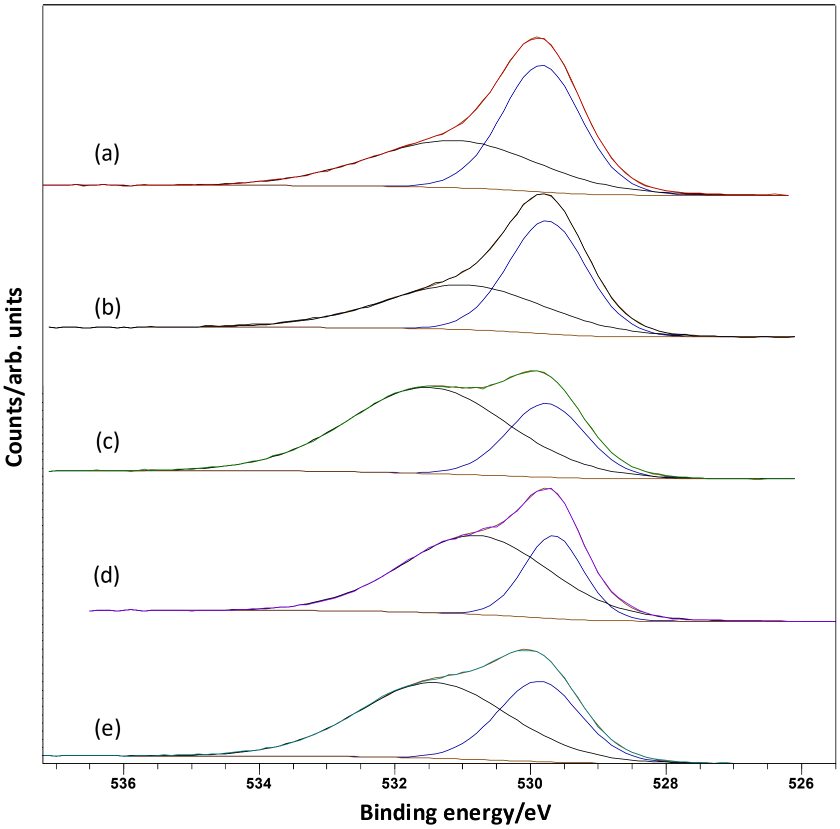

Figure 3.9. O 1s spectra for (a) sample 1; (b) sample 2; (c) sample 3; (d) sample 4 and (e) sample 5.

Table 3.2. Binding energy for the various species.

Sample	**Co 2p$_{3/2}$**	**Fe 2p$_{3/2}$**	**Ni 2p$_{3/2}$**	**O 1s**	
	Binding energy/eV§	Binding energy/eV§	Binding energy/eV§	Lattice oxide Binding energy/eV§	Defective oxide Binding energy/eV§
1	779.8	709.6	854.7	529.8	531.1
2	779.7	709.6	854.7	529.6	531.0
3	780.0	709.8	854.6	529.8	531.4
4	779.6	710.6	854.7	529.7	530.8
5	780.1	709.8	854.7	529.9	531.4

§ Binding energies are significant to 0.1 eV.

Table 3.3. O 1s spectral fitting parameters: binding energy (eV) and percentage of total area (%) for samples 1 – 5.

Sample	Peak/eV	%	Peak/eV	%	Ratio of defective O/lattice O
1	529.8	55.9	531.1	44.1	0.8
2	529.7	55.0	531.0	45.0	0.8
3	529.8	29.5	531.5	70.5	2.4
4	529.7	29.8	530.8	70.2	2.4
5	529.9	37.0	531.4	63.0	1.7

3.2.3. Proposed mechanism of $NiFe_2O_4@Co_3O_4$ formation

The synthesis described in this work is a homogenous deposition-precipitation route in which the cobalt hexamine complex (formed from the cobalt carbonate, ammonium carbonate and ammonium hydroxide in water) coordinates to the surface of the $NiFe_2O_4$ nanoparticle. A simplified view of the proposed mechanism of formation for Co_3O_4 on the surface of $NiFe_2O_4$ is given in Figure 3.10. Due to the high pH maintained during the synthesis, the surface of the $NiFe_2O_4$ is negatively charged (point of zero charge (PZC) of $NiFe_2O_4$ = 7) [36] allowing the formation of an inner sphere complex where the Co^{2+} present in the hexamine complex coordinates to the O^- originating from the surface hydroxyl groups (Step 1 in Figure 3.10). The Co^{2+} remaining in solution can then form (hydr)oxo-bridges with the inner sphere complex (Step 2 in Figure 3.10). This network propagates over the surface (Step 3 in Figure 3.10).[37] As the reaction progresses, the complex present on the surface of $NiFe_2O_4$ possibly forms a cobalt hydroxo-like surface. As this cobalt hydroxo-like network forms, the amine ligand goes into solution as NH_4^+ (Step 4 in Figure 3.10). This network then decomposes to form $Co(OH)_2$ nuclei which upon further heating oxidize to Co_3O_4 as a surface precipitate (Steps 5 and 6 in Figure 3.10).

An important point discussed by Bourikas *et al.*[37] is that in order for deposition to occur using this precipitation method, dilute aqueous solutions of the metal precursor are needed. Additionally, surface precipitation is achieved by slow and homogenous introduction of the material containing the hydroxyl ions. In fact, nucleation of the metal precursor in the bulk solution followed by precipitation can occur if the concentration of the metal precursor is too high. This hypothesis is supported by the findings of the characterization of the different samples prepared in this work where it was shown that at the highest concentration of Co (19.1 wt.%) no surface precipitate formed. Additionally, the former puts into context why the two-step synthesis was more successful in forming a core-shell structure using this method.

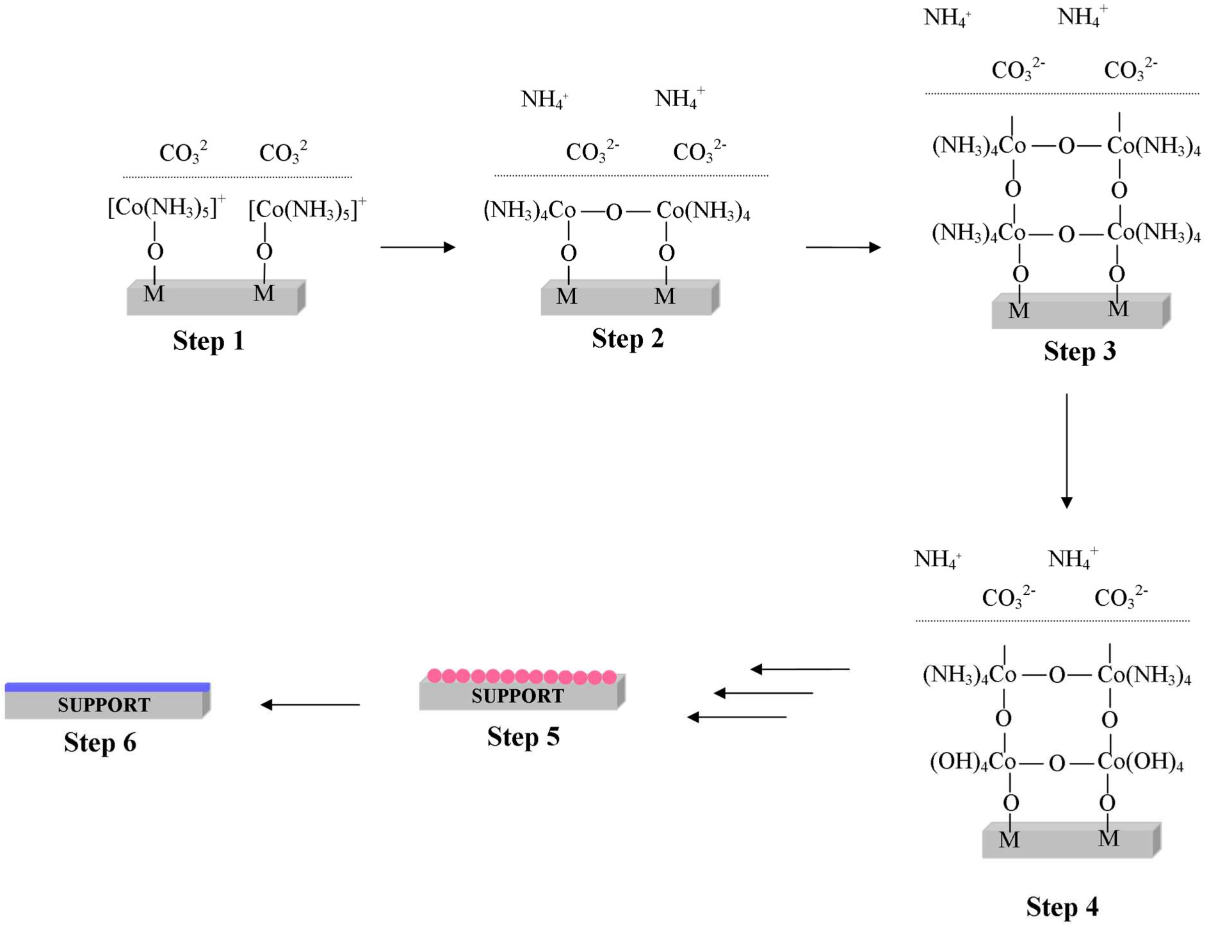

Figure 3.10. Proposed simplistic model of formation of the inner sphere surface complex, as well as surface oxide polymerization that leads to the formation of Co_3O_4 on the surface of $NiFe_2O_4$.

3.3 Chapter summary

Phase pure $NiFe_2O_4$ nanoparticles were used as a core for the growth of a Co_3O_4 shell which was achieved using a simple precipitation route. The concentration of cobalt in the synthesis solution was varied in the range of 6.3 – 19.1 wt.% cobalt using a one-step synthesis. Low concentrations of cobalt in solution (6.3 – 7.6 wt.%) resulted in the formation of a partial and non-uniform surface cobalt layer (1 – 5 nm) on some $NiFe_2O_4$ nanoparticles whilst higher concentrations (11.0 – 19.1 wt.%) caused bulk precipitation. A two-step synthesis (7.6 wt.% cobalt) resulted in the formation of a more complete cobalt layer (1 – 3 nm) around most $NiFe_2O_4$ nanoparticles. Raman spectroscopy and XPS showed that the cobalt in all samples was present as Co_3O_4.

Due to the small changes in the cobalt concentration for the one-step preparation, the cobalt layer, where present, had thicknesses that were similar amongst the various samples. Thus, the synthesis method used in this work was not ideal for forming various shell thicknesses. Additionally due to the precipitation nature of the reaction, self-nucleation shifted the shell formation toward crystallite formation when the cobalt concentration in solution was 11.0 wt.% and higher. Interestingly, the effect of the concentration of cobalt in solution was more so observed on the completeness of the shell around the $NiFe_2O_4$ nanoparticle and the distribution of nanoparticles with a core-shell structure than in the shell thickness. Overall, the two-step synthesis proved successful for the formation of a more complete shell around the core material.

3.4 References

[1] H.-K .Lin, H.-C. Chiu, H.-C. Tsai, S.-H. Chien, C.-B. Wang, Synthesis, characterization and catalytic oxidation of carbon monoxide over cobalt oxide, Catal. Lett., 88 (2003) 169-174.

[2] P. Konova, M. Stoyanova, A. Naydenov, S. Christoskova, D. Mehandjiev, Catalytic oxidation of VOCs and CO by ozone over alumina supported cobalt oxide, Appl. Catal. A: Gen., 298 (2006) 109-114.

[3] Q. Liu, L.-C. Wang, M. Chen, Y. Cao, H.-Y. He, K.-N. Fan, Dry citrate-precursor synthesized nanocrystalline cobalt oxide as highly active catalyst for total oxidation of propane, J. Catal., 263 (2009) 104-113.

[4] T. V. Choudhary, S. Banerjee, V. R. Choudhary, Catalysts for combustion of methane and lower alkanes, Appl. Catal. A: Gen., 234 (2002) 1-22.

[5] X. Xie, Y. Li, Z.-Q. Liu, M. Haruta, W. Shen, Low-temperature oxidation of CO catalysed by Co_3O_4 nanorods, Nature, 458 (2009) 746-749.

[6] M. Haneda, Y. Kintaichi, N. Bion, H. Hamada, Alkali metal-doped cobalt oxide catalysts for NO decomposition, Appl. Catal. B: Environ., 46 (2003) 473-482.

[7] B. S. Yeo, A. T. Bell, Enhanced activity of gold-supported cobalt oxide for the electrochemical evolution of oxygen, J. Am. Chem. Soc., 133 (2011) 5587-5593.

[8] Y. Liang, H. Wang, P. Diao, W. Chang, G. Hong, Y. Li, M. Gong, L. Xie, J. Zhou, J. Wang, T. Z. Reiger, F. Wei, H. Dai, Oxygen reduction electrocatalyst based on strongly coupled cobalt oxide nanocrystals and carbon nanotubes, J. Am. Chem. Soc., 134 (2012) 15849-15857.

[9] A. Y. Khodakov, W. Chu, P. Fongarland, Advances in the development of novel cobalt Fischer-Tropsch catalysts for the synthesis of long-chain hydrocarbons and clean fuels, Chem. Rev., 107 (2007) 1692-1744.

[10] V. R. Calderone, N. R. Shiju, D. Curulla-Ferre, S. Chambrey, A. Y. Khodakov, A. Rose, J. Thiessen, A. Jess, G. Rothenberg, De novo design of nanostructured iron-cobalt Fischer-Tropsch catalysts, Angew. Chem. Int. Ed., 52 (2013) 4397-4401.

[11] G. S. Sewell, C. T. O' Connor, E. van Steen, Reductive amination of ethanol with silica-supported cobalt and nickel catalysts, Appl. Catal. A: Gen., 125 (1995) 97-112.

[12] J. Zhang, J.-O. Muller, W. Zheng, D. Wang, D. Su, R. Schlogl, Individual Fe-Co alloy nanoparticles and carbon nanotubes: structural and catalytic properties, Nano Lett., 8 (2008) 2738-2743.

[13] V. R. Calderone, N. R. Shiju, G. Rothenberg, D. Curulla-Ferre, Core-shell particles with catalytic activity and the process of their preparation. Method of preparation of Fischer-Tropsch catalyst comprising said particles, European Patent Office, Europe, EP2740534A1, 2014.

[14] J.-M. Yan, X.-B. Zhang, T. Akita, M. Haruta, Q. Xu, One-step seeding growth of magnetically recyclable Au@Co core-shell nanoparticles: highly efficient catalyst for hydrolytic dehydrogenation of ammonia borane, J. Am. Chem. Soc., 132 (2010) 5326-5327.

[15] K. S. Kumar, V. B. Kumar, P. Paik, Recent advancement in functional core-shell nanoparticles of polymers: Synthesis, physical properties and applications in medical biotechnology, J. Nanoparticles, 2013 (2013) 1-24.

[16] M. Jin, H. Zhang, J. Wang, X. Zhong, N. Lu, Z. Li, Z. Xie, M. J. Kim, Y. Xia, Copper can still be epitaxially deposited on palladium nanocrystals to generate core shell nanocubes despite their large lattice mismatch, ACS Nano, 6 (2012) 2566-2573.

[17] M. Tsuji, D. Yamaguchi, M. Matsunaga, M. J. Alam, Epitaxial growth of Au@Cu core-shell nanocrystals prepared using the PVP-assisted polyol reduction method, Crystal Growth & Design, 10 (2010) 5129-5135.

[18] R. G. Chaudhuri, S. Paria, Core/Shell nanoparticles: classes, properties, synthesis mechanisms, characterization and applications, Chem. Rev., 112 (2012) 2373-2433.

[19] S. E. Habas, H. Lee, V. Radmilovic, G. A. Somorjai, P. Yang, Shaping binary metal nanocrystals through epitaxial seeded growth, Nat. Mater., 6 (2007) 692-697.

[20] S. H. Joo, J. Y. Park, C.-K. Tsung, Y. Yamada, P. Yang, G. A. Somorjai, Thermally stable Pt/mesoporous silica core-shell nanocatalysts for high-temperature reactions, Nat. Mater., 8 (2009) 126-131.

[21] C.-J. Zhong, M. M. Maye, Core-Shell nanoparticles as catalysts, Adv. Mater., 13 (2001) 1507-1511.

[22] O. S. Alexeev, B. C. Gates, Supported bimetallic cluster catalysts, Ind. Eng. Chem. Res., 42 (2003) 1571-1587.

[23] X. Duan, G. Qian, X. Zhou, D. Chen, W. Yuan, MCM-41 supported Co-Mo bimetallic catalysts for enhanced hydrogen production by ammonia decomposition, Chem. Eng. J., 207-208 (2012) 103-108.

[24] M. Wang, X. Pang, D. Zheng, Y. He, L. Sun, C. Lin, Z. Lin, Nonepitaxial growth of uniform and precisely size-tunable core/shell nanoparticles and their enhanced plasmon-driven photocatalysis, J. Mater. Chem., 4 (2016) 7190-7199.

[25] J. J. Fripiat, J. Helsen, Kinetics of decomposition of cobalt coordination complexes on montmorillonite surfaces, Clays and Clay Minerals, 14 (1966) 163-179.

[26] M. Figlarz, J. Guenot, J. N. Tournemolle, Morphological and topotactical aspects of the reactions $Co(OH)_2$ --> CoOOH and CoOOH --> Co_3O_4, J. Mater. Sci., 11 (1976) 2267-2270.

[27] C. Burda, X. Chen, R. Narayan, M. A. El-Sayed, Chemistry and properties of nanocrystals of different shapes, Chem. Rev., 105 (2005) 1025-1102.

[28] M. Perez, M. Dumont, D. Acevedo-Reyes, Implementation of classical nucleation and growth theories for precipitation, Acta Materialia, 56 (2008) 2119-2132.

[29] W. Annan, P. Qing, L. Yadong, Rod-shaped Au-Pd core-shell nanostructures, Chem. Mater., 23 (2011) 3217-3222.

[30] B. D. Hostermann, Raman Spectroscopic Study of Solid Solution Spinel Oxides, University of Nevada, Las Vegas, PhD, 2011.

[31] L. He, Z. Li, Z. Zhang, Rapid, low-temperature synthesis of single-crystalline Co_3O_4 nanorods on silicon substrates on a large scale, Nanotechnol., 19 (2008) 155606.

[32] M. C. Biesinger, B. P. Payne, A. P. Grosvenor, L. W. M. Lau, A. R. Greson, R. S. C. Smart, Resolving surface chemical states in XPS analysis of first row transition metals, oxides and hydroxides: Cr, Mn, Fe, Co and Ni, Surf. Sci., 257 (2011) 2717-2730.

[33] J.-H. Zhong, A.-L. Wang, G.-R. Li, J.-W. Wang, Y.-N. Ou, Y.-X. Tong, $Co_3O_4/Ni(OH)_2$ composite mesoporous nanosheet networks as a promising electrode for supercapacitor applications, J. Mater. Chem., 22 (2012) 5656-5665.

[34] T. J. Chuang, C. R. Brundle, D. W. Rice, Interpretation of the x-ray photoemission spectra of cobalt oxides and cobalt oxide surfaces, Surf. Sci., 59 (1976) 413-429.

[35] C. C. Chusuei, D. W. Goodman, Encyclopedia of physical science and technology: X-ray photoelectron spectroscopy, Third ed., Academic Press, 2002.

[36] M. Kosmulski, pH-dependent surface charging and points of zero charge. IV. Update and new approach, J. Colloid Interface Sci., 337 (2009) 439-448.

[37] K. Bourikas, C. Kordulis, A. Lycourghiotis, The role of the liquid-solid interface in the preparation of supported catalysts, Catal. Rev. Sci., 48 (2006) 363-444.

4 Exploring $MFe_2O_4@Co_3O_4$ (M = Ni, Zn) core-shell nanoparticles as precursors for Fischer-Tropsch catalysts

---

$NiFe_2O_4@Co_3O_4$ and $ZnFe_2O_4@Co_3O_4$ core-shell nanoparticles were synthesized and used as precursors for Fischer-Tropsch catalysts. The as-synthesized materials were determined to have an incomplete Co_3O_4 shell around the ferrite core with a maximum thickness of 3 nm. Reduction of these core-shell nanoparticles in pure hydrogen at 230°C and 250°C, respectively, resulted in the formation of small cobalt islands on the ferrite surface. Catalytic testing of the core-shell materials, $NiFe_2O_4@Co_3O_4$ and $ZnFe_2O_4@Co_3O_4$, after reduction showed a cobalt-time yield of 13.64 $\mu mol_{CO} \cdot g_{Co}^{-1} \cdot s^{-1}$ and 4.27 $\mu mol_{CO} \cdot g_{Co}^{-1} \cdot s^{-1}$ and a C_{5+} selectivity of 47 C-% and 68 C-%, respectively. The observed difference in cobalt-time yield and selectivity between $NiFe_2O_4@Co_3O_4$ and $ZnFe_2O_4@Co_3O_4$ core-shell nanoparticles was ascribed to a combination of effects that included the presence of cobalt islands over the surface of the core and the difference in extent of reduction of each core under Fischer-Tropsch synthesis conditions.

4.1 Introduction

Cobalt-based nanoparticles are the preferred catalyst for low temperature Fischer-Tropsch synthesis (FTS) to produce middle distillates and long-chain linear hydrocarbons. This is due to their high activity (particularly at high conversion), high selectivity to linear paraffins, low propensity to form carbon dioxide (CO_2) and stability against deactivation by water [1-3]. However, cobalt is expensive and considerable research is directed to optimize the efficient use of cobalt [1, 4]. It has been shown that the rate of cobalt-based Fischer-Tropsch synthesis increases strongly with increasing crystallite size and the optimum mass-specific activity is thought to be obtained with cobalt crystallites with an average size of *ca.* 6 – 8 nm [5-8]. This implies that only a small percentage of surface cobalt is directly involved in the reaction. In this regard, a possible reduction in the cost of cobalt-based catalysts can be achieved by replacing cobalt in the core of the catalyst crystallite, which is not directly involved in the reaction, with cheaper alternatives thereby forming core-shell structures. [9, 10].

Core-shell nanoparticles are created by hetero-topotactical growth of one material over another material. The core material and the shell thickness may be changed to alter the nanoparticle's properties *via* an electronic and/or a structural change [11]. Core-shell nanoparticles have been shown to have unique catalytic properties when compared to their monometallic counterparts [10, 12-14]. Core-shell nanoparticles may exhibit different adsorption behavior and subsequent dissociation of reactant molecules compared to pure monometallic systems as indicated using density functional theory [15-18]. Wu *et al.* [19] showed that the adsorption of carbon monoxide and water is weaker on $Co_6@Au_{32}$ core-shell nanoparticles (with a cobalt core and a gold shell) than on Co or Au_{38}. This was attributed to the influence of the cobalt atoms in the core on the geometry and electronic structure of the gold atoms at the surface. Wang *et al.* [20] calculated a shift in the d-band center for $Pd_3Co@Pt$ nanoparticles relative to Pd_3Co and Pt explaining the improved activity for the oxygen reduction reaction (ORR). Heemeier *et al.* [21] showed for Co-Pd nanoparticles approaching a core-shell structure that the strength of CO adsorption is weakened on partially covered surfaces, due to electronic effects. Qin *et al*. [22] invoked a change in the heat of adsorption of CO over Co@C core-shell nanoparticles to explain an enhanced Fischer-Tropsch activity. The presence of a carbon shell around the cobalt nanoparticles may have resulted in a synergistic effect.

The geometry of the core-shell nanoparticle, its composition and its surface structure may all have a strong effect on the ultimate catalytic performance [11, 23-25]. Thus, whilst the observed catalytic behavior of core-shell nanoparticles may be partly explained by the altered adsorption properties of the active metal, there may be a strong dependency on the structure of the active phase surface after activation. The structure of nanoparticles is known to be unstable especially when exposed to a reactive environment such as those used during the activation of the catalyst (hydrogen, carbon monoxide and elevated temperature) [26].

Hence, establishing the structure of these nanoparticles, particularly after activation, is essential to understand the relationship between the surface structure of the material and the mechanisms at play during catalysis. [27-30].

In this work, two oxides, *viz*. the inverse spinel nickel ferrite, $NiFe_2O_4$ [9] and the normal spinel zinc ferrite, $ZnFe_2O_4$ were used as cores on which a shell comprising of the normal spinel cobalt oxide, Co_3O_4, was grown. The core materials were chosen due to its similarity in crystal structure to Co_3O_4, as this was expected to promote the formation of a uniform epitaxially grown shell around the core [9, 31]. The as-synthesized $NiFe_2O_4$@Co_3O_4 and $ZnFe_2O_4$@Co_3O_4 core-shell nanoparticles were subsequently studied before and after reduction and compared to reference materials of Co_3O_4, $NiFe_2O_4$ and $ZnFe_2O_4$ nanoparticles using various *ex-situ* and *in-situ* techniques. Additionally, the influence of a reducing environment at different temperatures, on the nanoscale structure of each core-shell nanoparticle system was studied using *in-situ* TEM. The performance of these materials as catalyst precursors for the Fischer-Tropsch synthesis was tested.

4.2 Experimental

4.2.1 Preparation of Co_3O_4

Analytical grade cobalt nitrate hexahydrate ($Co(NO_3)_2.6H_2O$) and citric acid ($C_6H_8O_7$) were obtained from Sigma Aldrich. In a typical synthesis, a solution of $Co(NO_3)_2.6H_2O$ (2.0*M*) and a solution citric acid (2.5*M*) was prepared. The cobalt nitrate solution was added to the citric acid solution keeping the temperature at 30°C using a water bath. The metal nitrate-citric acid solution was stirred for 95 minutes before the temperature was increased to 60°C, at which temperature it was kept for two hours under stirring, resulting in the formation of a pink-purple gel. The formed gel was placed in a porcelain dish and oven-dried at 110°C for 24 hours. The as-formed resin was subsequently calcined in a muffle furnace at 350°C for five hours.

4.2.2 Preparation of $NiFe_2O_4$ and $ZnFe_2O_4$

Chapter 2 provides a more detailed description of the preparation of the ferrite nanoparticles. Briefly, the iron nitrate solution (2.0*M*) was added to a stirred citric acid solution (2.5*M*) followed by the addition of the nickel or zinc nitrate solution (1.2*M*). An iron/M (Fe/M) mole ratio of 2.3 (M is Ni or Zn) was used to avoid the formation of side products. The resulting metal nitrate-citric acid solution was stirred for 95 minutes before increasing the temperature to 60°C, at which temperature it was kept for two hours under stirring. A brown gel was formed which was subsequently oven-dried at 110°C for 24 hours. The as-formed resin was then calcined in a muffle furnace at 450°C for five hours.

4.2.3 Preparation of $NiFe_2O_4$@ Co_3O_4 and $ZnFe_2O_4$@ Co_3O_4

A detailed description of the synthesis of the core-shell nanoparticles is given in Chapter 3. Briefly, an aqueous solution of ammonium carbonate, $(NH_4)_2CO_3$ (0.8*M*) was mixed with 25 wt.% ammonia aqueous solution (3.6 mL). Cobalt carbonate, $CoCO_3$, was added to obtain a cobalt concentration of 0.05*M* and a pH of 11.5. The resulting cobalt containing suspension was then stirred at 45°C for two hours, after which the solution was filtered by gravity. This filtrate was added to a round bottom flask and ~ 0.05 g/mL of MFe_2O_4 (M = Ni or Zn) was added; the suspension was stirred at 85°C for six hours. The temperature was then increased to 95°C, at which it was kept for 24 hours under stirring. The solvent was subsequently removed under vacuum and the dried solid was rinsed with deionized water and again dried under vacuum. The obtained solid was oven-dried at 110°C for 12 hours. This procedure was repeated twice.

A targeted loading of 7.6 wt.% cobalt was desired since previous work (Chapter 3) showed that this would yield a cobalt shell around most MFe_2O_4 nanoparticles. A thinner shell would yield a greater economic benefit and also enable the effect of strain on the shell surface after activation and during catalysis to be studied more readily.

4.2.4 Characterization

X-ray powder diffraction (XRD) patterns were collected on a Bruker D8 Advance X-ray diffractometer equipped with a Co Kα X-ray source (λ=0.178897 nm). Phase identification of the diffraction data was done using Bruker DIFFRAC.EVA Version 2 or Panalytical's X'Pert HighScore Plus software was used while average crystallite sizes and relative phase abundances were obtained from Rietveld refinements using Bruker AXS TOPAS Version 4.1. The *in-situ* XRD measurements were performed in an Anton Paar XRK900 coupled to the Panalytical X'Pert Pro multi-purpose diffractometer. The *in-situ* XRD experiments were performed under a hydrogen flow (50 ml/min) and the sample was heated from room temperature to 230°C or 250°C using a heating rate of 5°C/min. Diffraction patterns were collected every 4 minutes, i.e. at intervals of 20°C. After the reduction, the reactor was flushed with helium for two hours and cooled to 40°C. Then, the temperature was increased to 230°C under synthesis gas (H_2/CO = 2, 50 ml/min). At this temperature, the pressure was increased to 16 bar over a five hour period. The reaction was maintained under these conditions for 16 hours and a diffractogram was collected in 20 min intervals. At the end of the experiment, the system was flushed was helium, de-pressurized and cooled to 40°C. Then, the catalyst was passivated in a mixture of helium (50 ml/min) and oxygen for three hours (O_2 flow rate was initially 2 ml/min and gradually increased to 6 ml/min). The used catalyst was unloaded into dry ice.

X-ray photoelectron spectroscopy (XPS) spectra were acquired at room temperature with a SPECS PHOIBOS 150 electron energy analyzer, using a Al K_α mono-chromatic photon source (hν= 1486.71 eV).

The analysis was carried out at the University of Johannesburg. Samples were mounted on a molybdenum sample holder using carbon tape. The overall (photon+analyser) energy resolution was set to 0.5eV for all the spectra shown here. A low energy electron flood gun was used to compensate for the charging of the sample (electron energy: 2eV; emission current: 20 μA).

Energy dispersive X-ray spectroscopy (EDS) was used to estimate the weight percent (wt.%) of cobalt present in each core-shell system. Prior to analysis, the catalyst powder was mounted in resin which was polished to obtain a smooth flat cross section. The prepared resin block was then coated with carbon and transferred into the Zeiss EVO 40 scanning electron microscope (SEM). EDS analyses were performed using a Bruker XFlash SDD detector that was controlled by Bruker Esprit software. The analysis was done at 20 kV using a probe current of 780 pA. Five EDS spectra was obtained at different regions of the sample and quantified using the PB-ZAF correction that is available with the Esprit software.

Prior to the TEM/STEM analysis, the crushed sample was dispersed in ethanol using an ultrasonication after which a small amount was transferred onto a holey carbon copper TEM grid (SPI Supplies, 300 mesh). A double aberration corrected JEOL ARM 200F transmission electron microscope operating at 200 kV (at the CHRTEM, Nelson Mandela University) was used for the *ex-situ* characterization of the nanoparticles. High angle annular dark field (HAADF) scanning transmission electron microscopy (STEM) as well as bright field (BF) STEM imaging at atomic resolution was used. Electron energy loss spectroscopy (EELS) Spectrum Imaging (SI) was performed using the DualEELS™ mode on the Gatan GIF Quantum ERS^{TM} spectrometer. This allows for the pixel by pixel acquisition of both the intense zero loss peak (ZLP) and the elemental edges during the same scan. A convergence semi-angle of 21.4 mrad was used for the STEM probe and the collection semi-angle of the spectrometer was 54.3 mrad at a camera length of 1 cm.

The *in-situ* TEM analysis was carried out on a FEI Titan G2 80 – 200 (S)TEM ChemiStem™ instrument operating at 200 kV at the University of Manchester. The instrument was equipped with Gatan GIF Quantum ERSTM spectrometer. STEM-HAADF images were recorded using FEI TIA software whilst EELS spectrum images were recorded using Gatan Digital Micrograph software. The gaseous e-Cell system used in the FEI Titan instrument was a Protochips Atmosphere holder with a customized low penumbra geometry beryllium lid. The e-Cell MEMS chips used to create the operating environment were a pair of 300µm thick Si wafers, each with a lithographically fabricated 3000 x 300µm electron transparent SiNx window. The top chip allows heating and has a window thickness of 30 nm while the bottom window is 50 nm thick. Spacers deposited onto the chips created a nominal vertical separation between the windows of ~ 5µm. During the measurements, the e-Cell was completely filled with pure hydrogen at nominally one bar pressure. The temperature was controlled by on-chip pre-calibrated heater elements controlled by an external computer system. The samples were crushed in ethanol and then a drop was placed onto the atmosphere side of the electron entrance of plasma cleaned SiNx windows and allowed to dry in a clean ambient temperature petri dish. The prepared e-Cell was sealed as per manufacturers specifications and specimens were allowed to stabilize at room temperature in the documented gaseous media prior to all measurements. Thereafter, the sample was heated to the desired temperature and allowed to remain there for one hour at a time before imaging and EELS was done. In order to ensure that electron beam artefacts were not influencing the results, images of selected regions of interest were acquired before and after thermal treatments. Additionally, after thermal treatments, different sample areas which were not analyzed previously were also measured to ensure that the results presented herein are representative and reproducible.

For characterization by Raman spectroscopy, the powders were placed on a microscope slide and measured using an inVia Raman system. All measurements were done using the 785 nm line of a solid-state diode laser with 0.1 mW power rating at the source. The beam was focused with a Leica microscope using a ×20 objective. Data was collected for the spectral range of 50 cm-1 – 2000 cm-1 for 10 seconds, scanned 20 times using a laser power of 0.1%. Wire software Version 4.1 was used for data capturing and instrument control. The Raman band of pure Si was measured before data accumulation commenced for calibration purposes.

Temperature Programmed Reduction (TPR) was performed on an AutoChem 2920 (Micrometrics, USA) by reducing the catalyst samples using pure hydrogen with a flow rate of 10 ml/min while the temperature was increased with a linear heating rate of 5°C/min from 50°C to 850°C. CO-TPD was also carried out on this instrument. Prior to the analysis, the catalyst was reduced in pure hydrogen (see

Table 4.1) for two hours to try to preferentially reduce the Co_3O_4 shell (a relatively short reduction time of one hour was used for the reduction of pure Co_3O_4 nanoparticles to minimize sintering). The sample was cooled to 0°C under a helium flow (10 ml/min), after which carbon monoxide was pulsed using five pulses at an interval of 10 minutes between each pulse/dose. After this, the sample was flushed at 0°C using helium (50 ml/min) for 6 hours. The sample was subsequently heated to 850°C using a heating rate of 10°C/min.

Table 4.1. Conditions for the activation of catalyst samples in hydrogen prior to characterization and the Fischer-Tropsch synthesis (Hydrogen space velocity = 6000 $ml_n \cdot g^{-1} \cdot hr^{-1}$).

Sample	$T_{reduction}$/°C	$t_{reduction}$/hours
Co_3O_4	300	1
$NiFe_2O_4$	230	2
$NiFe_2O_4$@Co_3O_4	230	2
$ZnFe_2O_4$	250	2
$ZnFe_2O_4$@Co_3O_4	250	2

The metal surface area was determined using pulse chemisorption. The samples were dried at 120°C for one hour and subsequently reduced in pure hydrogen using the activation conditions listed in

Table 4.1 (heating rate: 5°C/min). Thereafter, the samples were flushed under argon flow (50 ml/min) for one hour. H_2 was adsorbed at either 35°C or 100°C using pulse chemisorption in 10 pulses with a two-minute interval. The calculation used to determine the active metal surface area is given in Appendix A.

The degree of reduction was determined using oxygen (O_2) back titration on a Micromeritics ASAP 2020 Unit (Micromeritics, USA). Accordingly, a pre-weighed catalyst sample of about 200mg was degassed at 120°C for two hours. The sample was then cooled to ambient temperature under He flow. Thereafter, the sample was heated to the temperature given in

Table 4.1 at a rate of 5°C/min under a flow of pure H_2 (50 ml/min). The sample was kept at the reduction temperature for the period of time given in

Table 4.1. Subsequently, the sample was cooled to 200°C and evacuated for four hours. Then, the temperature was increased to the activation temperature (

Table 4.1) and O_2 titration was carried out. The calculation used to determine the active metal surface area is given in Appendix A.

The Fischer-Tropsch synthesis was performed at Sasol United Kingdom (SUK). The catalytic activity and selectivity were determined in a fixed bed reactor set-up containing four independent parallel reactor tubes each with inner diameter of 6.5mm. The catalysts (200mg) were each diluted with 3.1g SiC (320 grit) resulting in a catalyst bed length of ~ 6cm. The catalyst bed temperature was accurately controlled by means of a thermocouple in the middle of the bed. Prior to Fischer-Tropsch synthesis the samples were activated *in-situ* at elevated temperatures and atmospheric pressure (see

Table 4.1). After reduction, the temperature was changed to 200ºC and the pressure increased to 20 bar using H_2 and Ar. Synthesis gas (H_2/CO = 2) was then introduced and the temperature was gradually increased to 230ºC (ramp rate 0.5ºC/min). The reaction effluent was passed through a hot trap (190ºC) to collect the high boiling waxes and a cold trap (15ºC) to collect the water and low boiling organic product compounds. It should be noted here that the catalysts tested generated negligible quantities of liquid product and therefore the formation of other products could not be determined. The outlet gases were analyzed on-line using an Agilent 7890A Refinery Gas Analyzer equipped with a Flame Ionization Detector (FID) and two TCDs. Ar (~ 8%) was added to the feed and used as internal standard to determine conversion and product selectivity.

4.3 Results and discussion

Co_3O_4 nanoparticles were used as a reference for comparison whilst $NiFe_2O_4$ and $ZnFe_2O_4$ nanoparticles were used both as a reference and as a core around which a cobalt oxide shell was grown. Basic characterization of the ferrite nanoparticle systems are provided in Chapter 2. Co_3O_4 nanoparticles with an average size of 14 nm were synthesized (Appendix B; Table B.1). This material also contained Co(II)O (6.3%) and even some metallic cobalt (3.4%) (refer to Appendix B; Figure B.1 (a) and Table B.1). The metallic cobalt crystallites are comparatively large (see Table B.1). Metallic cobalt and Co(II)O may have formed during calcination by the reduction with various gases such as CO and NO. These gaseous compounds may originate from the decomposition of citric acid and nitrate ions [32-35]. The respective ferrite phase was identified in the diffraction pattern of $NiFe_2O_4$@Co_3O_4 and $ZnFe_2O_4$@Co_3O_4 core-shell nanoparticles with similar crystallite size to the bare core material (refer to Appendix B; Figure B.1 (c) and (e) and Table B.1).

The core-shell nanoparticles were analyzed and found to contain 8.3 wt.% cobalt. This would correspond to the formation of a shell of a thickness of 0.5 nm assuming uniform crystallite size for the ferrite nanoparticles of 1 nm and homogeneous deposition of the cobalt around these particles. As a result, the reflections due to the Co_3O_4 phase were not observed in the powder X-ray diffraction pattern of both $NiFe_2O_4$@Co_3O_4 and $ZnFe_2O_4$@Co_3O_4 core-shell nanoparticles. This is due to the fact that, assuming each catalyst has a uniform shell with thickness of 0.5 nm, there is insufficient material (Co_3O_4) available to produce a coherent X-ray scattering signal and hence it is unlikely that the diffraction pattern of the Co_3O_4 would be observed. Instead the penetrating X-rays would scatter more effectively from the core material and so it is unlikely that Co_3O_4 would be observed.

STEM-HAADF imaging were used to examine the core-shell $NiFe_2O_4$@Co_3O_4 and $ZnFe_2O_4$@Co_3O_4 nanoparticles. The similarity in the average atomic number (Z) and density between Co_3O_4 and the ferrite core complicate phase identification purely from HAADF image contrast (Figure 4.1 (a) and (b)). EELS spectrum imaging was therefore used to determine the location of the cobalt shell relative to the ferrite core (Figure 4.1 (c) and (d)). This showed that the thickness of the Co layer around the core is not uniform with a maximum thickness is *ca*. 3 nm. The obtained shell thickness in conjunction with the particle size of the ferrites implies that a large fraction of the ferrite nanoparticles has not been covered fully or not at all. An average shell thickness of 3 nm would imply that only 13.5% of the surface has been covered, whereas a shell thickness of 2 nm would imply coverage of the ferrite surface of 21.5%.

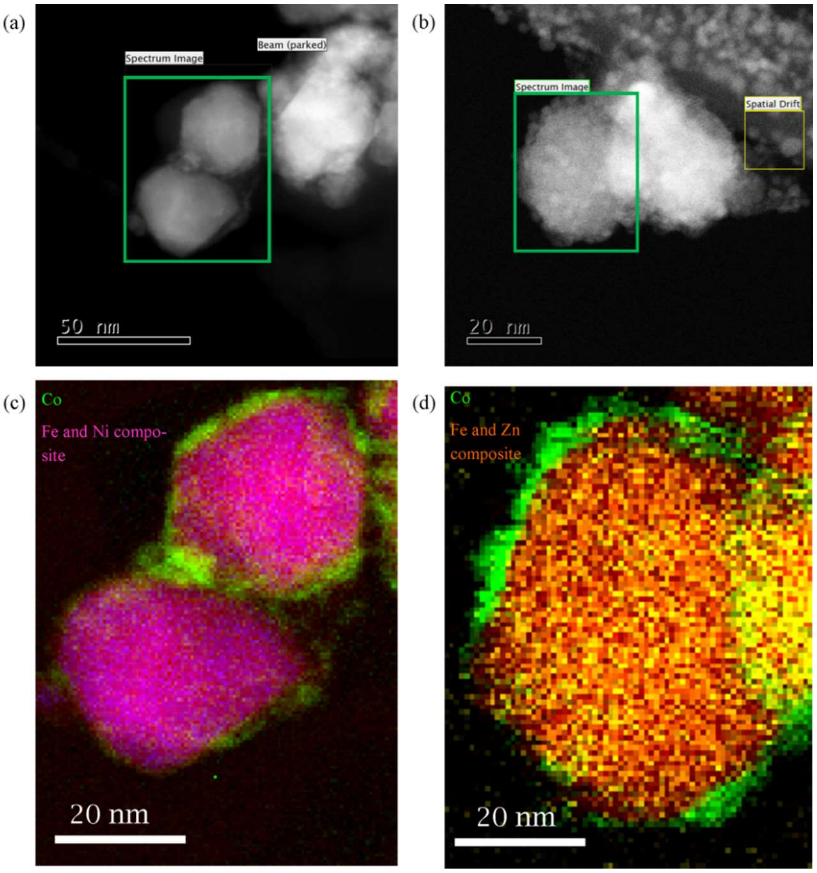

Figure 4.1. STEM-HAADF image of (a) $NiFe_2O_4@Co_3O_4$ and (b) $ZnFe_2O_4@Co_3O_4$ showing region where spectrum image was acquired and composite elemental map obtained from the EELS spectrum image of (c) $NiFe_2O_4@Co_3O_4$ and (d) $ZnFe_2O_4@Co_3O_4$.

Raman spectroscopy was used to determine the phase in which cobalt was present in the sample. Raman active modes of Co_3O_4 are found at 193 cm^{-1} (F^1_{2g}), 480 cm^{-1} (E_g), 520 cm^{-1} (F^2_{2g}), 671 cm^{-1} (F^3_{2g}) and 688 cm^{-1} (A_{1g}) [36] whilst the bands due to $NiFe_2O_4$ were found at 213 cm^{-1} (F^1_{2g}), 333 cm^{-1} (E_g), 484 cm^{-1} (F^2_{2g}), 571 cm^{-1} (F^3_{2g}) and 702 cm^{-1} (A_{1g}) with shoulder bands at 587 cm^{-1} and 680 cm^{-1} (see Figure 4.2 (a)). [37, 38] In comparison to the Raman spectrum of $NiFe_2O_4$, the Raman spectrum of $NiFe_2O_4@Co_3O_4$ nanoparticles shows an additional band at 190 cm^{-1} and a shoulder at 682 cm^{-1}. This suggests that (some) cobalt is present as Co_3O_4 (other bands due to Co_3O_4 overlap with the bands of the ferrite). $ZnFe_2O_4$ showed the expected Raman active modes, viz. at 245 cm^{-1} (E_g), 353 cm^{-1} (F^2_{2g}), 463 cm^{-1} (F^3_{2g}) and 635 cm^{-1} (A_{1g}) [37, 38] whilst the Raman spectrum of the $ZnFe_2O_4@Co_3O_4$ core-shell sample also showed an additional band at 190 cm^{-1}, 480 cm^{-1} and 685 cm^{-1} (Figure 4.2 (b)). Hence, it is concluded that Co_3O_4 is also present in $ZnFe_2O_4@Co_3O_4$ nanoparticles. The slight red-shift of the wavenumber for the Co_3O_4 F^1_{2g} and A_{1g} bands in the core-shell nanoparticles may be attributable to the formation of the shell structure influencing the coordination of the tetrahedral and octahedral sites [37, 39, 40], although it may also be linked to the agglomerated state of Co_3O_4 in the shell [41].

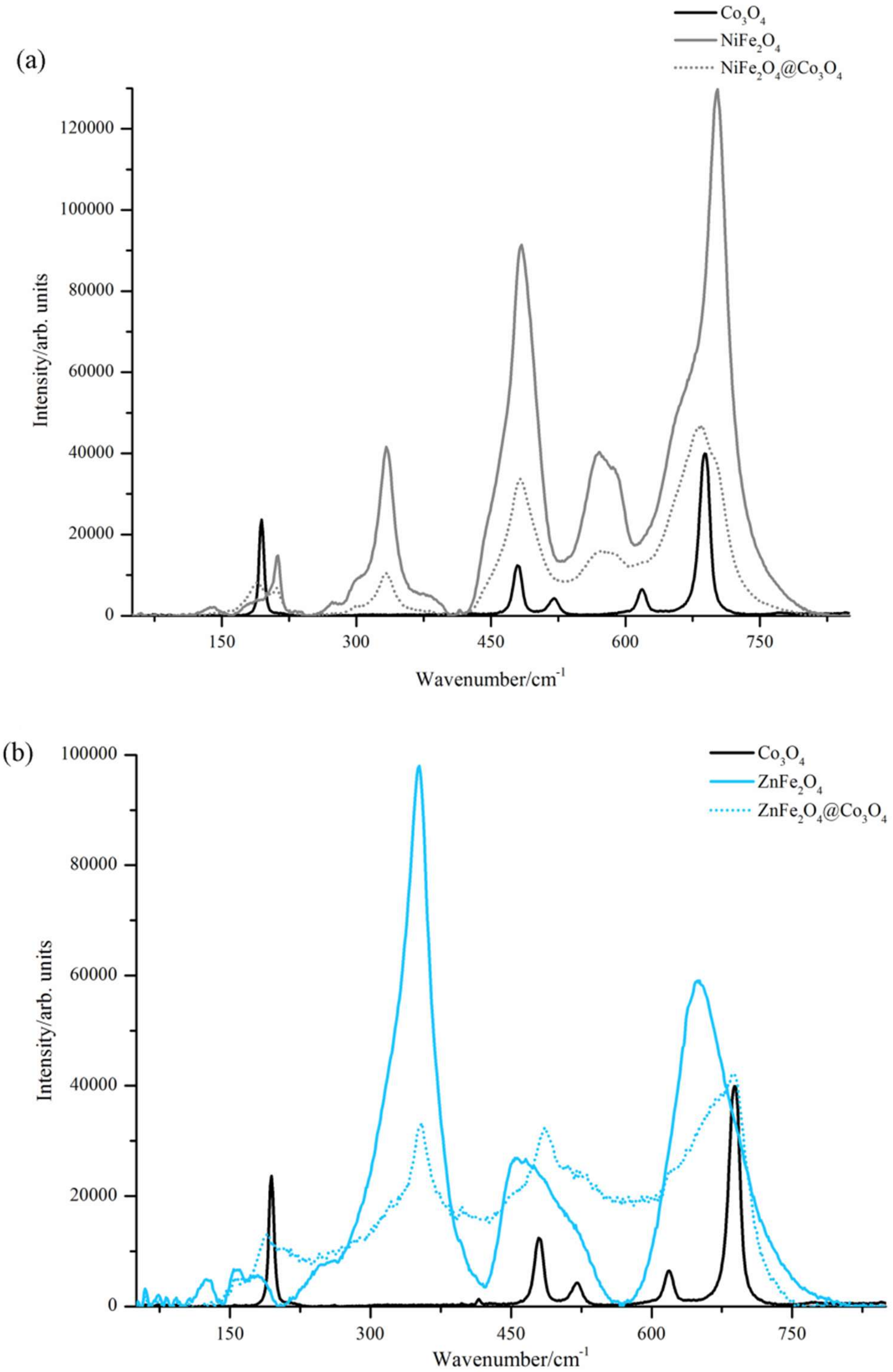

Figure 4.2. Raman spectra of (a) Co_3O_4, $NiFe_2O_4$ and $NiFe_2O_4@Co_3O_4$ and (b) Co_3O_4, $ZnFe_2O_4$ and $ZnFe_2O_4@Co_3O_4$.

The Co 2p core level XPS spectra for Co_3O_4 and the core-shell nanoparticles are shown in Figure 4.3. The Co 2p binding energy region is dominated by two peaks located at ~780eV and ~795eV, corresponding to the Co $2p_{3/2}$ and Co $2p_{1/2}$ spin orbit components respectively. The Co 2p main peaks for Co_3O_4 can be decomposed into two sub-components, which can be attributed to Co^{3+} (at 779.5eV and 794.6eV) and Co^{2+} (at 781.6eV and 796.7eV). The shake-up satellite peaks are located at 9eV on the higher binding energy side of the Co^{3+} doublet. The observed line shape is consistent with previously reported data on Co_3O_4 nanoparticles [42]. The ratio of peak areas of the two components shows that 62% of the Co ions are in the 3+ oxidation state and 38% in the 2+ oxidation state, close to the expected ratio for Co_3O_4 of Co^{3+}:Co^{2+} = 2. The core-shell structure in $NiFe_2O_4$@Co_3O_4 and $ZnFe_2O_4$@Co_3O_4 causes the line shape of the Co 2p core level to change. The two main peaks seem to have a weak feature at the low binding energy side. Furthermore, the shake-up satellites become broader and their centroid shifts towards lower binding energy by ~3eV. Both changes are consistent with the appearance of an additional spin-orbit doublet at 778.1eV and 793.2eV, which may be attributed to the presence of some Co^0 (or metallic Co) [43, 44] present in these samples. It is estimated that 19% of the cobalt in the as synthesized $NiFe_2O_4$@Co_3O_4 and 14% of the cobalt in the as synthesized $ZnFe_2O_4$@Co_3O_4 is present as zero-valent cobalt.

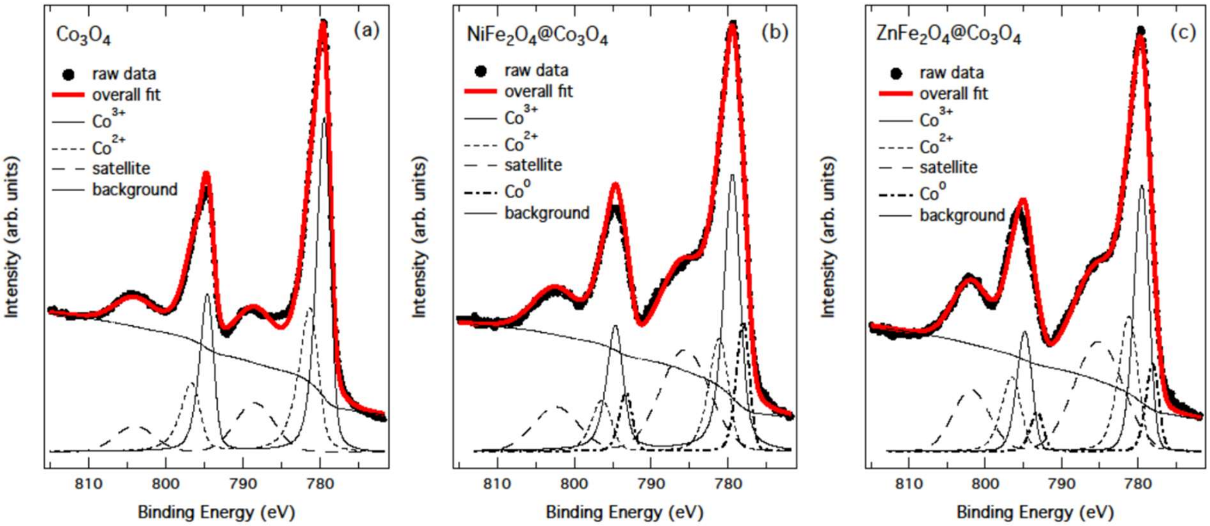

Figure 4.3. Co 2p core level spectra for (a) Co_3O_4, (b) $NiFe_2O_4$@Co_3O_4 and (c) $ZnFe_2O_4$@Co_3O_4 (Shirley-type background and the various spin-orbit doublets representing different oxidation states for Co is also shown).

Figure 4.4 shows the Fe 2p core level XPS spectra for the ferrites and the core-shell nanoparticles. The line shapes of the Fe 2p core level for the precursor ferrites, $NiFe_2O_4$ and $ZnFe_2O_4$, are composed of two main peaks at 710.6/711.0eV and 724.0/724.7eV, respectively, corresponding to the Fe $2p_{3/2}$ and Fe $2p_{1/2}$

spin orbit components. In addition, two broad satellites with centroids at 719.0/719.7eV and 732.4/733.0eV are observed originating from the screening effect of the surrounding oxygen atoms. The observed binding energies for the Fe $2p_{3/2}$ and Fe $2p_{1/2}$ spin are in line with those reported for the inverse spinel $NiFe_2O_4$ [45, 46] and $ZnFe_2O_4$ [43] are indicative for the presence of trivalent iron. The Fe 2p core level line shape of the core-shell nanoparticles changes quite substantially. The centroid of the Fe $2p_{3/2}$ and $2p_{1/2}$ peaks shifts to lower binding energy by 0.6eV. Furthermore, the spectral weight in the energy region between the main peaks and the corresponding satellites increases, resulting in a 2.1eV and 1.1eV shift of the $2p_{3/2}$ and $2p_{1/2}$ satellite's centroid towards lower binding energies, respectively. This is compatible with a change in the oxidation state of some Fe ions from 3+ to 2+ [45]. This would imply reduction of some Fe^{3+} resulting in the formation of Fe^{2+} similar to that observed with cobalt (vide supra). However, the spectral shift may also be caused by the core-shell environment.

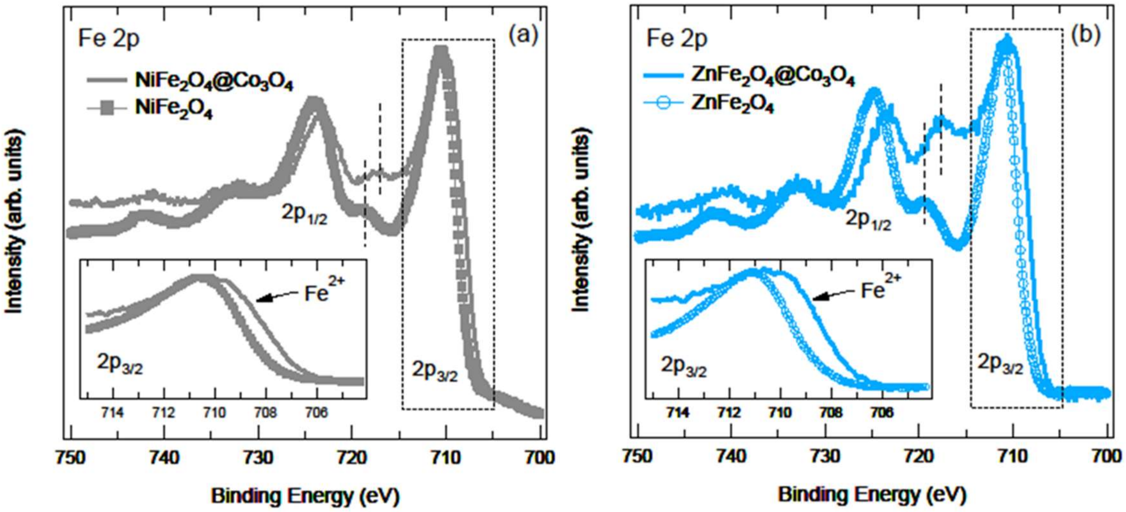

Figure 4.4. Fe 2p core level spectra for (a) $NiFe_2O_4$ and $NiFe_2O_4@Co_3O_4$, and (b) $ZnFe_2O_4$ and $ZnFe_2O_4@Co_3O_4$. The insets show the expanded Fe 2p3/2 peak region.

The Ni 2p core level for $NiFe_2O_4$ (Figure 4.5 (a)) shows Ni $2p_{3/2}$ and $2p_{1/2}$ peaks at 854.9eV and 872.4eV, respectively, in good agreement with Ni^{2+} in the bulk compound [45]. Satellite peaks at 6.5eV higher binding energy accompany both main peaks. In the core-shell material, $NiFe_2O_4@Co_3O_4$, the main Ni $2p_{3/2}$ and $2p_{1/2}$ peaks become slightly broader and the overall spectrum shifts towards lower binding energies by 1eV. This indicates that the oxidation state of Ni in the core-shell material remains 2+. The above-mentioned shift of 1eV might be attributed to the core-shell environment. The Zn 2p core level for $ZnFe_2O_4$ (Figure 4.5 (b)) displays Zn $2p_{3/2}$ and $2p_{1/2}$ peaks at 1021.4eV and 1044.5eV. The line shape is typical of the Zn in the 2+ oxidation state. Like the $NiFe_2O_4@Co_3O_4$ core-shell system, the Zn 2p peaks of

$ZnFe_2O_4$@Co_3O_4 nanoparticles shifts to a lower binding energy by 1.8eV in comparison to the Zn 2p peak of $ZnFe_2O_4$ without a significant change in the peak shape. This may be attributed again to a change of the chemical environment of the zinc ferrite forming a part of the core-shell material.

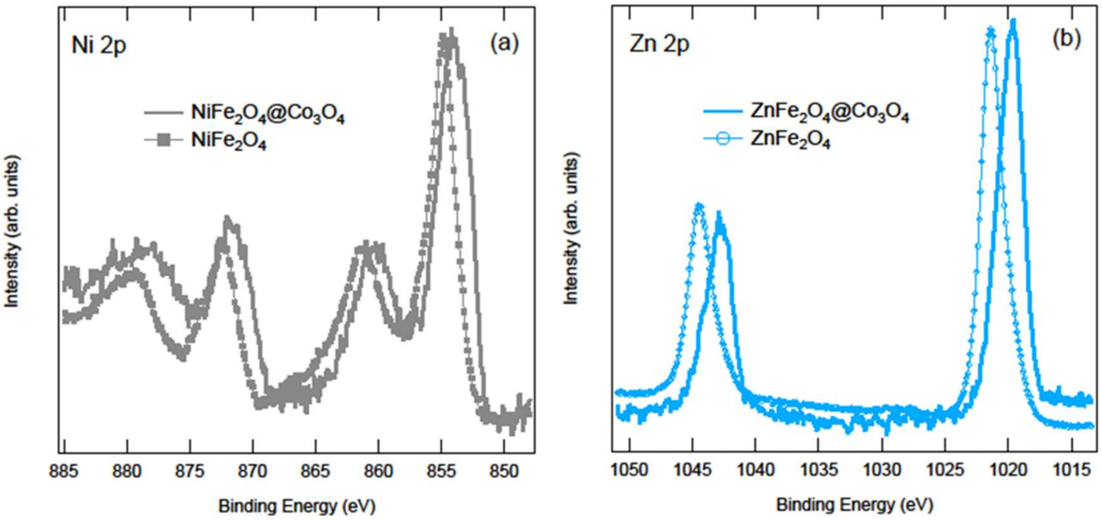

Figure 4.5. (a) Ni 2p core level spectra for $NiFe_2O_4$ and $NiFe_2O_4$@Co_3O_4 and (b) Zn 2p core level spectra for $ZnFe_2O_4$ and $ZnFe_2O_4$@Co_3O_4.

The reducibility of the nanoparticles was studied using H_2-TPR (see Figure 4.6). The experimental data was deconvoluted into separate reduction events using a log-normal skewed peak fitting. The resulting peak maxima are given in Table 4.2. The H_2-TPR profile of Co_3O_4 shows the presence of two major reduction peaks, with peak maxima at 241°C for peak B and 292°C for peak C, respectively, preceded by a shoulder. The presence of the low temperature shoulder peak with a peak maximum at *ca*. 223°C is typically ascribed to the reduction of CoOOH [47] or the reduction of residual nitrates [48, 49]. The reduction of nitrates may result in the formation of NO, which was indeed observed in the effluent using mass spectrometry (m/z = 30 (NO^+), refer to Figure B.2 in Appendix B) *albeit* with a peak maximum at a lower temperature of 176°C. It should be noted that the sample also contains some Co(II)O (vide supra), whose reduction may be more facile due to the lower activation energy for the reduction of cobaltous oxide [50] resulting this in a lower reduction temperature. It should be noted that the consumption of hydrogen ascribed to the shoulder (*ca*. 4.5% of the total amount of hydrogen consumed) corresponds roughly to the expected amount of hydrogen consumed for this sample containing 6.3 wt.% Co(II)O (5.3% of the total hydrogen consumption). The sample does contain metallic cobalt and close proximity of metallic cobalt and an oxide phase may enhance the reduction of the oxide phase by enhancing the flux of activated hydrogen *via* spill-over [51].

The reduction profile for $NiFe_2O_4$ shows an asymmetrical reduction peak which was fitted with three peaks with reduction maxima at 290 °C, 353 °C and 388 °C using a log-normal skewed peak shape (Figure 4.6 (b)). The reduction of $NiFe_2O_4$ may yield directly metallic nickel and magnetite (300 – 400 °C) which is subsequently either directly reduced to metallic Fe or *via* a FeO intermediate (500 – 800 °C) [52]. Alternatively, $NiFe_2O_4$ may undergo a reductive decomposition into NiO and magnetite [53] or even a thermal decomposition into NiO and hematite [54]. The poor resolution of the reduction peaks makes it difficult to describe the reduction pathway unequivocally. The peak areas obtained in the peak deconvolution are consistent with a reduction pathway, in which the initial step proceeds *via* the formation of NiO and magnetite (Fe_3O_4) (requiring 8% of the total amount of hydrogen consumed), followed by the reduction yielding simultaneously FeO and metallic nickel (requiring *ca*. 42% of the total amount of hydrogen consumed). In the last step, metallic iron is formed. Irrespective of the reduction pathway, Fe-Ni alloyed nanoparticles of various compositions may be formed upon reduction [54, 55].

The H_2-TPR profiles of $NiFe_2O_4@Co_3O_4$ show the presence of two additional peaks in the low temperature range of 50 – 300°C when compared to the reduction profile of $NiFe_2O_4$ (Figure 4.6 (b) and (d)). The maximum temperature for each of these reduction peaks are 164°C and 226°C (these reduction peaks coincides with the onset of the ferrite reduction). It is tempting to describe these low temperature reduction peaks to the step-wise reduction of the Co_3O_4 shell. However, the amount of hydrogen consumed, which can attributed to the first two reduction steps amounts to only 2% of the total amount of hydrogen consumed, which is at odds with the total amount of cobalt within the sample. Furthermore, the relative peak area of peak A to B is 1:1.5 (stoichiometrically the amount of hydrogen required for the first reduction step in the reduction of Co_3O_4 to CoO relative to the amount of hydrogen required for the second reduction step, CoO to Co, should be 1:3) [48, 56]. This suggests then that peak A and B is due to some reduction of Co_3O_4 at two different temperatures. The relative amount of hydrogen consumed, which is attributed to peak C, is significantly higher than the amount of hydrogen consumed for the same peak for $NiFe_2O_4$. If the reduction process for both $NiFe_2O_4$ and $NiFe_2O_4@Co_3O_4$ follows the same reduction steps, it may be assumed that hydrogen consumption attributable to the reduction of $NiFe_2O_4$ to NiO and Fe_3O_4 and to further reduction of the Co_3O_4 shell likely to metallic cobalt. It can be further noted that the reduction peaks attributable to the reduction of the ferrite structure are shifted to higher temperatures in the core-shell nanoparticles compared to $NiFe_2O_4$ implying that the reduction of the ferrite is impeded in the core-shell structure (Figure 4.6, Table 4.2).

The H_2-TPR profile of $ZnFe_2O_4$ (Figure 4.6 (c)) was fitted with five Gaussian shaped peaks with peak maxima at 311°C, 413°C, 450°C, 508°C and 768°C. The reduction of $ZnFe_2O_4$, is expected to yield initially ZnO and magnetite (between 350 and 500°C) [57], with the latter being further reduced at rather moderate temperatures. The peaks in the TPR profile are merged together and a detailed reduction pathway could not be resolved. The reduction of ZnO requires rather high temperatures [57], and may be represented by the peak *ca*. 700 – 900°C.

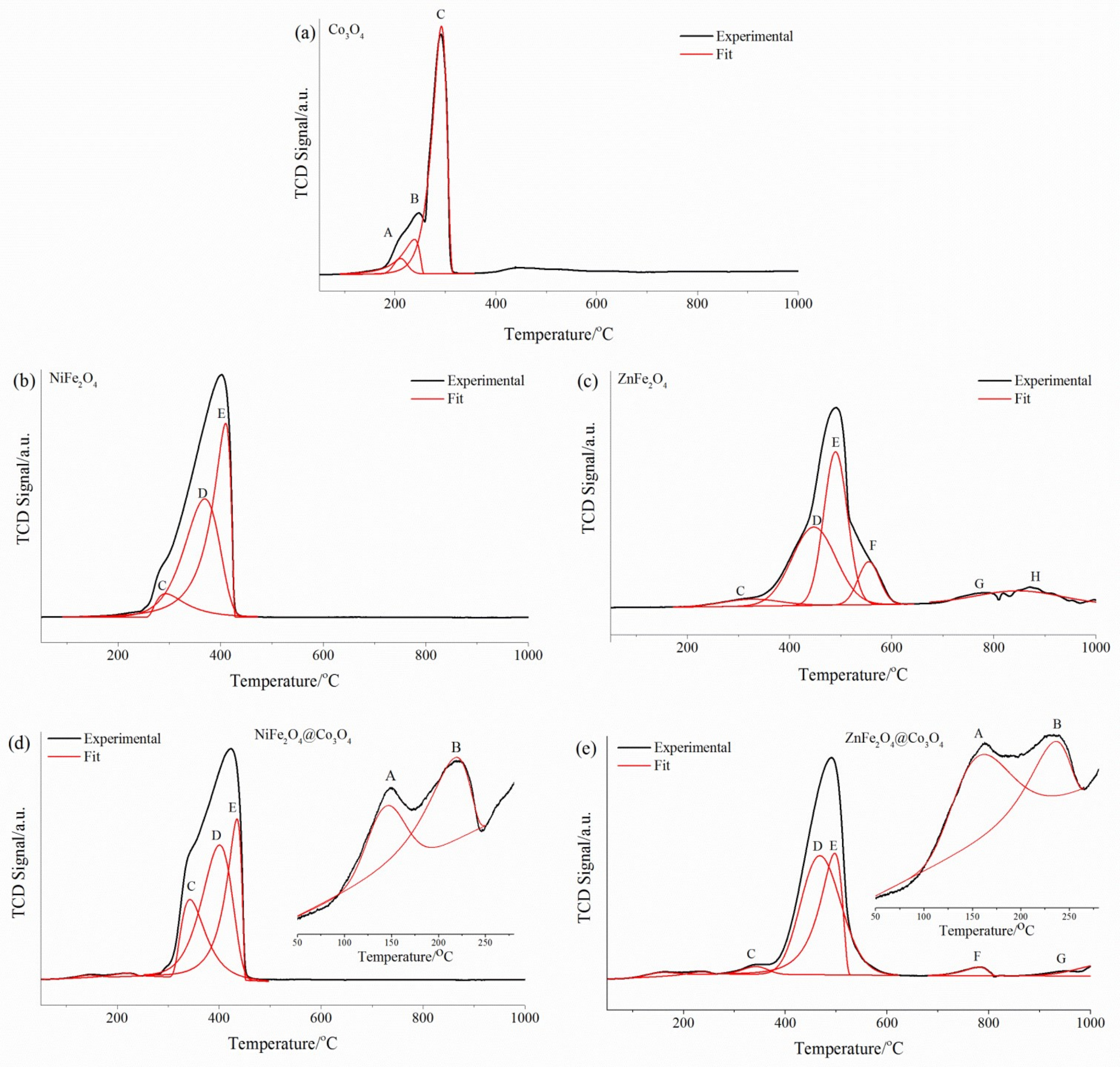

Figure 4.6. TPR profiles (a) Co_3O_4; (b) $NiFe_2O_4$; (c) $ZnFe_2O_4$; (d) $NiFe_2O_4$@Co_3O_4 and (e) $ZnFe_2O_4$@Co_3O_4. Where necessary, low temperature peaks are expanded for clarity on a separate intensity scale.

The H_2-TPR profiles of $ZnFe_2O_4$@Co_3O_4 also shows the presence of two additional peaks in the low temperature range of 50 – 300°C, with a peak maximum at 178°C and 244°C (Figure 4.6 (c) and (e)). The second reduction peak coincides with the onset of the ferrite reduction. Again, the relative hydrogen consumption for the reduction of the first two peaks is less than the expected amount, if the first two reduction peaks are ascribed to the consecutive Co_3O_4 → CoO → Co reduction [48, 56]. The first two reduction peaks in $ZnFe_2O_4@Co_3O_4$ occur at slightly higher temperatures than in $NiFe_2O_4@Co_3O_4$ (see Table 4.2). This might possibly indicate a stronger interaction between the shell and core in $ZnFe_2O_4@Co_3O_4$. It can be further noted that the reduction peaks attributable to the reduction of the $ZnFe_2O_4$ also occur at a higher temperature in $ZnFe_2O_4@Co_3O_4$ nanoparticles than in the single component ferrites (see Table 4.2).

Table 4.2. Temperature maxima and relative peak area from the H_2-TPR profiles of the various metal oxides (peak positions are indicated in Figure 4.6).

Parameter	**Peak**	**Sample**				
		Co_3O_4	$NiFe_2O_4$	$NiFe_2O_4@Co_3O_4$	$ZnFe_2O_4$	$ZnFe_2O_4@Co_3O_4$
T_{max}/°C	A	223	-	164	-	178
	B	247	-	226	-	244
	C	292	290	330	311	329
	D	-	353	377	413	435
	E	-	388	404	450	461
	F	-	-	-	508	711
	G	-	-	-	767	945
	H	-	-	-	880	> 1000
Relative H_2 consumption[a]/%	A	5	-	1	-	1
	B	14	-	1	-	1
	C	81	8	22	4	2
	D	-	46	45	36	52
	E	-	46	31	38	33
	F	-	-	-	10	2
	G	-	-	-	12	9
	H	-	-	-	n.d.[b]	n.a.[b]

[a] Hydrogen consumption normalized to the total amount of hydrogen consumed

[b] n.d.: not determined; n.a.: not applicable

In-situ reduction was performed in a XRD cell to analyze changes in the crystal structure of $NiFe_2O_4$ and $ZnFe_2O_4$ after the reduction from room temperature to 230 or 250°C for two hours, respectively. Further to that, synthesis gas ($H_2/CO = 2$) at 230°C and 16 bar pressure was introduced after reduction for 16 hours to evaluate the influence of the Fischer-Tropsch conditions on the reduced material (refer to Table 4.3). For $NiFe_2O_4$, metallic Ni (2.4 mass %) and NiO (3.8 mass %) was evidenced after a two hour hold time (see Table 4.3). After exposure to Fischer-Tropsch conditions, a Fe-Ni alloy, $Fe_{0.625}Ni_{0.375}$, was detected (7.4

mass %) and Fe_2C was present (7.1 mass %) (see Table 4.3). The reducing atmosphere of the Fischer-Tropsch conditions [58, 59] not only results in the formation of metallic nickel and iron which forms an alloy but also results in some carburization [60, 61]. Slight sintering of the $NiFe_2O_4$ crystallites occurred after activation and more especially, after exposure to Fischer-Tropsch conditions possibly due to exposure to water [60]. On the other hand, the crystallite size of metallic nickel was smaller (4.6 nm) after exposure to Fischer-Tropsch conditions than activation (10.6 nm). The variation in the crystallite size of nickel after exposure to each of the two conditions may be a consequence of the influence of syngas on the crystallinity and/or dispersion of the formed nickel over the ferrite surface. Chonco *et al.*[60] observed similar changes to the crystallite sizes of their Cu, Fe_3O_4 and $CuFe_2O_4$ nanoparticles after exposure to Fischer-Tropsch conditions.

Table 4.3. Relative phase abundance and average crystallite size of the various phases present after the activation in H_2 (230/250°C, two hours) and exposure to Fischer-Tropsch conditions ($T_{reaction}$ = 230°C, p = 16 bar) determined from the Rietveld refinement of experimental powder diffraction data obtained during the *in-situ* experiments.

	Phase	**H_2 activation**		**After exposure to Fischer-Tropsch conditions^f**	
		$NiFe_2O_4$^{c}	**$ZnFe_2O_4$^{d}**	**$NiFe_2O_4$**	**$ZnFe_2O_4$**
Relative phase abundance/mass %^{a}	MFe_2O_4^{e}	93.8 (0.1)	100 (0.0)	85.5 (0.2)	90.2 (0.3)
	NiO	3.8 (0.1)	-	-	-
	Ni	2.4 (0.1)	-	-	-
	$Fe_{0.625}Ni_{0.375}$	-	-	7.4 (0.2)	-
	Fe_2C	-	-	7.1 (0.2)	7.2 (0.2)
	$Zn_xFe_{1-x}O$	-	-	-	2.6 (0.2)
Average crystallite size /nm$^{a, b}$	MFe_2O_4^{e}	15.4 (0.1)	14.8 (0.3)	18.2 (0.1)	16.7 (0.3)
	NiO	17.2 (0.8)	-	-	-
	Ni	10.6 (0.5)	-	-	-
	$Fe_{0.625}Ni_{0.375}$	-	-	4.1 (0.1)	-
	Fe_2C	-	-	7.8 (0.3)	5.0 (0.2)
	$Zn_xFe_{1-x}O$	-	-	-	9.6 (0.9)

[a] Uncertainty are given in parenthesis

[b] Volume-weighted average crystallite size determined from the integral breadth

[c] M is Ni or Zn

[d] Activation at 230 °C for two hours

[e] Activation at 250 °C for two hours

[f] $T_{reaction}$ = 230 °C, p = 16 bar for 16 hours

For $ZnFe_2O_4$, after activation (250°C, two hours) only the spinel ferrite phase was present (Table 4.3) indicating that hydrogen treatment does not result in the formation of a crystalline reduced phase, as could be expected based on the H_2-TPR profile (vide supra), which showed a first small reduction peak with a peak maximum at *ca.* 311°C. Exposure to synthesis gas (16 bar, 230°C for 16 hours) resulted in a partial reductive decomposition yielding an iron substituted zinc oxide ($Zn_xFe_{1-x}O$) together with the formation of Fe_2C (Table 4.3). Similar to $NiFe_2O_4$, slight sintering of the $ZnFe_2O_4$ crystallites occurred after exposure to Fischer-Tropsch conditions.

The influence of the activation conditions, in a hydrogen environment, on the core-shell nanoparticles was evaluated by *in-situ* heating from room temperature to 230 – 300/350°C in a TEM. During the reduction process, the morphology of the core-shell particles was monitored using STEM-HAADF and EELS spectrum imaging. The STEM-HAADF images (see Figure 4.7) show the progression of one representative site of interest in $NiFe_2O_4$@Co_3O_4 while heating in 1 atm H_2 indicating the change in the structure of the nanoparticle during reduction. Subtle changes in the HAADF intensity were initially observed after an exposure to hydrogen for one hour at 230°C. After two hours at these conditions, growth of cobalt islands on the surface of the larger nickel ferrite nanoparticles was observed with sizes in the range of 1 – 3 nm (Figure 4.7 (c) and (e)). Further heating (280°C) resulted in the presence of distinct nanoparticles with sizes of the order of 3 – 5 nm. The changes in the crystallite morphology and size observed during reduction may be attributed to the mobility of cobalt atoms in the shell during the reduction process. It is clear therefore that under activation conditions the core-shell structure breaks down to form cobalt islands on the surface of the larger nanoparticle.

The morphological changes during the *in-situ* TEM reduction of $ZnFe_2O_4$@Co_3O_4 (see Figure 4.8) are similar to changes observed during the reduction of $NiFe_2O_4$@Co_3O_4 nanoparticles. These core-shell nanoparticles undergo reconstruction during its reduction as demonstrated by the subtle changes in the HAADF intensity. The patches of higher HAADF intensity suggest the formation of atomic clusters with higher average atomic number on the surface (highlighted by comparing the regions marked in Figure 4.8 (a) - yellow rectangle, 230°C - with the same nanoparticles in Figure 4.8 (b) - clusters highlighted by blue arrows, 280°C). At 350°C, cobalt crystallites of a size of *ca.* 3 nm have been formed. EELS spectrum imaging confirmed these crystallites are cobalt (see inset of Figure 4.8 (d)). Although the first evidence of changes to the crystallite morphology is observed at a similar temperature (230°C) for both core-shell systems, the formation of crystallites occurs at a higher temperature for $ZnFe_2O_4$@Co_3O_4 (350°C *versus* 280°C in the $NiFe_2O_4$@Co_3O_4 system).

The formation of islands of cobalt decorating the ferrite core upon reduction of the core-shell MFe_2O_4@Co_3O_4 nanoparticle may be due to the strain induced on the shell during the reduction. The isomorphic reduction of Co_3O_4 is associated with a volume reduction of 25%. The free energy of the system is then minimized by forming multiple islands on the surface of the ferrite core. It is thus proposed that reduction will lead initially to a cracked skin containing patches of the reduced metal of the ferrite core. Further heating of the core-shell nanoparticles in a hydrogen atmosphere will result in an increased the mobility of cobalt atoms resulting in the formation of individual cobalt nanoparticles (230 – 350°C). [27, 29, 30]

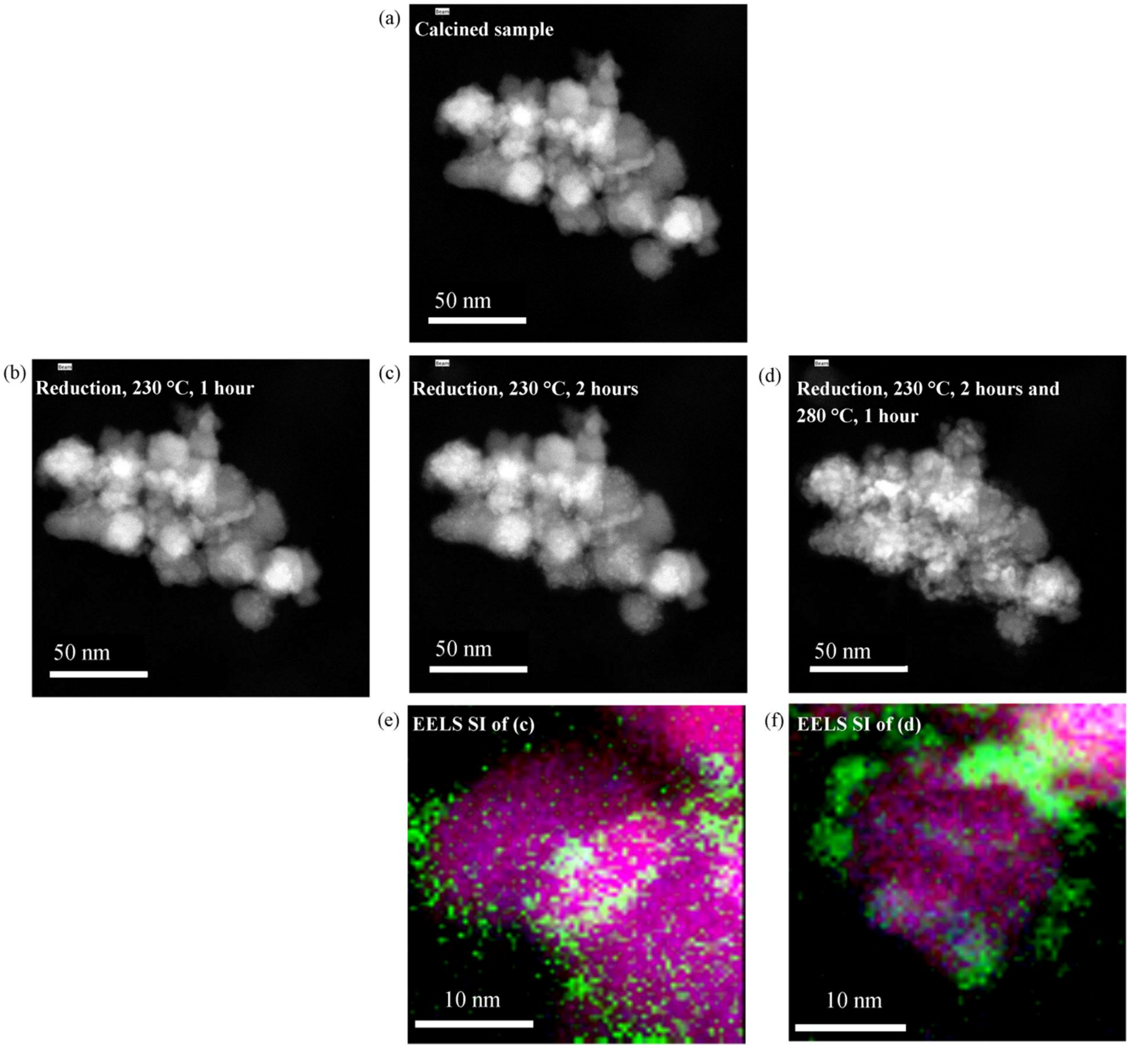

Figure 4.7. STEM-HAADF images of $NiFe_2O_4@Co_3O_4$ obtained (a) prior to reduction and during the *in-situ* TEM reduction at (b) 230°C, one atm for 1 hour; (c) 230°C, one atm for 2 hours; (d) with (c) heating step plus one of 280°C, one atm for 1 hour; (e) and (f) show the composite elemental maps obtained from the EELS spectrum images.

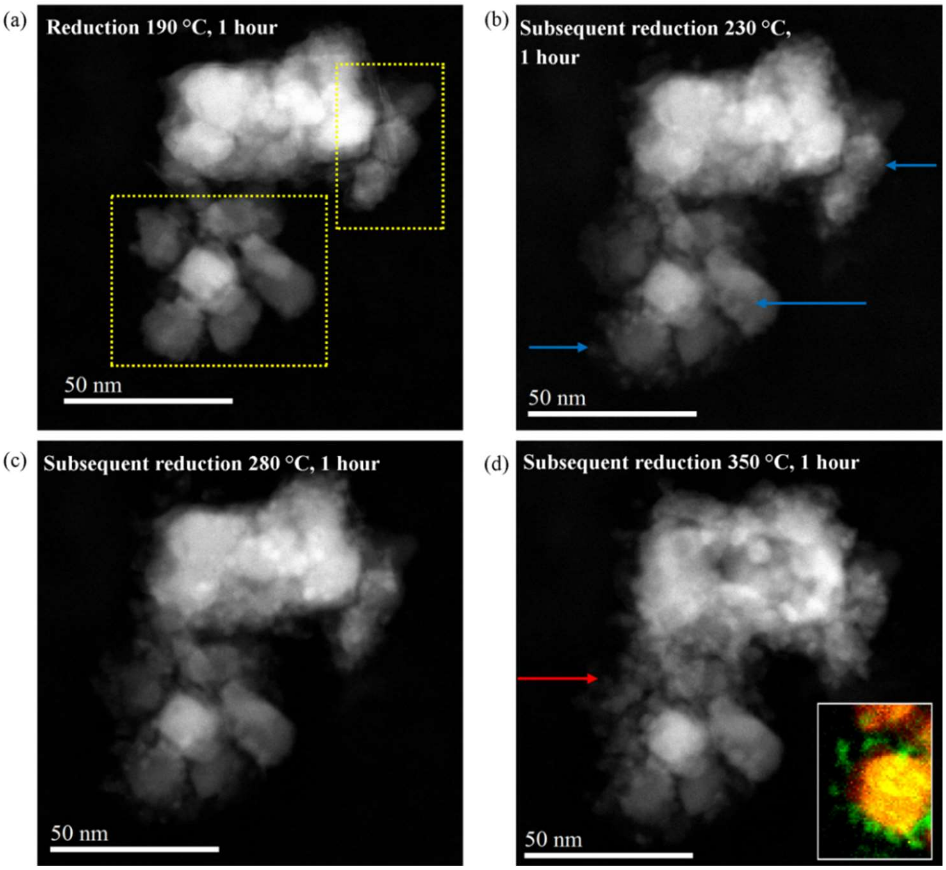

Figure 4.8. STEM-HAADF images of $ZnFe_2O_4@Co_3O_4$ obtained during the in-situ TEM reduction in pure H_2 at (a) 190°C, one atm for 1 hour (b) 230°C, one atm for 1 hour; (c) 280°C, one atm for 2 hours and (d) 350°C, one atm for 1 hour with inset showing the composite elemental map obtained from the EELS spectrum image (Co – green; Zn and Fe composite – orange).

To characterize the synthesized nanoparticles after activation, reduction procedures as set out in Table 4.1 were applied. Low reduction temperatures and a short time were used for the core-shell nanoparticles to ensure reduction of the shell with minimal sintering. It should be noted that partial reduction of $NiFe_2O_4$ into NiO (3.8 mass %) and metallic Ni (2.4 mass %) occurs at the applied reduction condition whilst no reduction of $ZnFe_2O$ was observed (see *in-situ* XRD data). Therefore, the degree of reduction and active metal surface area was not determined for $ZnFe_2O_4$.

A degree of reduction of 42% was obtained for $NiFe_2O_4$ and a low H_2 uptake was found which corresponded to an active metal surface area of 0.47 m^2 g^{-1}, assuming only the reduction of Ni^{2+}. For the cobalt-containing samples the obtained degree of reduction of the material was determined assuming only the reduction of Co_3O_4. The degree of reduction of the reference material, Co_3O_4, was rather low (51%; see Table 4.4) despite applying more severe reduction conditions. At the same time, the hydrogen uptake of the reduced catalyst was low (corresponding to a dispersion of 0.21% and active metal surface area of 1.10 m^2 g^{-1}). The low hydrogen uptake may however be attributed to the partially reduced nature of the individual catalyst particles. The surface may thus resemble the surface of an oxide to a greater extent than that of a metal.

Table 4.4. Characterization of the catalyst samples activated in hydrogen prior to the Fischer-Tropsch synthesis (Space velocity = 6000 ml$_n$·g^{-1}·hr^{-1}).

Sample	$T_{reduction}$/ °C	$t_{reduction}$/ hours	O_2-uptake[a]/ mmol g^{-1}	DOR[b]/%	H_2-uptake[c]/ µmol g^{-1}	Active metal surface area[d]/m^2 g^{-1}
Co_3O_4	300	1	4.28	51	13.4	1.10
$NiFe_2O_4$	230	2	n.d.[e]	n.a.[e]	1.8	n.a.[e]
$NiFe_2O_4$@Co_3O_4	230	2	0.57	62	10.3	0.85
$ZnFe_2O_4$	250	2	n.d.[e]	n.a.[e]	n.d.[e]	n.a.[e]
$ZnFe_2O_4$@Co_3O_4	250	2	0.30	31	5.4	0.44

[a] Amount of O_2 taken up in back titration after reduction

[b] Degree of reduction assuming only the reduction of Co_3O_4

[c] H_2-uptake on the reduced catalyst using pulse chemisorption

[d] Based on H_2-uptake assuming only metallic cobalt with 14.6 Co atoms/nm^2

[e] n.d.: not determined; n.a.: not applicable

The oxygen uptake on the reduced $NiFe_2O_4$@Co_3O_4 core-shell nanoparticles indicate a degree of reduction of 60%, assuming that oxygen is only consumed for the oxidation of cobalt to Co_3O_4. However, at these conditions some nickel ferrite may have undergone a reductive decomposition, e.g. to NiO and metallic Ni (vide supra). The O_2 back-titration may thus overestimate the degree of reduction of cobalt. The hydrogen uptake is low for $NiFe_2O_4$@Co_3O_4 core-shell nanoparticles thus corresponding to an active metal surface area of 0.85 m^2 g^{-1}.

The reduction of $ZnFe_2O_4$@Co_3O_4 is less facile than the reduction of $NiFe_2O_4$@Co_3O_4 as visualized using TPR. The obtained degree of reduction is thus less than the degree of reduction obtained with $NiFe_2O_4$@Co_3O_4 despite the slightly higher reduction temperature. Hence, the hydrogen uptake and metal surface area on the reduced $ZnFe_2O_4$@Co_3O_4 is proportionally less.

The strength of CO adsorption was probed using CO-TPD on the reduced samples (activation conditions are given in

Table 4.1). Desorption of CO (m/z = 28) was only observed over the reduced core-shell nanoparticles (Figure 4.9). H_2O (m/z = 18, possibly residual of the hydrogen pre-treatment) and CO_2 (m/z = 44, Figure 4.10) were observed in the effluent of the CO-TPD obtained over all reduced samples.

Desorption profiles of molecular CO for reduced $NiFe_2O_4$@Co_3O_4 and $ZnFe_2O_4$@Co_3O_4 were fitted with two Gaussian peaks. Desorption peaks were at 409°C and 640°C for $NiFe_2O_4$@Co_3O_4 reduced at 230°C and at 390°C and 679°C for $ZnFe_2O_4$@Co_3O_4 reduced at 250°C (Table 4.6). The presence of two peaks suggests that different binding states of CO on various cobalt surfaces may have been present [62, 63]. The high temperature peak at *ca*. 600°C may be due to desorption of the dissociative form of adsorbed CO [64-66]. The peak maximum of the shoulder preceding this high temperature peak seems to appear at a temperature (*ca*. 400°C), which is too high to be associated with desorption of associatively bounds CO, and may thus also originate from desorption of dissociated CO. However, here CO will desorb from a different surface with a weaker CO-binding and/or less facile diffusion of atomic carbon and/or oxygen.

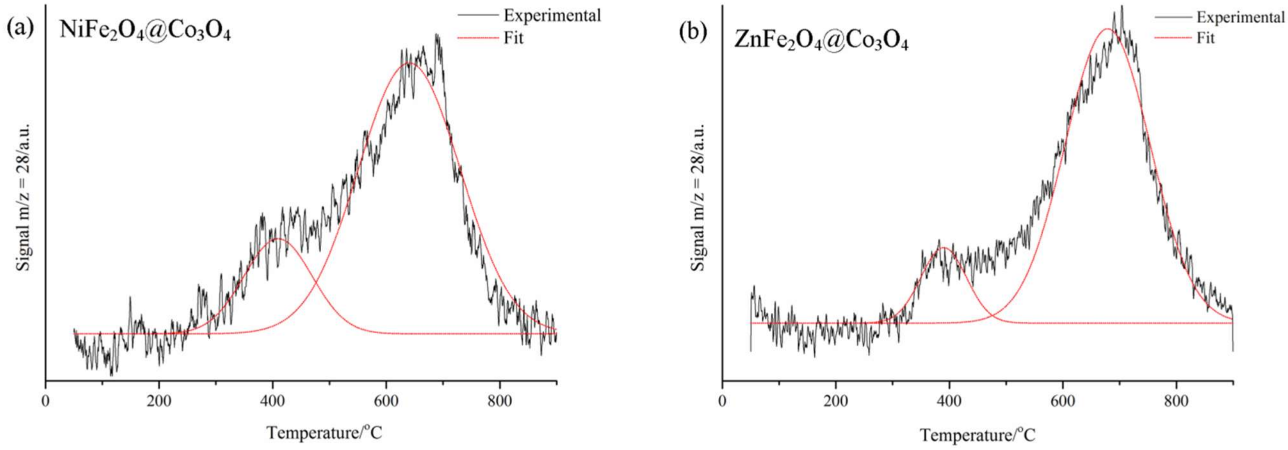

Figure 4.9. CO (m/z = 28) desorption profile over reduced (a) $NiFe_2O_4$@Co_3O_4 ($T_{reduction}$ = 230°C) and (b) $ZnFe_2O_4$@Co_3O_4 ($T_{reduction}$ = 250°C).

The formation of CO_2 was observed in the CO-TPD spectra of all reduced nanoparticles (Figure 4.10). The rate of formation of CO_2 during the CO-TPD over each of the reduced samples was fitted with four Gaussian peaks (positions are given in Table 4.5). The ferrite-containing samples all show the first evidence of CO_2 formation at *ca*. 100°C, whereas the first CO_2 formation over Co_3O_4 is only seen at *ca*. 200°C. It can further be noted that the relative amount of the first peak to the total amount of CO_2 formed is reduced for the core-shell nanoparticles. This may indicate that the low temperature CO_2 formation is associated with the CO-reduction of the ferrite rather than with the reduction of residual Co_3O_4. The CO_2 formation over Co_3O_4 at *ca*. 200°C may imply that this material is further reduced when exposed to Fischer-Tropsch conditions. The other peaks associated with CO_2 formation appear at much higher temperatures with peak maxima in the range of 350 – 700°C. CO_2 may originate here from further reduction of the nanoparticles [2, 7, 67, 68], carburization of e.g. magnetite [60, 68] or from recombination of dissociated CO with the co-generation of carbon. It should be noted that the onset of the peak occurs at rather low temperature and nanoparticles may reduce and/or carburize further during the Fischer-Tropsch synthesis.

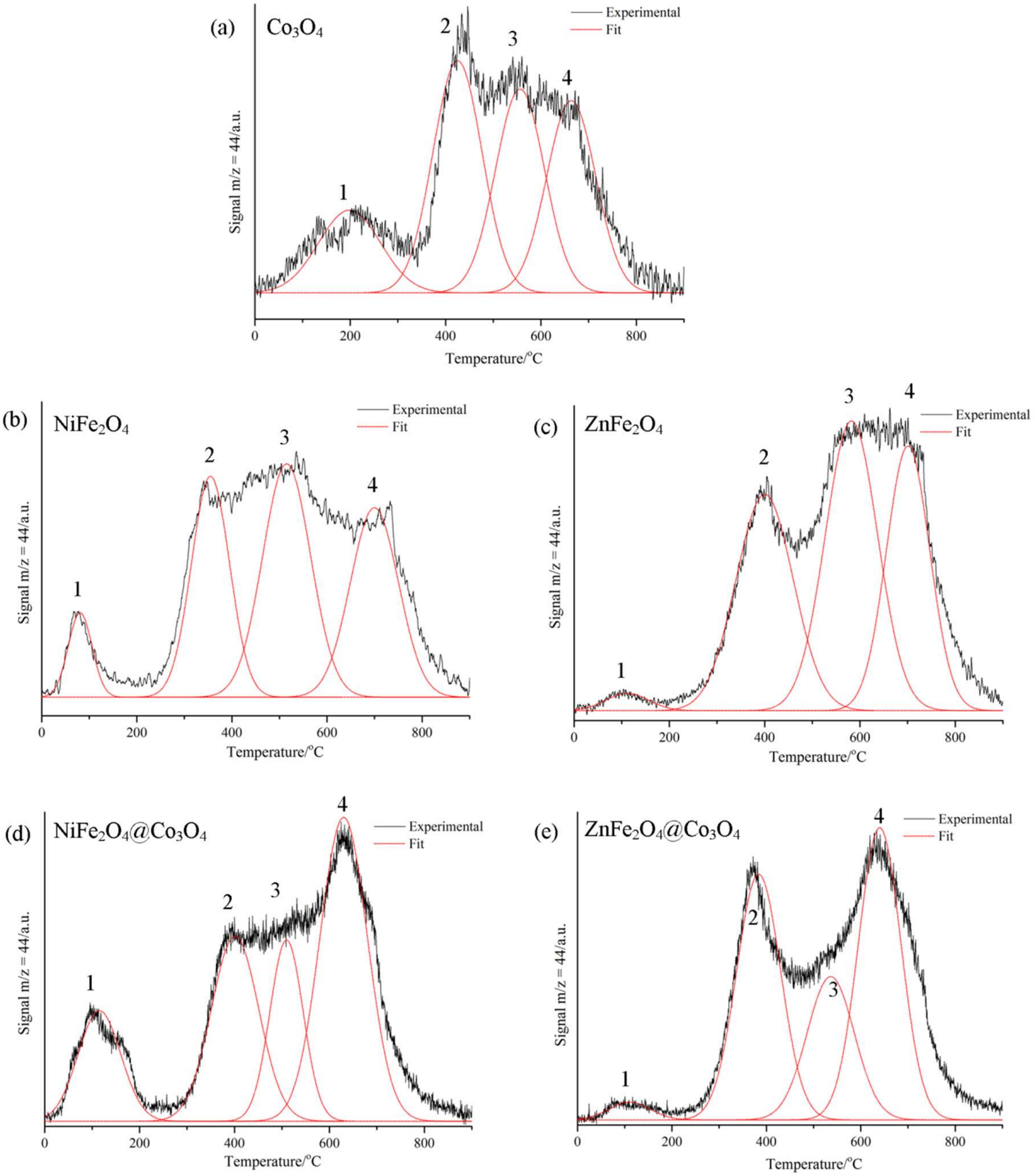

Figure 4.10. CO_2 in the effluent during the CO-TPD over reduced (a) Co_3O_4; (b) $NiFe_2O_4$; (c) $ZnFe_2O_4$; (d) $NiFe_2O_4$@Co_3O_4 and (e) $ZnFe_2O_4$@Co_3O_4 (reduction conditions given in

Table **4.1**).

Table 4.5. Summary of CO and CO_2 desorption temperatures.

Sample	**CO desorption temperature/°C**[§]		**CO_2 desorption temperature/°C**[¥]			
	Peak 1	Peak 2	Peak 1	Peak 2	Peak 3	Peak 4
Co_3O_4	None		199	425	556	664
$NiFe_2O_4$	None		81	355	515	700
$NiFe_2O_4@Co_3O_4$	409	640	115	388	510	630
$ZnFe_2O_4$	None		112	400	582	701
$ZnFe_2O_4@Co_3O_4$	390	679	110	384	536	640

[§] Error = 15 °C (at a 95 % confidence)

[¥] Error = 5 °C (at a 95 % confidence)

4.3.1 Fischer-Tropsch synthesis

The catalytic activity of the different nanoparticles was determined in a fixed bed reactor operating at 230 °C and 20 bar using the space velocity indicated in Table 4.6 after reduction of these materials (activation conditions is given in

Table 4.1). The CO conversion was below 6% for all materials tested.

Table 4.6. Activity and selectivity in the Fischer-Tropsch synthesis over the reduced materials (activation conditions given in

Table **4.1**; $T_{reaction}$ = 230°C, p = 20 bar, CO conversion = 4 ± 2%).

Sample	**Syngas SV**[a]**/ $ml_n\ g^{-1}\ hr^{-1}$**	**S_{CO2}**[b]**/ %**	**r_{FT}**[c]**/ $10^{-5}\ mol_{CO}\cdot g_{Co}^{-1}\cdot s^{-1}$**	**Fraction in organic product/C-%**		
				C_1	**$C_2 – C_4$**	**C_{5+}**
$NiFe_2O_4$	7286	5	n.d.	24	24	52
$NiFe_2O_4@Co_3O_4$	7755	4	1.36	29	24	47
$ZnFe_2O_4@Co_3O_4$	9583	4	0.42	17	15	68

[a] SV = Space velocity

[b] S_{CO2} refers to the CO_2 selectivity

[c] r_{FT} refers to the integral rate or cobalt-time yield

Reduced $NiFe_2O_4$ was active in the Fischer-Tropsch synthesis (see Table 4.6) with similar methane and $C_2 – C_4$ selectivity of 24 C-% and a C_{5+} selectivity of 52 C-%. The oxygen-back titration showed that some reduction occurred. An *in-situ* XRD study (see above) showed that after activating this material in hydrogen at 230°C, metallic Ni is present and exposure to Fischer-Tropsch conditions resulted in further reduction and carburization, yielding a Fe-Ni alloy ($Fe_{0.625}Ni_{0.375}$) and Fe_2C. The observed performance may be attributed to the presence of the Fe-Ni alloy which have been reported to be active for the Fischer-Tropsch synthesis and selective towards shorter chain hydrocarbons [69, 70]. Fe_xC is reported to be catalytically active for the Fischer-Tropsch synthesis [60, 61, 71].

CO-hydrogenation over $NiFe_2O_4@Co_3O_4$ core-shell nanoparticles was observed however the performance was not as anticipated. This was most likely due to the formation of small cobalt islands (1 – 3 nm) on the ferrite core after activation at 230°C (Figure 4.7). The activity contribution of cobalt is thus expected to be small, since it is well known that the turnover frequencies of cobalt-based Fischer-Tropsch catalysts decreases with decreasing crystallite size for cobalt crystallites smaller than 6 nm [6-8]. However, the cobalt-time-yield over $NiFe_2O_4@Co_3O_4$ (reduced at 230°C) was 13.64 $\mu mol_{CO} \cdot g_{Co}^{-1} \cdot s^{-1}$ and may originate from a combinative effect of the cobalt islands formed after reduction and a partially reduced/carburized nickel ferrite core (*in-situ* XRD of $NiFe_2O_4$ showed the formation of $Fe_{0.625}Ni_{0.375}$ and Fe_2C when exposed to Fischer-Tropsch conditions). The observed selectivity (see Table 4.6) is possibly due to the size of cobalt [6] and the CO-hydrogenation over $Fe_{0.625}Ni_{0.375}$ [69, 70].

$ZnFe_2O_4$ initially showed a rather low conversion and after 33 hours on stream, it was no longer active for the FTS reaction. The H_2-TPR showed that at the activation conditions (250°C, two hours), reduction of the ferrite is unlikely and this was confirmed by the *in-situ* XRD reduction (Table 4.5). However, after exposure to Fischer-Tropsch conditions, some reduction and carburization occurred which resulted in the formation of Fe_2C. The initial conversion observed may thus be attributed to the formed iron carbide [71]. Whilst it is difficult to ascertain the reason for the observed inactivity after a period of time on stream, it has been reported that $ZnFe_2O_4$ can hinder the formation the of iron carbide during the Fischer-Tropsch synthesis [72].

The cobalt-time-yield of the core-shell nanoparticle, $ZnFe_2O_4@Co_3O_4$ after the applied activation conditions is rather low (*ca*. 4.2 $\mu mol_{CO} \cdot g_{Co}^{-1} \cdot s^{-1}$, see Table 4.6). The lower cobalt-time-yield in comparison to $NiFe_2O_4@Co_3O_4$ core-shell nanoparticles can be partially rationalized by the low degree of reduction and active metal surface area. The *in-situ* XRD of the $ZnFe_2O_4$ core (see Table 4.3) showed that Zn-Fe oxides were primarily present under the Fischer-Tropsch synthesis conditions. Thus, the core is speculated to be inactive during the Fischer-Tropsch synthesis with reduced $ZnFe_2O_4@Co_3O_4$ core-shell nanoparticles. The former argument is supported by the inactivity of the $ZnFe_2O_4$ nanoparticles. It may then be that the cobalt, which was shown using *in-situ* TEM to be present as small cobalt islands after reduction, was mainly responsible for the observed performance. Despite the low activity, $ZnFe_2O_4@Co_3O_4$ showed a good selectivity toward C_{5+} (68 C-%). The methane selectivity obtained over $ZnFe_2O_4@Co_3O_4$ was significantly reduced (17 C-%) in comparison to the methane selectivity obtained over reduced $NiFe_2O_4$@Co_3O_4. This strengthens the argument that some methane formed over $NiFe_2O_4$@Co_3O_4 may be formed over $Fe_{0.625}Ni_{0.375}$ in this catalyst rather than primarily over cobalt.

The obtained selectivity towards CO_2 was between 4 and 5% for $NiFe_2O_4$, $NiFe_2O_4$@Co_3O_4 and $ZnFe_2O_4$@Co_3O_4 nanoparticles. Selectivity values, *albeit* higher than in this study, has previously been noted for various ferrite-based materials used for the Fischer-Tropsch synthesis [60, 61, 72]. There are generally three reasons that may account for the presence of CO_2 formed during the Fischer-Tropsch synthesis, *viz*. oxygen removal from the catalytically active phase, carburization of the oxide phase in the catalyst or the water-gas shift reaction with the co-generation of hydrogen [60, 61]. It was noted from the CO-TPD experiments that CO_2 formation may have originated from further reduction of the materials being studied. The similarity in CO_2 selectivity despite the variation in the CO conversion amongst the various materials tested for the Fischer-Tropsch synthesis leads to the speculation that CO_2 formation may largely be due to the further reduction of the metal oxide catalyst by the recombination of surface oxygen with adsorbed carbon monoxide [60, 61].

4.4 Chapter summary

Two core-shell nanoparticle systems, each with a Co_3O_4 shell and a different core material (namely, $NiFe_2O_4$ and $ZnFe_2O_4$), were synthesized, characterized and subjected to catalytic testing for the Fischer-Tropsch synthesis. Both the $NiFe_2O_4$@Co_3O_4 and $ZnFe_2O_4$@Co_3O_4 core-shell nanoparticles were determined to have a variable shell thickness around the core of up to 3 nm. *In-situ* TEM showed that under the applied activation conditions, each core-shell nanoparticle system underwent nanoscale restructuring after reduction at 230°C and 250°C for $NiFe_2O_4$@Co_3O_4 and $ZnFe_2O_4$@Co_3O_4 respectively. This effectively transformed the initial core-shell structure into one with 3 nm sized cobalt islands present on the ferrite surface after activation. Therefore, strain effects on the shell was not considered in the study further. $NiFe_2O_4$@Co_3O_4 and $ZnFe_2O_4$@Co_3O_4, although active for the Fischer-Tropsch synthesis, showed a cobalt-time yield of 13.6 $\mu mol_{CO} \cdot g_{Co}^{-1} \cdot s^{-1}$ and 4.2 $\mu mol_{CO} \cdot g_{Co}^{-1} \cdot s^{-1}$, respectively. A higher C_{5+} selectivity was obtained with $ZnFe_2O_4$@Co_3O_4 core-shell nanoparticles. The difference in performance between the two core-shell systems was partially attributed to the difference in degree of reduction and active metal surface area. The difference in the extent of reduction of each ferrite core identified during the Fischer-Tropsch synthesis may have also contributed to the observed activity and selectivity differences between $NiFe_2O_4$@Co_3O_4 and $ZnFe_2O_4$@Co_3O_4 core-shell nanoparticles. The variances in activity and selectivity observed between $NiFe_2O_4$@Co_3O_4 and $ZnFe_2O_4$@Co_3O_4 core-shell nanoparticles highlight the importance of selecting core materials that are less susceptible to structural modification during reduction and catalysis.

4.5 References

[1] A. Y. Khodakov, W. Chu, P. Fongarland, Advances in the development of novel cobalt Fischer-Tropsch catalysts for the synthesis of long-chain hydrocarbons and clean fuels, Chem. Rev., 107 (2007) 1692-1744.

[2] E. van Steen, M. Claeys, K. P. Möller, D. Nabaho, Comparing a cobalt-based catalyst with iron-based catalysts for the Fischer-Tropsch XTL-process operating at high conversion, Appl. Catal. A: Gen., 549 (2018) 51-59.

[3] Q. Zhang, J. Kang, Y. Wang, Development of novel catalysts for the Fischer-Tropsch synthesis: Tuning the product selectivity, Chem. Cat. Chem., 2 (2010) 1030-1058.

[4] J. P. den Breejen, J. R. A. Sietsma, H. Friedrich, J. H. Bitter, K. P. de Jong, Design of supported cobalt catalysts with maximum activity for the Fischer-Tropsch synthesis, J. Catal., 270 (2010) 146-152.

[5] A. Martinez, G. Prieto, Breaking the dispersion-reducibility dependence in oxide supported cobalt nanoparticles, J. Catal., 245 (2007) 470-476.

[6] G. L. Bezemer, J. H. Bitter, H. P. C. E. Kuipers, H. Oosterbeek, J. E. Holewijn, X. Xu, F. Kapteijn, A. J. van Dillen, K. P. de Jong, Cobalt particle size effects in the Fischer-Tropsch reaction studied with carbon nanofiber supported catalysts, J. Am. Chem. Soc., 128 (2006) 3956-3964.

[7] J. P. den Breejen, P. B. Radstake, G. L. Bezemer, J. H. Bitter, V. Frøseth, A. Holmen, K. P. de Jong, On the origin of the cobalt particle size effects in Fischer-Tropsch catalysis, J. Am. Chem. Soc., 131 (2009) 7197-7203.

[8] N. Fischer, E. van Steen, M. Claeys, Structure sensitivity of the Fischer-Tropsch activity and selectivity on alumina supported catalysts, J. Catal., 299 (2013) 67-80.

[9] A. Govender, W. Barnard, E. J. Olivier, R. P. Forbes, E. van Steen, J. H. Neethling, Synthesis and characterization of $NiFe_2O_4@Co_3O_4$ core-shell nanoparticles, Mater. Charac., 121 (2016) 93-102.

[10] A. U. Nilekar, S. Alayoglu, B. Eichhorn, M. Mavrikakis, Preferential CO oxidation in hydrogen: Reactivity of core-shell nanoparticle, J. Am. Chem. Soc., 132 (2010) 7418-7428.

[11] R. G. Chaudhuri, S. Paria, Core/Shell nanoparticles: classes, properties, synthesis mechanisms, characterization and applications, Chem. Rev., 112 (2012) 2373-2433.

[12] O. S. Alexeev, B. C. Gates, Supported bimetallic cluster catalysts, Ind. Eng. Chem. Res., 42 (2003) 1571-1587.

[13] T. Hirakawa, P. V. Kamat, Charge separation and catalytic activity of Ag@TiO_2 core-shell composite clusters under UV-irradiation, J. Am. Chem. Soc., 127 (2005) 3928-3924.

[14] X. Duan, G. Qian, X. Zhou, D. Chen, W. Yuan, MCM-41 supported Co-Mo bimetallic catalysts for enhanced hydrogen production by ammonia decomposition, Chem. Eng. J., 207-208 (2012) 103-108.

[15] K. A. Kuttiyiel, K. Sasaki, Y. Choi, D. Su, P. Liu, R. R. Adzic, Nitride stabilized PtNi core-shell nanocatalyst for high oxygen reduction acitivity, Nano Lett., 12 (2012) 6266-6271.

[16] P. Strasser, S. Koh, T. Anniyev, J. Greeley, K. More, C. Yu, Z. Liu, S. Kaya, D. Nordlund, H. Ogasawara, M. F. Toney, A. Nilsson, Lattice-strain control of the activity in dealloyed core-shell fuel cell catalysts, Nat. Chem., 2 (2010) 454-460.

[17] Y. Wang, N. Toshima, Preparation of Pd-Pt bimetallic colloids with controllable core/shell structures, J. Phys. Chem. B, 101 (1997) 5301.

[18] L. Bu, N. Zhang, S. Guo, X. Zhang, J. Li, J. Yao, T. Wu, G. Lu, J.-Y. Ma, D. Su, X. Huang, Biaxially strained PtPb/Pt core/shell nanoplate boosts oxygen reduction catalysis, Science, 354 (2016) 1410-1414.

[19] S.-K. Wu, R.-J. Lin, S. Jang, H.-L. Chen, S.-M. Wang, F.-Y. Li, Theoretical investigation of the mechanism of the water-gas shift reaction on cobalt@gold core-shell nanocluster, J. Phys. Chem. C, 118 (2014) 298-309.

[20] D. Wang, H. L. Xin, H. Wang, Y. Yu, E. Rus, D. A. Muller, F. J. DiSalvo, H. D. Abruna, Facile synthesis of carbon-supported Pd-Co core-shell nanoparticles as oxygen reduction electrocatalysts and their enhanced activity and stability with monolayer Pt decoration, Chem. Mater., 24 (2012) 2274-2281.

[21] M. Heemeier, A. F. Carlsson, M. Naschitzki, M. Schmal, M. Baumer, H.-J. Freund, Preparation and characterization of a model bimetallic catalyst: Co-Pd nanoparticles supported on Al_2O_3, Angew. Chem. Int. Ed., 41 (2002) 4073-4076.

[22] H. Qin, S. Kang, Y. Wang, H. Liu, Z. Ni, Y. Huang, Y. Li, X. Li, Lignin-based fabrication of Co@C core-shell nanoparticles as efficient catalyst for selective Fischer-Tropsch synthesis of C_{5+} compounds, ACS Sustainable Chem. Eng., 4 (2016) 1240-1247.

[23] C.-J. Zhong, M. M. Maye, Core-Shell assembled nanoparticles as catalysts, Adv. Mater., 13 (2001) 1507-1511.

[24] G. Li, Z. Tang, Noble metal nanoparticle@metal oxide core/yolk-shell nanostructures as catalysts: recent ptogress and perspective, Nanoscale, 6 (2014) 3995-4011.

[25] M. B. Gawande, A. Goswami, T. Asefa, H. Guo, A. V. Biradar, D.-L. Peng, R. Zboril, R. S. Varma, Core-shell nanoparticles: Synthesis and applications in catalysis and electrocatalysis, Chem. Soc. Rev., 44 (2015) 7540-7590.

[26] C. S. Bonifacio, S. Carenco, C. H. Wu, S. D. House, H. Bluhm, J. C. Yang, Thermal stability of core-shell nanoparticles: A combined in situ study by XPS and TEM, Chem. Mater., 27 (2015) 6960-6968.

[27] F. Calvo, Thermodynamics of nanoalloys, Phys. Chem. Chem. Phys., 17 (2015) 27922-27939.

[28] F. F. Tao, M. Salmeron, In situ studies of chemistry and structure of materials in reactive environments, Science, 331 (2011) 171-174.

[29] H. Liao, A. Fisher, Z. J. Xu, Surface segregation in bimetallic nanoparticles: A critical issue in electrocatalyst engineering, Small, 11 (2015) 3221-3246.

[30] T. Wen, K. M. Krishnan, Thermal stability and morphological transformations of Au_{core}-Co_{shell} nanocrucibles, J. Phys. Chem. C, 114 (2010) 14838-14842.

[31] V. R. Calderone, N. R. Shiju, D. Curulla-Ferre, S. Chambrey, A. Y. Khodakov, A. Rose, J. Thiessen, A. Jess, G. Rothenberg, De novo design of nanostructured iron-cobalt Fischer-Tropsch catalysts, Angew. Chem. Int. Ed., 52 (2013) 4397-4401.

[32] L. Shi, K. Tao, T. Kawabata, T. Shimamura, X. J. Zhang, N. Tsubaki, Surface impregnation combustion method to prepare nanostructured metallic catalysts without further reduction: As-burnt Co/SiO_2 catalysts for Fischer-Tropsch synthesis, ACS Catal., 1 (2011) 1225-1233.

[33] L. Shi, C. Zeng, Q. Lin, P. Lu, W. Niu, N. Tsubaki, Citric acid assisted one-step synthesis of highly dispersed metallic Co/SiO_2 without further reduction: As-prepared Co/SiO_2 catalysts for Fischer-Tropsch synthesis, Catal. Today, 228 (2014) 206-211.

[34] R. Phienluphon, L. Shi, J. Sun, W. Niu, P. Lu, P. Zhu, T. Vitidsant, Y. Yoneyama, Q. Chen, N. Tsubaki, Ruthenium promoted cobalt catalysts prepared by an autocombustion method directly used for Fischer-Tropsch synthesis without further reduction, Catal. Sci. Technol., 4 (2014) 3099-3107.

[35] Y. Jiang, S. Yang, Z. Hua, H. Huang, Sol-gel autocombustion synthesis of metals and metal alloys, Angew. Chem. Int. Ed., 48 (2009) 1-4.

[36] Y. Yao, Z. Yang, H. Sun, S. Wang, Hydrothermal synthesis of Co_3O_4-graphene for heterogeneous activation of peroxymonosulfate for decomposition of phenol, Ind. Eng. Chem. Res., 51 (2012) 14598-14965.

[37] B. D. Hostermann, Raman Spectroscopic Study of Solid Solution Spinel Oxides, University of Nevada, Las Vegas, PhD, 2011.

[38] Z. Z. Lazarevîc, C. Jovalekic, A. Milutinovic, M. J. Romcevic, N. Z. Romcevic, Preparation and characterization of nano ferrites, Acta. Phys. Pol. A, 121 (2012) 682.

[39] G. Ercolino, P. Stelmachowski, A. Kotarba, S. Specchia, Reactivity of mixed iron-cobalt spinels in the lean methane combustion, Top. Catal., doi:10.1007/s11244-017-0826-9 (2017) 1-10.

[40] N. Bahlawane, P. H. T. Ngamou, V. Vannier, T. Kottke, J. Heberle, K. Kohse-Höinghaus, Tailoring the properties and the reactivity of the spinel cobalt oxide, Phys. Chem. Chem. Phys., 11 (2009) 9224-9232.

[41] I. Lorite, J. J. Romero, J. F. Fernández, Effects of the agglomeration state on the Raman properties of Co_3O_4 nanoparticles, J. Raman Spectrosc., 43 (2012) 1443-1448.

[42] T. J. Chuang, C. R. Brundle, D. W. Rice, Interpretation of the x-ray photoemission spectra of cobalt oxides and cobalt oxide surfaces, Surf. Sci., 59 (1976) 413-429.

[43] M. I. Lukasiewicz, A. Wójcik-GIodowska, E. Guziewicz, A. Wolska, M. T. Klepka, P. DIuzewski, R. JakiIa, E. Lusakowska, K. Kopalko, W. Paszkowicz, ZnO, ZnMnO and ZnCoO films grown by atomic layer deposition, Semicond. Sci. Technol., 27 (2012) 074009-074023.

[44] R. Ba, Y. Zhao, L. Yu, J. Song, S. Huang, L. Zhong, Y. Sun, Y. Zhu, Synthesis of Co-based bimetallic nanocrystals with one-dimensional structure for selective control on syngas conversion, Nanoscale, 7 (2015) 12365-12371.

[45] M. Hoppe, S. Döring, M. Gorgoi, S. Cramm, M. Müller, Enhanced ferrimagnetism in auxetic $NiFe_2O_4$ in the cross over to the ultrathin-film limit, Phys. Rev. B, 91 (2015) 054418.

[46] O. Kuschel, Buß, W. Spiess, T. Schemme, J. Wöllermann, K. Balinski, A. T. N'Diaye, T. Kuschel, J. Wollschläger, K. Kuepper, From Fe_3O_4/NiO bilayers to $NiFe_2O_4$-like thin films through Ni interdiffusion, Phys. Rev. B, 94 (2016) 094423.

[47] Y. Li, Z. Zhao, A. Duan, G. Jiang, J. Liu, Comparative study on the formation and reduction of bulk and Al_2O_3-supported cobalt oxides by H_2 TPR technique, J. Phys. Chem. C, 113 (2009) 7186-7199.

[48] E. van Steen, G. S. Sewell, R. A. Makhote, C. Micklethwaite, H. Manstein, M. de Lange, C. T. O'Conner, TPR study on the preparation of impregnated Co/SiO_2 catalysts, J. Catal., 162 (1996) 220-230.

[49] S. Rane, Ø. Borg, J. Yag, E. Rytter, A. Holmen, Effect of alumina phases on hydrocarbon selectivity in Fischer-Tropsch synthesis, Appl. Catal. A: Gen., 388 (2010) 160-167.

[50] A. P. Petersen, R. P. Forbes, S. Govender, P. J. Kooyman, E. van Steen, Effect of alumina modification on the reducibility of Co_3O_4 crystallites studied on inverse-model catalysts, Catal. Lett., 148 (2018) 1215-1227.

[51] D. Nabaho, J. W. Niemantsverdiet, M. Claeys, E. van Steen, Hydrogen spillover in the Fischer-Tropsch synthesis: An analysis of gold as a promoter for cobalt-alumina catalysts, Catal. Today, 275 (2016) 27-34.

[52] H.-C. Shin, S.-C. Choi, Mechanism of M ferrites (M = Cu and Ni) in the CO_2 decomposition reaction, Chem. Mater., 13 (2001) 1238-1242.

[53] Y. Zhang, W. Wei, X. Yang, F. Wei, Reduction of Fe and Ni in Fe-Ni-O systems, J. Min. Metall. Sect. B-Metall., 49 (2013) 13-20.

[54] K. S. Abdel-Halim, M. Bahgat, O. A. Fouad, Thermal synthesis of nanocrystalline fcc Fe-Ni alloy by gaseous reduction of coprecipitated $NiFe_2O_4$ from secondary resources, Mater. Sci. Technol., 22 (2006) 1396-1400.

[55] D. Yu, M. Zhu, T. A. Utigard, M. Barati, TGA kinetic study on the hydrogen reduction of an iron nickel oxide, Min. Eng., 54 (2013) 32.

[56] H. Lin, Y.-W. Chen, The mechanism of reduction of cobalt by hydrogen, Mater. Chem. Phys., 85 (2004) 171-175.

[57] E. Junca, J. R. de Oliveira, T. A. G. Restivo, D. C. R. Espinosa, J. A. S. Tenório, Synthetic zinc ferrite reduction by means of mixtures containing hydrogen and carbon monoxide, J. Thern. Ananl. Calorim., 123 (2016) 631-641.

[58] A. M. Saib, D. J. Moodley, I. M. Ciobica, M. M. Hauman, B. H. Sigwebela, C. J. Westrate, J. W. Niemantsverdriet, J. van de Loosdrecht, Fundamental understanding of deactivation and regeneration of cobalt Fischer-Tropsch synthesis catalysts, Catal. Today, 154 (2010) 271-282.

[59] H. Karaca, O. V. Safonova, S. Chambrey, P. Fongarland, P. Roussel, A. Griboval-Constant, M. Lacroix, A. Y. Khodakov, Structure and catalytic performance of Pt-promoted alumina-supported cobalt catalysts under realistic conditions of Fischer-Tropsch synthesis, J. Catal., 277 (2011) 14-26.

[60] Z. H. Chonco, L. Lodya, M. Claeys, E. van Steen, Copper ferrites: A model for investigating the role of copper in the dynamic iron-based Fischer-Tropsch catalyst, J. Catal., 308 (2013) 363-373.

[61] Z. H. Chonco, A. Ferreira, L. Lodya, M. Claeys, E. van Steen, Comparing silver and copper as promoters in Fe-based Fischer-Tropsch catalysts using delafossite as a model compound, J. Catal., 307 (2013) 283-294.

[62] J. Lahtinen, J. Vaari, A. Talo, A. Vehanen, P. Hautojärvi, Adsorption and desorption measurements of CO and O_2 on cobalt, Vacuum, 41 (1990) 112-114.

[63] J. Lahtinen, J. Vaari, K. Kauraala, Adsorption and structure dependent desorption of CO on Co(0001), Surf. Sci., 418 (1998) 502-510.

[64] B. Viswanathan, R. Gopalakrishnan, R. Vetrivel, Temperature Programmed Desorption (TPD) of carbon monoxide from cobalt surfaces, React. Kinet. Catal. Lett., 18 (1981) 209-212.

[65] E. van Steen, E. L. Viljoen, J. van de Loosdrecht, M. Claeys, Evaluation of molydenum-modified alumina support materials for Co-based Fischer-Tropsch catalysts, Appl. Catal. A: Gen., 335 (2008) 56-63.

[66] R. Gopalakrishnan, B. Viswanathan, Temperature-Programmed desorption and Infrared studies on the activation of carbon monoxide on cobalt surfaces, J. Colloid Interface Sci., 102 (1984) 370-372.

[67] E. Rytter, T. H. Skagseth, S. Eri, A. O. Sjåstad, Cobalt Fischer-Tropsch catalysts using nickel promoter as a rhenium substitute to suppress deactivation, Ind. Eng. Chem. Res., 49 (2010) 4140-4148.

[68] M. Sarkari, F. Fazlollahi, A. Razmjooic, A. A. Mirzaei, Fischer-Tropsch synthesis on alumina supported iron-nickel catalysts: Effect of preparation methods, Chem. Biochem. Eng. Q, 25 (2011) 289-297.

[69] J. van de Loosdrecht, A. J. van Dillen, A. A. van der Horst, A. M. van der Kraan, J. W. Geus, Nickel-iron catalysts prepared by homogeneous deposition-precipitation of cyanide complexes on a titania support, Top. Catal., 2 (1995) 29-43.

[70] T. Li, H. Wang, Y. Yang, H. Xiang, Y. Li, Study on an iron-nickel bimetallic Fischer-Tropsch synthesis catalyst, Fuel Process. Technol., 118 (2014) 117-124.

[71] E. de Smit, B. M. Weckhuysen, The renaissance of iron-based Fischer-Tropsch synthesis: on the multifaceted catalyst deactivation behaviour, Chem. Soc. Rev., 37 (2008) 2758-2781.

[72] M. K. Gnanamani, H. H. Hamdeh, G. Jacobs, D. Qian, F. Liu, S. D. Hopps, G. A. Thomas, W. D. Shafer, Q. Xiao, Y. Hu, B. H. Davis, Fischer-Tropsch synthesis: effect of Cu, Mn and Zn addition on the activity and product selectivity of cobalt ferrite, RSC Adv., 6 (2016) 62356-62367.

5 The influence of mild reduction conditions on the structure and Fischer-Tropsch synthesis performance of reduced $NiFe_2O_4@Co_3O_4$ core-shell nanoparticles

---

Mild reduction conditions of 180°C (1 hour) was used to activate $NiFe_2O_4@Co_3O_4$ *core-shell nanoparticles prior to characterization and the Fischer-Tropsch synthesis. It was found that this moderate reduction treatment resulted in the retention of the core-shell structure after activation and under Fischer-Tropsch synthesis conditions. Therefore, a real core-shell structure was present during the Fischer-Tropsch synthesis and resulted in a cobalt-time yield of 8.40* $\mu mol_{CO} \cdot g_{Co}^{-1} \cdot s^{-1}$ *and a* C_{5+} *selectivity of 38 C-%. This result suggested that the presence of strain on the surface of the cobalt shell in* $NiFe_2O_4@Co_3O_4$ *core-shell nanoparticles reduced at 180 °C (1 hour) was influencing the catalytic performance. The Fischer-Tropsch synthesis activity over* $NiFe_2O_4@Co_3O_4$ *core-shell nanoparticles reduced at 180 °C (1 hour) was similar to unsupported* Co_3O_4 *(although the* C_{5+} *selectivity was higher (81 C-%) with unsupported* Co_3O_4*) and inferior to the activity of* $NiFe_2O_4@Co_3O_4$ *core-shell nanoparticles reduced at 230°C for 2 hours (13.6* $\mu mol_{CO} \cdot g_{Co}^{-1} \cdot s^{-1}$ *and* C_{5+} *selectivity of 47 C-%). The difference in activity and selectivity was attributed to the nanoscale structural and compositional differences induced by the different reduction conditions applied.*

5.1 Introduction

The Fischer-Tropsch synthesis (FTS), developed by Franz Fischer and Hans Tropsch, can be used for the conversion of natural gas, coal or biomass into a wide range of valuable hydrocarbon products [1]. Waxes and diesel can be obtained from the low temperature Fischer-Tropsch synthesis, for which, cobalt-based catalysts are preferred [2-4]. This is because a higher activity, hydrocarbon productivity and good stability can be obtained with these catalysts [5-8]. However, the high cost of cobalt requires that minimal cobalt is used whilst maintaining sufficient active metal surface area [4].

Core-shell nanoparticles are comprised of two or more metals or metal oxides and are made up of an inner layer material (core) and an outer layer material (shell).[9-11] The architecture of the core-shell nanoparticles is specifically designed to tune the activity of the metal shell through interactions with the core material [12]. As a result, these nanoparticles have been the subject of research interest in recent years owing to their unique properties and potential for more flexible design to achieve the desired functionality [9-11, 13-15]. Core-shell nanoparticles have been shown to be efficient catalysts for various reactions with a performance different to that observed over a monometallic catalyst/s and/or alloy comprised of the same metals [9-11, 14]. Such nanoparticles were also shown to be promising catalysts for the Fischer-Tropsch synthesis however the active cobalt metal was present as a core surrounded by either a metal oxide or metallic species shell [16-19]. Core-shell nanoparticles with a cobalt (II, III) oxide (Co_3O_4) shell around a core composed of a different metal oxide have also been used in the Fischer-Tropsch synthesis [20]. The advantage of the former core-shell nanoparticle system is that a reduced amount of expensive cobalt can be used. This morphology may result in a cheaper nanoparticle catalyst than one comprised of Co_3O_4 only.

In chapter 4, the synthesis and characterization of $NiFe_2O_4$@Co_3O_4 core-shell nanoparticles was reported (if needed, see [21]). The overall size and shell thickness observed for these nanoparticles translated into approximately 82% of the crystallite having been replaced by a material cheaper than cobalt. Apart from the savings that could be realized, $NiFe_2O_4$@Co_3O_4 core-shell nanoparticles were also found to be active for the Fischer-Tropsch synthesis. The observed performance though, was influenced by the restructuring of the cobalt shell after reduction at 230°C for 2 hours which effectively destroyed the core-shell structure. It was further observed that some reduction of the Co_3O_4 shell may occur at temperatures far below 230°C. Under reactive conditions, the morphology of nanoparticles are dynamic (thermally driven) and therefore the nanoscale structure and composition may change from the as-synthesized form as a function of the temperature and gaseous environments to which it is exposed [22-28]. Atomistic simulations showed that Pd@Pt and Pt@Pd core-shell structures underwent thermally driven structural evolutions [27]. Tao *et al.*[29] reported compositional and structural changes of Rh_xPd_{1-x} alloy catalysts supported on a silicon wafer upon exposure to different reactive environments. Structural changes of Co-

Pt and Co-Au core-shell nanoparticles and Ni-Co core-shell nanoparticles under heating were also noted by Wen *et al.*[28] and Bonifacio *et al.*[30] respectively. Carenco *et al.*[31] reported that the structure and composition of core-shell CuCo nanoparticles had changed after exposure to different gaseous environments. This may alter the physico-chemical properties and in particular the reactivity of the shell [14]. It was thus speculated that the restructuring of $NiFe_2O_4$@Co_3O_4 core-shell nanoparticles, observed after reduction at 230°C, may be minimized by utilizing a lower reduction temperature. Therefore, this work examined the effect of milder reduction conditions (180°C, 1 hour) on the structure, physico-chemical properties and Fischer-Tropsch synthesis performance of $NiFe_2O_4$@Co_3O_4 core-shell nanoparticles. Furthermore, the structure and composition of these nanoparticles, after exposure to Fischer-Tropsch synthesis conditions, was examined. A comparison was also made to previously reported data for $NiFe_2O_4$@Co_3O_4 core-shell nanoparticles reduced at 230°C for 2 hours.

5.2 Experimental

5.2.1 Synthesis of $NiFe_2O_4$@Co_3O_4

A detailed description of the synthesis of the core-shell nanoparticles is given elsewhere [21]. Briefly, a two-step synthesis was followed. In step 1, an aqueous solution (10 mL) of ammonium carbonate, $(NH_4)_2CO_3$ (8.50*M*) was mixed with 25 wt.% ammonia aqueous solution (3.6 mL). Cobalt carbonate, $CoCO_3$, was added to obtain a cobalt concentration of 0.05*M* and a pH of 11.5 was obtained. The resulting cobalt containing suspension was then stirred at 45°C for 2 hours. After this time, the solution was filtered by gravity. This filtrate was added to a round bottom flask and ~ 0.05 g/mL of $NiFe_2O_4$ was added; the suspension was stirred at 85°C for six hours. The temperature was then increased to 95°C and kept there for another 24 hours under stirring. The solvent was subsequently removed under vacuum and the dried solid was rinsed with deionized water and again dried under vacuum. The solid obtained was oven-dried at 110°C for 12 hours. In step 2, the cobalt precursor solution was made as per step 1; however, the suspension was added to the dried solid from step 1. The synthesis then followed the process outlined above.

5.2.2 Synthesis of Co_3O_4

Analytical grade cobalt nitrate hexahydrate ($Co(NO_3)_2.6H_2O$) and citric acid ($C_6H_8O_7$) were obtained from Sigma Aldrich. In a typical synthesis, a solution of $Co(NO_3)_2.6H_2O$ (2*M*) and a solution of citric acid (2.5*M*) was prepared. The cobalt nitrate containing solution was added to the citric acid containing solution in a water bath maintained at 30°C. The metal nitrate-citric acid solution was stirred for 95 minutes before the temperature was increased to 60°C. The metal nitrate-citric acid solution was kept at this temperature for 2 hours under stirring. After this time, a gel formed. The formed gel was placed in a porcelain dish and oven-dried at 110°C for 24 hours. The as-formed resin was subsequently calcined in a muffle furnace at 350°C for 5 hours.

5.2.3 Characterization

The *in-situ* X-ray diffraction (XRD) measurements were performed in an Anton Paar XRK900 coupled to the Panalytical X'Pert Pro multi-purpose diffractometer. The *in-situ* XRD experiments were performed under a hydrogen flow (50 ml/min) and the sample was heated from room temperature to 180 °C or 230°C (see Table 5.1) using a heating rate of 5°C/min. Diffraction patterns were collected at intervals of 20°C. After the reduction, the reactor was flushed with helium for 2 hours and cooled to 40°C. Then, the temperature was increased to 230°C under synthesis gas ($H_2/CO = 2$, 50 ml/min). At this temperature, the pressure was increased to 16 bar over a 5 hour period. The reaction was maintained under these conditions for 16 hours and a diffractogram was collected in 20 minute intervals. At the end of the experiment, the system was de-pressurized, flushed with helium and cooled to 40°C. The catalyst was subsequently passivated in a mixture of helium (50 ml/min) and oxygen for 3 hours (O_2 flow rate was initially 2 ml/min and gradually increased to 6 ml/min). The catalyst was unloaded into dry ice and referred to as the used catalyst.

Prior to the Transmission Electron Microscopy (TEM) analysis, the crushed sample was dispersed in ethanol using an ultrasonication after which a small amount was transferred onto a holey carbon copper TEM grid (SPI Supplies, 300 mesh). A double aberration corrected JEOL ARM 200F transmission electron microscope operating at 200 kV was used for the characterization of the used nanoparticles. High angle annular dark field (HAADF) scanning transmission electron microscopy (STEM) as well as bright field (BF) STEM imaging at atomic resolution was used. Electron energy loss spectroscopy (EELS) Spectrum Imaging (SI) was performed using the DualEELS^{TM} mode on the Gatan GIF Quantum ERS^{TM} spectrometer. This allows for the pixel by pixel acquisition of both the intense zero loss peak (ZLP) and the elemental edges during the same scan. A convergence semi-angle of 21.4 mrad was used for the STEM probe and the collection semi-angle of the spectrometer was 54.3 mrad at a camera length of 1 cm. The shell thickness and crystallite size were measured from the composite elemental maps generated from the EELS spectrum images and STEM-HAADF images, respectively, using Gatan Microscopy Suite® (GMS) 3.

The *in-situ* TEM analysis was carried out on a FEI Titan G2 80 – 200 (S)TEM ChemiStem™ instrument operating at 200 kV at the University of Manchester. The instrument was equipped with Gatan GIF Quantum ERS^{TM} spectrometer. STEM-HAADF images were recorded using FEI TIA software whilst EELS spectrum images were recorded using Gatan Digital Micrograph software. The gaseous e-Cell system used in the FEI Titan instrument was a Protochips Atmosphere holder with a customized low penumbra geometry beryllium lid. The e-Cell MEMS chips used to create the operating environment were a pair of 300 µm thick Si wafers, each with a lithographically fabricated 3000 x 300 µm electron transparent SiN_x window. The top chip allows heating and has a window thickness of 30 nm while the bottom window is 50 nm thick. Spacers deposited onto the chips created a nominal vertical separation between the windows of ~ 5 µm. During the measurements, the e-Cell was completely filled with pure hydrogen at a nominal pressure of 1 bar. The temperature was controlled by on-chip pre-calibrated heater elements controlled by an external computer system. The samples were crushed in ethanol and then a drop was placed onto the atmosphere side of the electron entrance of plasma cleaned SiN_x windows and allowed to dry in a clean ambient temperature petri dish. The prepared e-Cell was sealed as per manufacturers specifications and specimens were allowed to stabilize at room temperature in the documented gaseous media prior to all measurements. Thereafter, the sample was heated to the desired temperature and allowed to remain there for one hour at a time before imaging and EELS was done. In order to ensure that electron beam artefacts were not influencing the results, images of selected regions of interest were acquired before and after thermal treatments. Additionally, after thermal treatments, different sample areas which were not analyzed previously were also measured to ensure that the results presented herein are representative and reproducible.

The metal dispersion and the active metal surface area were determined using Temperature Programmed Desorption of hydrogen (H_2-TPD), which were performed on a AutoChem 2920 (Micrometrics, USA) equipped with a Thermal Conductivity Detector (TCD). Before each measurement, the samples were dried at 120°C for 1 hour and subsequently reduced in pure hydrogen using the activation conditions listed in Table 5.1 (heating rate of 5°C/min). Thereafter, the samples were flushed under argon flow (50 ml/min) for 1 hour. H_2 was adsorbed at 100°C using pulse chemisorption in 10 pulses with a 2 minute interval. The calculation for obtaining the dispersion and active metal surface area is given in Appendix B.

The degree of reduction was determined using oxygen (O_2) back titration on a Micromeritics ASAP 2020 Unit (Micromeritics, USA). Accordingly, a pre-weighed catalyst sample of about 200 mg was degassed at 120°C for two hours. After cooling to ambient temperature and exposing the sample to He, the sample was reduced in pure H_2 (50 ml/min) at the activation conditions given in Table 5.1 using a heating rate of 5°C/min. Subsequently, the sample was cooled down to 200°C and evacuated for 4 hours. Then, the temperature was increased to the activation temperature (Table 5.1) and O_2 titration was carried out. The degree of reduction was then determined from the O_2 uptake using the formula given in Appendix B.

The catalytic evaluations were conducted in a fixed bed reactor set-up containing four independent parallel reactor tubes each with inner diameter 6.5 mm. The catalysts (200 mg) were diluted with 3.1 g SiC (320 grit) which resulted in a catalyst bed length of ~ 6 cm. The catalyst bed temperature was accurately controlled by means of a thermocouple in the middle of the bed. The catalysts were activated *in-situ* in hydrogen prior to the Fischer-Tropsch synthesis (conditions given in Table 5.1). After reduction, the temperature was changed to 200°C and the pressure increased to 20 bar using hydrogen and argon. Synthesis gas ($H_2/CO = 2$) was then introduced and the temperature was increased to 230°C (ramp rate 0.5°C/min). The space velocity during the reaction was varied to achieve a CO conversion of 3 ± 1%. The reaction effluent was passed through a hot trap (190°C) to collect the high boiling waxes and a cold trap (15°C) to collect the water and low boiling organics product compounds. The outlet gases were analyzed on-line using an Agilent 7890A Refinery Gas Analyzer equipped with one Flame Ionization Detector (FID) and two TCD channels. Argon (~ 8 vol. %) was added to the feed and used as internal standard to determine conversion and product selectivity. The selectivity values are reported in C-% from syngas converted to hydrocarbons (i.e. excluding CO to CO_2 conversion).

Table 5.1. Conditions for the activation of the carious catalysts in hydrogen prior to the Fischer-Tropsch synthesis (Space velocity = 6000 $ml_n \cdot g^{-1} \cdot hr^{-1}$).

Sample	**$T_{reduction}$ /°C**	**$t_{reduction}$ /hours**
$NiFe_2O_4@Co_3O_4$	180	1
$NiFe_2O_4@Co_3O_4$	230	2
Co_3O_4	300	1

5.3 Results and discussion

The influence of mild reduction conditions (180°C) on the structure of the $NiFe_2O_4@Co_3O_4$ core-shell nanoparticles was investigated using *in-situ* TEM. As the reduction progressed, the morphology of the core-shell nanoparticles at different sites of interest was monitored using STEM-HAADF and/or EELS spectrum imaging. Low magnification STEM-HAADF images of one site of interest in $NiFe_2O_4@Co_3O_4$ nanoparticles while heating in 1 atm H_2 for 1 and 2 hours are shown in Figure 5.1. These images showed that the morphology of the crystallites appeared similar after each hold time. Hence, EELS spectrum imaging was only done after a two hour hold time. An additional observation of a different site of interest (Figure 5.2) showed that the morphology of the nanoparticles, post reduction at 180°C, compared to the morphology prior to the reduction, appears similar. The respective EELS spectrum image showed in both cases cobalt was present around the nickel ferrite core. This indicates that the core-shell structure remained intact after reduction at 180°C in H_2 at 1 atm.

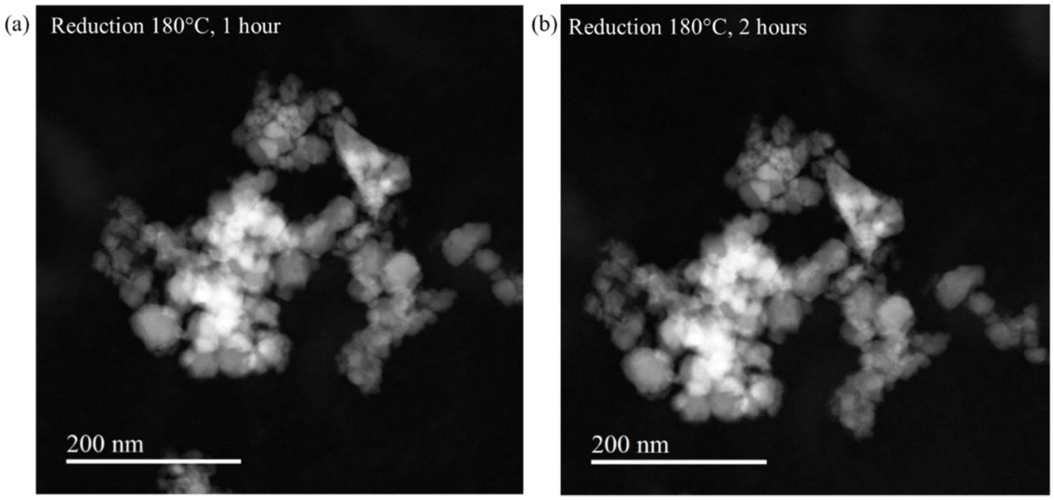

Figure 5.1. Low magnification STEM-HAADF image of $NiFe_2O_4@Co_3O_4$ core-shell nanoparticles obtained after heating in 1 atm pure H_2 at 180 °C for (a) 1 hour and (b) 2 hours.

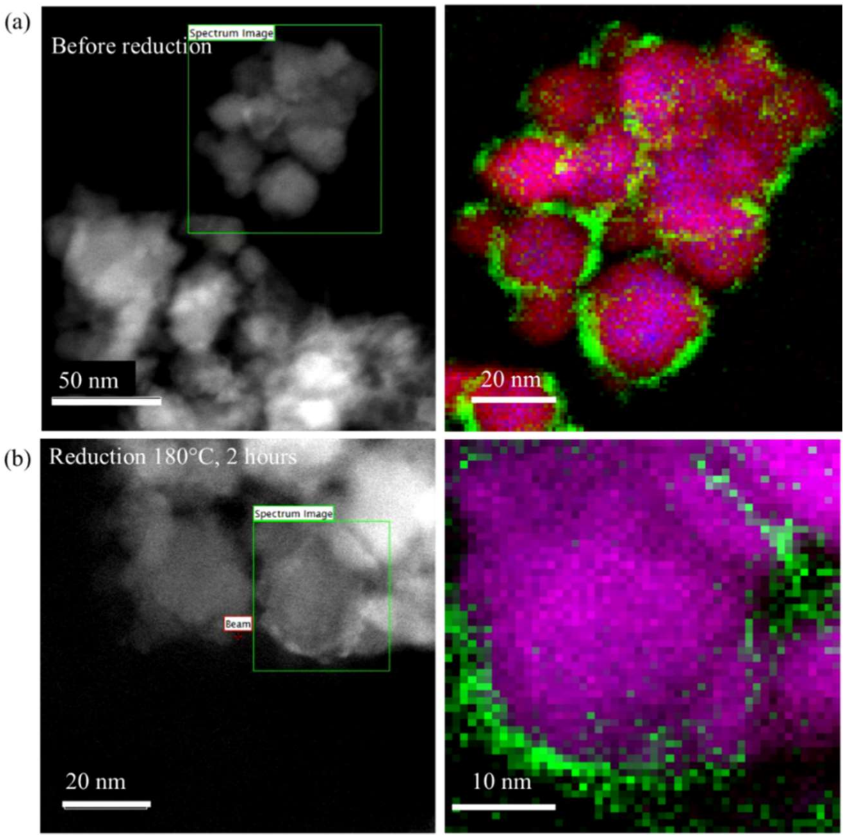

Figure 5.2. STEM-HAADF images of $NiFe_2O_4@Co_3O_4$ core-shell nanoparticles obtained (a) prior to reduction and during the *in-situ* TEM reduction at (b) 180 °C, in H_2 (1 atm) for 2 hours; corresponding composite elemental map obtained from EELS spectrum images is also shown.

The TEM derived shell thickness was expressed in terms of a shell thickness distribution and the histogram for $NiFe_2O_4@Co_3O_4$ core-shell nanoparticles prior to reduction and after reduction at 180°C (Figure B.3 (a) and (b) respectively in Appendix B) showed a lognormal distribution. The cumulative distribution function of the shell thickness (Figure 5.3) showed a minor shift in the shell thickness, particularly at a thickness below 2.3 nm. The average shell thickness, though, for $NiFe_2O_4@Co_3O_4$ core-shell nanoparticles prior to reduction was 2.5 nm and 2.6 nm for $NiFe_2O_4@Co_3O_4$ core-shell nanoparticles reduced at 180°C.

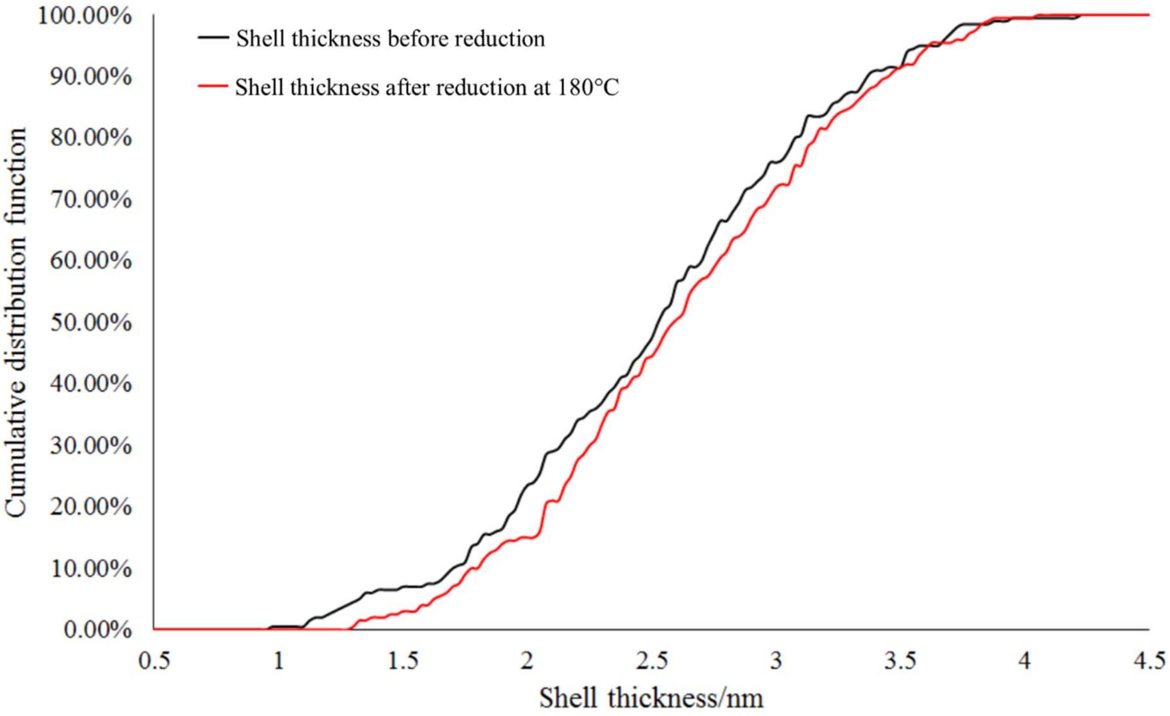

Figure 5.3. Cumulative distribution functions showing the shell thickness distribution of $NiFe_2O_4@Co_3O_4$ core-shell nanoparticles obtained prior to reduction and during the *in-situ* TEM reduction at 180 °C, in H_2 (1 atm) for 2 hours.

In order to ascertain whether the shell thickness distributions were statistically similar or different for $NiFe_2O_4@Co_3O_4$ core-shell nanoparticles prior to reduction and after reduction at 180°C, the Kolmogorov-Smirnov two-sample test was used [32]. The data is summarized in Table 5.2 and showed that the two distributions are not significantly different at a 95% confidence level. This is since the D statistic (calculated from the two cumulative distributions) was less than the value of D_{critical}. Additionally, the value of the asymptotic p-value indicated that the null hypothesis (the two distributions are statistically similar) could be accepted. This confirmed that reduction at 180°C in H_2 at 1 atm did not influence the thickness of the cobalt shell.

Table 5.2. Data derived from the Kolmogorov-Smirnov test[a] comparing the cumulative distribution functions of $NiFe_2O_4@Co_3O_4$ core-shell nanoparticles obtained prior to reduction and during the *in-situ* TEM reduction at 180°C, in H_2 (1 atm) for 2 hours.

Group range of $NiFe_2O_4@Co_3O_4$ core-shell nanoparticles	**n**[b]	**α**[c]	***D***[d]	$\boldsymbol{D}_{\textbf{critical}}$[e]	**Asymptotic p-value**[f]
Before reduction compared to after *in-situ* TEM reduction at 180 °C, in H_2 (1 atm) for 2 hours	200	0.05	0.065	0.14	0.74

[a] This is a nonparametric statistical test and can be used to evaluate histogram data for determining: (a) the continuity of a histogram and (b) to test the similarity or difference between two histograms [32].

[b] n represents the number of measurements per sample.

[c] α is the confidence level.

[d] *D* is the derived, real scalar statistic [32].

[e] D_{critical} is the published critical value and is a function of the confidence level and sample size. It can be calculated from: $\frac{1.36}{\sqrt{\frac{n_1+n_2}{n_1 n_2}}}$. [32]

[f] The asymptotic p-value is used for hypothesis testing and to determine whether the null hypothesis can be supported or rejected. p-values close to zero (<0.05) indicates that the null hypothesis can be rejected.[33]

For comparison, the results obtained in this present work are discussed relative to the previously used reduction conditions of 230°C for 2 hours (discussed in Chapter 4). A representative EELS spectrum from the Co-containing region was obtained before reduction, after reduction at 180°C and after reduction at 230°C for 2 hours (direct reduction) (Figure 5.4). It should be noted that each EELS spectrum is comprised of the contribution from the nanoparticle and the silicon nitride (SiN) window of the *in-situ* TEM cell (refer to Figure B.4 in Appendix B). Each EELS spectrum shows the presence of the Co-$L_{2,3}$ peaks. After each reduction, these peaks appear at slightly lower energies than prior to reduction (refer to Table 5.3) suggesting that metallic cobalt may have formed. The EELS spectrum of $NiFe_2O_4@Co_3O_4$ core-shell nanoparticles (reduced at 230°C for 2 hours) also showed the presence of the Fe-$L_{2,3}$ edge suggesting that some iron diffused to the nanoparticle surface.

A closer examination of the O-K edge (Figure 5.5, refer to Table 5.3) showed detectable changes in its fine structure after each reduction treatment. Specifically, prior to reduction, three characteristic peaks were present at around (i) 530eV; (ii) 542eV and (iii) 549eV. These peaks are similar to what is expected for cobalt oxides [34]. After reduction, the O-K edge showed the presence of a single peak at approximately 538eV. A similar peak was obtained with only SiN windows in place (i.e. in the absence of a sample) implying some oxidation of the SiN window. The absence of the pre-edge peak around 530eV, which is typically present in cobalt oxides, suggests that metallic cobalt [34-36] was present after treatment in hydrogen at both temperatures.

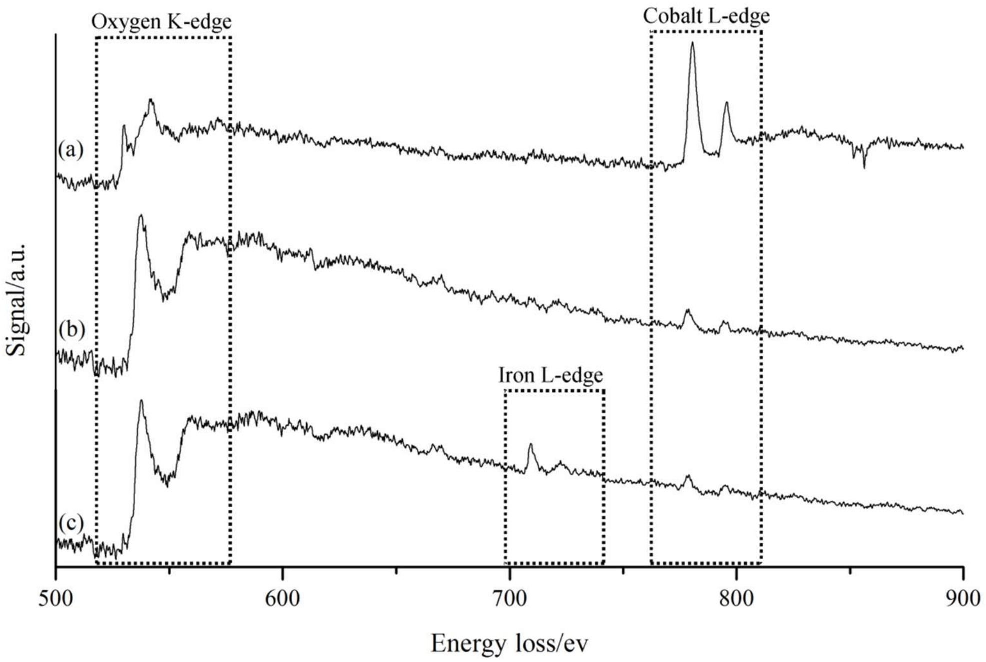

Figure 5.4. EELS spectrum obtained during the *in-situ* TEM analysis of $NiFe_2O_4@Co_3O_4$ core-shell nanoparticles (a) before reduction; (b) after reduction at 180°C in H_2 (1 atm) for 2 hours and (c) after reduction at 230°C in H_2 (1 atm) for 2 hours.

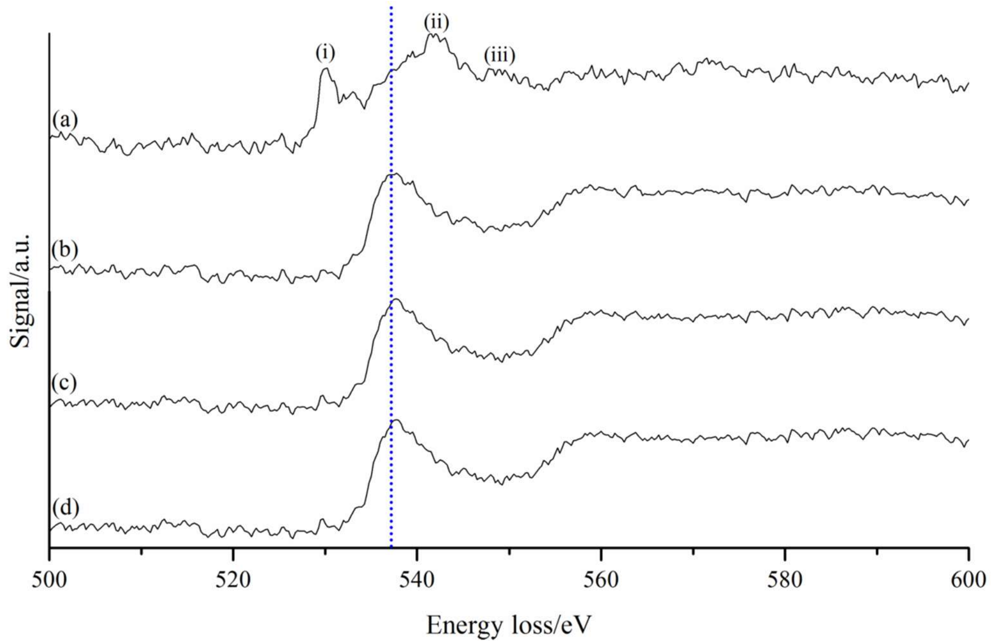

Figure 5.5. EELS spectrum showing the O-K edge region obtained during the *in-situ* TEM analysis of $NiFe_2O_4@Co_3O_4$ core-shell nanoparticles (a) before reduction; (b) after reduction at 180°C in H_2 (1 atm) for 2 hours; (c) after reduction at 230°C in H_2 (1 atm) for 2 hours and (d) SiN window of the cell. The blue dotted line shows the position of the O-K edge due to the SiN window.

Table 5.3. Peak positions from the EELS data shown in Figure 5.5.

Sample	EELS edge/eV				
	Co-L$_3$	**Co-L$_2$**	**Fe-L$_3$**	**Fe-L$_2$**	**O-K**
$NiFe_2O_4$@Co_3O_4 (before reduction)	780.5	796.0	-	-	530.3; 540.3; 542.0;549.0
$NiFe_2O_4$@Co_3O_4 (180°C, 2 hours)	778.8	795.5	-	-	537.0
$NiFe_2O_4$@Co_3O_4 (230°C, 2 hours)	779.0	795.3	709.5	722.5	538.0
SiN window	-	-	-	-	538.5

In Chapter 4, it was reported that cobalt islands of a size of *ca*. 3 nm had formed after reduction at 230°C. It was shown in Figure 5.2 that the composition and observed morphology after reduction at 180°C was different since the core-shell structure was retained. The possible presence of metallic cobalt after the hydrogen treatment at both temperatures suggests that whilst strain energy may influence the structure and composition of the $NiFe_2O_4$@Co_3O_4 core-shell nanoparticles, it may be that the low thermal energy provided by the reduction at 180°C encumbered atomistic restructuring/diffusion. As a result, the core-shell structure was retained with the shell containing only cobalt. It is known that increases in temperature can lead to changes in the structure and composition of (core-shell) nanoparticles [25, 26, 28, 30, 31, 37, 38].

The degree of reduction obtained for $NiFe_2O_4$@Co_3O_4 core-shell nanoparticles after mild reduction conditions (180°C, 1 hour) was determined using oxygen back-titration and assuming only the reduction of Co_3O_4 (Table 5.4). This showed a rather low oxygen uptake which corresponded to a degree of reduction of 21% which was much lower than the value obtained at the slightly higher activation conditions (230°C for 2 hours, 62%). This was expected considering the difference in the conditions used for activation and that the TPR profile showed only a partial reduction occurring below 180°C (Chapter 4). Conversely, the hydrogen uptake was higher over $NiFe_2O_4$@Co_3O_4 core-shell nanoparticles reduced at 180°C (1 hour) than when reduction was done at 230°C in hydrogen for 2 hours thus resulting in a higher active metal surface area. This may be attributed to the retention of the core-shell structure after activation at the low temperature. The lower active metal surface area found for $NiFe_2O_4$@Co_3O_4 core-shell nanoparticles reduced at 230°C (2 hours) could be a consequence of the formation of the cobalt islands over the surface of the core after reduction. Unsupported Co_3O_4 also showed a lower degree of reduction and a lower active metal area than the core-shell nanoparticles reduced at 180°C for 1 hour. The low H_2 uptake found for unsupported CO_3O_4 corresponds to an uncorrected dispersion of 0.2% and may be due to the absence of a support [6].

Table 5.4. Characterization of catalysts samples activated in hydrogen prior to the Fischer-Tropsch synthesis (Space velocity = 6000 $ml_n \cdot g^{-1} \cdot hr^{-1}$).

Sample	**O_2-uptake[a]/ mmol g_{Co}^{-1}**	**DOR[b]/%**	**H_2-uptake[c]/ µmol g_{Co}^{-1}**	**Active metal surface area[d]/ m^2 g_{Co}^{-1}**
$NiFe_2O_4@Co_3O_4$ (180°C, 1 hour)	0.20	21	21.9	1.74
$NiFe_2O_4@Co_3O_4$[e] (230°C, 2 hours)	0.57	62	10.3	0.85
Co_3O_4[e] (300°C, 1 hour)	4.28	51	13.4	1.10

[a] Amount of oxygen taken up in back-titration after reduction and per gram of catalyst.

[b] Degree of reduction assuming only the reduction of Co_3O_4 and a cobalt loading of 8.3 wt.% as reported in Chapter 4.

[c] H_2-uptake per gram of catalyst on the reduced catalyst using pulse chemisorption.

[d] Based on H_2-uptake assuming only metallic cobalt with 14.6 Co atoms/nm^2 and reported per gram of catalyst.

[e] First reported in Chapter 4.

The influence of each activation regime was further studied using *in-situ* XRD to monitor the changes in phase composition after reduction (either 180°C for 1 hour or 230°C for 2 hours) and exposure to Fischer-Tropsch synthesis conditions (230°C, $H_2/CO = 2$, 16 bar) (see Table 5.5). It should be noted that there may be some error on the relative phase abundance values due to the small crystallite size and structural similarity between the various phases under consideration. Nonetheless, after activation and exposure to Fischer-Tropsch synthesis conditions, peaks attributable to metallic cobalt were not observed in the XRD pattern of the $NiFe_2O_4@Co_3O_4$ core-shell nanoparticles which were reduced at 180°C for 1 hour. This result could have been expected since the *in-situ* TEM measurements showed only the presence of a thin cobalt layer with a thickness of a few nanometers after activation. However, after exposure to the Fischer-Tropsch synthesis conditions, an iron carbide phase and peaks characteristic of metallic nickel were also present indicating that under these conditions, further reduction and some carburization of the core material had occurred.

The activation of $NiFe_2O_4@Co_3O_4$ core-shell nanoparticles at a slightly higher temperature and longer time (230°C, 2 hours) showed that $NiFe_2O_4$ and an Fe-Ni alloy ($Fe_{0.625}Ni_{0.375}$) were present as crystalline phases after reduction (refer to Table 5.5). After exposure to Fischer-Tropsch synthesis conditions, these phases together with $Fe_{0.8}Ni_{0.2}$ and iron carbide (Fe_2C) were detected. This showed that the use of slightly harsher reduction conditions (230°C, 2 hours) had a noticeable impact on the phase composition after reduction and exposure to the Fischer-Tropsch synthesis. Further to this, the presence of more exposed core material on the surface after reduction at 230°C for 2 hours (refer to Chapter 4) may have eased the reduction of the core thereby leading to the formation of the alloy phases detected. After reduction at 230°C (2 hours) the size of the ferrite crystallites was larger (see Table 5.5) and increased further after exposure to Fischer-Tropsch synthesis conditions. Upon activation at milder conditions (180°C in hydrogen for 1 hour) an increase in the ferrite crystallite size was only evidenced after exposure to the Fischer-Tropsch synthesis conditions. This suggests that the observed changes in the size of the nickel ferrite crystallites may be an outcome of both exposure to sufficiently high temperature during reduction and further enhanced by exposure under Fischer-Tropsch synthesis conditions.

Table 5.5. Relative phase abundance and average crystallite size of the various phases present in $NiFe_2O_4@Co_3O_4$ after the activation in H_2 and exposure to Fischer-Tropsch conditions ($T_{reaction}$ = 230°C, p = 16 bar) determined from the Rietveld refinement of experimental powder X-ray diffraction data obtained during the *in-situ* experiments.

	Phase	**H_2 activation**		**After exposure to Fischer-Tropsch conditions**[c]	
		180°C, 1 hour	230°C, 2 hour	180°C, 1 hour	230°C, 2 hour
Relative phase abundance, mass %[a]	$NiFe_2O_4$	100 (0.0)	90.6 (0.3)	72.4 (0.5)	71.3 (1.5)
	Ni	-	-	8.2 (0.4)	-
	Fe_2C	-	-	19.5 (0.5)	11.6 (1.6)
	$Fe_{0.8}Ni_{0.2}$	-	-	-	13.6 (0.9)
	$Fe_{0.625}Ni_{0.375}$	-	9.4 (0.3)	-	3.6 (0.6)
Average crystallite size, nm[a, b]	$NiFe_2O_4$	13.6 (0.1)	15.6 (0.3)	16.9 (0.2)	19.9 (0.7)
	Ni	-	-	3.2 (0.2)	-
	Fe_2C	-	-	4.5 (0.2)	5.8 (1.0)
	$Fe_{0.8}Ni_{0.2}$	-	-	-	8.1 (0.8)
	$Fe_{0.625}Ni_{0.375}$	-	10.0 (0.5)	-	3.6 (0.6)

[a] Uncertainty given in parenthesis.

[b] Volume-weighted average crystallite size determined from the integral breadth.

[c] $T_{reaction}$ = 230 °C, p = 16 bar for 16 hours

The nanoscale structure of the passivated material from the *in-situ* XRD measurements (used nanoparticles) was also determined. STEM-HAADF images of $NiFe_2O_4@Co_3O_4$ core-shell nanoparticles after activation in H_2 at 180°C (1 hour) and exposure to Fischer-Tropsch synthesis conditions ($used_{180}$) showed a similar morphology to the fresh $NiFe_2O_4@Co_3O_4$ core-shell material (Figure 5.6). However, the crystallite size distribution which was fitted to a lognormal distribution (Figure 5.6 (c)) showed a shift in the distribution towards larger crystallite sizes for the nanoparticles after activation in H_2 at 180°C (1 hour) and exposure to Fischer-Tropsch synthesis conditions. The histograms of the crystallite size distribution is shown in Figure B.5 in Appendix B. It was also observed that the mean crystallite size range (at 95% confidence level) of the nanoparticles after activation in H_2 at 180°C (1 hour) and exposure to Fischer-

Tropsch synthesis conditions was larger (between 17.4 nm and 17.6 nm) than that of the fresh $NiFe_2O_4@Co_3O_4$ core-shell nanoparticles (13.6 nm – 13.8 nm) (see Table B.2 in Appendix B). There was also a slight difference in the width of the curves since the full width at half maximum (FWHM) increased from 11.8 nm for the fresh nanoparticles to 13.5 nm for $NiFe_2O_4@Co_3O_4$ core-shell nanoparticles after activation in H_2 at 180°C (1 hour) and exposure to Fischer-Tropsch synthesis conditions (see Table B.2 in Appendix B). This suggested that larger crystallites may have formed after reduction at 180°C and exposure to the Fischer-Tropsch synthesis conditions and was similar to the findings obtained from the *in-situ* XRD measurements (Table 5.5). Although sintering of the nickel ferrite nanoparticles may be possible [39, 40], it is more likely that the smaller ferrite nanoparticles identified in fresh $NiFe_2O_4@Co_3O_4$ core-shell nanoparticles are preferably converted into carbide, metallic nickel and the iron-nickel alloy. This is supported by the lower frequency of crystallites with sizes below 5 nm in $NiFe_2O_4@Co_3O_4$ core-shell nanoparticles after activation in H_2 at 180°C (1 hour) and exposure to Fischer-Tropsch synthesis conditions than in the fresh material (Figure 5.6).

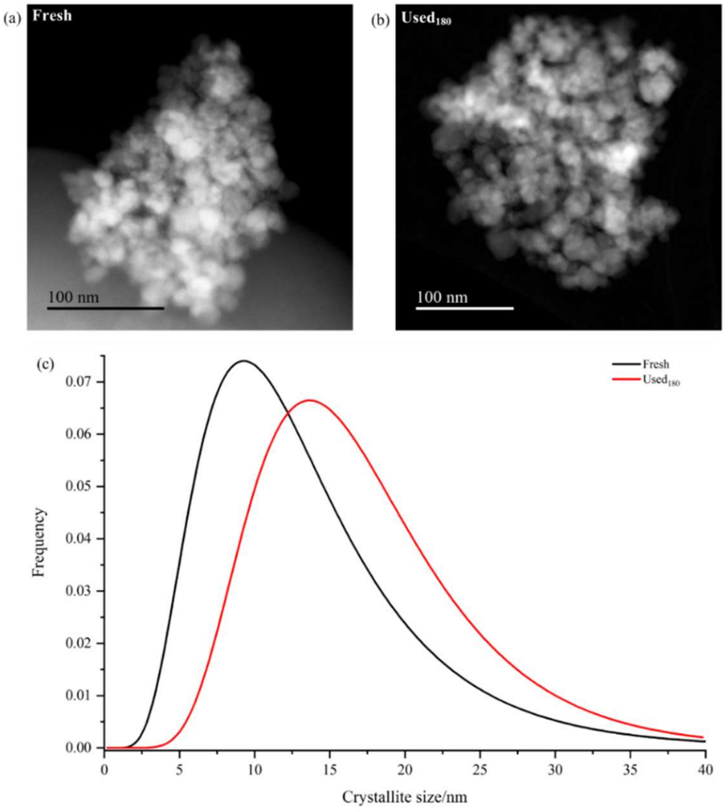

Figure 5.6. STEM-HAADF image of (a) fresh and (b) used $NiFe_2O_4@Co_3O_4$ core-shell nanoparticles obtained after reduction at 180°C (1 hour) and exposure to the Fischer-Tropsch synthesis ($T_{reaction}$ = 230°C, p = 16 bar) in an *in-situ* XRD reactor and (c) the comparison of the corresponding crystallite size distributions fitted onto a lognormal distribution function.

The Kolmogorov-Smirnov two-sample test was used to statistically compare the cumulative distribution function curves (Figure B.6 in Appendix B) of fresh and $NiFe_2O_4$@Co_3O_4 core-shell nanoparticles after activation in H_2 at 180°C (1 hour) and exposure to Fischer-Tropsch synthesis conditions. The results of this test (Table 5.6) showed that the crystallite size distribution curve of the nanoparticles after activation in H_2 at 180°C (1 hour) and exposure to Fischer-Tropsch synthesis conditions was statistically different to the fresh nanoparticles. This confirmed that the observed broadening and shift to larger sizes in $NiFe_2O_4$@Co_3O_4 core-shell nanoparticles after activation in H_2 at 180°C (1 hour) and exposure to Fischer-Tropsch synthesis conditions, in comparison to the fresh material, was significant.

Table 5.6. Data derived from the Kolmogorov-Smirnov test comparing the cumulative distribution functions of fresh $NiFe_2O_4$@Co_3O_4 core-shell nanoparticles and after reduction at 180°C (1 hour) and exposure to the Fischer-Tropsch synthesis ($used_{180}$).

Group range of $NiFe_2O_4$@Co_3O_4 core-shell nanoparticles	**n**[a]	**α**[b]	***D***[c]	***D*$_{critical}$**[d]	**Asymptotic p-value**[e]
Fresh compared to $used_{180}$	199	0.05	0.201	0.10	0.0005

[a] n represents the number of measurements per sample.

[b] α is the confidence level.

[c] *D* is the derived, real scalar statistic [32].

[d] $D_{critical}$ is the published critical value and is a function of the confidence level and sample size. It can be calculated from: $\frac{1.36}{\sqrt{\frac{n_1+n_2}{n_1 n_2}}}$. [32]

[e] The asymptotic p-value is used for hypothesis testing and to determine whether the null hypothesis can be supported or rejected. p-values close to zero (<0.05) indicates that the null hypothesis can be rejected.[33]

EELS spectrum image elemental maps of cobalt, iron and nickel (Figure 5.7) from $NiFe_2O_4$@Co_3O_4 core-shell nanoparticles after activation in H_2 at 180°C (1 hour) and exposure to Fischer-Tropsch synthesis conditions showed that cobalt was present over the surface of the ferrite core (refer to Figure 5.2). The core also appeared to have remained intact. The *in-situ* XRD and TEM results showed that after reduction at 180°C (1 hour) and exposure to Fischer-Tropsch synthesis conditions, some crystallite size changes may have occurred but the core-shell morphology was retained.

After reduction at 230°C for 2 hours and exposure to the Fischer-Tropsch synthesis conditions in an *in-situ* XRD reactor, the STEM-HAADF images of $NiFe_2O_4$@Co_3O_4 nanoparticles after reduction at 230°C (2 hour) and exposure to Fischer-Tropsch synthesis conditions showed a similar crystallite shape to the as-synthesized nanoparticles. However, careful examination of the EELS spectrum images from various regions of interest showed subtle differences. As shown in Figure 5.8, cobalt was no longer covering the surface of the Ni-Fe core nanoparticle, instead clusters of cobalt was observed amongst these nanoparticles. This suggested that cobalt had segregated upon exposure to Fischer-Tropsch synthesis conditions and the core-shell structure was no longer present. Another observation from the STEM-HAADF image shown in Figure 5.8 (a) is the likely onset of the formation of a hollow Ni-Fe oxide nanoparticle (indicated by orange arrow in Figure 5.8 (a)). This is evidenced from the presence of an oval core seemingly detached from the larger nanoparticle. The elemental maps of Fe and Ni (Figure 5.8 (c) and (d) respectively) suggest that this core is comprised of both of these species whilst the outer ring of the larger nanoparticles appears predominantly iron. Thus, it may be that as the $NiFe_2O_4$ nanoparticle is continuously exposed to the reducing environment of the Fischer-Tropsch synthesis conditions, Kirkendall porosity occurs, due to the difference in diffusion rate of two ion species [41]. If iron diffuses to the outer surface of the nanoparticle faster than nickel, this could lead to the observed nanoparticle structure and composition. With sufficient exposure, the formation of an iron rich hollow nanoparticle core is speculated.

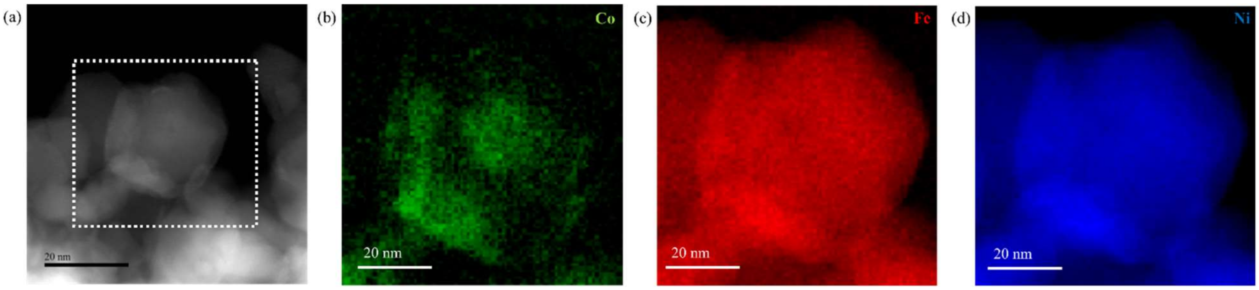

Figure 5.7. (a) STEM-HAADF image with the white square showing the region from which the EELS spectrum image was generated. (b) – (d) corresponding elemental maps for Co (green), Fe (red) and Ni (blue) obtained from the EELS spectrum images of used $NiFe_2O_4@Co_3O_4$ core-shell nanoparticles after reduction at 180°C (1 hour) and exposure to the Fischer-Tropsch synthesis ($T_{reaction}$ = 230°C, p = 16 bar) in an *in-situ* XRD reactor.

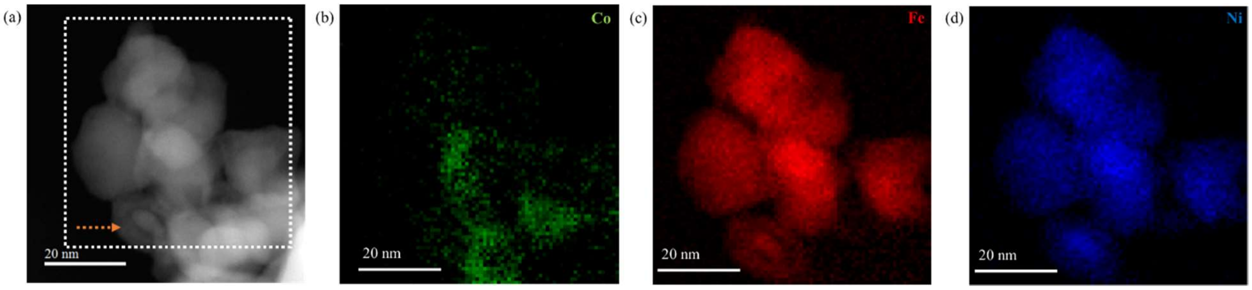

Figure 5.8. (a) STEM-HAADF image with the white square showing the region from which the EELS spectrum image was generated. (b) – (d) corresponding elemental maps for Co (green), Fe (red) and Ni (blue) obtained from the EELS spectrum images of used $NiFe_2O_4@Co_3O_4$ core-shell nanoparticles after reduction at 230°C (2 hours) and exposure to the Fischer-Tropsch synthesis ($T_{reaction}$ = 230°C, p = 16 bar) in an *in-situ* XRD reactor.

A different region of interest in $NiFe_2O_4@Co_3O_4$ nanoparticles after reduction at 230°C (2 hour) and exposure to Fischer-Tropsch synthesis conditions showed the presence of cobalt crystallites on a Ni-Fe nanoparticle (Figure 5.9). The red arrow indicated in the STEM-HAADF image (Figure 5.9 (a)) shows the presence of lattice fringes suggesting the formation of well-defined crystalline cobalt metal. This result is in agreement with the *in-situ* STEM-EELS measurements which showed the formation of cobalt crystallites. Thus, large cobalt crystallites may be formed from these cobalt clusters upon sufficient exposure to Fischer-Tropsch reaction conditions.

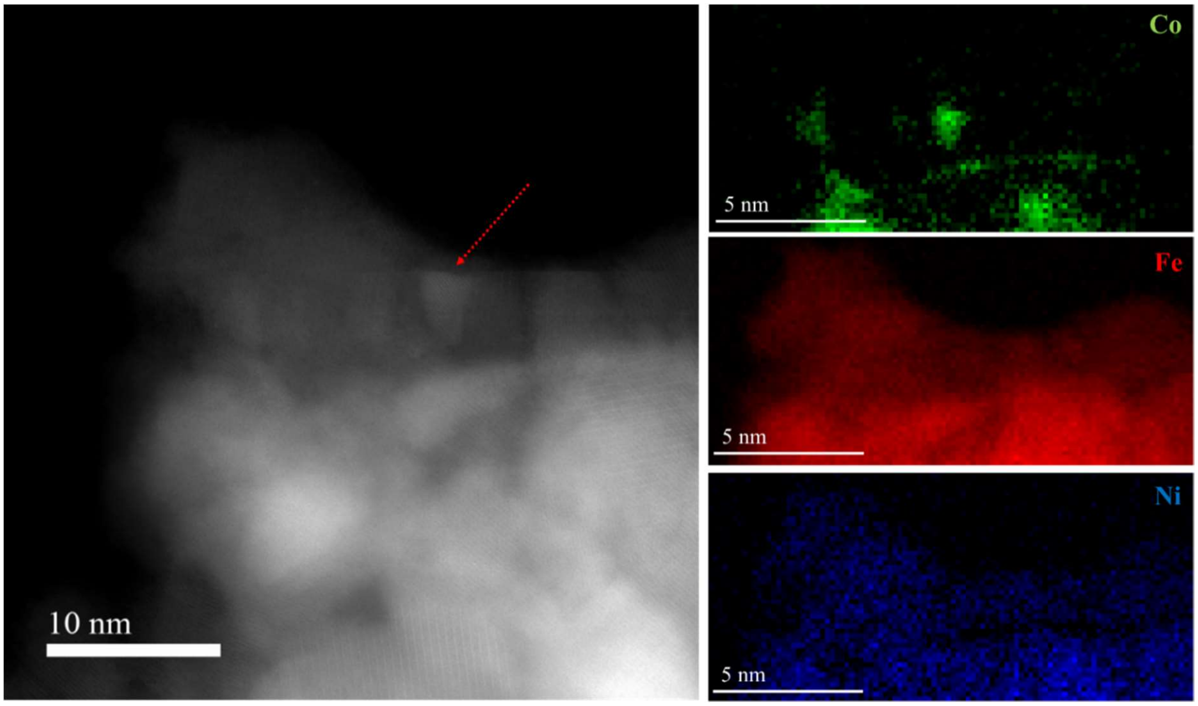

Figure 5.9. (a) STEM-HAADF image with the red arrow showing a cobalt metal crystallite. (c) – (d) corresponding elemental maps for Co (green), Fe (red) and Ni (blue) obtained from EELS spectrum imaging of another region of interest for the used $NiFe_2O_4@Co_3O_4$ core-shell nanoparticles after reduction at 230°C (2 hours) and exposure to the Fischer-Tropsch synthesis ($T_{reaction} = 230°C$, p = 16 bar) in an *in-situ* XRD reactor.

It was also seen that other nanoparticles had areas that were enriched with either iron (white circle in Figure 5.10 (b)) or nickel (white square in Figure 5.10 (b)). This indicated that migration of these species to the nanoparticle surface may have occurred. These areas could be an indication of initial reduction of the nanoparticles that would lead to the formation of iron-nickel alloys which was evident in the X-ray powder diffraction data (Table 5.5). The occurrence of surface migration isn't surprising since it is known that under FTS reactive conditions, the surface composition of nanoparticles may change due to the difference in surface energy between the two components [26].

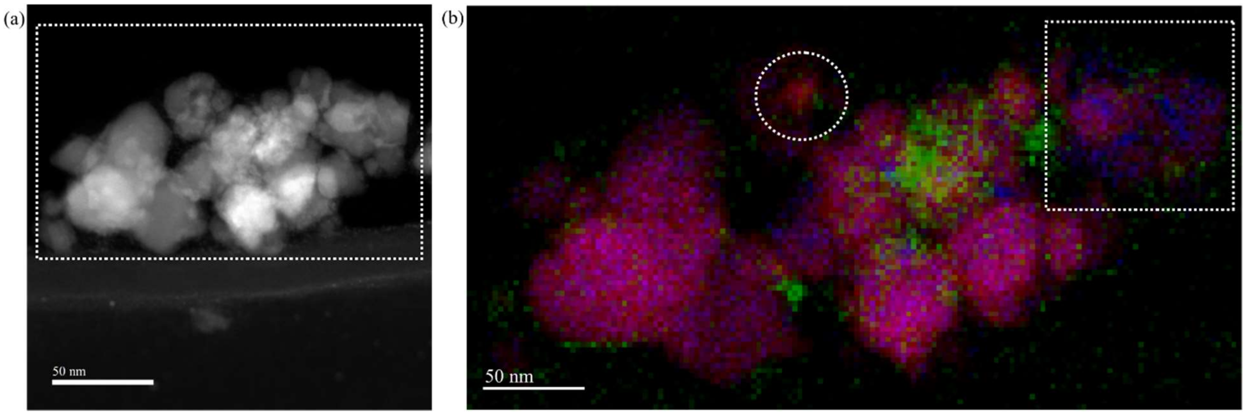

Figure 5.10. (a) STEM-HAADF image with the white rectangle showing the region from where the EELS spectrum image was generated and (b) corresponding composite elemental map obtained from EELS spectrum image of another region of interest for the used $NiFe_2O_4@Co_3O_4$ core-shell nanoparticles after reduction at 230°C (2 hours) and exposure to the Fischer-Tropsch synthesis ($T_{reaction}$ = 230°C, p = 16 bar) in an *in-situ* XRD reactor. Note: Co (green), Fe (red), Ni (blue) and Fe-Ni composite (pink).

The above results indicate that both the nanoparticle morphology and composition showed a dependence on the temperature and time used for reduction. The former was anticipated since nanoscale alterations comprising of structural and compositional changes are thermodynamically driven [26, 28].

5.3.1 Fischer-Tropsch synthesis

The catalytic activity of $NiFe_2O_4@Co_3O_4$ core-shell nanoparticles after activation at 180°C (1 hour) was determined in a fixed bed reactor operating at 230°C and 20 bar using the space velocity specified in Table 5.7 to obtain a CO conversion of 3 ± 1%. The active metal surface area (Table 5.4) obtained for $NiFe_2O_4@Co_3O_4$ core-shell nanoparticles (reduced at 180°C for 1 hour), despite the low degree of reduction, suggested that these nanoparticles would be active for the Fischer-Tropsch synthesis. However, the retention of the cobalt shell that was only a few nanometers thick, both after reduction and exposure to the Fischer-Tropsch synthesis (refer to Figure 5.2 and Figure 5.7, respectively), indicated that a different activity could be anticipated.

An integral rate (cobalt-time yield) of 8.40 $\mu mol_{CO} \cdot g_{Co}^{-1} \cdot s^{-1}$ with a C_{5+} selectivity of 37 C-% (see Table 5.7) was obtained for $NiFe_2O_4@Co_3O_4$ core-shell nanoparticles after activation at 180°C (1 hour). The surface-specific activity (TOF), calculated from the H_2-chemisorption, was 0.02 s^{-1}. The combination of metallic nickel and iron carbide phases (Table 5.5) and a thin cobalt shell may have resulted in the observed activity and high selectivity to short chain hydrocarbons ($C_1 – C_4$). It is known that nickel is a methanation catalyst under these conditions [42] and the activity of small cobalt crystallites (<6 nm) is low with a high methane selectivity [43]. The low degree of reduction of cobalt found after activation at 180°C for 1 hour (Table 5.4) may, to some extent, also account for the observed activity.

Table 5.7. Activity and selectivity in the Fischer-Tropsch synthesis over reduced materials (activation conditions given in Table 5.1; $T_{reaction}$ = 230°C, p = 20 bar at the specified syngas space velocity).

Catalyst	**Syngas SV[a]/ $ml_n \cdot g_{cat}^{-1} \cdot hr^{-1}$**	**Activity**		**TOF[d]/ s^{-1}**	**S_{CO2}[e]/ %**	**Fraction in organic product/C-%**		
		r_{FT} per g_{Co}[b]	**r_{FT} per g_{cat}[c]**			**C_1**	**$C_2 - C_4$**	**C_{5+}**
$NiFe_2O_4$@Co_3O_4 (180°C, 1 hour)	6149	0.84	0.07	0.02	4	34	29	37
$NiFe_2O_4$@Co_3O_4 (230°C, 2 hours)	7755	1.36	0.12	0.06	4	29	24	47
Co_3O_4 (300°C, 1 hour)	6350	0.64	0.48	0.18	0.5	9	10	81

[a] SV refers to space velocity

[b] r_{FT} is the integral rate or cobalt-time yield per gram of cobalt: 10^{-5} $mol_{CO} \cdot g_{Co}^{-1} \cdot s^{-1}$

[c] r_{FT} is the integral rate per gram of catalyst: 10^{-5} $mol_{CO} \cdot g_{cat}^{-1} \cdot s^{-1}$

[d] TOF is the turnover frequency based on H_2 chemisorption: $mol_{CO} \cdot mol_{Co(Surface)} \cdot s^{-1}$

[e] S refers to selectivity

A comparison can be made between $NiFe_2O_4$@Co_3O_4 core-shell nanoparticles and unsupported Co_3O_4 nanoparticles on the basis of the crystallite size of the as-synthesized nanoparticles. The $NiFe_2O_4$@Co_3O_4 core-shell nanoparticles (reduced at 180°C for 1 hour) have an approximate size of 17 nm whilst an average size of 14 nm was found for unsupported Co_3O_4 (refer to Chapter 4). Interestingly, at similar Fischer-Tropsch testing conditions, the integral rate obtained with $NiFe_2O_4$@Co_3O_4 core-shell nanoparticles (reduced at 180°C for 1 hour) per unit mass of cobalt, was marginally higher than that obtained with unsupported Co_3O_4 nanoparticles (8.40 $\mu mol_{CO} \cdot g_{Co}^{-1} \cdot s^{-1}$ and 6.43 $\mu mol_{CO} \cdot g_{Co}^{-1} \cdot s^{-1}$, respectively). Of course, the activity per gram of catalyst was, for unsupported Co_3O_4, much higher than $NiFe_2O_4$@Co_3O_4 core-shell nanoparticles (reduced at 180°C for 1 hour) due to the cobalt content. There is also a marked difference in the turnover frequency between these materials with unsupported Co_3O_4 having a value of 0.18 s^{-1} and the turnover frequency for $NiFe_2O_4$@Co_3O_4 core-shell nanoparticles (reduced at 180°C for 1 hour) was found to be 0.02 s^{-1}.

Although the active metal surface area of $NiFe_2O_4$@Co_3O_4 core-shell nanoparticles (reduced at 180°C for 1 hour) was slightly higher than that for unsupported Co_3O_4 nanoparticles, the rate per unit mass of cobalt was similar and TOF was lower. This was unexpected because the core-shell structure was retained in $NiFe_2O_4$@Co_3O_4 core-shell nanoparticles (reduced at 180°C for 1 hour) and other reports of core-shell nanoparticle systems with metals such as Pd, Co, Ni and Pt were reported to have an activity much higher than the monometallic catalyst in various reactions [44-50]. Upon reduction of the cobalt shell, lattice mismatch between the reduced cobalt metal shell and metal oxide core may have resulted in strain effects due to lateral expansion of the cobalt shell [51]. When the lattice of the shell material expands, the *d*-orbital narrows and the center of the *d*-band moves closer to the Fermi level. Consequently, the adsorbate may bind stronger to the metal surface. Therefore, it is proposed that CO and dissociated C and O atoms and reaction intermediates bind strongly to the shell surface in $NiFe_2O_4@Co_3O_4$ core-shell nanoparticles after activation at 180°C (1 hour), thus lowering the catalytic activity. The strong adsorption of reactants and intermediates was also used by Den Breejen *et al.*[52] to rationalize the lower catalytic activity of cobalt crystallites smaller than 6 nm in the Fischer-Tropsch synthesis.

There was also a noticeable difference in C_{5+} selectivity where unsupported Co_3O_4 showed a value of 81 C-% and $NiFe_2O_4@Co_3O_4$ core-shell nanoparticles (reduced at 180°C for 1 hour) had a value of 38 C-%. Additionally, the C_1 selectivity was 34 C-% for $NiFe_2O_4@Co_3O_4$ core-shell nanoparticles (reduced at 180°C for 1 hour) whilst a selectivity of 9 C-% toward C_1 was found for unsupported Co_3O_4. Whilst the selectivity differences may be related to a change in the ratio of sites responsible for chain growth [53] between $NiFe_2O_4@Co_3O_4$ core-shell nanoparticles and unsupported Co_3O_4, the difference in phase composition between the catalysts could also govern the observed selectivity. It is suggested that when cobalt is present as a thin shell over a $NiFe_2O_4$ core together with the multiple phases identified after activation and exposure to Fischer-Tropsch synthesis conditions (refer to Table 5.5), a lower chain growth probability and increased coverage of dissociated hydrogen may be present in $NiFe_2O_4@Co_3O_4$ core-shell nanoparticles (reduced at 180°C for 1 hour) than in unsupported Co_3O_4. According to Bezemer *et al.*[43], in cobalt-based catalysts with a higher methane selectivity, a lower chain growth probability and an increased coverage of dissociated hydrogen was found. Although a reduction in cost for cobalt-based catalysts used for the Fischer-Tropsch synthesis is highly desirable, the use of core-shell nanoparticles with a cobalt shell thickness in the range of 3 nm appears inadequate for obtaining an acceptable product selectivity. Thus, in future designs of core-shell nanoparticles with a cobalt shell, there may be a trade-off between cost and catalytic performance.

The CO conversion obtained in the Fischer-Tropsch synthesis at 230°C and 20 bar with $NiFe_2O_4@Co_3O_4$ core-shell nanoparticles reduced at 230°C for 2 hours was in the range of 2 – 4%. A significantly lower activity after mild reduction conditions (180°C for 1 hour) was obtained than after reduction at 230°C for 2 hours ($0.84\ mol_{CO}\cdot g_{Co}^{-1}\cdot s^{-1}$ *versus* $1.36\ mol_{CO}\cdot g_{Co}^{-1}\cdot s^{-1}$, respectively, see Table 5.7). Similarly, the turnover frequency was lower for $NiFe_2O_4@Co_3O_4$ core-shell nanoparticles that were reduced at 180°C for 1 hour ($0.02\ s^{-1}$) than when reduction was done at 230°C for 2 hours ($0.06\ s^{-1}$). Despite the higher active metal surface area after reduction at 180°C (1 hour) (Table 5.4), the difference in the degree of reduction after each reduction condition could have influenced the observed activity. However, further reduction is likely to occur under the Fischer-Tropsch synthesis conditions [54] which was shown to influence the nanoscale structure and the extent to which the $NiFe_2O_4$ core was reduced (refer to Figure 5.7 – Figure 5.10 and Table 5.5). It should also be noted that the C_{5+} selectivity is also lower when the reduction was done at a 180°C for 1 hour.

The $NiFe_2O_4$@Co_3O_4 core-shell nanoparticles after reduction at 180°C for 1 hour have a core-shell structure with tensile strain likely present on the cobalt shell surface. As discussed earlier, this could result in a stronger CO adsorption and more carbon on the surface which may lead to an increased residence time of the monomer units for the Fischer-Tropsch synthesis. With the former and a more hydrogenating surface, a higher methane selectivity and lower activity can be expected [43, 55]. Metallic nickel that was found to be present in $NiFe_2O_4$@Co_3O_4 nanoparticles under Fischer-Tropsch conditions and after reduction at 180°C (1 hour) (Table 5.5) is known to be a methanation catalyst [42] and could also influence the catalytic performance. The $NiFe_2O_4$@Co_3O_4 core-shell nanoparticles reduced at 230°C for 2 hours showed the presence of small cobalt islands over the ferrite surface, thus behaving more like small nano-sized crystallites (with the activity and selectivity, slightly, obscured by the transformation of the ferrite). The iron-nickel alloys, identified in this material after reduction at 230°C (2 hours) and exposure to Fischer-Tropsch conditions, has also been reported to be active for the reaction and to have an effect on the activity and selectivity due to synergistic effects [56-58]. Thus, the use of different reduction conditions can alter the catalytic performance during the Fischer-Tropsch synthesis due to its effects on the nanoscale structure and phase composition of $NiFe_2O_4$@Co_3O_4 core-shell nanoparticles.

5.4 Chapter summary

$NiFe_2O_4$@Co_3O_4 core-shell nanoparticles were reduced at 180°C for 1 hour and subsequently tested for its activity in the Fischer-Tropsch synthesis at 230°C and 20 bar. After reduction, it was observed that the core-shell structure was retained and metallic cobalt appeared to have formed as a shell surrounding the ferrite core. The shell thickness after reduction was similar to that of the as-prepared core-shell nanoparticles (*ca*. 3 nm). It was also shown that $NiFe_2O_4$@Co_3O_4 core-shell nanoparticles (180°C, 1 hour) had a slightly higher activity per gram of cobalt than unsupported Co_3O_4. However, a lower C_{5+} selectivity was obtained with the core-shell nanoparticles. The reduction at 180°C for 1 hour yielded a lower activity and higher methane selectivity than when reduction was done at 230°C for 2 hours. Owing to the core-shell structure present in $NiFe_2O_4$@Co_3O_4 core-shell nanoparticles (180°C, 1 hour), a combination of strain effects and phases formed under Fischer-Tropsch synthesis conditions was speculated to have contributed to the observed performance differences.

5.5 References

[1] H. Schulz, Short history and present trends of Fischer–Tropsch synthesis, Appl. Catal. A: Gen., 186 (1999) 3-12.

[2] A. M. Saib, D. J. Moodley, I. M. Ciobica, M. M. Hauman, B. H. Sigwebela, C. J. Westrate, J. W. Niemantsverdriet, J. van de Loosdrecht, Fundamental understanding of deactivation and regeneration of cobalt Fischer-Tropsch synthesis catalysts, Catal. Today, 154 (2010) 271-282.

[3] A. Y. Khodakov, Fischer-Tropsch Synthesis: relations between structure of cobalt catalysts and their catalytic performance, Catal. Today, 144 (2009) 251-257.

[4] M. E. Dry, The Fischer-Tropsch process: 1950-2000, Catal. Today, 71 (2002) 227-241.

[5] H. Wang, W. Zhou, J.-X. Liu, R. Si, G. Sun, M.-Q. Zhong, H.-Y. Su, H.-B. Zhao, J. A. Rodriguez, S. J. Pennycook, J.-C. Idrobo, W.-X. Li, Y. Kou, D. Ma, Platinum-modulated cobalt nanocatalysts for low-temperature aqueous-phase Fischer Tropsch synthesis, J. Am. Chem. Soc., 135 (2013) 4149-4158.

[6] A. Y. Khodakov, W. Chu, P. Fongarland, Advances in the development of novel cobalt Fischer-Tropsch catalysts for the synthesis of long-chain hydrocarbons and clean fuels, Chem. Rev., 107 (2007) 1692-1744.

[7] Q. Zhang, J. Kang, Y. Wang, Development of novel catalysts for the Fischer-Tropsch synthesis: Tuning the product selectivity, Chem. Cat. Chem., 2 (2010) 1030-1058.

[8] E. van Steen, H. Schulz, Polymerisation kinetics of the Fischer-Tropsch CO hydrogenation using iron and cobalt based catalysts, Appl. Catal. A: Gen., 186 (1999) 309-320.

[9] L. Gan, R. Yu, J. Luo, Z. Cheng, J. Zhu, Lattice strain distributions in individual dealloyed Pt-Fe catalyst nanoparticles, J. Phys. Chem. Lett., 3 (2012) 934-938.

[10] R. G. Chaudhuri, S. Paria, Core/Shell nanoparticles: classes, properties, synthesis mechanisms, characterization and applications, Chem. Rev., 112 (2012) 2373-2433.

[11] M. B. Gawande, A. Goswami, T. Asefa, H. Guo, A. V. Biradar, D.-L. Peng, R. Zboril, R. S. Varma, Core-shell nanoparticles: Synthesis and applications in catalysis and electrocatalysis, Chem. Soc. Rev., 44 (2015) 7540-7590.

[12] S. Alayoglu, P. Zavalij, B. Eichhorn, Q. Wang, A. I. Frenkel, P. Chupas, Structural and architectutal evaluation of bimetallic nanoparticles: A case study of Pt-Ru core-shell and alloy nanoaprticles, ACS Nano, 3 (2009) 3127.

[13] Y.-F. Zhu, N. Zhao, B. Jin, M. Zhao, Q. Jiang, High thermal stability of core-shell structures dominated by negative interface energy, Phys. Chem. Chem. Phys., 19 (2017) 9253-9260.

[14] H.-L. Jiang, T. Akita, T. Ishida, M. Haruta, Q. Xu, Synergistic catalysis of Au@Ag core-shell nanoparticles stabilized on metal-organic framework, J. Am. Chem. Soc., 133 (2011) 1304-1306.

[15] H. Akbarzadeh, E. Mehrjouei, A. N. Shamkhali, M. Abbaspour, S. Salemi, S. Ramezanzadeh, New molecular insights into the stability of Ni-Pd hollow nanoparticles, Inorg. Chem. Front., 4 (2017) 1679-1690.

[16] R. Xie, D. Li, B. Hou, J. Wang, L. Jia, Y. Sun, Solvothermally derived Co_3O_4@*m*-SiO_2 nanocomposite for Fischer-Tropsch synthesis, Catal. Comm., 12 (2011) 380-383.

[17] A. Mosayebi, A. Haghtalab, The comprehensive kinetic modelling of the Fischer-Tropsch synthesis over Co@Ru/Al_2O_3 core-shell structure catalyst, Chem. Eng. J., 259 (2015) 191-204.

[18] R. Xie, H. Wang, P. Gao, L. Xia, Z. Zhang, T. Zhao, Y. Sun, Core@shell Co_3O_4@C-*m*-SiO_2 catalysts with inert C modified mesoporous channel for desired middle distillate, Appl. Catal. A: Gen., 492 (2015) 93-99.

[19] H. Qin, S. King, Y. Wang, H. Li, Z. Ni, Y. Huang, Y. Li, X. Li, Lignin-based fabrication of Co@C core-shell nanoparticles as efficient catalyst for selective Fischer-Tropsch synthesis of C_{5+} compounds, ACS Sustainable Chem. Eng., 4 (2016) 1240-1247.

[20] V.R.Calderone, N.R.Shiju, D.Curulla-Ferre, S.Chambrey, A.Khodakov, A.Rose, J.Thiessen, A.Jess, G.Rothenberg, De novo design of nanostructured iron-cobalt Fischer-Tropsch catalysts, Angew. Chem. Int. Ed., 52 (2013) 4397-4401.

[21] A. Govender, W. Barnard, E. J. Olivier, R. P. Forbes, E. van Steen, J. H. Neethling, Synthesis and characterization of $NiFe_2O_4$@Co_3O_4 core-shell nanoparticles, Mater. Charac., 121 (2016) 93-102.

[22] S. Zhang, L. Nguyen, Y. Zhu, S. Zhan, C.-K. Tsung, F. F. Tao, In-situ studies of nanocatalysis, Acc. Chem. Res., 46 (2013) 1731-1739.

[23] F. F. Tao, M. Salmeron, In situ studies of chemistry and structure of materials in reactive environments, Science, 331 (2011) 171-174.

[24] E. Prestat, M. A. Kulzick, P. J. Dietrich, M. Smith, E.-P. Tien, M. G. Burke, S. J. Haigh, N. J. Zaluzec, In Situ industrial bimetallic catalyst characterization using scanning transmission electron microscopy and X-ray absorption spectroscopy at one atmosphere and elevated temperature, Chem. Phys. Chem., 18 (2017) 2151-2156.

[25] P. L. Hansen, J. B. Wagner, S. Helveg, J. R. Rostrup-Nielsen, B. S. Clausen, H. Topsoe, Atom-resolved imaging of dynamic shape changes in supported copper nanocrystals, Science, 295 (2002) 2053-2055.

[26] H. Liao, A. Fisher, Z. J. Xu, Surface segregation in bimetallic nanoparticles: A critical issue in electrocatalyst engineering, Small, 11 (2015) 3221-3246.

[27] R. Huang, Y.-H. Wen, Z.-Z. Zhu, S.-G. Sun, Pt-Pd bimetallic catalysts: Structural and thermal stabilities of core-shell and alloyed nanoparticles, J. Phys. Chem. C, 116 (2012) 8664-8671.

[28] T. Wen, K. M. Krishnan, Thermal stability and morphological transformations of Au_{core}-Co_{shell} nanocrucibles, J. Phys. Chem. C, 114 (2010) 14838-14842.

[29] F. Tao, M. E. Grass, Y. Zhang, D. R. Butcher, F. Aksoy, S. Aloni, V. Altoe, S. Alayoglu, J. R. Renzas, C.-K. Tsung, Z. Zhu, Z. Liu, M. Salmeron, G. A. Somorjai, Evolution of structure and chemistry of bimetallic nanoparticle catalysts under reaction conditions, J. Am. Chem. Soc., 132 (2010) 8697-8703.

[30] C. S. Bonifacio, S. Carenco, C. H. Wu, S. D. House, H. Bluhm, J. C. Yang, Thermal stability of core-shell nanoparticles: A combined in situ study by XPS and TEM, Chem. Mater., 27 (2015) 6960-6968.

[31] S. Carenco, A. Tuxen, M. Chintapalli, E. Pach, C. Escudero, T. D. Ewers, P. Jiang, F. Borondics, G. Thornton, A. P. Alivisatos, H. Bluhm, J. Guo, M. Salmeron, Dealloying of cobalt from CuCo nanoparticles under syngas exposure, J. Phys. Chem. C, 117 (2013) 6259-6266.

[32] I. T. Young, Proof wihtout prejudice: Use of the Kolmogorov-Smirnov test for the analysis of histograms from flow systems and other sources, J. Histochem. Cytochem., 25 (1977) 935-941.

[33] A. McCluskey, A. G. Lalkhen, Statistics IV: Interpreting the results of statistical tests, Continuing Education in Anaesthesia Critical Care & Pain, 7 (2007) 208-212.

[34] Z. Zhang, Surface effects in the energy loss near edge structure of different cobalt oxides, Ultramicroscopy, 107 (2007) 598-603.

[35] D. Barreca, A. Gasparotto, O. I. Lebedev, C. Maccato, A. Pozza, E. Tondello, S. Turner, G. van Tendeloo, Controlled vapo-phase synthesis of cobalt oxide nanomaterials woth tuned composition and spatial organization, Cryst. Eng. Comm., 12 (2010) 2185-2197.

[36] R. Dehghan, T. W. Hansen, J. B. Wagner, E. Rytter, In-situ reduction of promoted cobalt oxide supported on alumina by environmental transmission electron microscopy, Catal. Lett., 141 (2011) 754-761.

[37] F. Calvo, Thermodynamics of nanoalloys, Phys. Chem. Chem. Phys., 17 (2015) 27922-27939.

[38] H. L. Xin, S. Alayoglu, R. Tao, A. Genc, C.-M. Wang, L. Kovarik, E. A. Stach, L.-W. Wang, M. Salmeron, G. A. Somorjai, H. Zheng, Revealing the atomic restructuring of Pt-Co nanoparticles, Nano Lett., 14 (2014) 3203-3207.

[39] Z. H. Chonco, A. Ferreira, L. Lodya, M. Claeys, E. van Steen, Comparing silver and copper as promoters in Fe-based Fischer-Tropsch catalysts using delafossite as a model compound, J. Catal., 307 (2013) 283-294.

[40] Z. H. Chonco, L. Lodya, M. Claeys, E. van Steen, Copper ferrites: A model for investigating the role of copper in the dynamic iron-based Fischer-Tropsch catalyst, J. Catal., 308 (2013) 363-373.

[41] H. J. Fan, U. Gosele, M. Zacharias, Formation of nanotubes and hollow nanoparticles based on Kirkendall and diffusion processes: A review, Small, 3 (2007) 1660-1671.

[42] M. A. Vannice, The catalytic synthesis of hydrocarbons from H_2/CO mixtures over the group VIII metals: IV The kinetic behaviour of CO hydrogenation over Ni catalysts, J. Catal., 44 (1976) 152-162.

[43] G. L. Bezemer, J. H. Bitter, H. P. C. E. Kuipers, H. Oosterbeek, J. E. Holewijn, X. Xu, F. Kapteijn, A. J. van Dillen, K. P. de Jong, Cobalt particle size effects in the Fischer-Tropsch reaction studied with carbon nanofiber supported catalysts, J. Am. Chem. Soc., 128 (2006) 3956-3964.

[44] D. Wang, H. L. Xin, R. Hovden, H. Wang, Y. Yu, D. A. Muller, F. J. DiSalvo, H. D. Abruna, Structurally ordered intermetallic platinum-cobalt core-shell nanoparticles with enhanced activity and stability as oxygen reduction electrocatalysts, Nat. Mater., 12 (2012) 81-87.

[45] L. Wang, W. Gao, Z. Liu, Z. Zeng, Y. Liu, M. Giroux, M. Chi, G. Wang, J. Greeley, X. Pan, C. Wang, Core-shell nanostructured cobalt-platinum electrocatalysts with enhanced durability, ACS Catal., 8 (2018) 35-42.

[46] L. Yang, M. B. Vukmirovic, D. Su, K. Sasaki, J. A. Herron, M. Mavrikakis, S. Liao, R. R. Adzic, Tuning the catalytic activity of Ru@Pt core-shell nanoparticles for oxygen reduction reaction by varying the shell thickness, J. Phys. Chem. C, 117 (2013) 1748-1753.

[47] M. Liu, W. Tang, Z. Xie, H. Yu, H. Yin, Y. Xu, S. Zhao, S. Zhou, Design of highly efficient Pt-SnO_2 hydrogenation nanocatalysts using Pt@Sn core-shell nanoparticles, ACS Catal., 7 (2017) 1583-1591.

[48] S. Alayoglu, A. U. Nilekar, M. Mavrikakis, B. Eichhorn, Ru-Pt core-shell nanoparticles for preferential oxidation of carbon monoxide in hydrogen, Nat. Mater., 7 (2008) 333-338.

[49] S. Garcia, R. M. Anderson, H. Celio, N. Dahal, A. Dolocan, J. Zhou, S. M. Humphrey, Microwave synthesis of Au-Rh core-shell nanoparticles and implications of the shell thickness in hydrogenation catalysis, Chem. Commun., 49 (2013) 4241-4243.

[50] X. Zhao, S. Chen, Z. Fang, J. Ding, W. Sang, Y. Wang, J. Zhao, Z. Peng, J. Zeng, Octahedral Pd@$Pt_{1.8}Ni$ core-shell nanocrystals with ultrathin PtNi alloy shells as active catalysts for oxygen reduction reaction, J. Am. Chem. Soc., 137 (2015) 2804-2807.

[51] M. V. Rastei, B. Heinrich, L. Limot, P. A. Ignatiev, V. S. Stepanyuk, P. Bruno, J. P. Bucher, Size-dependent surface states of strained cobalt nanoislands on Cu (111), Phys. Rev. Lett., PRL 99 (2007) 246102-246101-246102-246104.

[52] J. P. den Breejen, P. B. Radstake, G. L. Bezemer, J. H. Bitter, V. Frøseth, A. Holmen, K. P. de Jong, On the origin of the cobalt particle size effects in Fischer-Tropsch catalysis, J. Am. Chem. Soc., 131 (2009) 7197-7203.

[53] P. van Helden, J.-A. van den Berg, M. A. Petersen, W. Janse van Rensburg, I. M. Ciobîca, J. van de Loosdrecht, Computational investigation of the kinetics and mechanism of the initial steps of the Fischer-Tropsch synthesis on cobalt, Faraday Discuss., 197 (2017) 117-151.

[54] J. van de Loosdrecht, B. Balzhinimaev, J.-A. Dalmon, J. W. Niemantsverdriet, S. V. Tsybylya, A. M. Saib, P. J. van Berge, J. L. Visagie, Cobalt Fischer-Tropsch synthesis: Deactivation by oxidation?, Catal. Today, 123 (2007) 293-302.

[55] J. P. den Breejen, P. B. Radstake, G. L. Bezemer, J. H. Bitter, V. Froseth, A. Holmen, K. P. de Jong, On the origin of the cobalt particle size effects in Fischer-Tropsch caταλψσισ, J. Am. Chem. Soc., 131 (2009) 7197-7203.

[56] J. van de Loosdrecht, A. J. van Dillen, A. A. van der Horst, A. M. van der Kraan, J. W. Geus, Nickel-iron catalysts prepared by homogeneous deposition-precipitation of cyanide complexes on a titania support, Top. Catal., 2 (1995) 29-43.

[57] H. O. Torshizi, S. Vahid, A. A. Mirzaei, Effect of calcination conditions on the structure and catalytic performance of MgO supported Fe-Co-Ni catalyst for CO hydrogenation, J. Nat. Gas Sci. Eng., 17 (2014) 110-118.

[58] M. Feyzi, A. A. Mirzaei, H. R. Bozorgzadeh, Effects of preparation and operation conditions on precipitated iron nickel catalysts for Fischer-Tropsch synthesis, J. Nat. Gas Sci. Chem., 19 (2010) 341-353.

6 Silica supported $NiFe_2O_4@Co_3O_4$ core-shell nanoparticles as precursors for Fischer-Tropsch catalysts

Stöber silica spheres were used to support for $NiFe_2O_4@Co_3O_4$ core-shell nanoparticles. Prior to characterization and the Fischer-Tropsch synthesis, $NiFe_2O_4@Co_3O_4/SiO_2$ was reduced at either 180°C for 1 hour or 230°C for 2 hours. A higher reduction temperature resulted in a higher cobalt-time yield (23.80 $\mu mol_{CO} \cdot g_{Co}^{-1} \cdot s^{-1}$) in comparison to a reduction at 180°C (1 hour). After reduction at 230°C for 2 hours and exposure to Fischer-Tropsch synthesis conditions, the core-shell structure was retained in $NiFe_2O_4@Co_3O_4/SiO_2$, which might be due to reducing the contact between individual core-shell nanoparticles by anchoring the core-shell nanoparticles on to the Stöber silica spheres support. The influence of the support was clearly seen after reduction at 230°C (2 hours) due to the higher activity, with similar product selectivities, obtained with $NiFe_2O_4@Co_3O_4/SiO_2$.

6.1 Introduction

The Fischer-Tropsch synthesis is an efficient process for the production of high quality hydrocarbons from syngas (a mixture of CO and H_2) [1-6]. Whilst metals such as cobalt, iron and ruthenium have been shown to be active for the Fischer-Tropsch synthesis, cobalt is usually preferred for the low temperature Fischer-Tropsch synthesis. The inclination toward cobalt-based catalysts is not only due to its effectiveness in the production of higher hydrocarbons, but also because these catalysts have a high activity per unit mass, are more resistant to oxidation than iron-based catalysts and have a low activity for the formation of CO_2. [1-6] However, there is a high cost associated with the use of cobalt as the catalytically active material and therefore there is a need to optimize its utilization [7, 8]. Recently, the synthesis of cobalt-based catalysts with a core-shell structure has been reported as an attractive route to reduce the content of cobalt in the catalyst and thereby its cost [7-10]. There has been a growing interest in the synthesis and application of core-shell nanoparticles since the combination of two different components [11-13] may yield unique catalytic properties different to those comprising individual or alloyed components [11-18]. Cobalt-based core-shell nanoparticles, where cobalt is either present as the core or the shell, have been shown to be an alternative catalyst for the Fischer-Tropsch synthesis [1, 5-8, 19] (see also Chapter 4 and Chapter 5).

In conventional heterogeneous catalysts, a support is used to anchor the catalytically active metal particles. For cobalt-based catalysts, this might increase the density of active metallic cobalt sites on the surface and thus improve the catalytic performance [2, 6, 20]. Anchoring the catalytically active species would reduce the likelihood for sintering. Furthermore, supporting the catalytically active material would reduce the heat generation per unit reactor volume resulting in more isothermal conditions and furthermore may improve the mechanical integrity of the catalyst. Whilst a variation in the support type may influence the product selectivity, the overall impact of the support on the Fischer-Tropsch synthesis behavior of cobalt-based catalysts is complex. This is since the degree of reduction; dispersion, crystallite size, (which are influenced by the metal-support interaction) and the pore structure of the catalyst/support are significant factors in determining the effect of the support on the Fischer-Tropsch activity and selectivity [21, 22]. Among the available support choices (alumina, silica, titania, carbon, etc.), the cobalt-silica interaction is known to be relatively weak, which may lead to a more facile reduction of the cobalt [2, 21].

Core-shell nanoparticles have also been anchored on various supports in an effort to further alter its catalytic properties [1, 6, 8, 9, 11, 23-28]. Wang *et al.*[20] examined the use of a high thermally conductive core-shell material, $Al_2O_3@Al$, as a support for cobalt. In comparison to the conventional catalyst (Co/Al_2O_3), the $Co/Al_2O_3@Al$ catalyst showed a higher CO conversion and C_{5+} selectivity during the Fischer-Tropsch synthesis. The improved C_{5+} selectivity was ascribed to the macro-mesoporous structure of the core-shell support. The authors also indicated that the temperature remained fairly similar across the catalyst bed as a result of the high thermal conductivity of the Al_2O_3@Al support. Calderone *et al.*[9] described the formation of Fe_3O_4@Co_3O_4 core-shell nanoparticles supported on mesoporous silica and stated that the presence of the support assisted in retaining the core-shell structure under reducing conditions.

Supported core-shell nanoparticles have also been used for other reactions such as H_2 oxidation [24]; the water gas shift reaction [23]; oxidation of formic acid [26] and methanol [29] and dehalogenation reactions and reduction of olefins [11]. MWCNTs anchors core-shell nanoparticles thus resulting in minimal aggregation and sintering [23]. Carbon-based materials were also used to support core-shell nanoparticles by Xu *et al.*[26] (PtAu@Pt core-shell nanoparticles), Goswami *et al.*[11] (Pd@Pt core-shell nanoparticles) and Cho *et al.*[30] (PdPt@Pt core-shell nanoparticles). The supported core-shell nanoparticles had an improved stability and conversion in comparison to the unsupported core-shell nanoparticles.

Owing to the beneficial effects that has been reported for supported core-shell nanoparticles, $NiFe_2O_4$@Co_3O_4 core-shell nanoparticles were supported on silica (Stöber spheres) to determine the effect of supporting $NiFe_2O_4$@Co_3O_4 core-shell nanoparticles on the physico-chemical properties and its performance in the Fischer-Tropsch synthesis. These $NiFe_2O_4$@Co_3O_4 core-shell nanoparticles have previously been shown to be active for the Fischer-Tropsch synthesis after activation at either 180°C for 1 hour or 230°C for 2 hours (Chapters 4 and 5). The performance of $NiFe_2O_4$@Co_3O_4/SiO_2 pretreated at similar conditions will be compared to that obtained with unsupported $NiFe_2O_4$@Co_3O_4 core-shell nanoparticles.

6.2 Experimental

6.2.1 Synthesis of Stöber spheres

Silica (SiO_2) microspheres (Stöber spheres) were synthesized according to the procedures described by Stöber *et al.*[31]. Briefly, 400 mL of ethanol (Merck) was added to 50 mL ammonia solution (28.0 – 30.0%, Merck, for analysis). The mixture was stirred for 3 minutes before 50 mL tetraethyoxysilane (TEOS, Merck, for analysis) was added and the reaction was allowed to proceed for 24 hours. The resulting slurry was dried under vacuum to remove the solvent and the white powder that remained was then oven-dried overnight at 110°C. The powder was calcined in a static air furnace at 400°C for four hours.

6.2.2 Synthesis of $NiFe_2O_4$@Co_3O_4

A detailed description of the synthesis of the core-shell nanoparticles is given in chapter 4 (see also [7]). Briefly, a two-step synthesis was followed. In Step 1, an aqueous solution (10 mL) of ammonium carbonate,

$(NH_4)_2CO_3$ (8.50*M*) was mixed with 25 wt.% ammonia aqueous solution (3.6 mL). Cobalt carbonate, $CoCO_3$, was added to obtain a cobalt concentration of 0.05*M* and a pH of 11.5. The resulting cobalt containing suspension was then stirred at 45°C for 2 hours, after which the solution was filtered by gravity. This filtrate was added to a round bottom flask and ~ 0.05 g/mL of $NiFe_2O_4$ was added; the suspension was stirred at 85°C for 6 hours. The temperature was then increased to 95°C, at which it was kept under stirring for 24 hours. The solvent was subsequently removed under vacuum and the dried solid was rinsed with deionized water and again dried under vacuum. The obtained solid was oven-dried at 110°C for 12 hours. In step 2, the solution containing the cobalt precursor was made as per step 1; however, the dried solid obtained in step 1 was added to the solution to make a suspension of *ca*. 0.05 g/mL. The synthesis then followed the process outlined above. This resulted in a final cobalt loading of 8.3 wt. %.

6.2.3 Synthesis of silica supported $NiFe_2O_4$@Co_3O_4

The synthesis procedure was adapted from the procedure described by Dad *et al.*[32]. The $NiFe_2O_4$@Co_3O_4 core-shell nanoparticles (~ 3g) was added to 250 mL toluene and sonicated for 30 minutes. Then, Stöber spheres (~ 5g) were added to the core-shell nanoparticle suspension and sonicated for a further 90 minutes after which it was stirred at 90°C to slowly evaporate the toluene. The solid powder that remained was oven-dried at 70°C overnight and subsequently calcined in a static air furnace at 250°C for 5 hours. The cobalt loading in this material was determined to be 3 wt. % using SEM-EDS.

6.2.4 Characterization

Prior to the TEM/STEM analysis, the crushed sample was dispersed in ethanol using an ultrasonication after which a small amount was transferred onto a holey carbon copper TEM grid (SPI Supplies, 300 mesh). A double aberration corrected JEOL ARM 200F transmission electron microscope operating at 200 kV was used for the *ex-situ* characterization of the nanoparticles. High angle annular dark field (HAADF) scanning transmission electron microscopy (STEM) as well as bright field (BF) STEM imaging at atomic resolution was used. Electron energy loss spectroscopy (EELS) Spectrum Imaging (SI) was performed using the DualEELS^{TM} mode on the Gatan GIF Quantum ERS^{TM} spectrometer. This allows for the pixel by pixel acquisition of both the intense zero loss peak (ZLP) and the elemental edges during the same scan. A convergence semi-angle of 21.4 mrad was used for the STEM probe and the collection semi-angle of the spectrometer was 54.3 mrad at a camera length of 1 cm.

X-ray powder diffraction (XRD) patterns were collected on a Bruker D8 Advance X-ray diffractometer equipped with a Co Kα X-ray source (λ=0.178897 nm). Phase identification of the diffraction data was done using Bruker DIFFRAC.EVA Version 2 or Panalytical's X'Pert HighScore Plus software was used while average crystallite sizes and relative phase abundances were obtained from Rietveld refinements using Bruker AXS TOPAS Version 4.1. The *in-situ* XRD measurements were performed in an Anton Paar XRK900 coupled to the Panalytical X'Pert Pro multi-purpose diffractometer. The *in-situ* XRD experiments were performed under a hydrogen flow (50 ml/min) and the sample was heated from room temperature to 230°C using a heating rate of 5°C/min. Diffraction patterns were collected at intervals of 20°C. After the reduction, the reactor was flushed with helium for 2 hours and cooled to 40°C. Subsequently, the temperature was increased to 230°C under synthesis gas (H_2/CO = 2, 50 ml/min). At this temperature, the pressure was increased to 16 bar over a 5 hour period. The reaction was maintained under these conditions for 16 hours and a diffractogram was collected in 20 min intervals. At the end of the experiment, the system was flushed with helium, de-pressurized and cooled to 40°C. Following this, the catalyst material was passivated in a mixture of helium (50 ml/min) and oxygen for 3 hours (O_2 flow rate was initially 2 ml/min and gradually increased to 6 ml/min). The used catalyst was unloaded into dry ice.

Nitrogen isotherms at – 196°C were measured using a Micromeritics ASAP 2480 surface area and porosity analyzer. Prior to analysis, the samples we degassed under vacuum for 5 hours at 200°C. Nitrogen isotherms were obtained in both adsorption and desorption modes. The surface area of the supports and catalysts were determined by the Brunauer-Emmett-Teller (BET) method. The total pore volume was calculated from the amount of vapor adsorbed at a relative pressure (P/P_0) of 0.99. The average pore diameter was determined from the desorption curves using the Brunauer-Joyner-Halenda (BJH) model.

Temperature Programmed Reduction (TPR) profiles of the samples were obtained with the AutoChem 2920 (Micrometrics, USA) equipped with a TCD by reducing the catalyst samples using pure hydrogen with a flow rate of 10 ml/min while the temperature was increased from 50°C to 1000°C at a rate of 5°C/min. H_2-Temperature Programmed Desorption (TPD) was carried out on the AutoChem 2920 (Micrometrics, USA). The samples were dried at 120°C for one hour. Then, the catalyst was reduced in pure hydrogen using the activation conditions listed in Table 6.1 and using a heating rate of 5°C/min. Thereafter, the samples were flushed under argon flow (50 ml/min) for 1 hour. H_2 was adsorbed at 100°C using pulse chemisorption in 10 pulses with a 2 minute interval.

The catalytic evaluations were carried at Sasol United Kingdom (SUK) Ltd. and were conducted in a fixed bed reactor set-up containing four independent parallel reactor tubes each with inner diameter 6.5 mm. The catalysts (200mg) were each diluted with 3.1g SiC (320 grit) resulting in a catalyst bed length of ~ 6 cm. The catalyst bed temperature was accurately controlled by means of a thermocouple in the middle of the bed. Prior to Fischer-Tropsch synthesis the samples were activated *in-situ* at elevated temperatures and atmospheric pressure (see Table 6.1). After reduction, the temperature was changed to 200°C and the pressure increased to 20 bar using H_2 and Ar. Synthesis gas (H_2/CO = 2) was then introduced and the temperature was increased to 230°C (ramp rate 0.5°C/min). The space velocity was adjusted to maintain a CO conversion below 10% amongst the various catalysts. The reaction effluent was passed through a hot trap (190°C) to collect the high boiling waxes and a cold trap (15°C) to collect the water and low boiling organic product compounds. The outlet gases was analyzed on-line using an Agilent 7890A Refinery Gas Analyzer equipped with a Flame Ionization Detector (FID) and two TCDs. Ar (~ 8%) was added to the feed and used as internal standard to determine conversion and product selectivity. The selectivities are reported in C-% from carbon monoxide converted to hydrocarbons (i.e. excluding CO to CO_2 conversion).

Table 6.1. Conditions for the *in-situ* activation in hydrogen of unsupported and silica supported $NiFe_2O_4@Co_3O_4$ core-shell nanoparticles.

Catalyst	$T_{reduction}$/°C	$t_{reduction}$/hours	H_2 space velocity/ml_n $g_{catalst}^{-1}$ hr^{-1}
$NiFe_2O_4@Co_3O_4$ and $NiFe_2O_4@Co_3O_4/SiO_2$	180	1	6000
$NiFe_2O_4@Co_3O_4$ and $NiFe_2O_4@Co_3O_4/SiO_2$	230	2	

6.3 Results and discussion

The BF-TEM image of the Stöber silica spheres (Figure 6.1) shows uniform round particles with a relatively smooth surface. The crystallite size distribution for these particles was fitted to a lognormal distribution (Figure B.7 in Appendix B) and showed a mean size range between 188.4 nm (at a 95% confidence). These particles had a surface area of 54 m^2 g^{-1} and a pore volume of 0.14 ml g^{-1} with mesopores being present of an average pore diameter of 9 nm (refer to Appendix B, Table B.3).

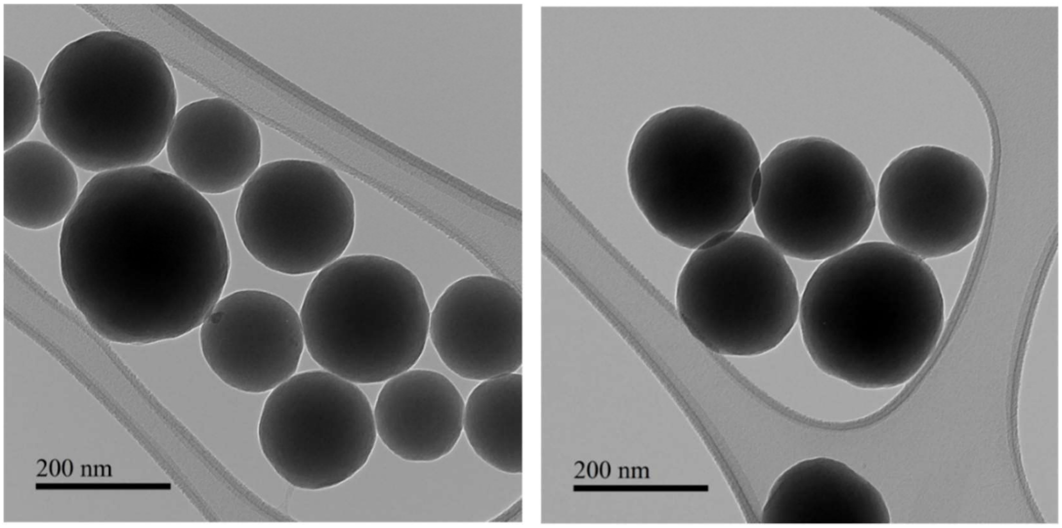

Figure 6.1. BF-TEM image of the Stöber silica spheres prepared.

Reflections characteristic of $NiFe_2O_4$ ($L_{vol\text{-}IB}$ = 12 nm) were present in the X-ray powder diffraction pattern of $NiFe_2O_4$@Co_3O_4/SiO_2 with a broad peak between 2θ = 25° and 35° assigned to the amorphous Stöber silica spheres support (see Figure B.8 and Table B.4 in Appendix B). The absence of reflections for Co_3O_4 has previously been explained (Chapter 4) as being due to the thin Co_3O_4 shell that would inhibit coherent scattering resulting in the formation of a diffraction pattern.

The $NiFe_2O_4$@Co_3O_4 core-shell nanoparticles (see inset of Figure 6.2 (b)) were anchored on the Stöber silica spheres (Figure 6.2). However as shown in the annular dark field (ADF) images, some nanoparticles remained unsupported (Figure 6.2 (a)) whilst some were present within agglomerates on the surface of the silica spheres (Figure 6.2 (b)) and others dispersed as individual nanoparticles (Figure 6.2 (c)) on the support. Nonetheless, the presence of $NiFe_2O_4$@Co_3O_4 core-shell nanoparticles on the support surface is also reflected in its BET surface area (37 $m^2\ g^{-1}$) which was lower relative to the Stöber silica spheres (54 $m^2\ g^{-1}$). In comparison to Stöber silica spheres, negligible changes to the pore volume and average pore size were evidenced for $NiFe_2O_4$@Co_3O_4/SiO_2 (Table B.3, Appendix B). Similar results were reported by Haghtalab and Mosayebi [1] for their Co@Ru/γ-Al_2O_3.

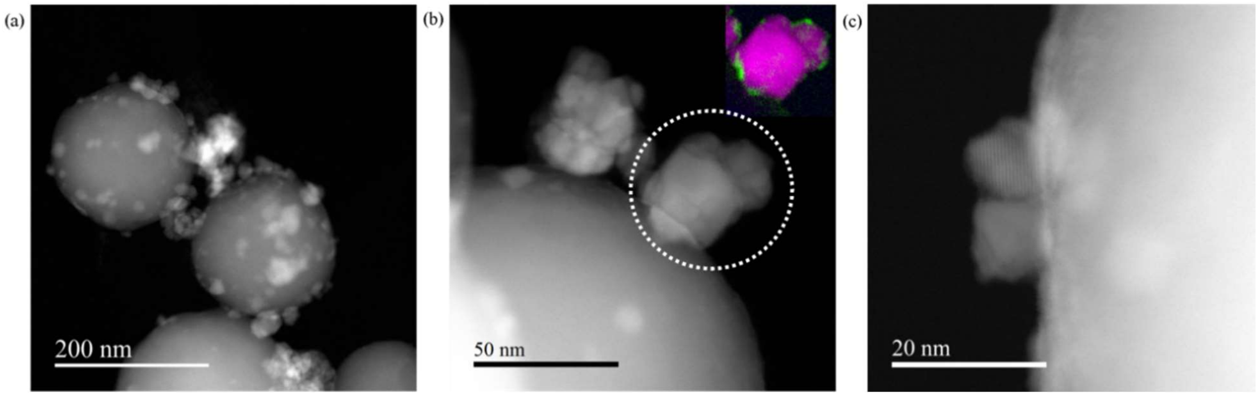

Figure 6.2. (a) – (c): ADF images of $NiFe_2O_4$@Co_3O_4 core-shell nanoparticles supported on silica spheres. The inset in (b) shows the EELS SI map of the nanoparticle indicated by the white dashed circle. Note: green represents cobalt and the NiFe composite is shown in pink.

The TPR-profiles of $NiFe_2O_4$@Co_3O_4/SiO_2 were similar in shape to the TPR-profile of $NiFe_2O_4$@Co_3O_4, although the temperature maxima occurred at different temperatures (refer to Table B.5 in Appendix B). This may be a consequence of the different masses used for each replicate (refer to Table B.5 in Appendix B) and/or nanoparticle-support interaction. The Co_3O_4 shell on $NiFe_2O_4$@Co_3O_4 core-shell nanoparticles was partially reduced between 50 and 250°C (see chapter 4). Examining this temperature region in the TPR profile of $NiFe_2O_4$@Co_3O_4/SiO_2 (see inset in Figure 6.3) shows the subtle appearance of two peaks, at slightly higher temperature, than in the reduction profile of the corresponding unsupported material. Similar to the reduction profile of the unsupported $NiFe_2O_4@Co_3O_4$ core-shell nanoparticles, the onset of reduction observed for $NiFe_2O_4@Co_3O_4/SiO_2$ is around 100°C. It is possible that further reduction of the shell occurs whilst the ferrite core is reducing which was demonstrated for $NiFe_2O_4@Co_3O_4$ core-shell nanoparticles (see Chapter 4).

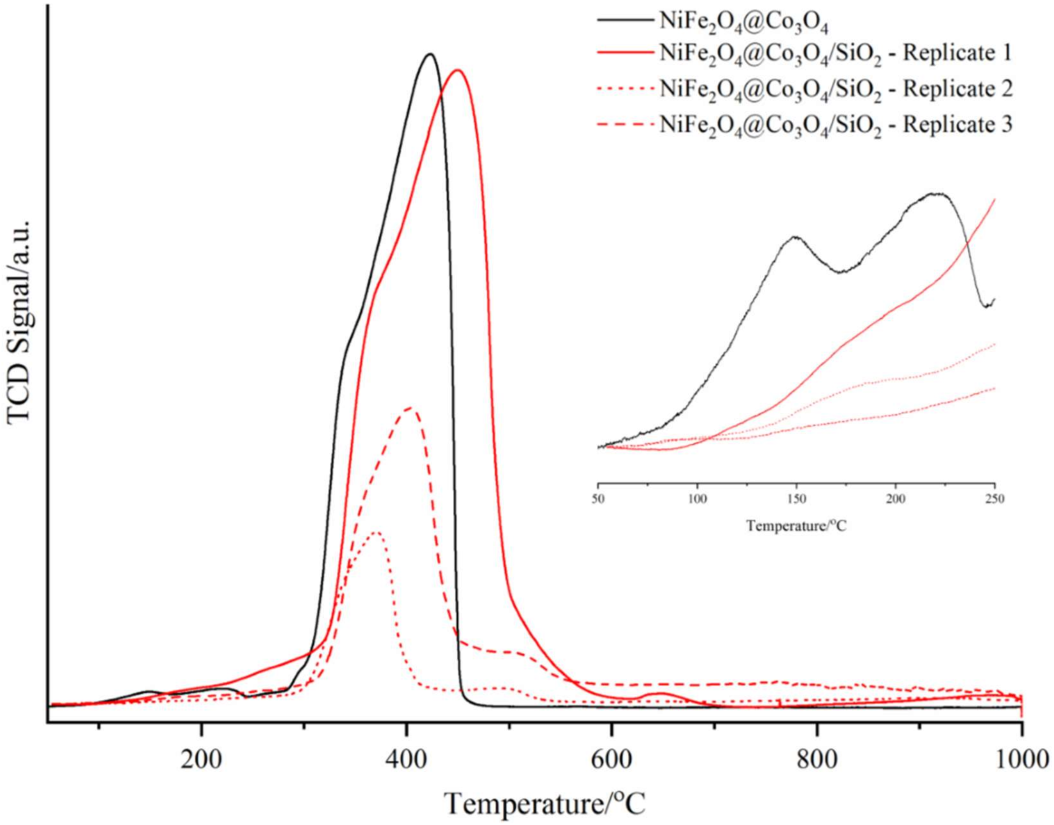

Figure 6.3. TPR profile of $NiFe_2O_4@Co_3O_4$ and $NiFe_2O_4@Co_3O_4/SiO_2$. The inset shows the low temperature peaks which was expanded for clarity on a separate intensity scale.

Above 300°C, the reduction of the ferrite core occurs and the TPR profile shown in Figure 6.3 shows a slight shift to higher temperature for the supported core-shell nanoparticles. However, the repeat measurements showed that reduction also occurred at similar or lower temperatures to the unsupported material (refer to Table B.5 in Appendix for temperature maxima and Figure B.9 – Figure B.11 for fitted profiles). It is known that interactions between nanoparticles and the support may introduce a difference in the reduction temperature/s between unsupported and supported materials [2, 6, 19]. Thus, the presence of some nanoparticle-support interaction is likely however variation in the reduction temperature amongst the replicate analysis may also be due to the different mass used for each replicate.

In-depth detail on the $NiFe_2O_4$ reduction pathway was provided in Chapter 4 where it was shown that the reduction of $NiFe_2O_4$ occurs *via* the formation of NiO and magnetite that is subsequently reduced to FeO and metallic Ni. The last step in its reduction pathway is the formation of metallic iron. Each of the former reduction steps occurs at a different temperatures in the supported material. In fact, it may be that the peak above 450°C in the three replicates of the TPR profile of $NiFe_2O_4@Co_3O_4/SiO_2$ is due to the reduction of FeO into metallic iron with a strong metal-support interaction. It should be noted that in one repeat, this reduction peak was found at ~ 650°C. Similar observations, with respect to the high temperature reduction peak, in the reduction profile of Ni-Fe supported on SBA-15 were reported by Kathiraser *et al.*[33].

Previous work discussed the use of two different reduction regimes, namely, 180°C for 1 hour and 230°C for 2 hours (Chapter 5) for the activation of unsupported $NiFe_2O_4@Co_3O_4$ core-shell nanoparticles. These reduction conditions were also applied to the Stöber silica spheres supported $NiFe_2O_4@Co_3O_4$ core-shell nanoparticles. After reduction at 180°C (1 hour), the hydrogen uptake for both the supported and unsupported core-shell nanoparticles was low (Table 6.2) resulting in a similar active metal surface area. After reduction at 230°C (2 hours), there was a marked increase in hydrogen uptake for $NiFe_2O_4@Co_3O_4/SiO_2$ in comparison to the unsupported nanoparticles (Table 6.2). As a result, the active metal surface area increased to 3.77 $m^2\ g^{-1}$ as compared to 0.85 $m^2\ g^{-1}$ for the unsupported $NiFe_2O_4@Co_3O_4$ core-shell nanoparticles. Interestingly, a comparison of the active metal surface area for $NiFe_2O_4@Co_3O_4/SiO_2$ after each reduction regime shows that this property increased after reduction at 230°C (2 hours) relative to after reduction at 180°C (1 hour). This is different to what was observed for the unsupported material where the active metal surface area decreased after reduction at 230°C (two hours) and was attributed to the loss of the core-shell structure (Chapter 5).

Table 6.2. Results from H_2 pulse chemisorption of the catalyst samples activated in hydrogen.

Results	**Reduction at 180°C for 1 hour**		**Reduction at 230°C for 2 hours**	
	$NiFe_2O_4@Co_3O_4$	$NiFe_2O_4@Co_3O_4/SiO_2$	$NiFe_2O_4@Co_3O_4$	$NiFe_2O_4@Co_3O_4/SiO_2$
H_2-uptake^a/µmol g_{Co}^{-1}	21.9	21.0	10.3	47.3
Active metal surface area^b/$m^2\ g_{Co}^{-1}$	1.74	1.67	0.85	3.77

[a] H_2-uptake on the reduced catalyst using pulse chemisorption

[b] Based on H_2-uptake assuming only metallic cobalt with 14.6 Co atoms/nm^2

6.3.1 Fischer-Tropsch synthesis

The cobalt-time yield after reduction at 180°C (1 hour) was similar for both unsupported and Stöber silica spheres supported $NiFe_2O_4@Co_3O_4$ core-shell nanoparticles (Figure 6.4) when tested for the Fischer-Tropsch synthesis at 230°C, 20 bar (CO conversion = 3 ± 1%; note that the space velocity was lowered for $NiFe_2O_4@Co_3O_4/SiO_2$ due to the lower amount of cobalt per gram of catalyst).

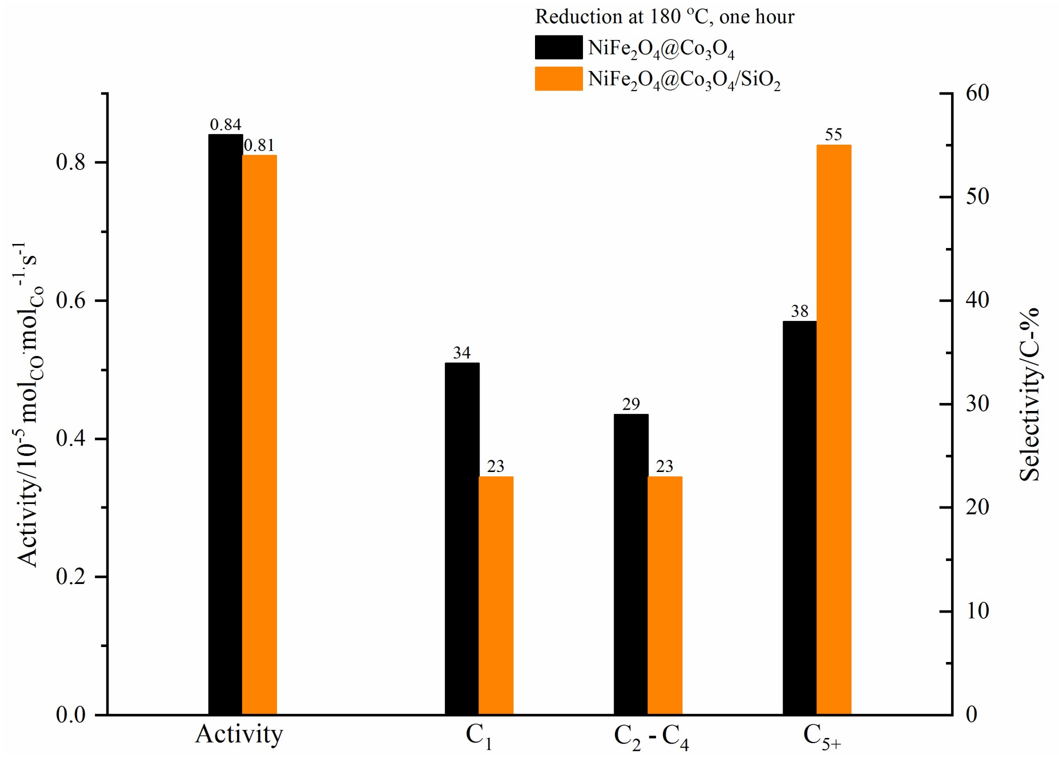

Figure 6.4. Comparison of activity and selectivity ($T_{reaction}$ = 230°C, p = 20 bar, CO conversion = 3 ± 1%) between unsupported and Stöber silica spheres supported $NiFe_2O_4@Co_3O_4$ core-shell nanoparticles activated at 180°C for 1 hour (space velocity of 6149 and 1520 $ml_n\ g^{-1}\ h^{-1}$ respectively).

The similarity in active metal surface per gram of cobalt calculated for each catalyst (refer to Table 6.2) may also account for the similarity in activity per gram of cobalt. The C_1 and $C_2 – C_4$ selectivity was 23 C-%, respectively, for $NiFe_2O_4@Co_3O_4/SiO_2$ with a C_{5+} selectivity of 55 C-%. In contrast, unsupported $NiFe_2O_4@Co_3O_4$ core-shell nanoparticles had a lower C_{5+} selectivity of 38 C-% and a C_1 and $C_2 – C_4$ selectivity of 34 C-% and 29 C-%, respectively. The difference in product distribution between unsupported and silica supported $NiFe_2O_4@Co_3O_4$ core-shell nanoparticles may be due to the different gas velocity used. The $C_2 – C_4$ olefin selectivity (Table 6.3) was found to be lower for $NiFe_2O_4@Co_3O_4/SiO_2$ than unsupported $NiFe_2O_4@Co_3O_4$ core-shell nanoparticles. Owing to the higher C_{5+} selectivity, lower methane selectivity and lower olefin selectivity, it is suggested that the lower space velocity (higher residence time) used during the Fischer-Tropsch synthesis with $NiFe_2O_4@Co_3O_4/SiO_2$ may have caused selective readsorption of α-olefins and chain initiation [34] thereby resulting in the observed product distribution. A lower space velocity has been shown to influence the readsorption of α-olefins thus resulting in the reversal of the β-dehydrogenation step leading to a higher C_{5+} selectivity and a lower methane and lower olefin selectivity within the reaction product [34-37]. The physical structure of the support, may to some extent, also influence the product distribution due to intrapellet diffusion that could affect readsorption and chain initiation by α-olefins [38]. It may be speculated that under the Fischer-Tropsch synthesis, the core may also play a trivial role in the performance of these $NiFe_2O_4@Co_3O_4/SiO_2$ core-shell nanoparticles since the ferrite core seems to be minimally affected upon exposure to the low temperature reduction conditions and the Fischer-Tropsch synthesis (see chapter 5, Figure 5.7 and chapter 5, Table 5.5).

Table 6.3. Olefin selectivity in the Fischer-Tropsch synthesis over the reduced unsupported and Stöber silica spheres supported $NiFe_2O_4@Co_3O_4$ core-shell nanoparticles (Reduction at 180°C (1 hour); $T_{reaction} = 230°C$, p = 20 bar; CO conversion = 3 ± 1%).

Sample	**Syngas SV[a]/ $ml_n\ g_{catalyst}^{-1}\ hr^{-1}$**	**Olefin selectivity/mol-%**		
		C_2	C_3	C_4
$NiFe_2O_4@Co_3O_4$	6149	3.9	7.2	3.0
$NiFe_2O_4@Co_3O_4/SiO_2$	1520	b.d.[b]	2.1	b.d.[b]

[a] SV = Space velocity.

[b] b.d. refers to below detection limit.

Prior to examining the performance of $NiFe_2O_4@Co_3O_4/SiO_2$ after reduction at 230°C (2 hours), the phase composition and structure of the used material (after reduction and exposure to the Fischer-Tropsch synthesis) was studied. After reduction at 230°C (2 hours), the physico-chemical properties of unsupported and Stöber silica spheres supported $NiFe_2O_4@Co_3O_4$ core-shell nanoparticles showed a noticeable difference as indicated above. This suggested that the presence of the support may have altered the phase composition and/or nanoscale structure present after reduction and exposure to Fischer-Tropsch synthesis conditions. Therefore, *in-situ* reduction (230°C, 2 hours) and exposure to Fischer-Tropsch synthesis conditions (230°C, 16 bar, 16 hours) was carried out in a XRD cell to determine the changes, if any, in the phase composition and structure of $NiFe_2O_4@Co_3O_4$ core-shell nanoparticles supported on Stöber silica spheres (see Table 6.4) .

Table 6.4. Relative phase abundance and average crystallite size of the various phases present in $NiFe_2O_4@Co_3O_4/SiO_2$ after activation in H_2 at 230°C (2 hours) and exposure to Fischer-Tropsch conditions ($T_{reaction}$ = 230°C, p = 16 bar) determined from the Rietveld refinement of experimental powder diffraction data obtained during the *in-situ* experiments.

	Phase	**H_2 activation**		**After exposure to Fischer-Tropsch conditions[c]**	
		Unsupported $NiFe_2O_4@Co_3O_4$	$NiFe_2O_4@Co_3O_4/SiO_2$	Unsupported $NiFe_2O_4@Co_3O_4$	$NiFe_2O_4@Co_3O_4/SiO_2$
Relative phase abundance, mass %[a]	$NiFe_2O_4$	90.6 (0.3)	81.4 (0.4)	71.3 (1.5)	68.2 (0.5)
	Fe_2C	-	-	11.6 (1.6)	
	$Fe_{0.8}Ni_{0.2}$	-	13.2 (0.4)	13.6 (0.9)	24.5 (0.5)
	$Fe_{0.625}Ni_{0.375}$	9.4 (0.3)	5.4 (0.2)	3.6 (0.6)	7.3 (0.2)
Average crystallite size, nm[a, b]	$NiFe_2O_4$	15.6 (0.3)	14.0 (0.2)	19.9 (0.7)	14.5 (0.3)
	Fe_2C	-	-	5.8 (1.0)	-
	$Fe_{0.8}Ni_{0.2}$	-	8.3 (0.4)	8.1 (0.8)	4.1 (0.2)
	$Fe_{0.625}Ni_{0.375}$	10.0 (0.5)	155.0 (49.0)	3.6 (0.6)	110.3 (21.3)

[a] Uncertainty given in parenthesis.

[b] Volume-weighted average crystallite size determined from the integral breadth.

[c] $T_{reaction}$ = 230°C, p = 16 bar for 16 hours

After activation at 230°C (2 hours) and exposure to the Fischer-Tropsch synthesis conditions, $NiFe_2O_4$ and iron-nickel alloys ($Fe_{0.8}Ni_{0.2}$ and $Fe_{0.625}Ni_{0.375}$) were present in $NiFe_2O_4@Co_3O_4/SiO_2$ (Table 6.4). These phases were also identified in unsupported $NiFe_2O_4@Co_3O_4$ core-shell nanoparticles after exposure to the same conditions. Smaller crystallites of $Fe_{0.8}Ni_{0.2}$ were present in $NiFe_2O_4@Co_3O_4/SiO_2$ whilst the $NiFe_2O_4$ crystallites were similar in size after exposure to the Fischer-Tropsch conditions as to the size determined in the reduced nanoparticles. It is also worth noting that the size of $Fe_{0.8}Ni_{0.2}$ crystallites were smaller in $NiFe_2O_4@Co_3O_4/SiO_2$ than in the unsupported material, after reduction and exposure to Fischer-Tropsch synthesis conditions.

The STEM-HAADF image (Figure 6.5 (a)) indicated that the crystallite morphology of the core-shell nanoparticles in $NiFe_2O_4@Co_3O_4/SiO_2$ after reduction at 230°C (2 hours) and exposure to Fischer-Tropsch synthesis conditions was similar to the as-synthesized material (refer to Figure 6.2). In fact, EELS spectrum imaging (Figure 6.5 (b) and (c)) showed that the core-shell structure was still present with a cobalt shell approximately 2 nm thick around the Ni-Fe core. In contrast to unsupported $NiFe_2O_4@Co_3O_4$ core-shell nanoparticles that was reduced at 230°C for 2 hours prior to being exposed to Fischer-Tropsch synthesis conditions (refer to Chapter 5, Figure 5.8 – Figure 5.10), this finding showed that the use of Stöber silica spheres minimized changes to the nanoparticle structure. This may be ascribed to the support reducing the contact between individual core-shell nanoparticles. These results also demonstrated that the use of a support aided in stabilizing the core-shell structure under reduction and reaction conditions. Calderone *et al*.[9] indicated that the use of a mesoporous silica support for their Fe_3O_4@Co_3O_4 core-shell nanoparticles may have been beneficial for retaining the core-shell structure under reducing conditions. It is likely then that the core-shell structure as well as the presence of two Fe-Ni alloys after exposure to reactive conditions resulted in the observed active metal surface area (Table 6.2). It should be noted that Ni-Fe nanoparticles were observed on the support surface after reduction at 230°C (2 hours) and exposure to Fischer-Tropsch conditions (refer to Figure 6.5). It was previously shown (refer to chapter 3) that some $NiFe_2O_4$ nanoparticles did not have a cobalt shell in the as-synthesized $NiFe_2O_4$@Co_3O_4 core-shell nanoparticles and therefore it may be that these nanoparticles are the Ni-Fe nanoparticles observed in Figure 6.5.

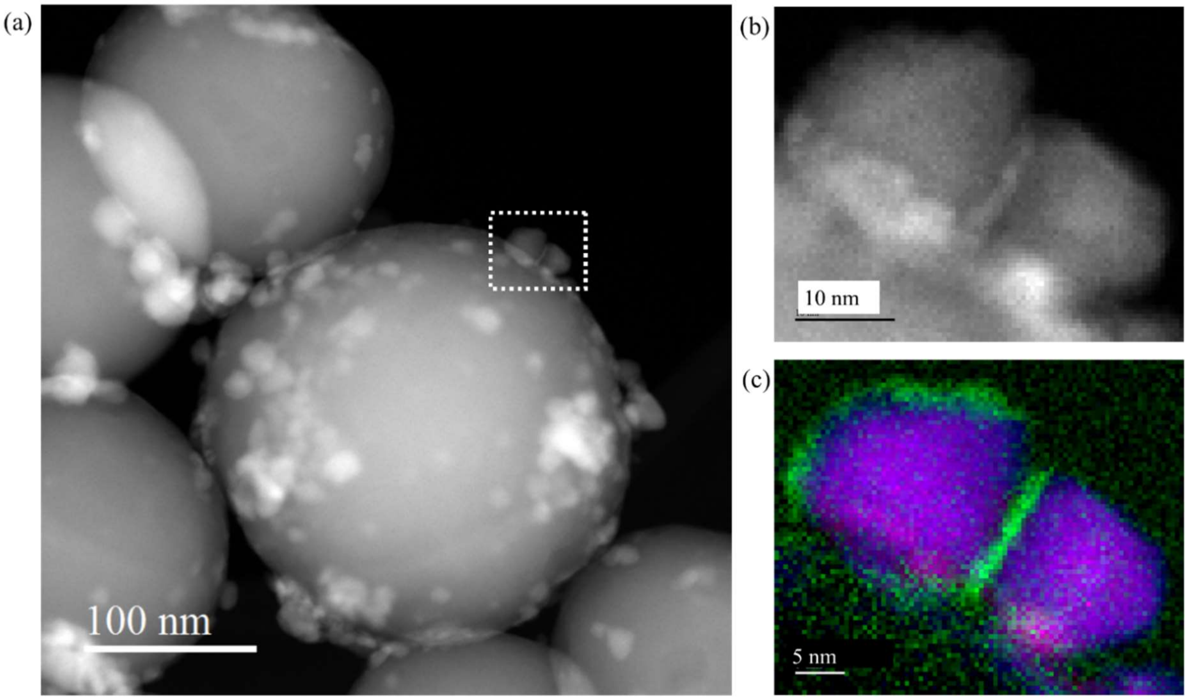

Figure 6.5. (a) STEM-HAADF image of $NiFe_2O_4$@Co_3O_4 core-shell nanoparticles supported on silica spheres after reduction at 230°C (2 hours) and exposure to Fischer-Tropsch synthesis conditions ($T_{reaction}$ = 230°C, 20 bar) in an *in-situ* XRD cell. The white rectangle shows the region from which the EELS spectrum images was generated; (b) DF image and (c) composite elemental map obtained from the EELS spectrum images of the nanoparticles indicated by the white dashed rectangle in (a). Note: green represents cobalt and the Ni-Fe composite is shown in indigo.

The catalytic performance in the Fischer-Tropsch synthesis (230°C, 20 bar, CO conversion = 3 ± 1%) of unsupported and Stöber silica spheres supported $NiFe_2O_4$@Co_3O_4 core-shell nanoparticles, reduced at

230°C (2 hours) is shown in Figure 6.6. There was a marked increase in the catalytic activity obtained with $NiFe_2O_4@Co_3O_4/SiO_2$ when compared to unsupported $NiFe_2O_4@Co_3O_4$ core-shell nanoparticles possibly due to the activity of the $Fe_{0.8}Ni_{0.2}$ nanoparticles present in $NiFe_2O_4@Co_3O_4/SiO_2$. The difference in nanoscale structure after reduction and exposure to Fischer-Tropsch conditions may have also played a role in the observed activity. The similarity in the product distribution between the catalysts suggested that the factors which influenced selectivity of unsupported $NiFe_2O_4@Co_3O_4$ core-shell nanoparticles (Chapter 4 and 5) could have affected product formation over $NiFe_2O_4@Co_3O_4/SiO_2$.

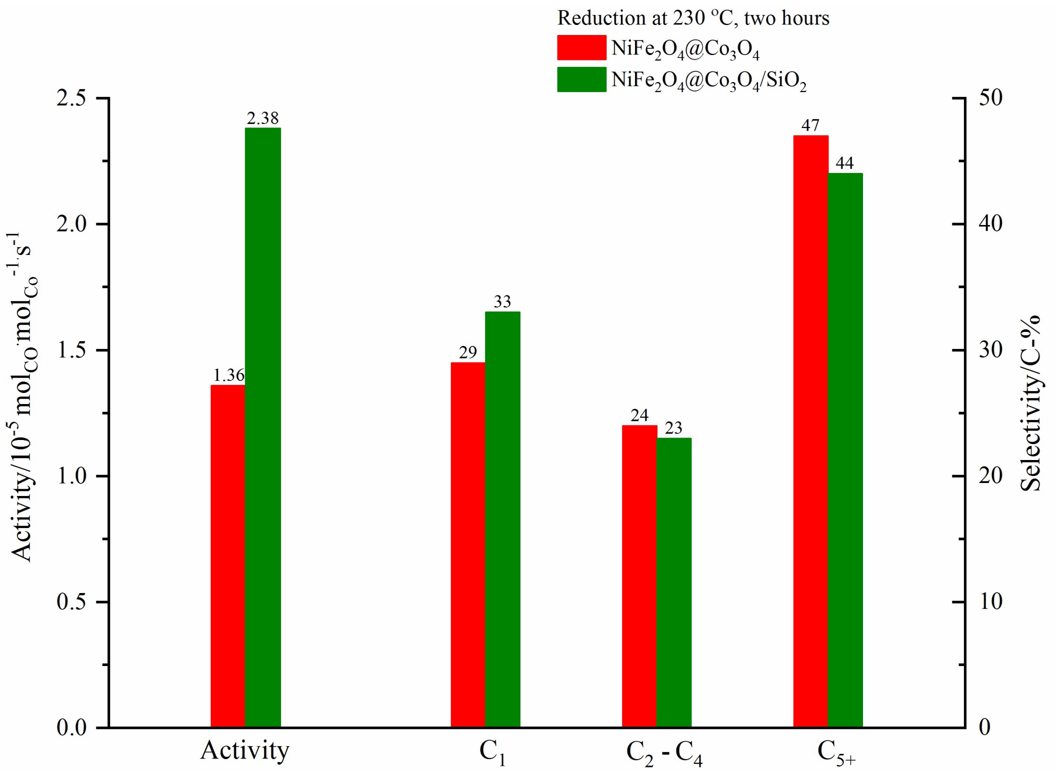

Figure 6.6. Comparison of activity and selectivity ($T_{reaction}$ = 230°C, p = 20 bar, CO conversion = 3 ± 1%) between unsupported and Stöber silica spheres supported $NiFe_2O_4@Co_3O_4$ core-shell nanoparticles activated at 230°C for 2 hours (space velocity between 7755 and 9299 $ml_n\ g^{-1}\ h^{-1}$).

A comparison of the performance of $NiFe_2O_4@Co_3O_4/SiO_2$ activated at two different reduction conditions (as give in Table 6.1) is given in Table 6.5. At these conditions, the CO conversion was 3 ± 1%. The activation conditions was shown to have an influence on the cobalt-time yield, where activation at 180°C (1 hour) resulted in a lower cobalt-time yield (8.06 $\mu mol_{CO} \cdot g_{Co}^{-1} \cdot s^{-1}$) than when activation was done at 230°C (2 hours) (23.83 $\mu mol_{CO} \cdot g_{Co}^{-1} \cdot s^{-1}$). It was previously speculated that the higher activity obtained with reduction at 230°C (2 hours) was due to the contribution from the shell and the partially reduced core (Ni-Fe alloys) (Chapter 4 and 5). The former is likely applicable to $NiFe_2O_4@Co_3O_4/SiO_2$. It should be noted that the higher active metal surface could have also contributed to the activity after activation at 230°C (2 hours) (see Table 6.2).

Table 6.5. Activity and selectivity in the Fischer-Tropsch synthesis over the reduced $NiFe_2O_4@Co_3O_4/SiO_2$ (activation conditions given in Table 6.1; $T_{reaction}$ = 230°C, p = 20 bar; CO conversion = 3 ± 1%).

Sample	**Syngas SV**[a]**/ ml$_n$ g$_{catalyst}^{-1}$ hr^{-1}**	**S_{CO2}**[b]**/ %**	**r_{FT}**[c]**/ 10^{-5} mol$_{CO}$·g$_{Co}^{-1}$·s^{-1}**	**Fraction in organic product/C-%**		
				C_1	$C_2 – C_4$	C_{5+}
Reduction at 180°C, 1 hour	1520	3	0.81	23	22	55
Reduction at 230°C, 2 hours	9299	3	2.38	33	23	44

[a] SV = Space velocity

[b] S_{CO2} refers to the CO_2 selectivity

[c] r_{FT} refers to the integral rate or cobalt-time yield

Table 6.6. Olefin selectivity in the Fischer-Tropsch synthesis over the reduced Stöber silica spheres supported $NiFe_2O_4@Co_3O_4$ core-shell nanoparticles (Activation conditions given in Table 6.1; $T_{reaction}$ = 230°C, p = 20 bar; CO conversion = 3 ± 1%).

Sample	**Syngas SV**[a]**/ ml$_n$ g$_{catalyst}^{-1}$ hr^{-1}**	**Olefin selectivity/mol-%**		
		C_2	C_3	C_4
Reduction at 180°C, 1 hour	1520	b.d.[b]	2.1	b.d.[b]
Reduction at 230°C, 2 hours	9299	1.7	5.8	1.6

[a] SV = Space velocity.

[b] b.d. refers to below detection limit.

There is a marked difference in the C_1 selectivity between $NiFe_2O_4@Co_3O_4/SiO_2$ (reduced at 180°C, 1 hour) and $NiFe_2O_4@Co_3O_4/SiO_2$ (reduced at 230°C, 2 hours). The lower C_1 selectivity (23 C-%) after the application of a milder reduction condition was accompanied by an increased C_{5+} selectivity (55 C-%). On the other hand, after activation at 230°C (2 hours), the C_{5+} selectivity was 44 C-% whilst a 33 C-% selectivity towards C_1 was determined. The selectivity towards $C_2 – C_4$ products was similar with each reduction condition. Additionally, the selectivity to $C_2 – C_4$ olefins was higher with $NiFe_2O_4@Co_3O_4/SiO_2$ (reduced at 230°C, 2 hours) than the material reduced at the lower temperature (Table 6.6). This indicates that the observed selectivity differences is a possible outcome of the different syngas velocity used. It was discussed earlier that the lower gas velocity used for $NiFe_2O_4@Co_3O_4/SiO_2$ (reduced at 180°C, 1 hour) may influence secondary reactions where the re-adsorption of olefins may reverse a surface chain termination pathway by permitting α-olefins to re-enter the chain growth pathways [34].

6.4 Chapter summary

$NiFe_2O_4$@Co_3O_4 core-shell nanoparticles were supported on Stöber silica spheres. This material was reduced at either 180°C (1 hour) or 230°C (2 hours) prior to characterization and the Fischer-Tropsch synthesis. A similar activity was found for unsupported and supported $NiFe_2O_4$@Co_3O_4 core-shell nanoparticles after reduction at 180°C (1 hour) and therefore the influence of the support could not be properly established. However, after reduction at 230°C for 2 hours, there was an increase in cobalt-time yield of the supported nanoparticles in comparison to the unsupported material. This was likely due to $Fe_{0.8}Ni_{0.2}$ in supported $NiFe_2O_4$@Co_3O_4 core-shell nanoparticles after reduction at 230°C (2 hours). The C_{5+} selectivity was similar between unsupported and Stöber silica spheres supported $NiFe_2O_4$@Co_3O_4 core-shell nanoparticles and may have been due to the similar phase composition present in both materials after reduction at 230°C (2 hours) and exposure to Fischer-Tropsch synthesis conditions. Similar to the findings of chapter 5, the reduction conditions influenced the Fischer-Tropsch synthesis performance of the $NiFe_2O_4$@Co_3O_4/SiO_2 core-shell nanoparticles. Reduction at 230°C (2 hours) showed a higher activity (23.80 $\mu mol_{CO} \cdot g_{Co}^{-1} \cdot s^{-1}$) than was obtained when reduction was done at milder reduction condition. $NiFe_2O_4$@Co_3O_4/SiO_2 (180°C, 1 hour) showed a higher C_{5+} selectivity (55 C-%) than the material reduced at 230°C for 2 hours (44 C-%) and was a likely effect of the lower syngas space velocity used for the material reduced at the lower temperature. An important finding of this work was that the use of Stöber silica spheres resulted in $NiFe_2O_4$@Co_3O_4 core-shell nanoparticles retaining the core-shell structure even after reduction at 230°C and exposure to Fischer-Tropsch conditions.

6.5 References

[1] A. Haghtalab, A. Mosayebi, Co@Ru nanoparticle with core-shell structure supported over ã-Al_2O_3 for Fischer-Tropsch synthesis, Int. J. Hydrogen Energy, 39 (2014) 18882-18893.

[2] A. Martínez, C. López, F. Márquez, I. Díaz, Fischer-Tropsch synthesis of hydrocarbons over mesoporous co/SBA-15 catalysts: the influence of metal loading, cobalt precursor and promoters, J. Catal., 220 (2003) 486-499.

[3] A. Y. Khodakov, R. Bechara, A. Griboval-Constant, Fischer-Tropsch synthesis over silica supported cobalt catalysts: mesoporous structure versus cobalt surface density, Appl. Catal. A: Gen., 254 (2003) 273-288.

[4] A. Y. Khodakov, Fischer-Tropsch Synthesis: relations between structure of cobalt catalysts and their catalytic performance, Catal. Today, 144 (2009) 251-257.

[5] H. Qin, S. King, Y. Wang, H. Li, Z. Ni, Y. Huang, Y. Li, X. Li, Lignin-based fabrication of Co@C core-shell nanoparticles as efficient catalyst for selective Fischer-Tropsch synthesis of C_{5+} compounds, ACS Sustainable Chem. Eng., 4 (2016) 1240-1247.

[6] R. Xie, H. Wang, P. Gao, L. Xia, Z. Zhang, T. Zhao, Y. Sun, Core@shell Co_3O_4@C-*m*-SiO_2 catalysts with inert C modified mesoporous channel for desired middle distillate, Appl. Catal. A: Gen., 492 (2015) 93-99.

[7] A. Govender, W. Barnard, E. J. Olivier, R. P. Forbes, E. van Steen, J. H. Neethling, Synthesis and characterization of $NiFe_2O_4$@Co_3O_4 core-shell nanoparticles, Mater. Charac., 121 (2016) 93-102.

[8] V. R. Calderone, N. R. Shiju, D. Curulla-Ferre, S. Chambrey, A. Y. Khodakov, A. Rose, J. Thiessen, A. Jess, G. Rothenberg, De novo design of nanostructured iron-cobalt Fischer-Tropsch catalysts, Angew. Chem. Int. Ed., 52 (2013) 4397-4401.

[9] V. R. Calderone, N. R. Shiju, G. Rothenberg, D. Curulla-Ferre, Core-shell particles with catalytic activity, United States Patent, United States, US 9,539,563 B2, 2018.

[10] V. R. Calderone, N. R. Shiju, G. Rothenberg, D. Curulla-Ferre, Core-shell particles with catalytic activity and the process of their preparation. Method of preparation of Fischer-Tropsch catalyst comprising said particles, European Patent Office, Europe, EP2740534A1, 2014.

[11] A. Goswami, A. K. Rathi, C. Aparicio, O. Tomanec, M. Petr, R. Pocklanova, M. B. Gawande, R. S. Varma, R. Zboril, In situ generation of Pd-Pt core-shell nanoparticles on reduced graphene oxide (Pd@Pt/rGO) using microwaves: Applications in dehalogenation reactions and reduction of olefins, ACS Appl. Mater. Interfaces, 9 (2017) 2815-2824.

[12] M. B. Gawande, A. Goswami, T. Asefa, H. Guo, A. V. Biradar, D.-L. Peng, R. Zboril, R. S. Varma, Core-shell nanoparticles: Synthesis and applications in catalysis and electrocatalysis, Chem. Soc. Rev., 44 (2015) 7540-7590.

[13] R. G. Chaudhuri, S. Paria, Core/Shell nanoparticles: classes, properties, synthesis mechanisms, characterization and applications, Chem. Rev., 112 (2012) 2373-2433.

[14] A. U. Nilekar, S. Alayoglu, B. Eichhorn, M. Mavrikakis, Preferential CO oxidation in hydrogen: Reactivity of core-shell nanoparticle, J. Am. Chem. Soc., 132 (2010) 7418-7428.

[15] C.-J. Zhong, M. M. Maye, Core-Shell nanoparticles as catalysts, Adv. Mater., 13 (2001) 1507-1511.

[16] H.-L. Jiang, T. Akita, T. Ishida, M. Haruta, Q. Xu, Synergistic catalysis of Au@Ag core-shell nanoparticles stabilized on metal-organic framework, J. Am. Chem. Soc., 133 (2011) 1304-1306.

[17] H. M. Song, D. H. Anjum, R. Sougrat, M. N. Hedhili, N. M. Khashab, Hollow Au@Pd and Au@Pt core-shell nanoparticles as electrocatalysts for ethanol oxidation reactions, J. Mater. Chem., 22 (2012) 24959-25506.

[18] T. Hirakawa, P. V. Kamat, Charge separation and catalytic activity of Ag@TiO_2 core-shell composite clusters under UV-irradiation, J. Am. Chem. Soc., 127 (2005) 3928-3924.

[19] R. Xie, D. Li, B. Hou, J. Wang, L. Jia, Y. Sun, Solvothermally derived Co_3O_4@*m*-SiO_2 nanocomposite for Fischer-Tropsch synthesis, Catal. Comm., 12 (2011) 380-383.

[20] D. Wang, C. Chen, J. Wang, L. Jia, B. Hou, D. Li, High thermal conductive core-shell structured Al_2O_3@Al composite supported cobalt catalyst for Fischer-Tropsch synthesis, Appl. Catal. A: Gen., 527 (2016) 60-71.

[21] A. Y. Khodakov, W. Chu, P. Fongarland, Advances in the development of novel cobalt Fischer-Tropsch catalysts for the synthesis of long-chain hydrocarbons and clean fuels, Chem. Rev., 107 (2007) 1692-1744.

[22] Q. Zhang, J. Kang, Y. Wang, Development of novel catalysts for the Fischer-Tropsch synthesis: Tuning the product selectivity, Chem. Cat. Chem., 2 (2010) 1030-1058.

[23] A. Beltram, M. Melchionna, T. Montini, L. Nasi, R. J. Gorte, M. Prato, P. Fornasiero, Improved activity and stability of Pd@CeO_2 core-shell catalysts hybridized with multi-walled carbon nanotubes in the water gas shift reaction, Catal. Today, 253 (2015) 142-148.

[24] K. Sasaki, K. A. Kuttiyiel, L. Barrio, D. Su, A. I. Frenkel, N. Marinkovic, D. Mahajan, R. R. Adzic, Carbon-supported IrNi core-shell nanoparticles: Synthesis, characterization and catalytic activity, J. Phys. Chem. C, 115 (2011) 9894-9902.

[25] A. Mosayebi, R. Abedini, H. Bakhshi, Ni@Pd nanoparticle with core-shell structure supported over $A\lambda_2O_3$ for partial oxidation process of butane to syngas, Int. J. Hydrogen Energy, 42 (2017) 18941 - 18950.

[26] H. Xu, B. Yan, S. Li, J. Wang, C. Wang, J. Guo, Y. Du, N-doped graphene supported PtAu/Pt intermetallic core/dendritic shell nanocrystals for efficient electrocatalystic oxidation of formic acid, Chem. Eng. J., 334 (2018) 2638-2646.

[27] X. Zou, Z. Rui, H. Ji, Core-shell NiO@PdO nanoparticles supported on alumina as an advanced catalyst for methane oxidation, ACS Catal., 7 (2017) 1615-1625.

[28] Z. Yang, X. Zheng, J. Zheng, Facile synthesis of three-dimensional porous Au@Pt core-shell nanoflowers supported on graphene oxide for highly selective and selective detection of hydrazine, Chem. Eng. J., 327 (2017) 431-440.

[29] J. Zeng, J. Yang, J. Y. Lee, W. Zhou, Preparation of carbon-supported core-shell Au-Pt nanoparticles for methanol oxidation reaction: The promotional effect of the Au core, J. Phys. Chem. B, 110 (2006) 24606-24611.

[30] K. Y. Cho, Y. S. Yeom, H. Y. Seo, P. Kumar, A. S. Lee, K.-Y. Baek, H. G. Yoon, Molybdenum-doped PdPt@Pt core-shell octahedra supported by ionic block copolymer-functionalized graphene as a highly active and durable oxygen reduction electrocatalyst, ACS Appl. Mater. Interfaces, 9 (2017) 1524-1535.

[31] W. Stöber, A. Fink, E. Bohn, Controlled growth of monodisperse silica spheres in the micron size range, J. Colloid Interface Sci., 26 (1968) 62-69.

[32] M. Dad, R. J. Lancee, M. Janse van Vuuren, J. van de Loosdrecht, J. W. H. Niemantsverdriet, H. O. A. Fredriksson, SiO_2-supported Fe & Mn colloids - Fischer-Tropsch synthesis on 3D model catalysts, Appl. Catal. A: Gen., 537 (2017) 83-92.

[33] Y. Kathiraser, J. Ashok, S. Kawi, Synthesis and evaluation of highly dispersed SBA-15 supported Ni-Fe bimetallic catalysts for steam reforming of biomass derived tar reaction, Catal. Sci. Technol., 6 (2016) 4327-4336.

[34] E. Iglesia, S. C. Reyes, R. J. Madon, Transport-enhanced alpha-olefin readsoprtion pathways in Ru-catalyzed hydrocarbon synthesis, J. Catal., 129 (1991) 238-256.

[35] E. Iglesia, Fischer-Tropsch synthesis on cobalt catalysts: Structural requirements and reaction pathyways, Studies in Surf. Sci. Catal., 107 (1997) 153-162.

[36] E. W. Kuipers, C. Scheper, J. H. Wilson, I. H. Vinkenburg, H. Oosterbeek, Non-ASF product dsitributions due to secondary reactions during Fischer-Tropsch synthesis, J. Catal., 158 (1996) 288-300.

[37] V. Sage, Y. Sun, P. Hazewinkel, T. Bhatelia, L. Braconnier, L. Tang, K. Chiang, M. Batten, N. Burke, Modified product selectivity in Fischer-Tropsch synthesis by catalyst pretreatment, Fuel Process. Technol., 167 (2017) 183-192.

[38] E. Iglesia, S. L. Soled, R. A. Fiato, Fischer-Tropsch synthesis on cobalt and ruthenium. Metal dispersion and support effects on reaction rate and selectivity, J. Catal., 137 (1992) 212-224.

7 Conclusion

Core-shell nanoparticles with either a nickel ferrite ($NiFe_2O_4$) core or a zinc ferrite ($ZnFe_2O_4$) core and a cobalt (II, III) oxide (Co_3O_4) shell ($NiFe_2O_4$@Co_3O_4 and $ZnFe_2O_4$@Co_3O_4 respectively) were synthesized and characterized.

The inverted spinel, $NiFe_2O_4$ and the normal spinel, $ZnFe_2O_4$ were first synthesized using the citrate precursor method. Each ferrite was phase pure with an average crystallite size of 14 nm. The production of ferrite nanoparticles with the former characteristics was dependent on the calcination temperature and the molar ratio of Fe/M (where M is either Ni or Zn). Although small nanoparticles were obtained using the citrate precursor method, the crystallite size, fitted with a lognormal distribution function was wide with crystallite sizes from 5 nm to 40 nm.

The premade $NiFe_2O_4$ nanoparticles were used as a core to optimize the synthesis of the core-shell nanoparticles. This was achieved using a simple homogeneous deposition precipitation method where the cobalt (II, III) oxide was formed after synthesis thus eliminating the need for calcination. Concentrations of cobalt in the synthesis solution between 6.3 and 7.6 wt.% cobalt yielded a partial, non-uniform shell whilst higher concentrations resulted in the formation of Co_3O_4 nanoparticles over the $NiFe_2O_4$ surface. Hence, a two-step synthesis was used to obtain core-shell nanoparticles with a more uniform coverage of the $NiFe_2O_4$ surface than the one-step synthesis. The cobalt shell was between 1 and 3 nm thick for the core-shell nanoparticles prepared with the two-step synthesis and the final cobalt loading was 8.3 wt.%. The two-step synthesis was also used to prepare $ZnFe_2O_4$@Co_3O_4 core-shell nanoparticles with a similar shell coverage and thickness as in $NiFe_2O_4$@Co_3O_4 core-shell nanoparticles.

The physico-chemical properties and the catalytic behavior during the Fischer-Tropsch synthesis of $NiFe_2O_4$@Co_3O_4 and $ZnFe_2O_4$@Co_3O_4 core-shell nanoparticles were examined and compared to each other to determine the effect of cobalt present in a shell surrounding a ferrite core. An important finding of the work was that the reduction of the unsupported $NiFe_2O_4$@Co_3O_4 and $ZnFe_2O_4$@Co_3O_4 core-shell nanoparticles, at 230°C and 250°C respectively, destroyed the core-shell structure. This is the first report of the change in nanoscale structure of these core-shell nanoparticle systems. Owing to the loss of the core-shell structure, the influence of strain on the catalytic performance was not further investigated here. The Fischer-Tropsch synthesis over reduced $NiFe_2O_4$@Co_3O_4 and $ZnFe_2O_4$@Co_3O_4 core-shell nanoparticles showed a cobalt-time yield of 13.64 $\mu mol_{CO} \cdot g_{Co}^{-1} \cdot s^{-1}$ and 4.27 $\mu mol_{CO} \cdot g_{Co}^{-1} \cdot s^{-1}$, respectively. The higher activity obtained with $NiFe_2O_4$@Co_3O_4 core-shell nanoparticles was ascribed to the presence of metallic cobalt, iron-nickel alloy and iron carbide (formed from the partial reduction and carburization of the nickel ferrite core under Fischer-Tropsch synthesis conditions).

The use of mild reduction (180°C, 1 hour) was shown to result in the retention of the core-shell structure after reduction and exposure to the Fischer-Tropsch synthesis conditions. Additionally, metallic nickel and iron carbide was identified under reaction conditions. Therefore, a system with a true core-shell structure could be studied for the Fischer-Tropsch synthesis. A low activity and C_{5+} selectivity (8.40 $\mu mol_{CO} \cdot g_{Co}^{-1} \cdot s^{-1}$ and 38 C-% respectively) was found for $NiFe_2O_4@Co_3O_4$ core-shell nanoparticles after reduction at 180°C (1 hour). The activity of $NiFe_2O_4@Co_3O_4$ core-shell nanoparticles after reduction at 180°C (1 hour) was slightly higher than that obtained with unsupported Co_3O_4. The C_{5+} selectivity was higher (81 C-%) with the unsupported Co_3O_4 than $NiFe_2O_4@Co_3O_4$ core-shell nanoparticles reduced at 180°C (1hour). The difference in performance between the core-shell nanoparticles and unsupported Co_3O_4 was possibly due to the lattice strain induced onto the shell. The performance determined for $NiFe_2O_4@Co_3O_4$ core-shell nanoparticles after reduction at 180°C (1 hour) was poorer than that found for these nanoparticles after reduction at 230°C for 2 hours. However, strain effects contributed to a lower activity of the core-shell nanoparticles than would have been expected.

$NiFe_2O_4@Co_3O_4$ core-shell nanoparticles was also supported on Stöber silica spheres. As evidenced with the unsupported material, the use of different reduction conditions (180°C for 1 hour or 230°C for 2 hours) altered the properties and performance of the $NiFe_2O_4@Co_3O_4$ core-shell nanoparticles. The use of a support for $NiFe_2O_4@Co_3O_4$ core-shell nanoparticles showed that the core-shell structure of the as-synthesized material was still present after exposure to reduction at 230°C (2 hours) and Fischer-Tropsch conditions. $NiFe_2O_4@Co_3O_4/SiO_2$ had a higher cobalt-time yield with a similar C_{5+} selectivity than the unsupported material when reduction was done at 230°C for 2 hours. The former was attributed to the higher cobalt metal surface area, the retention of the core-shell structure as well the iron-nickel alloys present after reduction and exposure to Fischer-Tropsch conditions. The use of Stöber silica spheres was shown to be beneficial for retaining the core-shell structure and improving the Fischer-Tropsch synthesis performance of $NiFe_2O_4@Co_3O_4$ core-shell nanoparticles.

This work has shown that there is an opportunity for pursuing the development of core-shell nanoparticles with a cobalt shell for the Fischer-Tropsch synthesis. Furthermore, first reports on the influence of reduction conditions on the $MFe_2O_4@Co_3O_4$ core-shell nanoparticles has been presented. This showed that controlling the reduction conditions may be used as a route for retaining the core-shell structure under Fischer-Tropsch conditions. Additionally, the use of a silica-based support has been shown to be beneficial for retaining the core-shell structure even after reduction and exposure to Fischer-Tropsch conditions. This study has shown that there is a fundamental need for *in-situ* characterization of nanoparticles after exposure to activation and/or reaction conditions to better formulate the structure-activity relationship. The findings of this study has laid the foundation for future research endeavors on core-shell nanoparticles with a cobalt shell.

It may be beneficial for future work, that other synthesis routes are examined for preparing the metal oxide core material with specific focus on yielding a more uniform crystallite morphology with a narrower crystallite size distribution. In maintaining the use of the two-step synthesis described in this work for the synthesis of core-shell nanoparticles, future work could examine whether a variation in the shell thickness may be achieved by using differently sized core nanoparticles. This could be such that smaller crystallite sizes would yield a thinner shell. Another parameter than may be of interest, would be to vary the mass of the core used for the synthesis whilst keeping the concentration of cobalt in the precursor solution unchanged. It is also possible to examine the effect of a calcination step on the structure of the core-shell nanoparticle as this could potentially change the coverage of the core by the shell material and alter the strength of the interaction between the shell and the core.

The comparison between $NiFe_2O_4$@Co_3O_4 and $ZnFe_2O_4$@Co_3O_4 core-shell nanoparticles revealed important considerations for future designs of X@Co_3O_4 core-shell systems (where X represents a suitable metal oxide core). Two strategies can be explored here depending on whether a reactive or non-reactive core is used. For reactive cores, a complete cobalt shell around the core nanoparticles may be preferred to limit the role of the partially or uncovered core nanoparticles. For non-reactive cores, the synthesis method employed in this study may be satisfactory. It is important to consider whether the core or core-shell materials would undergo structural modification during reduction and catalysis. Consideration should also be given to whether Fischer-Tropsch active phases can form from the core material under the applied reduction and testing conditions. Prospective endeavors should focus on the selection of a core material with an appropriate size range of core materials synthesized, sufficient cobalt concentration and a suitable synthesis method to ensure complete Co_3O_4 shell formation of the desired thickness around the core nanoparticles. It may also be of interest in future systems, that routes to minimize the strain on the surface be examined, e.g. by increasing the thickness of the cobalt shell.

8 Appendix A: Calculations

The dispersion of cobalt was estimated using the following formula:

$$\text{Dispersion} = \frac{\text{Volume } H_2 \text{ adsorbed}}{22414 \text{ ml/mol}} \times \frac{\text{Molar mass of cobalt}}{\text{Wt. \% Co in catalyst}} \times \text{stoichiometric factor of } 2 \times 10000.$$

The active metal surface area was determined from:

$$\text{Active metal surface area of cobalt} =$$

$$\frac{\text{Volume } H_2 \text{ adsorbed}}{22414 \text{ ml/mol}} \times \text{Avogadro's number} \times \text{stoichiometric factor of } 2 \times \text{cross-sectional area of a cobalt atom}$$

.

The degree of reduction was calculated using:

$$\text{Degree of reduction of cobalt} = \frac{\text{Moles of cobalt oxidized}}{\text{Moles of cobalt in sample}} \times 100.$$

The cobalt-time yield (activity) was determined from:

Corrected CO space velocity = Syngas space velocity x 0.33

$$\text{Activity in } \mathrm{mmol_{CO} \cdot g^{-1} \cdot hr^{-1}} = \frac{\text{Corrected CO space velocity}}{\text{STP}} \text{ x CO conversion x } 1000$$

$$\text{Activity in } \mathrm{mmol_{CO} \cdot g_{Co}^{-1} \cdot hr^{-1}} = \frac{\text{activity in } \mathrm{mmol_{CO} \cdot g^{-1} \cdot hr^{-1}}}{\text{Cobalt loading}}$$

$$\text{Activity in } \mathrm{mol_{CO} \cdot g_{Co}^{-1} \cdot s^{-1}} = \frac{\text{Activity in } \mathrm{mmol_{CO} \cdot g_{Co}^{-1} \cdot hr^{-1 \div 1000}}}{3600}$$

The turnover frequency (TOF) was determined from:

$$\text{TOF} = \frac{\text{Activity in } \mathrm{mol_{CO} \cdot g_{Co}^{-1} \cdot s^{-1}}}{\text{2 x moles of hydrogen uptake from chemisorption}}$$

9 Appendix B: Additional characterization results and discussion

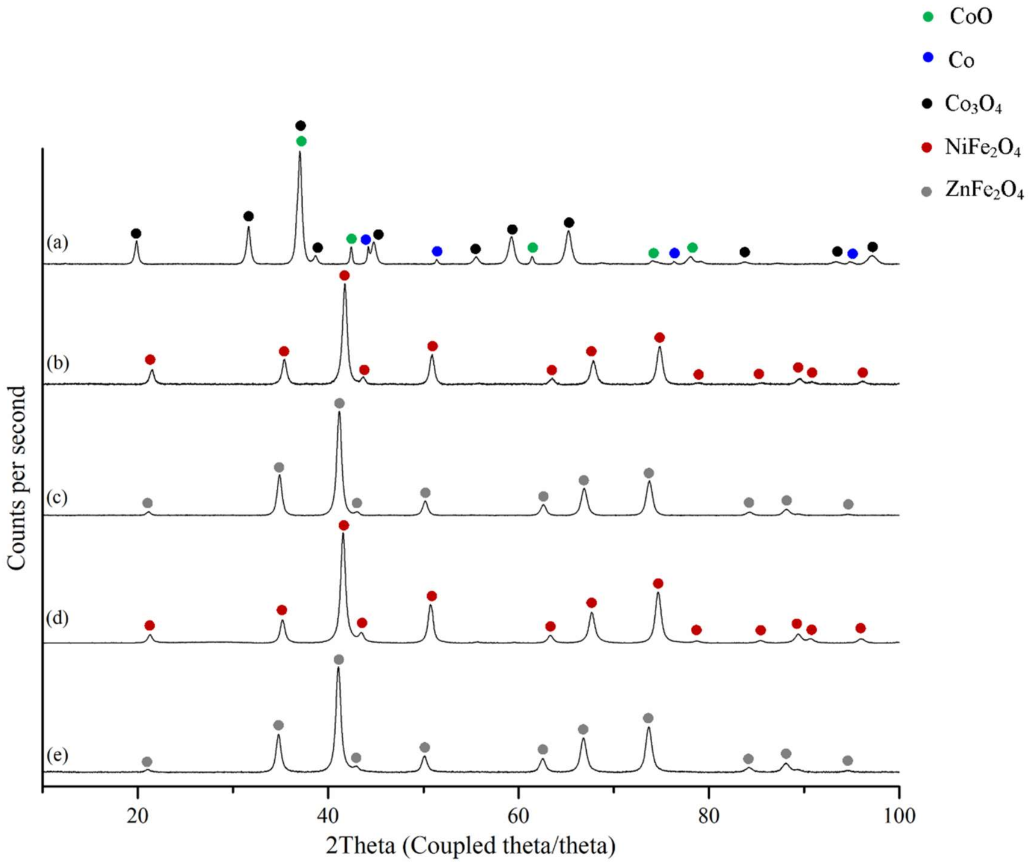

Figure B.1. Powder X-ray diffraction pattern of (a) Co_3O_4 nanoparticles; (b) $NiFe_2O_4$; (c) $ZnFe_2O_4$; (d) $NiFe_2O_4$@Co_3O_4 and (e) $ZnFe_2O_4$@Co_3O_4.

Table B.1. Phases present in the sample analyzed and the abundance and average crystallite size as determined using Rietveld refinement of the powder XRD data.

Sample	**Phases**	**Relative abundance /mass %**	**$d_{crystal}$[a] /nm**	**χ^2 /%**	**R_{wp} /%**
	Co_3O_4	90.3	14		
Co_3O_4	CoO	6.3	47	2.6	1.9
	Co	3.4	41		
$NiFe_2O_4$	$NiFe_2O_4$	100	14	1.2	2.2
Co_3O_4@$NiFe_2O_4$	$NiFe_2O_4$	100	15	6.2	3.7
$ZnFe_2O_4$	$ZnFe_2O_4$	100	14	2.6	1.7
Co_3O_4@$ZnFe_2O_4$	$ZnFe_2O_4$	100	14	2.2	1.9

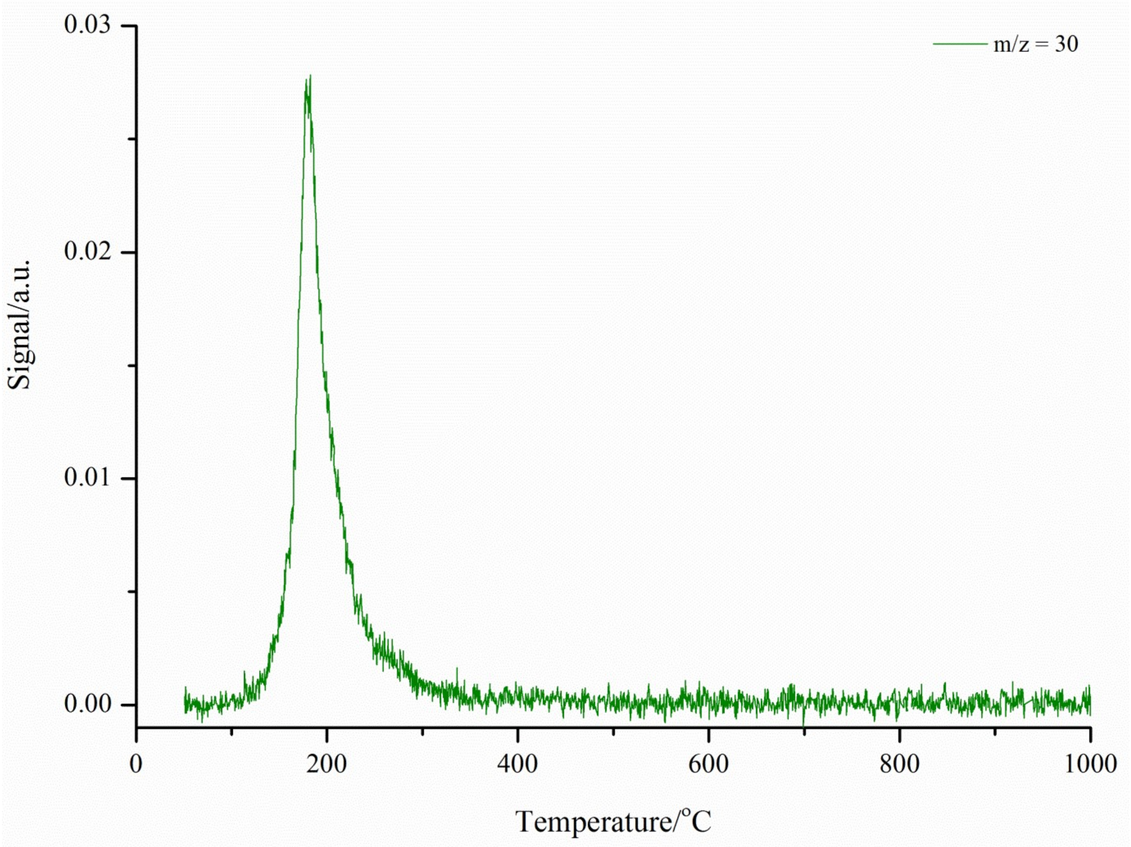

Figure B.2. Profile of NO^+ (m/z = 30) determined in the effluent gas from the TPR of Co_3O_4.

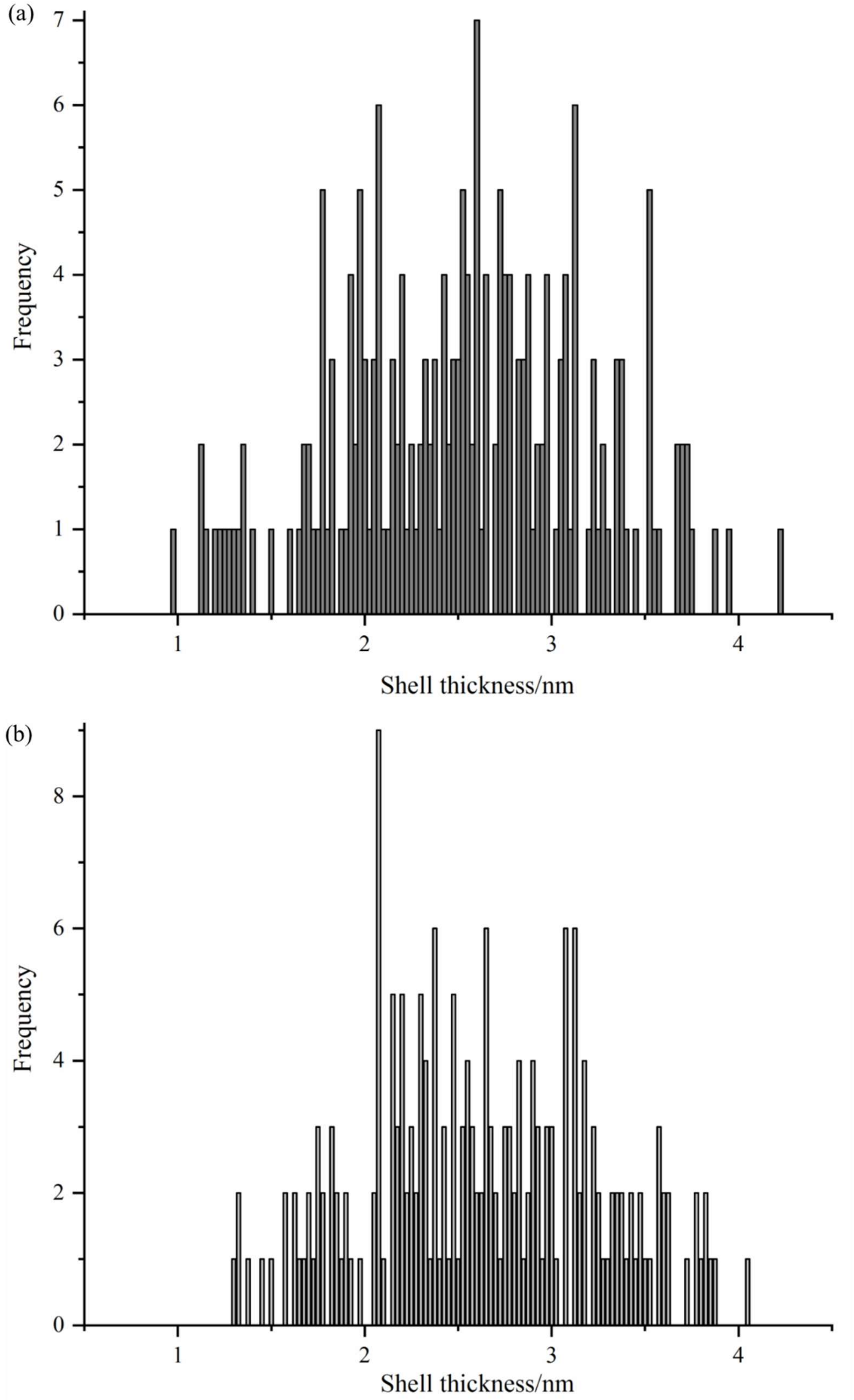

Figure B.3. Histogram of the shell thickness distribution for $NiFe_2O_4$@Co_3O_4 core-shell nanoparticles obtained (a) prior to reduction and during the *in-situ* TEM reduction at (b) 180°C in H_2 (1 atm) for 2 hours.

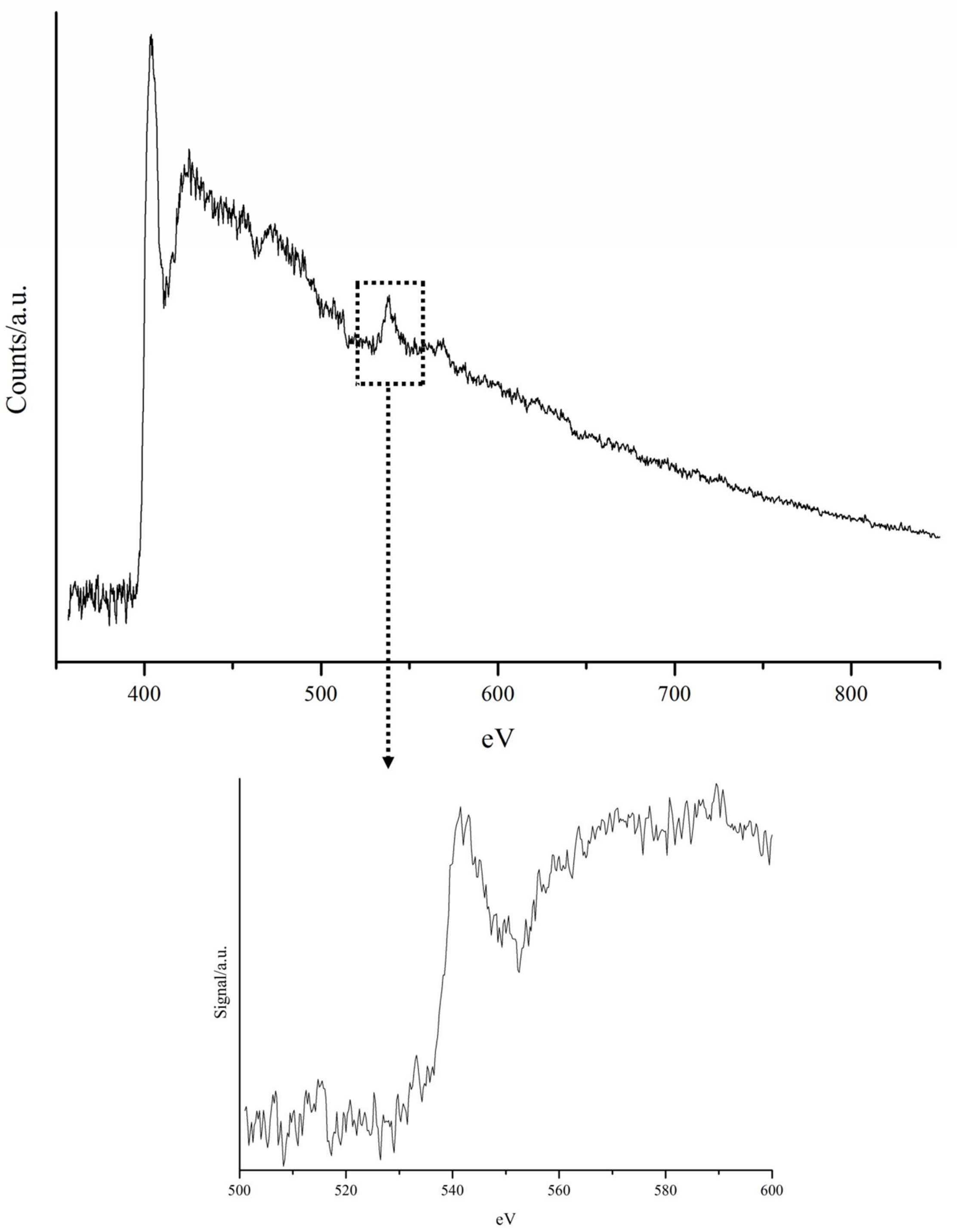

Figure B.4: EELS spectrum of the SiN window of the *in-situ* TEM cell. The O-K edge is zoomed in for clarity.

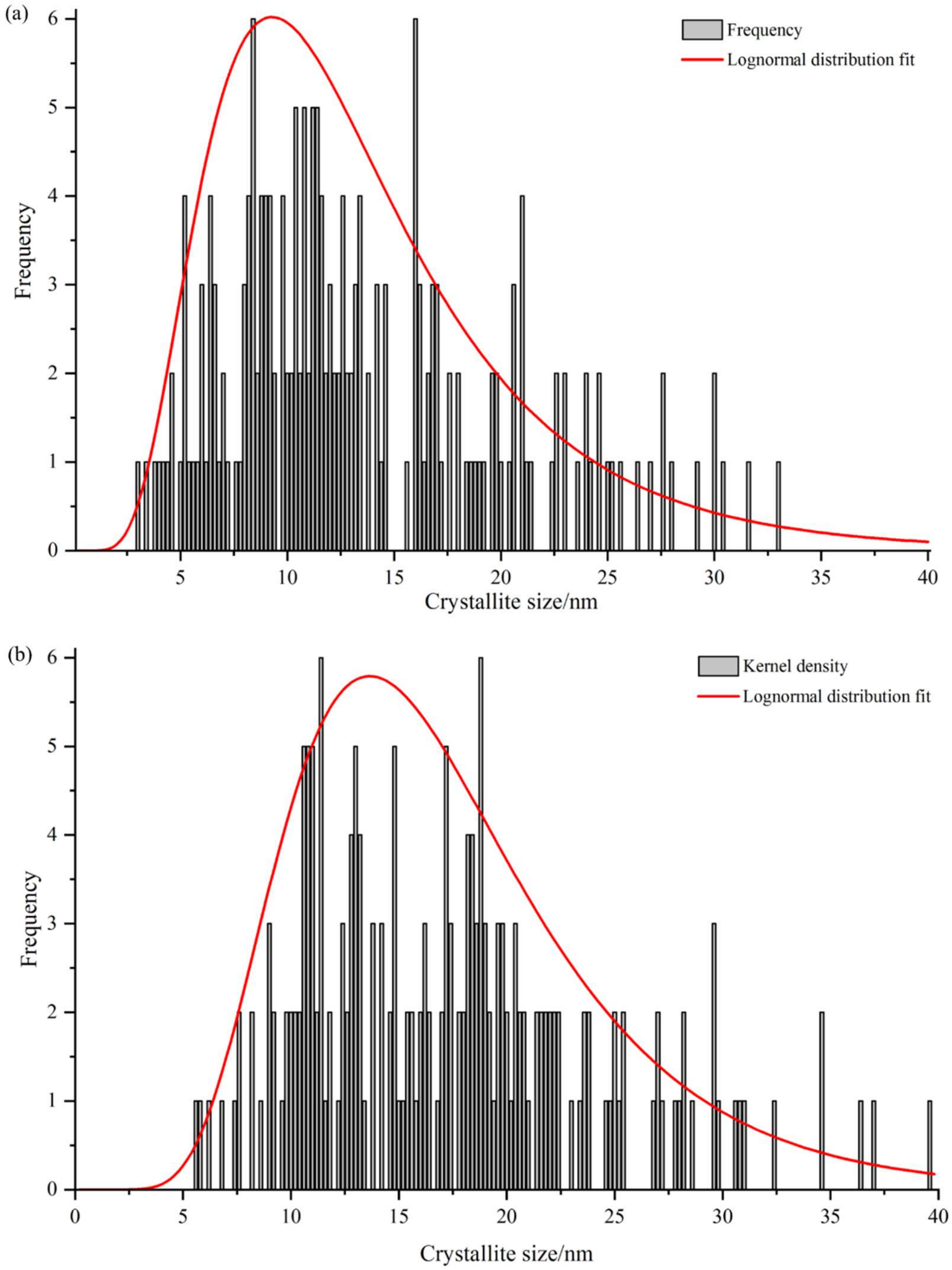

Figure B.5. Histogram of the crystallite size distribution for $NiFe_2O_4@Co_3O_4$ core-shell nanoparticles (a) fresh and (b) after reduction at 180°C (1 hour) and exposure to Fischer-Tropsch synthesis conditions (used$_{180}$).

Table B.2. Statistical data obtained from the lognormal distribution functions fitted onto the NiFe2O4@Co3O4 crystallite size data.

Sample	**Mode**	**95% CI[a] (Mode)**	**Median**	**95% CI[a] (Median)**	**Mean**	**95% CI[a] (Mean)**	**FWHM[b]**	**95% CI[a] FWHM**
$NiFe_2O_4$@Co_3O_4, fresh	9.3	9.2 – 9.3	12.0	12.0 – 12.1	13.7	13.6 – 13.8	11.8	11.7 – 11.9
$NiFe_2O_4$@Co_3O_4, $used_{180}$	13.7	13.6 – 13.8	16.1	16.0 – 16.2	17.5	17.4 – 17.6	13.5	13.4 – 13.7

[a] CI refers to the confidence interval.

[b] FWHM is the full width at half maximum.

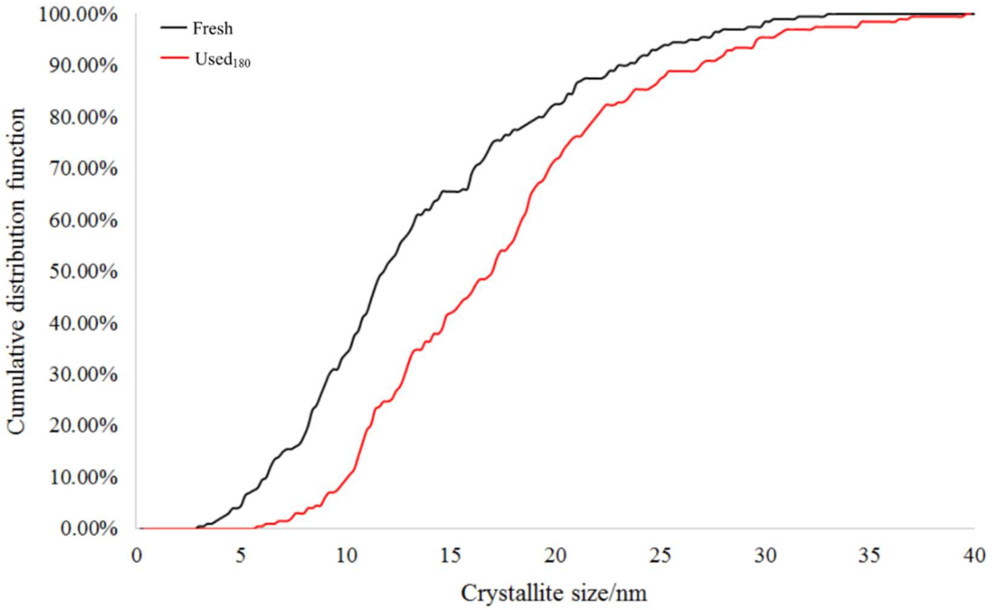

Figure B.6. Cumulative distribution functions showing the crystallite distribution of $NiFe_2O_4$@Co_3O_4 core-shell nanoparticles obtained prior to reduction and after reduction at 180°C (1 hour) and exposure to Fischer-Tropsch synthesis conditions ($used_{180}$).

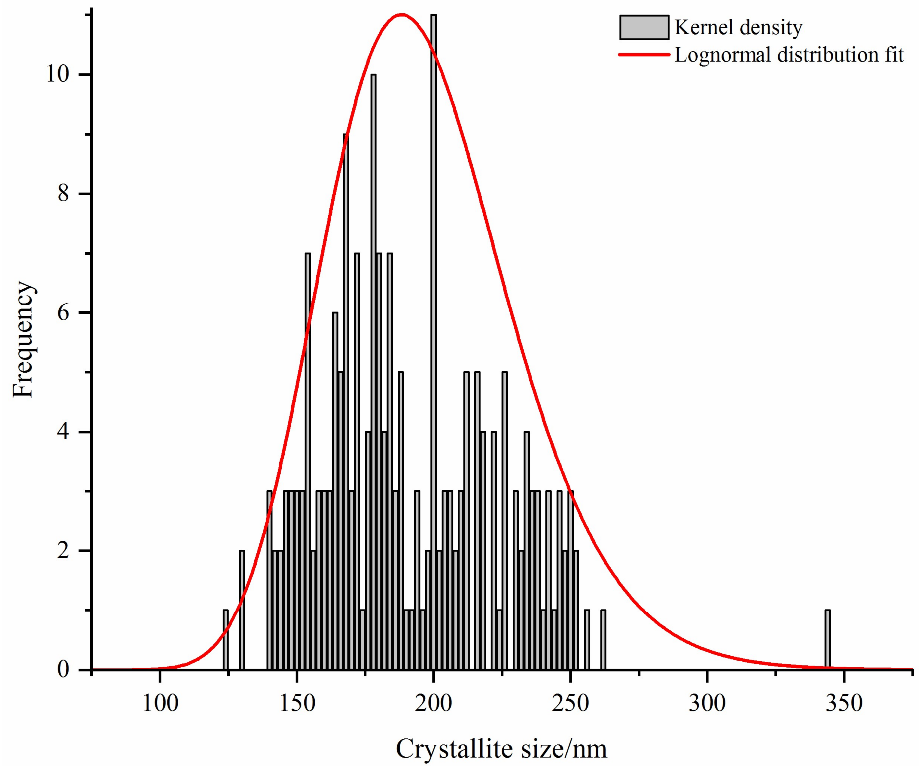

Figure B.7. Histogram of the crystallite size distribution for Stöber silica spheres.

Table B.3. N_2-physisorption results for Stöber silica spheres and supported $NiFe_2O_4@Co_3O_4$.

Sample	**BET surface area[a]/m^2 g^{-1}**	**BJH desorption pore volume[b]/cm^3 g^{-1}**	**BJH desorption average pore diameter[c]/nm**
Stöber silica spheres	54	0.14	9.1
$NiFe_2O_4@Co_3O_4/SiO_2$	37	0.10	7.5

[a] Error = ± 6 m^2 g^{-1}

[b] Error = ± 0.08 cm^3 g^{-1}

[c] Error = ± 1.5 nm

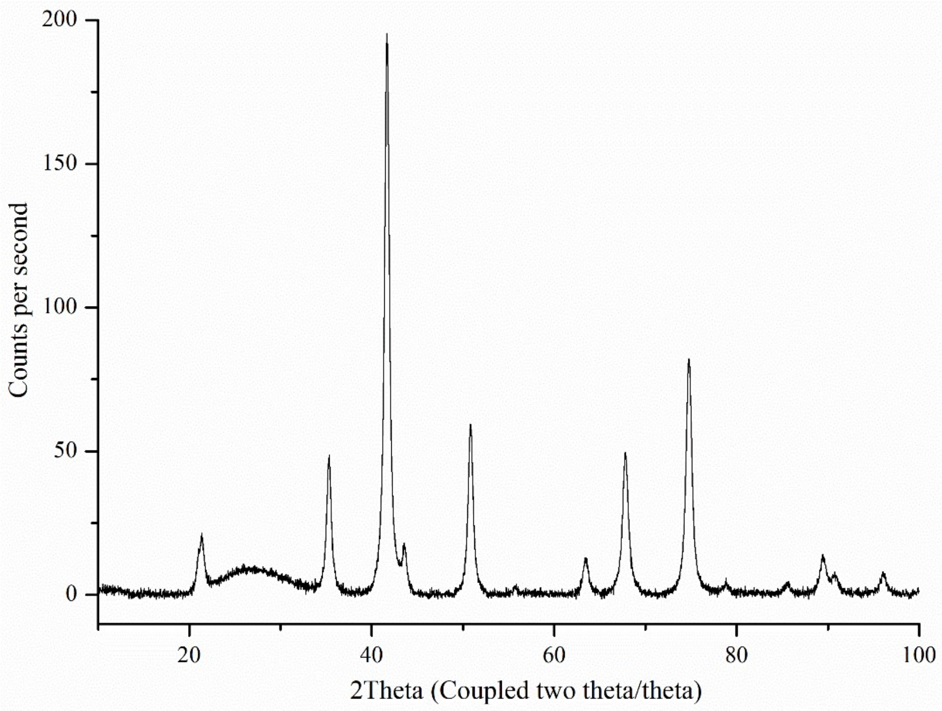

Figure B.8. Powder X-ray diffraction pattern of $NiFe_2O_4@Co_3O_4/SiO_2$.

Table B.4. Phases present in the sample analyzed and the abundance and average crystallite size as determined using Rietveld refinement of the powder XRD data.

Sample	χ^2/%	R_{wp}/%	Phase	Relative abundance/mass %	L_{vol}-IB/nm
$NiFe_2O_4@Co_3O_4/SiO_2$	1.5	1.4	$NiFe_2O_4$	100	12

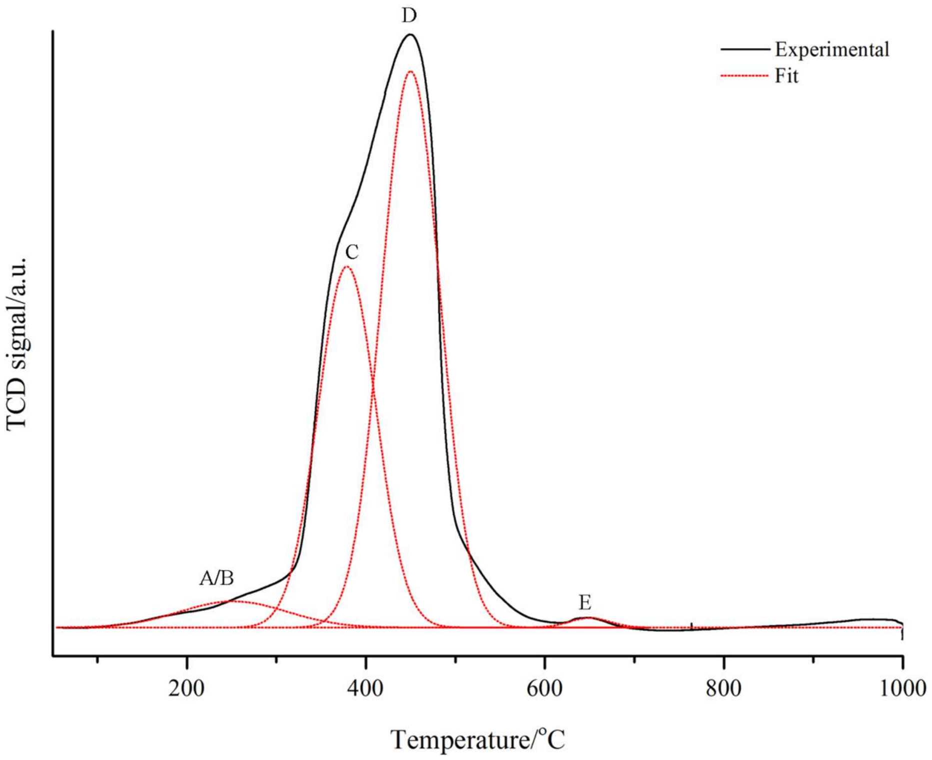

Figure B.9. TPR profile of $NiFe_2O_4@Co_3O_4/SiO_2$ (replicate 1) showing peak fitting and positions.

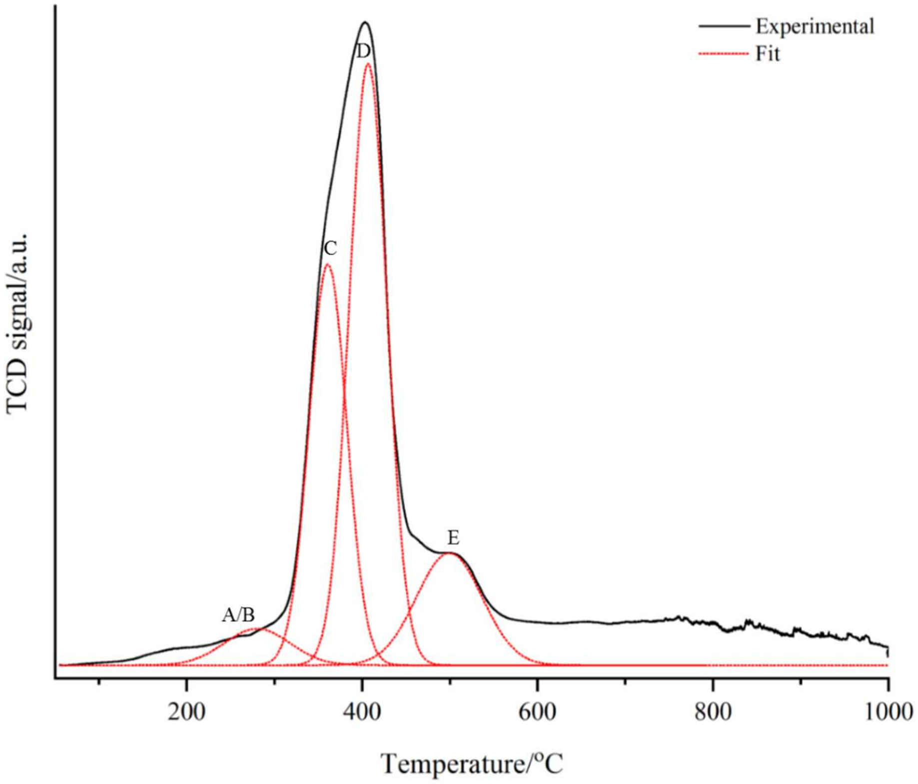

Figure B.10. TPR profile of $NiFe_2O_4@Co_3O_4/SiO_2$ (replicate 2) showing peak fitting and positions.

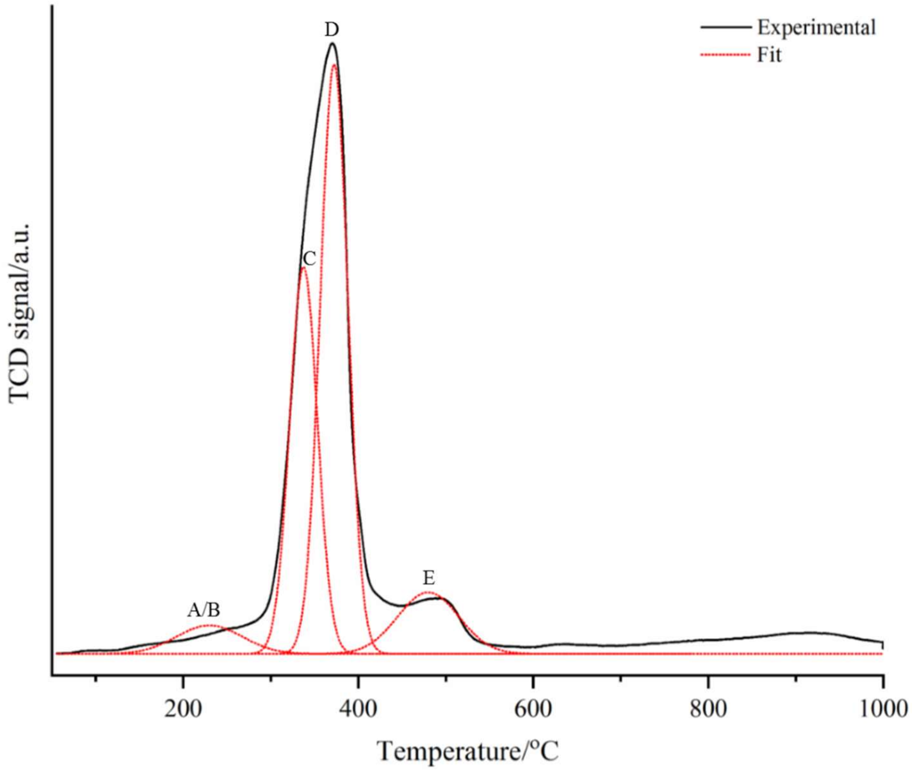

Figure B.11. TPR profile of $NiFe_2O_4@Co_3O_4/SiO_2$ (replicate 3) showing peak fitting and positions.

Table B.5. Temperature maxima from the H_2-TPR profiles of $NiFe_2O_4@Co_3O_4$ and $NiFe_2O_4@Co_3O_4/SiO_2$. The peak positions for $NiFe_2O_4@Co_3O_4$ were given in Figure 4.3 in Chapter 4 whilst that for $NiFe_2O_4@Co_3O_4/SiO_2$ is given in Figure B.9 – Figure B.11.

Sample	**Mass used/g**	**T_{max}/°C**				
		Peak A	**Peak B**	**Peak C**	**Peak D**	**Peak E**
$NiFe_2O_4@Co_3O_4$	0.0512	164	226	330	377	404
$NiFe_2O_4@Co_3O_4/SiO_2$ (replicate 1)	0.524	252		379	450	650
$NiFe_2O_4@Co_3O_4/SiO_2$ (replicate 2)	0.0530	280		361	407	499
$NiFe_2O_4@Co_3O_4/SiO_2$ (replicate 3)	0.049	230		338	372	480